GNSS Propagation Channel Modeling in Constrained Environments: Contribution to the Improvement of the Geolocation Service Quality/

Ni Zhu

N° d'ordre: | * | * | *

Institut Français des Sciences et Technologies des Transports, de l'Aménagement et des Réseaux
Université de Lille

THÈSE de Doctorat

en

Sciences de l'Information et de la Communication

par

Ni ZHU

Doctorat délivré par l'Université de Lille

GNSS Propagation Channel Modeling in Constrained Environments: Contribution to the Improvement of the Geolocation Service Quality

Modélisation du Canal de Propagation GNSS en Milieu Contraint: Contribution à l'Amélioration de la Qualité de Service de Géolocalisation

Soutenue le 2 Octobre 2018 devant le jury d'examen :

Rapporteurs	
Pr. Heidi Kuusniemi	Finnish Geospatial Research Institute (FGI), NLS, Finland Director, Digital Economy, University of Vaasa, Finland
Pr. Alessandro Neri	Engineering Department of the University Roma Tre, Italy
Examinateurs	
Pr. Jean-Yves Tourneret	INP-ENSEEIHT, Toulouse, France
Pr. Maan El Badaoui El Najjar	Université de Lille
Directeurs de thèse	
Dr. Marion Berbineau	Directrice de Recherche, COSYS/LEOST, IFSTTAR
Dr. David Bétaille	Directeur de Recherche, COSYS/SII, IFSTTAR
Encadrante de thèse	
Dr. Juliette Marais	Chargée de Recherche, COSYS/LEOST, IFSTTAR
Invités	
Mme. Sarab Tay Guyot	Ingénieure de Recherche, AKKA Technologie, France
Mr. Bernard Bonhoure	Expert Navigation GNSS, CNES, Toulouse, France

École Doctorale Sciences pour l'ingénieur ED 072 - PRES Université Lille Nord de France

GNSS Propagation Channel Modeling in constrained environments: Contribution to the improvement of the geolocation service quality

Abstract : From user guidance applications to trains or road vehicles fleet management, Global Navigation Satellite System (GNSS)-based positioning systems are more and more spread and used in urban environments. However, urban environments present great challenges for GNSS positioning since numbers of obstacles result in signal attenuations and blockages, which can cause large errors. Yet, for new GNSS land applications, knowing the certainty of one's localization is of great importance especially for the liability/safety critical applications such as automated driving, electronic road tolling or railway signaling. The concept of GNSS integrity, which is defined as a measure of trust to be placed in the correctness of the information supplied by the total system, can help to meet this requirement.

Although GNSS integrity has been firstly developed and formalized in the aviation field, the algorithms developed for the aerospace domain cannot be introduced directly to the GNSS land applications. This is because a high data redundancy exists in the aviation domain and a basic hypothesis that only one failure occurs at a time is made for aviation schemes, which are not the case for the urban users. It is a great challenge to extend the integrity monitoring algorithms to GNSS urban applications.

The main objective of this PhD research work is to improve the performance of GNSS positioning in urban environment, especially the performance of accuracy and integrity. Under this framework, two research directions were investigated:

- The first direction of this PhD research mainly consists of GNSS measurement error characterization in order to improve the positioning accuracy in stringent environments. Several error models existed in the literature are investigated and evaluated, for instance the signal carrier-power-to-noise-density ratio (C/N0) dependent variance model, the satellite elevation dependent variance model as well as the Dirichlet Process Mixture (DPM) model. A new hybrid model is proposed while involving the contribution of the digital map to distinguish the signal reception state LOS/NLOS.

- The second direction contributes to the Fault Detection and Exclusion (FDE) techniques so as to improve the GNSS integrity performance in urban environments. Different FDE methods, which can be potentially applied on the land GNSS-based applications, are investigated and compared with real GPS data collected in urban canyon. Two classes of FDE strategies are involved: the snapshot Least-Square-Residual (LSR)-based one and the sequential Extended-Kalman-Filter (EKF) innovation-based one. A new method of HPL computation by taking into consideration of the potential prior fault is proposed.

Then, these two research directions are combined together and the computation of Horizontal Protection Level (HPL) is added at the next step so that a complete integrity monitoring scheme is constructed.

The results with real GPS data collected in urban canyon show that the accuracy and integrity performance of positioning can be improved with the proposed scheme compared to the traditional approaches. The proposed integrity monitoring scheme is promising to be implemented in the low-cost GNSS commercial receivers for urban transport applications.

Keywords : GNSS, Integrity monitoring, Fault Detection and Exclusion (FDE), Urban environments.

Modélisation du canal de propagation GNSS en milieu contraint: Contribution à l'amélioration de la qualité de service de géolocalisation

Résumé : Au cours des dernières décennies, de plus en plus d'applications de transport urbain basées sur les systèmes de positionnement par satellites (GNSS) ont vu le jour. Des applications exigent une fiabilité critique comme le télépéage basé sur l'utilisation du GNSS, pour lesquelles des erreurs de positionnement peuvent entraîner de graves conséquences. Pourtant, les environnements urbains présentent de grands défis pour le positionnement GNSS en raison de l'existence des trajets multiples et des signaux NLOS (None-Line-of-Sight). Le concept d'intégrité GNSS, qui est défini comme une mesure de confiance qui peut être placée dans l'exactitude des informations fournies par le système de navigation, peut aider à répondre à cette exigence.

Bien que l'intégrité GNSS ait d'abord été développée et formalisée dans le domaine de l'aviation, les algorithmes développés pour l'aérospatial ne peuvent pas être introduits directement dans les applications terrestres. Parce qu'il existe une forte redondance des données en ciel dégagé et que l'hypothèse d'une seule défaillance à la fois est faite pour les applications aéronautiques. C'est un grand défi d'étendre les algorithmes de surveillance de l'intégrité GNSS aux applications terrestres et notamment urbaines.

L'objectif principal de cette recherche est d'améliorer la performance du positionnement GNSS en milieu urbain, en particulier les performances de précision et d'intégrité. Dans ce cadre, deux directions de travail ont été prises:

- La première direction consiste principalement en la caractérisation d'erreurs de mesure GNSS afin d'améliorer la précision de positionnement dans les environnements contraints. Plusieurs modèles d'erreur existant dans la littérature sont étudiés et évalués. Un nouveau modèle hybride est proposé qui implique la contribution de la carte numérique pour distinguer l'état de réception du signal LOS/NLOS ainsi que les corrections des erreurs de pseudorange.
- La seconde direction contribue aux techniques de détection et d'exclusion des défauts (FDE) afin d'améliorer les performances de l'intégrité GNSS dans les environnements urbains. Différentes méthodes FDE, qui peuvent être potentiellement appliquées en navigation GNSS terrestre, sont étudiées et comparées avec des données GPS collectées dans des canyons urbains. Deux classes de stratégies FDE sont examinés: l'une fondée sur l'instantané LSR (Least-Squares-Residual) et l'autre basée sur l'innovation séquentielle Extended-Kalman-Filter (EKF). Et le calcul du niveau de protection horizontal (HPL) est ajouté à la prochaine étape. Une nouvelle méthode de calcul HPL prenant en compte un potentiel défaut immédiatement antérieur est proposée.

Ensuite, ces deux directions de travail sont combinées de sorte qu'un système complet de surveillance de l'intégrité est construit. Les résultats avec les données réelles montrent que la précision et l'intégrité du positionnement peuvent être améliorées avec le système proposé par rapport aux approches traditionnelles. Le système de surveillance de l'intégrité proposé est prometteur dans les récepteurs commerciaux GNSS à faible coût pour les applications de transport urbain.

Mots clés : GNSS, la surveillance de l'intégrité, la détection et l'exclusion des défauts (FDE), l'environnement urbain

Acknowledgment

This PhD research work was carried out in the IFSTTAR (French Institute of Science and Technology for Transport, Development and Networks) with the financial support of the CNES (Centre National d'Études Spatiales) and the Region Hauts-de-France.

J'adresse mes premiers remerciements et ma reconnaissance à mes directeurs de thèse: Marion Berbineau et David Bétaille, Directeurs de Recherche (DR) à l'IFSTTAR. Je tiens à remercier également mon encadrante de thèse Juliette Marais, Chargée de Recherche (CR) à l'IFSTTAR. Je vous remercie pour avoir dirigé et de m'avoir aidée à construire mon projet de thèse au cours de ces trois dernières années avec votre sens pédagogique. Merci pour la confiance que vous m'avez accordée, la patience et les encouragements que vous m'avez donnés. J'ai beaucoup apprécié travailler avec vous. En particulier, merci à Marion et Juliette de m'avoir accueillie au sein du laboratoire LEOST (Laboratoire Électronique Ondes et Signaux pour les Transports) à Villeneuve d'Ascq pendant les deux premières années de thèse. Merci à David de m'avoir accueillie au sein du laboratoire SII (Structures et Instrumentation Intégrée) pendant la troisième année de thèse à Nantes.

I would like to express my thanks to the jury of this thesis for attending my defense in particular Prof. Heidi Kuusniemi and Prof. Alessandro Neri, who kindly accepted to review my dissertation during their vacation. Many thanks for your constructive comments and remarks which help me to improve the quality of the thesis.

Mes remerciements iront également à l'endroit de mes chers collègues de l'IFSTTAR, avec qui j'ai pu travaller dans une très bonne ambiance. Merci à mes amis doctorants (docteurs) à l'IFSTTAR de Villeneuve d'Ascq: Lucas, Hussein, Pierre, Ci, Baisi, Zeting... J'oublie pas le "bowling" de départ que vous avez organisé pour moi. Merci également mes collègues de l'IFSTTAR Nantes, en particulier Vincent et Jean d'avoir accepté de m'accueillir pendant la troisième année de thèse au sein du laboratoire SII.

Je remercie Mr. Bernard Bonhoure, mon responsable de CNES, de suivre ma thèse et de participer à des réunions d'avancement de ma thèse.

Finally, I would like to express my gratitude to my family. I want to thank my parents Zhiwei, Linchun and my brother Yichao for their love and encouragement. I would like to thank my husband, Zhiqiang, for his endless support and the sacrifice he made. Of course, I don't forget to thank my dearest daughter, Fabienne, who is my sweetest burden and brightens my life.

N. ZHU Nantes - September 18^{th} 2018.

Contents

List of Figures

List of Tables

Acronyms

ABAS Airborne-Based Augmentation System.

AL Alert Limit.

ARAIM Advanced Receiver Autonomous Integrity Monitoring.

ATM Air Traffic Management.

BDS BeiDou Navigation Satellite System.

CDF Cumulative Distribution Function.

CS Cycle Slip.

CT Classic Test.

DLL Delay Lock Loop.

DoF Degree of Freedom.

DOP Dilution of Precision.

DP Dirichlet Process.

DPM Dirichlet Process Mixture.

ECA Error Characterization Approach.

ECEF Earth-Centered Earth-Fixed.

EGNOS European Geostationary Navigation Overlay Service.

EKF Extended Kalman Filter.

ERTMS European Rail Traffic Management System.

ESA European Space Agency.

ETC Electronic Toll Collection.

EU European Union.

FB Forward-Backward.

FDE Fault Detection and Exclusion.

GAGAN GPS Aided Geo Augmented Navigation.

GBAS Ground-Based Augmentation System.

GDOP Geometric Dilution of Precision.

GIVE Grid Ionosphere Vertical Error.

GLONASS GLObal Navigation Satellite Systems.

GNSS Global Navigation Satellite Systems.

GPS Global Positioning Systems.

GT Global Test.

HAL Horizontal Alert Limit.

HDOP Horizontal Dilution of Precision.

HMI Hazardously Misleading Information.

HPE Horizontal Position Error.

HPL Horizontal Protection Level.

HSI Horizontal Safety Index.

HUL Horizontal Uncertainty Level.

IBCT Innovation-based Classic Test.

IBPL Isotropy-Based Protection Level.

ICR Isotropic Confidence Ratio.

IGP Ionospheric Grid Points.

INS Inertial Navigation System.

IR Integrity Risk.

IW Inverse-Wishart.

JMS Jump Markov System.

KF Kalman Filter.

LAAS Local Area Augmentation System.

LBS Location-Based Service.

LHCP Left-Handed Circular Polarization.

LOS Line-of-Sight.

LS Least Squares.

LT Local Test.

MCMF Multi-Constellation Multi-Frequency.

MDB Minimum Detectable Bias.

MHSS Multiple Hypothesis Separation Solution.

MI Misleading Information.

MRA Measurement Rejection Approach.

MSAS Multi-functional Satellite Augmentation System.

MSF Major Satellite Failure.

NIS Normalized Innovation Squared.

NLOS Non-Line-of-Sight.

NSSE Normalized Sum of Squared Error.

OLS Ordinary Least Squares.

PDF Probability Density Function.

PDOP Position Dilution of Precision.

PE Position Error.

PL Protection Level.

PLL Phase Lock Loop.

PRN Pseudo Random Noise.

PVT Position, Velocity and Timing.

RAIM Receiver Autonomous Integrity Monitoring.

RANSAC RANdom SAmple Consensus.

RHCP Right-Handed Circular Polarization.

RNP Required Navigation Performance.

RPM Random Probability Measure.

RRP Ratio of Reliable Positions.

RTCA Radio Technical Commission for Aeronautics.

SBAS Satellite-Based Augmentation System.

SISA Signal-In-Space Accuracy.

SoL Safety-of-Life.

ST Subset Test.

TDOP Time Dilution of Precision.

TOA Time of Arrival.

TTA Time to Alert.

UAV Unmanned Aerial Vehicle.

UDRE User Differential Range Error.

UERE User Equivalent Range Error.

UIRE User Ionosphere Range Error.

UIVE User Ionosphere Vertical Error.

UMF Unobservable Multiple Fault.

UMM Urban Multipath Model.

URA User Range Accuracy.

UTM Urban Trench Model.

VAL Vertical Alert Limit.

VDOP Vertical Dilution of Precision.

VPL Vertical Protection Level.

WAAS Wide Area Augmentation System.

WEKF Weighted Extended Kalman Filter.

WLS Weighted Least Squares.

Chapter 1

Introduction

Contents

1.1 General Context

Global Navigation Satellite Systems (GNSS) refers to the total constellations of satellites providing signals from space that transmit positioning and timing data to GNSS receivers. GNSS receivers are able to estimate their own positions with the help of its ranging measurements. Several GNSS constellations exist. Two of them are currently fully functional at a global level: the Global Positioning Systems (GPS) which is maintained by the United States Government, and the GLObal Navigation Satellite Systems (GLONASS) which is operated by the Russian Aerospace Defense Forces. Two additional systems are being planned and completed: the Galileo positioning system by the European Union (EU) and the European Space Agency (ESA), and the Chinese BEIDOU/Compass navigation system. They shall be fully functional by 2020 at the earliest.

In the past decades, GNSS have continually evolved and the domains of GNSS-based applications have much extended. These GNSS applications cover a variety of market segments [1]:

- Aviation: This segment continues to increasingly rely on GNSS, including the newly emerging Unmanned Aerial Vehicles (UAVs);
- Road: More and more GNSS-based road transport applications appear recently, especially the liability critical applications (such as the autonomous vehicles, the Electronic Toll Collection (ETC), *etc.*). New challenges arise for GNSS since not only accuracy but also integrity are required by these applications;
- Rail: Railways have already introduced satellite-based localization systems for non-safety related applications. Driven by economic reasons, the use of these systems for new services and, in particular, their introduction in signaling system is seriously investigated today and tested all around the world (such as the European Rail Traffic Management System (ERTMS)). [2]
- Location-Based Service (LBS): This segment covers lots of GNSS applications in daily life, such as the typical software applications for smartphones which require knowledge about where the user is located. According the user's positions, the LBS could provide the user with the nearest sites of interest (restaurants, banks, post offices *etc.*);
- Others: GNSS-based applications are not limited to the segments above. A wide range of GNSS-based applications exist such as maritime navigation, agriculture management, timing and synchronization for different sectors, *etc.*

Among all the GNSS-based applications mentioned above, there is a high coverage of urban applications. The demand for cost-effective but highly capable GNSS navigation devices for urban utility is clearly growing at an exponential rate. GNSS-based urban applications

present challenging tasks for GNSS navigation since GNSS signals are distorted by multipath and attenuated by fading effects due to numerous obstacles in urban environments.

For certain newly emerged urban GNSS-based applications, such as ETC or the ERTMS mentioned above, not only the positioning accuracy but also its reliability is required. And the latter has recently attracted more and more attention from urban GNSS users. If we reclassify all the GNSS-based applications based on the level of reliability, they can be divided into the following three categories:

- Safety-critical: This refers to the applications, in which the occurrence of a positioning error can lead to death or physical injuries. We can also call them Safety-of-Life (SoL) services. A typical example of this category is the GNSS-based Air Traffic Management (ATM);
- Liability-critical: For liability-critical applications, the computed Position, Velocity and/or Time (PVT) are used as the basis for legal decisions or economic transactions. Large positioning errors can lead to wrong legal decisions or wrong charge computations such as for ETC.
- No liability: This category include all the other GNSS-based applications which don't fit the two categories mentioned above. For instance, the LBS applications are no liability.

In fact, the reliability defined here corresponds to one of the Required Navigation Performance (RNP) parameters for aviation navigation (Fig.1.1): integrity. Integrity is defined as a measure of trust which can be placed in the correctness of the information supplied by the total system [3]. Traditionally, integrity monitoring has focused on the safety-critical applications such as approach or landing phases of airplanes. The integrity monitoring algorithms for aviation utility are well designed (such as the Receiver Autonomous Integrity Monitoring (RAIM)) and the corresponding specifications are set in detail in [4]. And this research is still being progressing towards the use of Multi-Constellation Multi-Frequency (MCMF) GNSS, such as the Advanced Receiver Autonomous Integrity Monitoring (ARAIM). Meanwhile, several GNSS augmentation systems (such as the American Wide Area Augmentation System (WAAS) and the European Geostationary Navigation Overlay Service (EGNOS)) transmit integrity information, which can help guarantee the positioning integrity for civil aviation users.

Nevertheless, the existing aviation integrity monitoring algorithms, their specifications as well as the integrity information provided by augmentation systems are not appropriate to be used directly for applications in urban environments. This is because urban environment is quite different from the open-sky.

Urban environments present great challenges to common commercial GNSS receivers. The

Figure 1.1 – GNSS Required Navigation Performance (RNP) Parameters for Aviation Navigation

main difficulty for GNSS positioning in urban environments is the existence of local effects due to the nearby obstacles. The most harmful ones are known as Non-Line-of-Sight (NLOS) reception and the multipath interference. These two phenomena are not exactly the same although sometimes they occur together. The multipath phenomenon refers to the case that the reflected signals are received together with the Line-of-Sight (LOS) signal while the NLOS reception occurs when the LOS signal is blocked and only the reflected signal is received. The latter one is particularly common in dense urban areas where tall buildings block lots of signals. The multipath phenomenon and the NLOS receptions strongly affect the positioning quality that can introduce large errors (up to several kilometers). Moreover, the satellite visibility is usually poor in urban canyon because of obstacles.

However, the algorithms developed in aviation fields are under the assumption that only one failure occurs at a time and based on the fact that a high data redundancy exists. These are hardly true in urban environments due to the reasons mentioned above.

No doubt, it is essential to guarantee the positioning performances, such as accuracy and integrity, for urban transport applications, especially the liability critical ones. How to improve positioning accuracy by eliminating the frequent measurement faults and how to correctly transfer the concept of integrity from civil aviation applications to the mass-market urban GNSS applications are currently hot topics since no well-developed integrity monitoring algorithm is ready to be implemented by the urban applications in real time.

1.2 Research Objectives

As described in the previous paragraphs, GNSS positioning performances, especially accuracy and integrity, are usually poor in urban environments due to existing local effects. For personal navigation applications, especially liability-critical ones, knowing one's positions as well as the certainty of the positioning information provided by navigation system are extremely important. The global objective of this research work is to improve the geolocation service quality of GNSS in constrained environments. The geolocation performances targeted here in this research work are mainly GNSS positioning accuracy and integrity with the presence of severe signal disturbances such as multipath and NLOS.

Thus, more precisely, this overall objective can be divided into the following sub-objectives:

1. The first phase of this thesis is mainly to better characterize the GNSS measurement errors in stringent environments in order to improve GNSS positioning accuracy. So it is necessary to analyze the main sources of GNSS measurement errors especially the local effects induced by multipath and the NLOS receptions. This includes:

   - To review and to implement the existing measurement error models, which allow considering the real-time local effects. To evaluate and to compare their performance with real GNSS data collected in urban environments.

   - To propose new error models which can better characterize measurement errors in urban environments for low-cost commercial GNSS receivers.

2. The second main part of this research work is to guarantee the GNSS positioning integrity for urban personal navigation applications as well as the liability critical ones. That is to say, the erroneous measurements should be detected and further identified if possible. Ideally, if the detection, identification and exclusion of faulty measurements can be properly done, the GNSS positioning integrity can be well guaranteed and its accuracy can also be improved. But the challenges lie on the fact that, firstly, in urban environments, there is often not enough redundancy to realize the identification or even detection. Secondly, when the multiple simultaneous faults happen, the erroneous measurements can possibly correlate among them or even be "absorbed" by their geometry in such a way as to produce a large position error but very small residuals [5], which will make these faults unobservable by the integrity monitoring algorithms. All these challenges make this topic a hot issue in the current GNSS research society.

   Due to the complexity of the GNSS integrity monitoring in urban environments described above, the following sub-objectives will be studied in this thesis:

   - To review the state of the art of the existing integrity monitoring techniques for

aviation and road transport utilities. To understand the difficulties and limitations of implementing the existing integrity monitoring algorithms for urban transport applications;

- To analyze and to evaluate the existing Fault Detection and Exclusion (FDE) algorithms allowing eliminating multiple faults in order to summarize their advantages and disadvantages.

3. Based on the first two phases of research work above, a complete integrity monitoring scheme for low cost urban navigation equipments will be proposed. More precisely, if the first part of this research work concerning the characterization of the measurement errors can be effectively done, it can already reduce or correct measurement errors from upstream of the system. Then, this can already contribute to improving the capability of FDE. Finally, a statistical position error bound, Horizontal Protection Level (HPL), can be calculated. Though the total processing adds complexity to the computation of navigation solution, this integrity monitoring system can enhance navigation accuracy or at least when the fault identification is not available, the system can provide warning to users in the case of unreliable positioning.

   Other sensor hybridizations can be involved afterwards in order to achieve a possibly sub-meter or lane-level accuracy but this is not included in the objective of this thesis.

1.3 Main Contributions and Publications

1.3.1 Main Contributions

The main contributions of this thesis are as follows:

- Providing a complete review of the state of the art for the GNSS positioning integrity monitoring in urban environments while analyzing the limitations of the existing integrity algorithms established in aviation domain as well as the possible research directions around this issue;
- Presenting and analyzing the existing GNSS measurement error models which allow taking into account the real-time local effects. These models are tested and evaluated with real GPS data collected in urban canyons using Weighted Least Squares (WLS) estimator;
- Proposing a novel GNSS measurement error model which combines the information of C/N_0 (carrier-power-to-noise-density ratio), satellite elevations, the signal reception state LOS/NLOS as well as the range corrections for NLOS signals. The signal reception

states and the range corrections are provided by error models established with the help of digital maps, *i.e.*, the Urban Trench Model (UTM) and the Urban Multipath Model (UMM);

- Optimizing the Urban Trench Model (UTM) model by developing a simplified ray tracing model called Urban Multipath Model (UMM) while getting rid of the infinite length street assumption;
- Analyzing and evaluating several HPL computation methods for the snapshot residual-based Receiver Autonomous Integrity Monitoring (RAIM) existing in the literature while choosing the one adapted best for urban GNSS-based applications.
- Evaluating the performance of several FDE techniques with real GPS data, including Classic Test (CT), Subset Test (ST), iterative Local Test (LT), Forward-Backward (FB) Test as well as the Danish Method;
- Proposing the concept of Weighted Extended Kalman Filter (WEKF) by scaling the measurement covariance matrix with the help of more realistic error models;
- Analyzing the differences located between the WLS residual-based snapshot FDE and the Extended Kalman Filter (EKF) innovation-based FDE. Their performances are evaluated with real GPS data collected in urban environments.
- Proposing a complete GNSS integrity monitoring scheme for low cost urban transport navigation system by combining the accuracy enhancement module and the FDE techniques with two classes of estimators (WLS or EKF). The HPL are also calculated and evaluated.
- Proposing a HPL computation method in the framework of EKF innovation-based integrity monitoring algorithm by taking into consideration the potential impact of the former fault on the current navigation solution.

The proposed scheme can enhance GNSS navigation accuracy as well as integrity in stringent environments. This thesis evaluated both snapshot and sequential filtering integrity monitoring approaches. Further extensions, such as hybridizations with different sensors, are possible but not included in the framework of this thesis.

1.3.2 List of Publications

In the framework of this PhD research work, the following publications are published in some international conferences or journals:

* [P1]: Ni Zhu, Juliette Marais, David Bétaille, Marion Berbineau (2017). Evaluation and Comparison of GNSS Navigation Algorithms Including FDE for Urban Transport

Applications, *Proceedings of the Institute of Navigation (ION) International Technical Meeting (ITM)*, January 30-February 2, 2017, Monterey, California, United States.

* [P2]: Ni Zhu, Juliette Marais, David Bétaille, Marion Berbineau (2017). Evaluation and Comparison of GNSS Navigation Integrity Monitoring Algorithms for Urban Transport Applications, *Young Research Seminar (YRS)*, May 16-18, 2017, Berlin, Germany.

* [P3]: Ni Zhu, Juliette Marais, David Bétaille, Marion Berbineau (2018). GNSS Position Integrity in Urban Environments: A Review of Literature. IEEE Transactions on Intelligent Transportation Systems (ITS), Vol.19, Issue 9, pp2762-2778, 17p. DOI: 10.1109/TITS.2017.2766768.

* [P4]: Ni Zhu, David Bétaille, Juliette Marais, Marion Berbineau (2018). GNSS Integrity Enhancement for Urban Transport Applications by Error Characterization and Fault Detection and Exclusion (FDE), *Les Journées Scientifiques 2018 d'URSI (Union Radio-Scientifique Internationale)-France, Géolocalisation et Navigation*, March 28-29, 2018, Meudon, France.

* [P5]: Ni Zhu, David Bétaille, Juliette Marais, Marion Berbineau (2018). Extended Kalman Filter (EKF) Innovation-based Integrity Monitoring Scheme with C/N0 Weighting, *2018 IEEE 4th International Forum on Research and Technology for Society and Industry (RTSI) (RTSI 2018)*, September 10-13, 2018, Palermo, Italy.

* [P6]: Ni Zhu, David Bétaille, Juliette Marais, Marion Berbineau (2018). GNSS Integrity Enhancement for Urban Transport Applications by Error Characterization and Fault Detection and Exclusion (FDE), REE: Revue de l'électricité et de l'électronique after the conference of the URSI (International Union of Radio Science) 2018.

* [P7]: Ni Zhu, David Bétaille, Juliette Marais, Marion Berbineau, GNSS Integrity Monitoring Schemes for Terrestrial Applications in Harsh Environments, submitted to IEEE Intelligent Transportation Systems Magazine (Special Issue on GNSS for ITS) the 1st September.

1.4 Organization and Structure of the Dissertation

With the two main objectives defined above, i.e., to improve the GNSS positioning accuracy and to guarantee its integrity in urban environments, the main content of this dissertation is divided into three parts, in which, 8 chapters are included. Fig. 1.2 depicts the structure of this thesis, which is organized as follows:

* **Part I**. The first part contains the literature review, inside which there are two chapters:

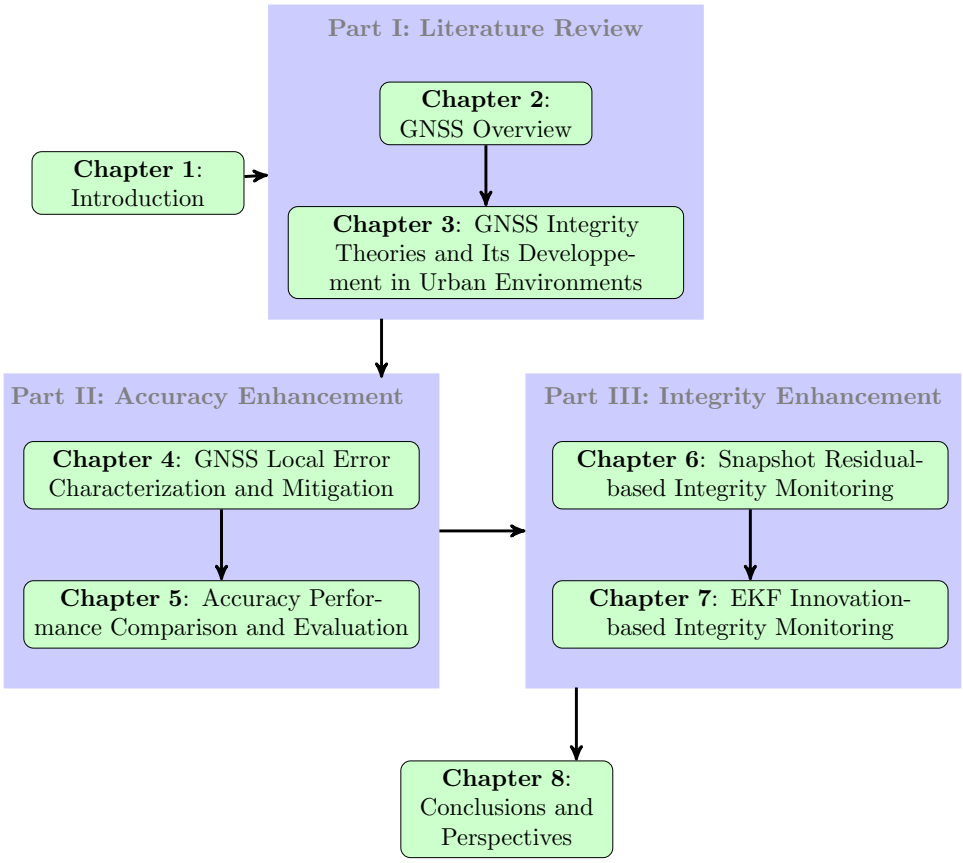

Figure 1.2 – Structure of the Dissertation

- ***Chapter 2*** provides an overview of GNSS system. This includes the introduction of GNSS measurement models, error sources as well as different GNSS position estimators;
- ***Chapter 3*** presents the current state of the art of the GNSS position integrity monitoring in urban environments.

* **Part II**. The second part includes two chapters which mainly address the local effects in urban environments and the error characterizations:

- ***Chapter 4*** deals with the characterization of the errors due to local effects in constraint environments. Several error models existing in the literature are discussed. Moreover, a hybrid model, taking into consideration the the information of C/N_0 (carrier-power-to-noise-density ratio), satellite elevations, the signal reception state LOS/NLOS as well as the range corrections provided by the geometry feature of the digital map, is proposed.
- ***Chapter 5*** firstly makes the calibration for the error models described in Chapter

4. Then these error models are evaluated and tested with real GPS data collected in urban canyons by Weighted Least Squares (WLS) estimators. The accuracy performance is compared.

* **Part III**. The third part includes also two chapters concerning the integrity monitoring with two classes of approaches:
  - ***Chapter 6*** proposes a complete snapshot residual-based integrity monitoring scheme. Five FDE techniques and several HPL computation methods are discussed. Finally, the complete scheme is evaluated with real GPS data collected in urban canyons.
  - ***Chapter 7*** aims at designing an Extended Kalman Filter (EKF) innovation-based integrity monitoring approach, which is a parallel class with the snapshot approach in Chapter 6. Firstly, the concept of Weighted Extended Kalman Filter (WEKF) is proposed by implementing several error models evaluated in Chapter 5 into the EKF. Then, the derivation of HPL computation in the framework of innovation-based approach is made and a new method of HPL computation is proposed. The complete scheme is evaluated with real data collected in urban canyons.
* ***Chapter 8*** draws the conclusions and addresses the possible perspectives for future work.

Part I

LITERATURE REVIEW

Chapter 2

Global Navigation Satellite Systems (GNSS)

Contents

Summary

This chapter aims at introducing the fundamental theories and backgrouds of the Global Navigation Satellite Systems (GNSS). The review of GNSS principles in this section can facilitate the comprehension of the integrity monitoring theories in following chapters. The discussion of this chapter is mainly based on [6–8] and other references mentioned in the text.

The structure of this chapter is as follows: it begins with an overview of GNSS positioning principles. This followed by an introduction of GNSS measurement models and their mathematical expressions. Then the measurement error sources will be detailed according to signal propagation channel. Finally, different GNSS position estimators will be briefly introduced.

2.1 Introduction of the Global Navigation Satellite Systems (GNSS)

2.1.1 An Overview of GNSS

Global Navigation Satellite Systems (GNSS) is a generic term denoting the constellations of satellites providing signals from space that transmit positioning and timing data which enable users to determine their three-dimensional position with global coverage. Several GNSS constellations exist. The US Global Positioning System (GPS) is fully operational since 1995. The Russian GLObal NAvigation Satellite System (GLONASS) was restored to full operation in December 2011. The Chinese BeiDou Navigation Satellite System (BDS) and the European GALILEO system are currently under development although the BDS started an initial operating service (Phase II) in late December 2011 and Galileo has been declared operational in december 2016 for initial services.

Generally speaking, a GNSS constellation can be divided into three major segments as shown in Fig.2.1:

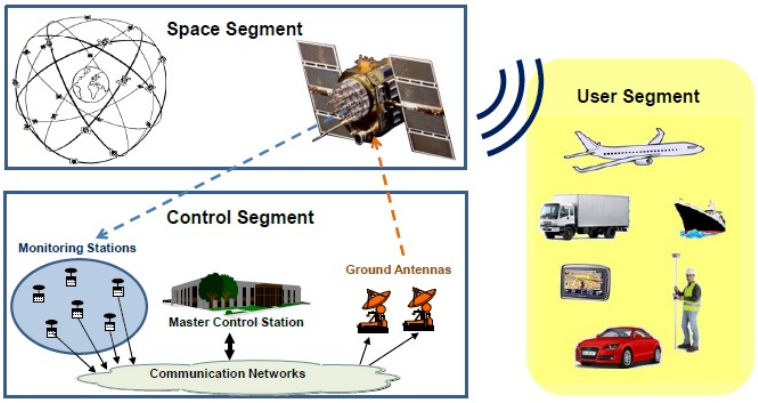

Figure 2.1 – GNSS architecture

- **Space segment**: This segment comprises the satellites from which users make ranging measurements. The main functions of the space segment are to generate and transmit code and carrier phase signals, and to store and broadcast the navigation messages uploaded by the control segment. The space segment of a GNSS constellation with global coverage must ensure at least four satellite in view simultaneously from any point on the Earth's surface at any time.
- **Control segment**: This segment is also referred to as the ground segment, which is responsible for the proper operation and functioning of the system. It is usually composed of a network of ground infrastructures, such as control stations, ground antennas, *etc.* They can help to control and maintain the satellite constellation status, to predict

ephemeris and satellite clock evolution as well as to update the navigation messages for all the satellites.

- **User segment**: This segment refers to all kinds of user receiving equipments, typically referred to as "GNSS receivers". GNSS receivers are capable of receiving GNSS signals transmitted by satellites, determining the pseudo-distances (or other measurements), then providing Position, Velocity and Timing (PVT) solutions.

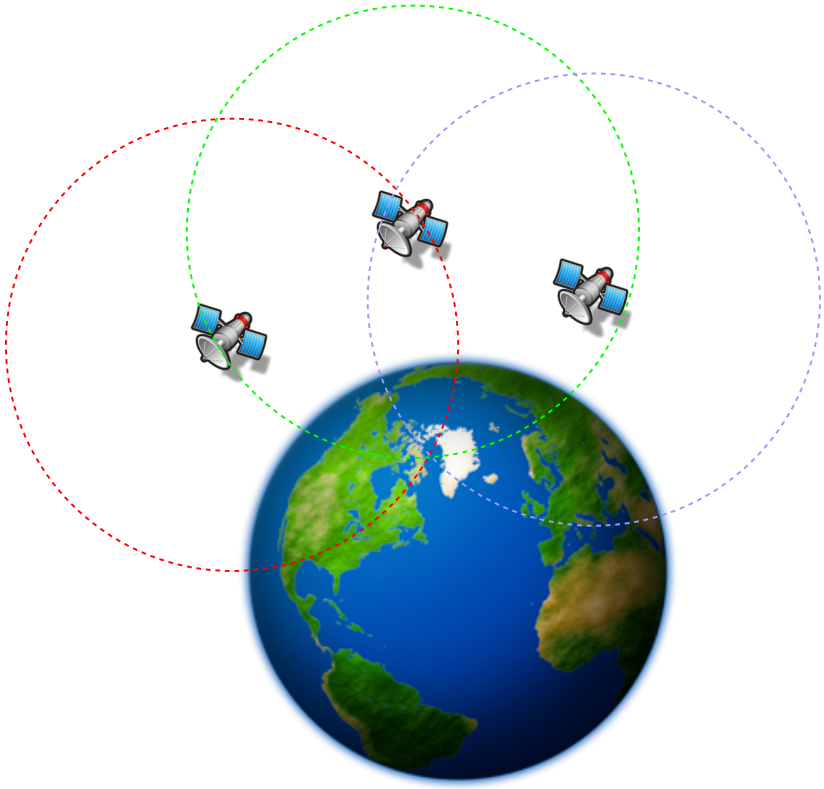

Figure 2.2 – GNSS-based Trilateration

GNSS receivers utilize the concept of one-way Time of Arrival (TOA) ranging and trilateration mechanism to determine its position on the surface of the Earth. That is to say, the receiver will measure the time it takes for a signal transmitted by a satellite at a known location to reach the receiver itself. The signal propagation is multiplied by the speed of light to obtain the emitter-to-receiver distance, which is called pseudo-distance or pseudo-range. As a result of this measurement process, the user would be located on the surface of the sphere centered on the satellite with the corresponding measured pseudo-range as radius (shown in Fig.2.2). If several pseudo-range measurements can be simultaneously made by different satellites, the user will be located on the intersection of several spheres centered at each satellite. In order to determine user positions in three dimensions (x_u, y_u, z_u) as well as the receiver clock offset with respect to system time δt_u, at least four pseudo-range measurements are needed.

2.1.2 GNSS augmentation systems

For aviation utilities, the performances of the standalone GNSS cannot meet the signal-in-space requirements for certain flight modes, such as the accuracy for precision approaches and integrity monitoring for any operation. For this reason, different augmentation systems are developed in order to enhance the GNSS performance and allow its use in civil aviation to meet the ICAO specifications.

The main augmentation systems can be classed into three categories according to the source of information from which the user receive the augmentation information:

- **Ground-Based Augmentation System (GBAS)**: The augmentation information of GBAS is provided by groud-based transmitters. Based on a network of ground station references, GBAS can provide estimates of common-mode errors and detect GNSS faults and anomalies. And integrity information can be obtained by comparing the true position of the ground reference and the estimated position obtained from the GNSS. This kind of augmentation system is mainly used at a local level, typically in airports. An example of the GBAS is the Local Area Augmentation System (LAAS), which is based on real-time differential correction of the GPS signal.

- **Satellite-Based Augmentation System (SBAS)**: The augmentation information of SBAS is provided by satellite-based transmitters. SBAS transmits differential corrections and integrity messages for navigation satellites that are within sight of a network of stations, typically deployed for an entire continent. All the SBAS satellites signals covering a given zone are monitored in order to update the error model at the raw range measurement level. Several famous example of SBAS: the US Wide Area Augmentation System (WAAS), the European European Geostationary Navigation Overlay Service (EGNOS), the Japanese Multi-functional Satellite Augmentation System (MSAS) and the Indian GPS Aided Geo Augmented Navigation (GAGAN).

- **Airborne-Based Augmentation System (ABAS)**: The augmentation information of ABAS is autonomously calculated within the aircraft equipment. It can provide integrity monitoring for the position solution using redundant information within the GNSS constellation. ABAS is usually referred to as Receiver Autonomous Integrity Monitoring (RAIM) when GNSS information (range measurements) is exclusively used and as Aircraft Autonomous Integrity Monitoring (AAIM) when information from additional on-board sensors (e.g. barometric altimeter, clock and Inertial Navigation System, INS) are also used.

2.2 Measurement Models

The GNSS pseudorange measurement model is a key input for the design of integrity monitoring algorithms and the prediction of the statistical positioning error bounds since it summarizes measurement error budgets. In general, GNSS receivers provide two main types of pseudorange measurements from satellites: code and carrier phase measurements.

A code peudorange measurement P is obtained as the time difference between the emission time and reception time of the signal. This time is then scaled by the speed of light c to obtain the pseudodistance. A carrier phase pseudorange measurement ϕ is obtained by estimating the phase shift of the local carrier. This phase can be expressed as a distance by converting radians into meters using the carrier wavelength.

The code pseudorange measurement P and the carrier phase pseudorange measurement ϕ at the epoch k for the satellite i can be mathematically described with the following equations in units of length:

$$P^i(k) = \rho^i(k) + c(\delta t_u(k) - \delta t^i(k)) + d_I^i(k) + d_T^i(k) + D_{mult}^i(k) + n_p^i(k) \tag{2.1}$$

$$\phi^i(k) = \rho^i(k) + c(\delta t_u(k) - \delta t^i(k)) - d_I^i(k) + d_T^i(k) + \phi_{mult}^i(k) + n_\phi^i(k) + N^i\lambda^i \tag{2.2}$$

where,
- ρ^i represents the true geometric distances between the receiver and the satellite i;
- δt_u represents the advance of the receiver clock with respect to system time;
- δt^i represents the advance of the satellite clock with respect to system time;
- d_I^i represents the ionospheric propagation delay residual;
- d_T^i represents the tropospheric propagation delay residual;
- D_{mult}^i and ϕ_{mult}^i represent the error due to multipath on the code and phase pseudo-ranges;
- n_p^i and n_ϕ^i represent measurement noises on code and phase pseudo-ranges;
- N^i represents the carrier phase ambiguity;
- λ^i represents the wavelength of the carrier.

We can see from the expressions above that the differences between the code and phase pseudorange measurements are located mainly on the residual error due to ionospheric propagation and the presence of an unknown integer number of carrier phase cycles N^i, which is called ambiguity:

- The ionospheric effects on carrier phase pseudorange measurements is an advance while on code pseudorange measurements is a delay. This is due to the differences of the refractive index. The phase refractive index is less than the unity resulting in a phase velocity that is greater than the speed of light in vacuum (i.e., phase advance) while the group refractive index is greater than the unity resulting in a group velocity that is less than the speed of light in vacuum (i.e., group delay). [9]

- The carrier phase pseudorange measurements are ambiguous. The solution of the integer ambiguity N, the number of whole cycles on the path from satellite to receiver, is the key to fast and high precision GNSS positioning. But the ambiguity resolution is more difficult in urban environments since the existence of local effects can lead to frequent tracking loss and Cycle Slip (CS).

Besides, the two kinds of pseudo-range measurements possess different characteristics:

- The code pseudorange measurements are robust and not ambiguous. But they are more affected by tracking errors due to noise and multipath. They are the basic measurements generally used to estimate the position.
- The carrier phase pseudorange measurements are less affected by tracking errors due to noise and multipath. But they are not robust due to frequent measurement losses (loss of carrier tracking) and Cycle Slip (CS). Moreover, the presence of ambiguity prevents carrier phase measurements from acting as absolute measurements to estimate the PVT. The process to fix these ambiguities is very sophisticated especially in adverse reception conditions such as urban canyons.

As a result, we will only concentrate on the code pseudorange measurements during this research work.

In order to determine the user position in three dimensions (x, y, z) and the receiver clock offset δt_u, the code pseudorange measurements can be rewritten into following form by developing the true geometry distance as a function of user and satellite positions:

$$P^i(k) = \sqrt{(x(k) - x^i(k))^2 + (y(k) - y^i(k))^2 + (z(k) - z^i(k))^2} + c\delta t_u(k) + e^i(k) \tag{2.3}$$

where:
- x, y, z are the Cartesian coordinates of the receiver antenna at the time of signal reception expressed in an Earth-centered Earth-fixed (ECEF) reference frame;
- x^i, y^i, z^i are the Cartesian coordinates of the ith satellite antenna at the time of signal emission expressed in an ECEF reference frame;
- $e^i(k)$ represents the sum of the code measurement errors mentioned in Eq. (2.1), i.e., $e^i(k) = d_I^i(k) + d_T^i(k) + D_{mult}^i(k) + n_p^i(k) - c\delta t_i(k)$.

The non-linear relationship in Eq. 2.3 can be expressed in the following vector form:

$$Y(k) = h(X(k)) + E(k) \tag{2.4}$$

where,
- $Y(k)$ represents the pseudorange measurement vector at epoch k with size $[m \times 1]$;
- X represents the navigation solution vector at epoch k with size $[n \times 1]$;

- $E(k)$ represent pseudorange measurement error vector at epoch k with size $[m \times n]$;

Pseudorange measurement errors are the addition of nominal errors and faults:

$$E = \varepsilon + B \tag{2.5}$$

where,
- ε represents the nominal error vector with size $[m \times 1]$;
- B represents the fault vector with size $[m \times 1]$.

2.3 Error Sources

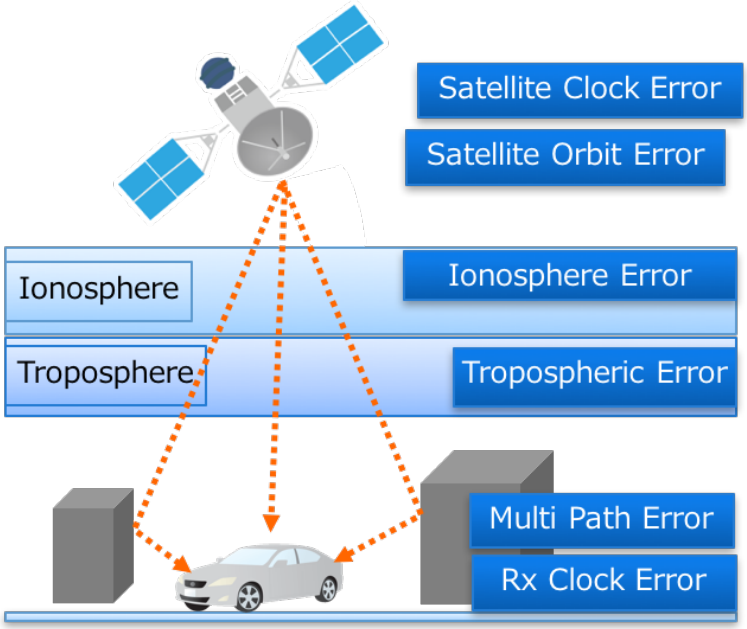

Figure 2.3 – GNSS Measurement Error Sources

2.3.1 Nominal Error Sources

The nominal error model characterizes the pseudorange measurement errors that are present when all GNSS segments are working according to their specifications and the magnitudes of other external error sources have typical values. GNSS measurements are affected by several error sources mainly including satellite clock and orbit error tropospheric residual error, ionospheric residual error, multipath error as well as the receiver noise error as shown in Fig. 2.3. All these nominal errors are modeled as zero-mean independent normal distributions in civil

aviation standards and classic GNSS integrity monitoring theories are designed under this assumption. The summary of the total error budget affecting a pseudorange is called the User Equivalent Range Error (UERE). Since the error components are assumed to be independent, the UERE for a given satellite can be approximated as a zero mean Gaussian random variable whose variance is determined as the sum of the variance of each error component [6]. That is to say, the nominal measurement error ε can be modeled as a zero-mean Gaussian distribution with a known variance σ^2_{UERE}:

$$\varepsilon \sim N(0, \sigma^2_{\text{UERE}}) \tag{2.6}$$

Then, the variance of the UERE can be written as:

$$\sigma^2_{\text{UERE}} = \sigma^2_{\text{URA}} + \sigma^2_{\text{iono}} + \sigma^2_{\text{tropo}} + \sigma^2_{\text{multipath}} + \sigma^2_{\text{noise}} \tag{2.7}$$

where,

σ^2_{URA}: User Range Accuracy (URA) is an estimation of ephemeris and satellite clock errors. Ephemeris errors result from a mismatch between the actual location of the satellite and the predicted satellite position as broadcast in the navigation message. Satellite clock errors are due to satellite clock offset with regard to GPS time. The distribution of every satellite's range error is modeled by overbounding a zero mean Gaussian distribution with standard deviation equal to URA [10, 11], which varies from 0.35 to 3.9 m for different GPS generations. For Galileo, the parameter Signal-In-Space Accuracy (SISA) corresponds to the GPS URA [12], which equals to 0.85 m. Besides, Satellite-Based Augmentation System (SBAS) can also provide satellite clock and ephemeris corrections by applying fast and slow correction models. The former is applied to correct the rapid changing satellite clock errors and the latter is to correct the slow changing errors in ephemeris and the long term satellite clock errors. This correction is characterized by the User Differential Range Error (UDRE), which is typically around 0.3 m for EGNOS operational area [13].

σ^2_{iono}: represents the ionospheric residual error. Ionosphere is the ionized part of the earth's upper atmosphere lying between about 60 km to 1000 km. It is characterized by a highly dynamical plasma density, which are formed principally by photo-ionization under the effect of solar radiation. A trans-ionospheric radio wave propagating through the plasma experiences a propagation delay / phase advance of the signal causing a travel distance or time larger / smaller than the real one. The ionospheric delay for satellites at low elevation is almost three times than the satellite at the zenith and the delay is longer during the day than at night. The delay ranges from 3 m up to 45 m. [6]

GNSS receivers systematically correct the ionospheric errors. For single frequency receivers, different ionospheric error models are applied, such as the Klobuchar model [14] for GPS civil signals, the NeQuick model for Galileo signals [15]. These models can help correct at least 50% (with Klobuchar model) to 70% (with NeQuick model) of the ionospheric delay for single frequency receivers [14,16]. Besides, the Satellite-Based Augmentation System (SBAS) can also provide GPS L1 ionospheric delay corrections at the pre-defined Ionospheric Grid Points (IGP). Users are supplied with the mapping of Grid Ionosphere Vertical Error (GIVE), which indicates the standard deviation of the overbounding zero-mean normally distributed residual error model that remains after applying the corrections to signals received at the zenith of each IGP. If user is not exactly located on the predefined IGP, interpolations of GIVEs of neighboring IGPs may be needed in order to calculate the ionospheric delay at their own position. In this case, this parameter is called User Ionosphere Vertical Error (UIVE). Finally, the UIVE is scaled by a mapping function in order to take into consideration the elevation of satellite. This final result is called User Ionosphere Range Error (UIRE), which is the standard deviation of the ionospheric residual error provided by SBAS.

For dual-frequency receivers, the first order ionospheric delay can be removed by combining the pseudorange measurements from two different frequencies since the ionospheric delay is frequency-dependent. But higher order error still remain with neglected amplitudes (at the zenith 0-2 cm for second order ionospheric delay and 0-2 mm for third order [17]).

$\sigma^2_{\mathbf{tropo}}$**:** represents the tropospheric residual error. The troposphere is the lower part of the atmosphere, which is non-dispersive for frequencies up to 15 GHz [6]. This delay is a function of the tropospheric refractive index, which depends on the local temperature, pressure and relative humidity. Since it is a local phenomenon, there is no corrections broadcast in GNSS navigation messages. It is estimated and corrected by user segment thus the tropospheric residual errors depend on the model used by users. The tropospheric delay model specified in [18] for civil aviation GPS/WAAS airborne equipment is based on the University of New Brunswick (UNB3) tropospheric delay model while simplifying the computational burden. The tropospheric delay varies from about 2.4 m for a satellite at zenith and the user at sea level to about 25 m for a satellite at an elevation angle of approximately 5°.

$\sigma^2_{\mathbf{multipath}}$**:** represents the multipath error. Multipath refers to the phenomenon that a signal arrives at the receiver via reflections or diffractions and they are combined with the LOS signal. The sum of the LOS and the NLOS signals induce a biased measurement. In aviation domain, nominal multipath errors are generally considered as ranging errors

due to multipath from the aircraft structure. Following model is validated and adopted by Radio Technical Commission for Aeronautics (RTCA) for GPS L1 C/A [19] mainly using data during normal flight tests:

$$\sigma_{\text{multipath}}[i] = 0.13 + 0.53e^{(-\theta_i/10)} \tag{2.8}$$

where, θ_i represents the elevation angle for ith satellite in degrees. This model is only applicable for an aircraft in flight and not to an aircraft on the ground. We can see from this model that nominal multipath errors are far from sufficient for GNSS receivers in urban environment since numbers of obstacles exist which can cause range errors up to several kilometers. This is will be discussed in the following section as faulty case multipath errors.

σ^2_{noise}: represents the noise of receivers. The main error source of receiver comes from the tracking loop such as Delay Lock Loop (DLL) and Phase Lock Loop (PLL). This mainly includes thermal noise jitter, dynamic stress noise etc. Several models exist in literature for different discriminators [20, 21].

Table 2.1 – A Summary of GPS Pseudorange Error Budget [7, 22]

Error Sources	**Potential Size**	**Residual Error (after Corrections)**	**Standard Deviation of the Residual Error**
Satellite Clock Error	2 m	0 m (DGPS)	1 m
Ephemeris Error	2 m	0.1 m (DGPS)	0.45 m
Ionospheric Error	2-10 m (zenith)	1-5 m (Mono-frequency)	4 m
		1 m (Dual-frequency)	0.1 m
		0.2 m (DGPS)	–
Tropospheric Error	2.3-2.5 m (zenith)	0.1-1 m	0.2 m
		0.2 m (DGPS)	
Multipath Error	0.5-1 m (open-sky)	–	–
	$>$ 150 m (constraint environments)	–	–
Receiver Noise	0.25-1 m	–	–

Table 2.1 gives a report about the GPS pseudorange error budget summary. What should be emphasized is that, except the multipath error model, all the other error models established in aeronautic domain can be applied to the urban GNSS applications since they have been thoroughly tested for Safety-of-Life (SoL) applications. Errors due to multipath and other local effects should be considered and characterized specifically for receivers in urban environment since the multipath error can even achieve several kilometers in challenging environments. This will be discussed in detail in chapter 4.

2.3.2 Error Sources in Fault Cases

A measurement fault is said to occur when a significantly large error in the range measurement (whether that error is due to an anomaly of the satellite itself or to environmental effects on the satellite ranging signal such as multipath or interference) may potentially cause an integrity failure [23]. Integrity is the measure of the trust that can be placed in the correctness of the information supplied by a navigation system, which includes the ability of the system to provide timely warnings to users when the system should not be used for navigation. An integrity failure occurs when an Hazardously Misleading Information (HMI) is produced but no warning is provided by the system. In this case, a faulty measurement is also called an outlier. Faulty case errors are modeled as a bias which is added into the nominal case error. That is say, the fault vector B in Eq. (2.5) can be expressed as:

$$B = [b_1, b_2, \cdots, b_m]^T \tag{2.9}$$

where, b_i are biases of the ith measurement.

Different possible sources exist for measurement faults. Here are some main sources of faulty measurements:

- **satellite failures:** this mainly includes Major Satellite Failure (MSF) and smaller satellite failure.
  - * MSF defined to be a condition over a time interval during which a healthy GPS satellite's ranging signal error (excluding atmospheric and receiver error) exceeds the range error limit [24]. This error limit L_{MSF} is defined as:

$$L_{\text{MSF}} = max(4.42 \times URA, 30\ m) \tag{2.10}$$

  - * smaller satellite failure [25]: This mainly includes satellite signal deformation and distortion (so-called "Evil Waveforms"), the code carrier divergence, ephemeris error and the GNSS signal fault.
- **Large and irregular ionospheric delay:** This may be caused by the scintillation effects. Scintillation refers to random fluctuations in the received wave field strength ("signal fading"), as well as phase and group delay caused by the irregular structure of the propagation medium. Ionospheric scintillations are random rapid variations in the intensity and phase of the received signals resulting from plasma density irregularities in the ionosphere [26]. These scintillation activities can occur at both high or low latitude level, such as the 11-year solar cycle or certain magnetic activities, etc.
- **High power and large multipath or NLOS reception:** In urban environments, due to the presence of numbers of obstacles, high power and large multipath may occur.

The NLOS reception is also particularly frequent due to the lack of LOS signal reception. Multipath effects and NLOS receptions are strongly environment dependent, which is difficult to be modeled. And it is extremely harmful to GNSS positioning since it can induce a range error up to several kilometers or even cause the receiver tracking loops to lose lock. We will discuss in detail about this effect and the techniques of mitigation later in the Chapter 3.

2.4 GNSS Position Estimators

The whole GNSS positioning procedure includes three main tasks: acquisition, tracking and positioning as shown in Fig. 2.4. The acquisition process tries to detect the presence of the useful signals and to give a rough estimate of main parameters (e.g., code delay and Doppler frequency) in order to prepare for the signal tracking. With the output of acquisition procedure, the receiver should be able to track the signal in order to estimate accurately the signal propagation time and its Doppler. Once the propagation time is estimated, the code pseudoranges measurements can be calculated by multiplying the light speed. The final task of the receiver is to compute the user position.

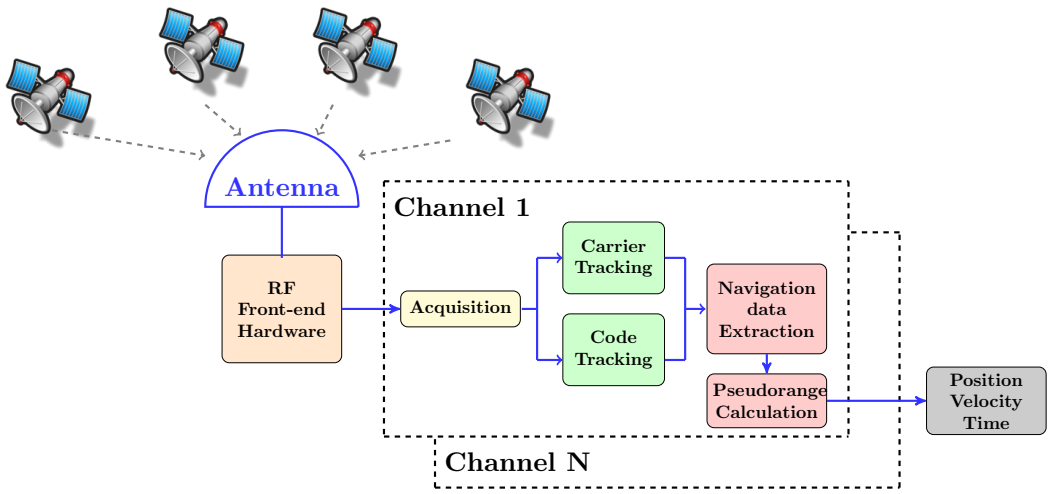

Figure 2.4 – Architecture of a Classic GNSS digital receiver

Different strategies exist in order to estimate the user's position from the measured code pseudoranges, which can be classified into two main categories: the snapshot estimator and the sequential estimator. The former ones only use the information of the current epoch and the latter one takes into consideration also the previous epochs. The most classic snapshot-type estimators are the Least Squares (LS) estimator and its variant Weighted Least Squares (WLS). And the most typical sequential estimator is the Kalman Filter (KF) as well as its

variant Extended Kalman Filter (EKF). In the following section, we will mainly introduce the estimators mentioned above as well as other some other GNSS position estimation aiding approaches.

2.4.1 Least Square Estimator and Weighted Least Square Estimator

In the framework of snapshot estimators, the Least Squares (LS) is one of the most commonly used estimators for GNSS position estimation with pseudorange measurements. As described in Section 2.2, GNSS code pseudorange measurement model can be generally expressed as follow:

$$P^i(k) = \rho^i(k) + c\delta t_u(k) + e^i(k) \tag{2.11}$$

The true geometrical distance between the ith satellite and the receiver ρ^i can be written as a function of user position (x, y, z) and satellite position (x^i, y^i, z^i) in the Earth-Centered Earth-Fixed (ECEF) frame:

$$\rho^i = \sqrt{(x - x^i)^2 + (y - y^i)^2 + (z - z^i)^2} \tag{2.12}$$

This function between the measurements and the navigation solution is non-linear. Thus, an iterative least squares estimation technique is applied by linearizing the measurement model around successive estimations of the navigation solution.

Denoting

$$h^i(X) = \sqrt{(x - x^i)^2 + (y - y^i)^2 + (z - z^i)^2} + b_u \tag{2.13}$$

where,
- $X = [x, y, z, b_u]^T$ represents the true navigation solution vector with four unknowns;
- $b_u = c\delta t_u$ represents the user clock offset with respect to GNSS system time in meter.

Then, the linearization will be made by choosing an initial estimation of the navigation solution $\hat{X}_0$. This initial estimation can be determined by using past measurements or information from other sensors, so the true navigation solution can be written as:

$$X = \hat{X}_0 + \Delta X \tag{2.14}$$

where, $\Delta X = [\Delta x, \Delta y, \Delta z, \Delta b_u]^T$ represents the increments of the navigation solution.

The first-order Taylor expansion of $h^i(X)$ around the initial estimation $\hat{X}_0$ is:

$$h^i(\hat{X}_0 + \Delta X) \simeq h^i(\hat{X}_0) + \frac{\partial h^i}{\partial X}(\hat{X}_0) \times \Delta X \tag{2.15}$$

And the partial derivatives can be further expressed as:

$$\frac{\partial h^i}{\partial x}(\hat{X}_0) = \frac{\hat{x}_0 - x^i}{\sqrt{(\hat{x}_0 - x^i)^2 + (\hat{y}_0 - y^i)^2 + (\hat{z}_0 - z^i)^2}} \tag{2.16}$$

$$\frac{\partial h^i}{\partial y}(\hat{X}_0) = \frac{\hat{y}_0 - y^i}{\sqrt{(\hat{x}_0 - x^i)^2 + (\hat{y}_0 - y^i)^2 + (\hat{z}_0 - z^i)^2}} \tag{2.17}$$

$$\frac{\partial h^i}{\partial z}(\hat{X}_0) = \frac{\hat{z}_0 - z^i}{\sqrt{(\hat{x}_0 - x^i)^2 + (\hat{y}_0 - y^i)^2 + (\hat{z}_0 - z^i)^2}} \tag{2.18}$$

$$\frac{\partial h^i}{\partial b_u}(\hat{X}_0) = 1 \tag{2.19}$$

Consequently, at epoch k, the navigation equation in vector form of Eq. (2.4) can be rewritten as:

$$Y(k) - h(\hat{X}_0(k)) = H \times \Delta X(k) + E(k) \tag{2.20}$$

where, the observation matrix $H = \frac{\partial h}{\partial X}(\hat{X}_0)$, which is:

$$H = \begin{bmatrix} \frac{\partial h^1}{\partial x}(\hat{X}_0(k)) & \frac{\partial h^1}{\partial y}(\hat{X}_0(k)) & \frac{\partial h^1}{\partial z}(\hat{X}_0(k)) & \frac{\partial h^1}{\partial b_u}(\hat{X}_0(k)) \\ \vdots & \vdots & \vdots & \vdots \\ \frac{\partial h^m}{\partial x}(\hat{X}_0(k)) & \frac{\partial h^m}{\partial y}(\hat{X}_0(k)) & \frac{\partial h^m}{\partial z}(\hat{X}_0(k)) & \frac{\partial h^m}{\partial b_u}(\hat{X}_0(k)) \end{bmatrix} \tag{2.21}$$

In fact, the matrix H is composed of the unit direction vector a^i between the linearization point and the ith satellite:

$$a^i = (a^i_x, a^i_y, a^i_z) \tag{2.22}$$

with

$$\begin{aligned} a^i_x &= \frac{\hat{x}_0 - x^i}{\hat{\rho}^i} \\ a^i_y &= \frac{\hat{y}_0 - y^i}{\hat{\rho}^i} \\ a^i_z &= \frac{\hat{z}_0 - z^i}{\hat{\rho}^i} \end{aligned} \tag{2.23}$$

and $\hat{\rho}^i = \sqrt{(\hat{x}_0 - x^i)^2 + (\hat{y}_0 - y^i)^2 + (\hat{z}_0 - z^i)^2}$.

As a result, the matrix H can be re-written as:

$$H = \begin{bmatrix} a^1_x & a^1_y & a^1_z & 1 \\ \vdots & \vdots & \vdots & \vdots \\ a^m_x & a^m_y & a^m_z & 1 \end{bmatrix} \tag{2.24}$$

Let us denote $\Delta Y = Y(k) - h(\hat{X}_0(k))$, which represents the deviation between the pseudorange measurements and the predicted noiseless measurements that receiver would have made if its

state is at $\hat{X}_0(k)$, then Eq. (2.20) can be simplified as following linear model:

$$\Delta Y(k) = H \times \Delta X(k) + E(k) \tag{2.25}$$

The least square estimator aims at seeking an estimation of ΔX which can minimize the norm of the residual vector R_{SE}:

$$R_{SE} = \hat{r}^T \cdot \hat{r} \tag{2.26}$$

where, $\hat{r}$ represents the residual vector which is defined as:

$$\hat{r} = \Delta Y(k) - H \times \Delta \hat{X} \tag{2.27}$$

Finally, the Least Squares (LS) estimation of the $\Delta \hat{X}(k)$ is:

$$\Delta \hat{X}_{LS}(k) = (H^T H)^{-1} H^T \times \Delta Y(k) \tag{2.28}$$

What should be mentioned is that, in this LS navigation solution, the quality matrix $Q = (H^T H)^{-1}$ is often used to compute the Dilution of Precision (DOP), which is an indicator of the geometry quality of the user/satellite configuration [6]. More precisely, Q is a 4×4 matrix which can be expressed as:

$$Q = \begin{bmatrix} q_{xx} & q_{xy} & q_{xz} & q_{xt} \\ q_{yx} & q_{yy} & q_{yz} & q_{yt} \\ q_{zx} & q_{zy} & q_{zz} & q_{zt} \\ q_{tx} & q_{ty} & q_{tz} & q_{tt} \end{bmatrix} \tag{2.29}$$

As a result, several DOP parameters, i.e., Geometric Dilution of Precision (GDOP), Position Dilution of Precision (PDOP) and Time Dilution of Precision (TDOP), can be defined as follows:

$$GDOP = \sqrt{q_{xx} + q_{yy} + q_{zz} + q_{tt}} \tag{2.30}$$

$$PDOP = \sqrt{q_{xx} + q_{yy} + q_{zz}} \tag{2.31}$$

$$TDOP = \sqrt{q_{tt}} \tag{2.32}$$

If the matrix H is expressed in a local East-North-Up (ENU) fram, the Horizontal Dilution of Precision (HDOP) and Vertical Dilution of Precision (VDOP) can be also calculated:

$$HDOP = \sqrt{q_{ee} + q_{nn}} \tag{2.33}$$

$$VDOP = \sqrt{q_{uu}} \tag{2.34}$$

Returning back now to the navigation solution: if the error covariance matrix of measurement is known, then the Weighted Least Squares (WLS) estimation is:

$$\Delta\hat{X}_{WLS}(k) = (H^T\Sigma^{-1}H)^{-1}H^T\Sigma^{-1} \times \Delta Y(k) \tag{2.35}$$

where, $\Sigma = cov(E(k))$ denotes the measurement error covariance matrix. Supposing the measurement error of each receiver channel is independent, Σ can be further expressed as a diagonal matrix with measurement variance as its diagonal components:

$$\Sigma = \begin{bmatrix} \sigma_1^2 & 0 & \dots & 0 \\ 0 & \sigma_2^2 & \dots & 0 \\ \vdots & \vdots & \ddots & \vdots \\ 0 & 0 & \dots & \sigma_m^2 \end{bmatrix} \tag{2.36}$$

This estimation of $\Delta\hat{X}$ can be made in several iterations until the convergence of its norm. And the estimation of the navigation solution can be updated in each iteration by this increments $\Delta\hat{X}$.

The WLS estimator can provide better accuracy performance than the LS estimator thanks to the information in the covariance matrix. In fact, with WLS, measurements with bigger error variances will contribute less weights in the position estimation while measurements with smaller error variance will contribute huge weights. This is a pre-process of optimization if the error variances are characterized correctly. It is proved that the WLS estimator is the Best Linear Unbiased Estimator (BLUE) which reaches the Cramer-Rao lower bound [27].

2.4.2 Kalman Filter (KF) Position Estimator

The user Position, Velocity and Timing (PVT) solutions obtained from the Least Squares (LS) estimator and Weighted Least Squares (WLS) estimator can be noisy since they may be corrupted by measurement noises and other error sources mentioned previously. One method for computing smoothed navigation solutions is Kalman Filter (KF).

The KF is a widely used tool in a broad class of estimation problems, which is introduced in 1960 by Dr. R. E. Kalman [28]. The filter depends on measurements as well as a dynamic model of the GNSS receiver platform motion. It can estimate different user states and its corresponding error variance by optimally weighting information from the system dynamic model and current measurements. For linear system models, KF can provide an unbiased estimation.

Thanks to its recursive nature and ability to hybridize system dynamics with measurements from different sensors, the KF and one of its variant Extended Kalman Filter (EKF) are

used in many navigation system including systems with multiple sensor hybridization such as Inertial Navigation System (INS).

2.4.2.1 Standard Kalman Filter

The KF can solve the general problem of trying to estimate the state $x \in \Re^n$ of a discrete-time controlled process that is governed by the linear stochastic difference equation:

$$x_k = Fx_{k-1} + Gu_{k-1} + w_{k-1} \tag{2.37}$$

with measurement $z \in \Re^m$ which can be written as:

$$z_k = H_k x_k + v_k \tag{2.38}$$

The random variables w_k and v_k represent respectively the process and measurement noises. They are assumed to follow zero-mean Gaussian distributions independently:

$$w \sim \mathcal{N}(0, Q) \tag{2.39}$$

$$v \sim \mathcal{N}(0, R) \tag{2.40}$$

where, Q and R represent respectively the process noise covariance and the measurement covariance, which are two parameters to be set according to system and measurement characteristics. They are supposed to be diagonal and can be either constant or not.

The $n \times n$ matrix F in Eq. (2.37) is the state transition matrix which relates x_{k-1} to x_k in the absence of either a driving function or process noise. It can be derived from the system dynamic motion model. The $n \times l$ matrix G relates the optional control input vector $u \in \Re^l$ to the state vector x. The $m \times n$ matrix H in the measurement equation (2.38) provides the noiseless connection between the state vector and the measurement z_k.

Denoting $\hat{x}_k^- \in \Re^n$ an *a priori* state estimate at epoch k given the state estimate at last epoch as well as the system dynamic model and $\hat{x}_k \in \Re^n$ an *a posteriori* state estimate at epoch k given the measurement z_k. Then the *a priori* and *a posteriori* error can be defined as:

$$\begin{aligned} e_k^- &= x_k - \hat{x}_k^- \\ e_k &= x_k - \hat{x}_k \end{aligned} \tag{2.41}$$

So the *a priori* and *a posteriori* estimate state error variances are:

$$\begin{aligned} P_k^- &= E[e_k^- e_k^{-T}] \\ P_k &= E[e_k e_k^T] \end{aligned} \tag{2.42}$$

KF uses a linear blending of the *a priori* estimate $\hat{x}_k^-$ and a weighted difference between the actual measurement z_k and a measurement prediction $H\hat{x}_k^-$ in order to update and improve the *a priori* state estimate:

$$\hat{x}_k = \hat{x}_k^- + K_k(z_k - H_k\hat{x}_k^-) \tag{2.43}$$

The difference $z_k - H_k\hat{x}_k^-$ in Eq. (2.43) is called innovation (or predicted residual), which reflects the discrepancy between the predicted measurement and the actual measurement. A residual of zero means that the two are in complete agreement.

The $n \times m$ matrix K in Eq. (2.43) is named Kalman gain (or blending factor) which minimizes the *a posteriori* state error covariance in Eq. (2.42) and can be written in the following form [29–31]:

$$\begin{aligned} K_k &= P_k^- H_k^T (H_k P_k^- H_k^T + R_k)^{-1} \\ &= \frac{P_k^- H_k^T}{H_k P_k^- H_k^T + R_k} \end{aligned} \tag{2.44}$$

By observing the above expression of Kalman gain, we can see that, if the *a priori* state estimate error covariance P_k^- approaches zero, the Kalman gain will also approach zero, which means that the innovation term will be weighted less heavily and the system dynamic model will be trusted more:

$$\lim_{P_k^- \to 0} K_k = 0 \tag{2.45}$$

On the contrary, if the measurement error covariance matrix R approaches zero, the Kalman gain will give more weight to the innovation and the measurement will be trusted more:

$$\lim_{R_k \to 0} K_k = H_k^{-1} \tag{2.46}$$

The KF algorithm includes two main stages: prediction and update. More precisely, they can be described by the following five equations, which are the basis of the Kalman Filtering:

- **Prediction**

$$\hat{x}_k^- = F\hat{x}_{k-1} + Gu_{k-1} \tag{2.47}$$

$$P_k^- = FP_{k-1}F^T + Q \tag{2.48}$$

- **Update**

$$K_k = P_k^- H_k^T (H_k P_k^- H_k^T + R_k)^{-1} \tag{2.49}$$

$$\hat{x}_k = \hat{x}_k^- + K_k(z_k - H_k\hat{x}_k^-) \tag{2.50}$$

$$P_k = (I - K_k H_k)P_k^- \tag{2.51}$$

Fig. 2.5 shows us the flowchart of the Kalman Filtering procedures. After initializing the filter, the *a priori* state vector $\hat{x}_k^-$ and its covariance matrix P_k^- can be predicted with the help of the transition matrix F and the process noise covariance matrix Q as in Eq. (2.47) and Eq. (2.48). Then in the update stage, the Kalman gain will be calculated as in Eq. (2.49). And the *a posteriori* state estimate $\hat{x}_k$ will be generated by correcting the *a priori* state vector with weighted innovation in Eq. (2.50). The final step is to calculate the *a posteriori* state estimate error covariance P_k via Eq. (2.51).

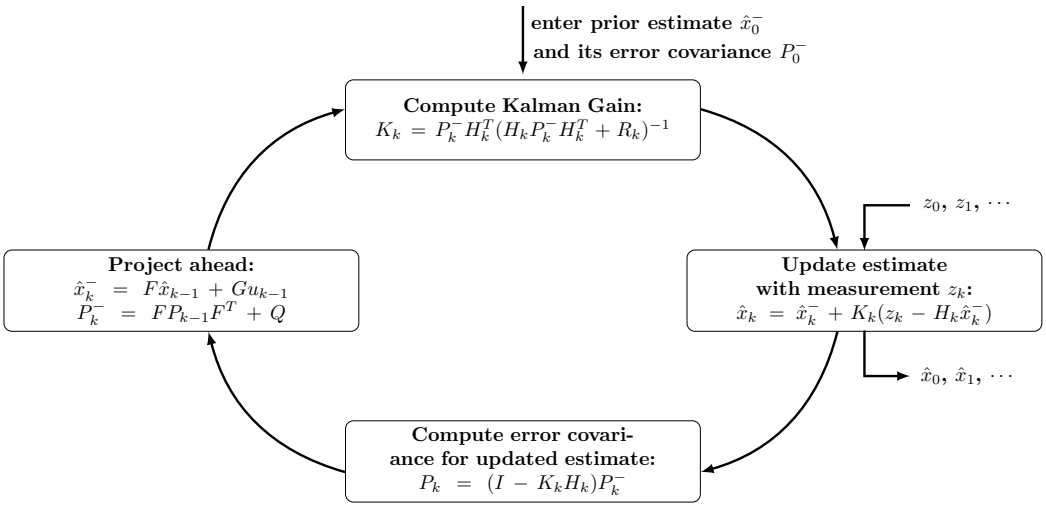

Figure 2.5 – Kalman Filter Loop [30]

2.4.2.2 Extended Kalman Filter (EKF)

As described in the last section, the standard KF addresses the general problem of trying to estimate the state $x \in \Re^n$ of a discrete-time controlled process that is governed by a *linear* stochastic difference equation. But in reality, the process to be estimated is often non-linear. One of the variants of the KF, named Extended Kalman Filter (EKF), is designed to solve the non-linear problems.

Assuming the state vector $x \in \Re^n$, and it is governed by a non-linear model:

$$x_k = f(x_{k-1}, u_{k-1}, w_{k-1}) \tag{2.52}$$

The measurement $z \in \Re^m$ can be modeled as:

$$z_k = h(x_k, v_k) \tag{2.53}$$

where, the random variable w_k and v_k represent respectively the process and measurement noises as previously mentioned in Eq. (2.37) and Eq. (2.38).

Here, the transition function $f(x_{k-1}, u_{k-1}, w_{k-1})$ and the measurement model $h(x_k, v_k)$ are non-linear. So we can linearize them by computing the Jacobian matrix of the functions $f(x_{k-1}, u_{k-1}, w_{k-1})$ and $h(x_k, v_k)$ around the state estimation at the last epoch x_{k-1}:

$$F_k = \frac{\partial f}{\partial x}(x_{k-1}) \tag{2.54}$$

$$H_k = \frac{\partial h}{\partial x}(x_{k-1}) \tag{2.55}$$

Once the transition model and the measurement model are linearized, the standard KF algorithm described in the previous section can be applied while keeping the non-linear function in the state prediction and update. That is to say, the EKF algorithm can be summarized as:

- **Prediction**

$$\hat{x}_k^- = f(\hat{x}_{k-1}, u_{k-1}) \tag{2.56}$$

$$P_k^- = F_k P_{k-1} F_k^T + Q \tag{2.57}$$

- **Update**

$$K_k = P_k^- H_k^T (H_k P_k^- H_k^T + R_k)^{-1} \tag{2.58}$$

$$\hat{x}_k = \hat{x}_k^- + K_k(z_k - h(\hat{x}_k^-)) \tag{2.59}$$

$$P_k = (I - K_k H_k) P_k^- \tag{2.60}$$

2.4.3 Performance Improvement with Other Aiding Approaches

Except for the basic positioning techniques mentioned in the previous sections, other approaches exist to improve the GNSS positioning performances. We will present briefly several of them in the following text.

* **GNSS/INS Integration**

A large body of research work contributes to the hybridization of the GNSS and the Inertial Navigation System (INS). An INS is a navigation aid that uses a computer, motion sensors (accelerometers), rotation sensors (gyroscopes) and occasionally magnetic sensors (magnetometers), to continuously calculate by dead reckoning the position, the orientation and the velocity (direction and speed of movement) of a moving object without the need for external references.

Thanks to the complementary nature of GNSS and INS, the integration of these two systems can deliver more robust and reliable systems than either of the individual systems. This is because, on the one hand, INS short-term errors are relatively small, but they degrade rapidly with time and are unbounded so external aiding is necessary [32]. On the other hand, GNSS can provide bounded accuracy and more stable in long-term.

Moreover, INS can provide accurate short term data with very high rate which can be used to interpolate GNSS measurements. And the measurements of INS are less disturbed by outages such as signal blocking or interference, which is more robust to some extent.

Different strategies of GNSS/INS integration exist [33]:

- Uncoupled Integration;
- Loose Integration;
- Tight Integration;
- Deep/Ultra-tight Integration;

* **Map Matching**

Digital road maps can be used as an aiding approach for GNSS navigation for land vehicles by map-matching. Map-matching algorithms integrate positioning data with spatial road network data to identify the correct link on which a vehicle is traveling and to determine the location of a vehicle on a link [34].

Since the emergence of the novel applications such as autonomous vehicles and the automated toll-collection system, the demand of a high positioning quality is continuously growing. For these kinds of applications, map-matching algorithm could be used as a key component to improve the performance of systems especially in urban canyons. With the help of a 3D digital map, the GNSS signal reception state LOS/NLOS can be distinguished [35, 36] and the pseudorange error can be further corrected by computing the additional distances of the NLOS signals, which will be applied later in this thesis.

Different map-matching techniques exist in the literature, such as:

- Geometric analysis [37, 38];
- Topological analysis [39, 40];
- Probabilistic map-matching algorithms [41, 42];
- Other advanced map-matching algorithms (e.g., EKF [43], particle filter [44].)

However, the performance of map-matching techniques strongly depends on the map accuracy and availability. Positioning performances can be improved with high accuracy map but maps with poor accuracy will involve additional errors into positioning procedures. Moreover, the necessity of updating in order to keep coherence with the real road configuration is another limitation of the digital map-based techniques.

Chapter 3

GNSS Position Integrity Theory

Contents

Summary

This chapter will present the theoretical foundations of GNSS position integrity especially its expansion to urban transport applications. Beginning with basic terminology and definition of integrity monitoring, it is followed by an introduction of famous classic integrity monitoring algorithms for aviation utility: the Receiver Autonomous Integrity Monitoring (RAIM). Then different FDE approaches will be discussed. Finally, the problematic and complexity of integrity monitoring in urban environments will be analyzed and the state of the art of existing integrity monitoring approaches in urban environment will be summarized.

Part of the work presented in this chapter is the subject of the published journal paper in IEEE Transactions on Intelligent Transportation Systems [45].

3.1 Introduction

The GNSS integrity concept has been firstly developed and formalized in the aviation field for Safety-of-Life (SoL) applications [18]. It is defined as a measure of trust which can be placed in the correctness of the information supplied by the total system [46]. As one of the most essential performance parameters, GNSS integrity has recently attracted interest from other transportation fields especially in the urban environment. This is because the GNSS-based urban applications proved to be a huge and appealing market which is currently in a constant growth [47].

For GNSS-based urban applications such as in the rail and in the vehicular domains, knowing the certainty of one's localization is of great importance. The framework of GNSS integrity in urban environment is firstly introduced especially in the vehicle domain, for instance, the famous Liability Critical Applications. Here, the computed Position, Velocity and/or Time (PVT) are used as the basis for legal decisions or economic transactions [5, 48], such as Electronic Toll Collection (ETC) and Pay as you Drive insurance. In such kinds of scenarios, large errors can lead to consequences such as wrong legal decisions or wrong charge computation as the example shown in Fig. 3.1. In rail where GNSS-based solutions are expected to replace the use of physical balises placed along the track, one should demonstrate a high level of performances especially in link with integrity. Indeed, the new system shall be as safe as the replaced one and the integrity is one of the indicators for safety [49]. In addition, an increasing number of Unmanned Aerial Vehicles (UAV) in urban environment require also high integrity performances since multipath effects associate with their low-level flights [50]. Consequently, it is necessary and important to bound the errors and to ensure that the probability of errors not properly bounded is below a certain limit in order to reduce the probability of the harmful effects and to guarantee the correctness and fairness of the decision. These requirements attach extreme importance to the concept of positioning integrity in urban environments.

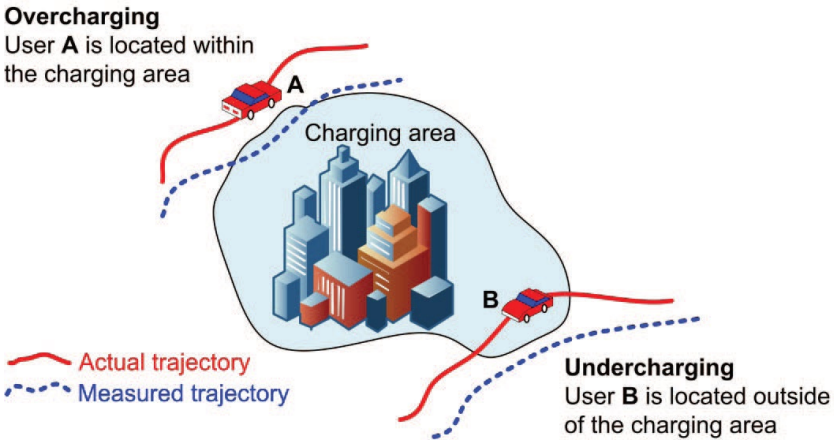

Figure 3.1 – An example of impact of positioning for Road User Charge [51]

However, the urban environment presents great challenges to common commercial GNSS receivers [52, 53]. This is mainly because the GNSS positioning performance can be severely degraded by the limited satellite visibility, multipath effect, interference and other undesired impairments such as foliage attenuation [54–56]. Much research has been developed in terms of techniques to mitigate the effect of multipath interference and Non-line-of-sight (NLOS) signals at different levels, for example, the antenna design techniques [57, 58], the receiver-based techniques [59], as well as the post-receiver techniques [60], which help to improve accuracy and reliability of the GNSS positioning in urban environment. But these techniques are still an issue to be ceaselessly developed especially for its compatibility and robustness to different stringent environments.

Despite the existing difficulties, introducing the integrity concept to urban GNSS receivers is more and more attractive as a result of emerging GNSS-based applications in stringent environments. But the integrity monitoring algorithms developed in the aviation domain cannot be transported directly into the urban vehicle applications. This is because, on the one hand, the integrity monitoring algorithms developed in the aviation context are established on the fact that a high data redundancy exists, which is not the case in the urban context. On the other hand, the single-fault assumption made in the aerospace applications is not true for urban GNSS receivers due to the potentially large and frequent errors provoked by multipath interference and NLOS. [61]

This chapter is organized as follows: Section 3.2 introduces definitions and theoretical foundations about GNSS navigation performance criteria as well as some parameters of integrity. Section 3.3 presents the traditional integrity monitoring approaches in the aviation context especially the Receiver Autonomous Integrity Monitoring (RAIM), which is applied for aviation receivers. Then Section 3.4 analyzes the limitation of the classic integrity monitoring approaches in the urban context by summarizing the complexity of the GNSS signal reception in the urban environment and gives a structured overview of the existing integrity monitoring approaches for the urban GNSS receivers. Finally, Section 3.5 will discuss about different Fault Detection and Exclusion (FDE) approaches which can be potentially applied for integrity monitoring of GNSS-based urban transport applications.

3.2 Terminology and Definitions

3.2.1 GNSS Navigation Performance Criteria

Generally, when talking about the performance of GNSS, we will necessarily mention the four criteria: accuracy, integrity, continuity and availability which are defined as follows:

Accuracy of an estimated or measured position and velocity of a vehicle at a given time is the degree of conformance of these position and velocity with the true ones of the vehicle [3]. Accuracy is related to the statistical features of merit of position or velocity error. So accuracy metrics are often built from the statistical distribution of the errors. Thus, the accuracy specifications are often given at a certain percentile of the Cumulative Distribution Function (CDF) (*e.g.*, 95^{th} percentile). Generally, for ITS applications, as specified by the European Committee for Standardization (CEN) and European Committee for Electrotechnical Standardization (CENELEC), accuracy is represented with a set of three statistical values given by the 50^{th}, 75^{th} and 95^{th} percentiles of the CDF of the position error [62].

Integrity is conventionally defined as follow:

Definition 1 *Integrity is a measure of trust that can be placed in the correctness of the information supplied by a navigation system [3].*

This concept is originally introduced in the aviation context in the last decades in order to measure the influence of the navigation performance on the safety. Since the concept of integrity was intended for Safety-of-Life (SoL) applications, it also includes the ability of the system to provide timely warnings to users when some system anomaly results in unacceptable navigation accuracy [3, 63]. In summary, it is an indicator of veracity and trustworthiness that can be placed in the information supplied by the navigation system.

Recently, integrity monitoring has been more and more introduced into road transport especially for the liability critical applications. Under this context, the definition of integrity is re-adapted, for instance, by the SaPPART (Satellite Positioning Performance Assessment for Road Transport) action [51] as following:

Definition 2 *Integrity is a general performance feature referring to the trust a user can have in the delivered value of a given position or velocity quantity (e.g., horizontal position). This feature applies to 2 additional quantities associated to the value delivered at each epoch of pseudo-range measurement: the Protection Level (PL) and the associated Integrity Risk (IR).*

The definitions of the parameters (e.g., PL, IR) mentioned in the definition above will be detailed hereafter in the following section.

Continuity is the probability that the specified system performance (accuracy and integrity) will be maintained for the duration of a phase of operation, presuming that the system was available at the beginning of that phase of operation. Hence it expresses reliable operation (no failure) of the system during the specific time interval given that the

system was operating at the start of the operation.

Under the context of mass-market applications, unlike integrity, which is important for liability critical applications, the concept of continuity is essential especially for the Location-Based Service (LBS) [64]. These kinds of services refer to the software applications for mobile devices that require knowledge about where the mobile device is located. For instance, based on the knowledge of users' positions, LBS can provide the nearest points of interest (bank, restaurant, etc). For these applications, the continuity of the user positions is more important than other criteria since ideally the service should be available anywhere at anytime.

Availability is officially defined by ICAO as the percentage of time that the services of the system are usable by the navigator, which is an indication of the ability of the system to provide reliable information within the specified coverage area. But for the road GNSS applications, this feature can be defined in many different ways according to application needs. For example, for certain applications, availability can be the percentage of the measurement epochs where the considered output is delivered with the required performance or simply where the considered output is delivered by the terminal, whatever its quality.

In fact, the criteria mentioned above come from the Required Navigation Performance (RNP) concept. These criteria are related to each other as shown in Fig.3.2. We can see that accuracy is the base and the starting point of the performance pyramid which is specified at a certain confidence level (*e.g.,* %95).

Then, there is a direct link between the definition of integrity and accuracy because the condition when a system should not be used for navigation is a lack of confidence in accuracy. And the continuity is the probability that accuracy and integrity will be maintained over a certain period. So continuity builds upon both accuracy and integrity. Finally, the definition of availability contains the notion of reliable information. To be reliable, the information must meet the accuracy, integrity and continuity specifications. Thus, availability is based on the assumption of certain levels of accuracy, integrity and continuity.

Except for these classic performance criteria from the aeronautical RNP, in the context of urban GNSS applications, other important performance features of GNSS can also include: robustness to spoofing and jamming, indoor penetration *etc* [65]. This research work will only focus on the positioning accuracy and integrity aspect.

Figure 3.2 – Navigation Performance Pyramid: Accuracy, Integrity, Continuity and Availability

3.2.2 Basic Definitions of Integrity Parameters

As mentioned in the previous section, integrity is defined as a measure of trust that can be placed in the correctness of the information supplied by a navigation system and it includes the ability of the system to provide timely warnings to users when the system should not be used for navigation [3, 63]. This definition can be clarified thanks to four main parameters: Alert Limit (AL), Integrity Risk (IR), Time to Alert (TTA) and Protection Level (PL).

Alert Limit (AL) represents the largest position error allowable for safe operation, more precisely, it is defined as follow [3]:

Definition 3 *Horizontal Alert Limit (HAL) is the radius of a circle in the horizontal plane (the local plane tangent to the WGS-84 ellipsoid), with its center being at the true position, which describes the region that is required to contain the indicated horizontal position with the required probability for a particular navigation mode.*

Definition 4 *Vertical Alert Limit (VAL) is half the length of a segment on the vertical axis (perpendicular to the horizontal plane of WGS-84 ellipsoid), with its center being at the true position, that describes the region that is required to contain the indicated vertical position with the required probability for a particular navigation mode.*

In the urban context, generally we are only interested in the horizontal dimension.

Time to Alert (TTA) is the maximum allowable elapsed time from the onset of a posi-

tioning failure until the equipment announces the alert [3]. So with this parameter, the integrity risk can be specified in a time interval.

Integrity Risk (IR) is the probability of providing a signal that is out of tolerance without warning the user in a given period of time [3]. It defines the maximum probability with which a receiver is allowed to provide position failures not detected by the integrity monitoring system [66].

Protection Level (PL) is a parameter of the integrity concept which will be well highlighted in urban vehicular contexts. It is formally defined as:

Definition 5 *The PL is a statistical error bound computed so as to guarantee that the probability of the absolute position error exceeding the said number is smaller than or equal to the target integrity risk [3].*

Similar to the definition of AL, PL is also typically defined separately for the horizontal plane (Horizontal Protection Level (HPL)) and the vertical direction (Vertical Protection Level (VPL)). And here we only focus on the horizontal dimension which is defined as:

Definition 6 *The HPL is the radius of a circle in the horizontal plane (the local plane tangent to the WGS-84 ellipsoid), with its center being at the true position, that describes the region assured to contain the indicated horizontal position. It is a horizontal region where the missed detection and false alert requirements are met for the chosen set of satellites when autonomous fault detection is used [18].*

Generally, the AL is specified according to the targeted applications and the PL is calculated by users. Since the position error is not observable, the decision of alert is done by comparing the AL specified and the PL calculated, more precisely:

- If $PL > AL$, the alert triggers;
- If $PL < AL$, the alert does not trigger.

3.2.3 Integrity Events

In the context of integrity monitoring, according to the relationship between AL, PL and Position Error (PE), integrity events can be summarized as follows:

Integrity Failure is an integrity event that lasts for longer than the TTA and with no alarm raised within the TTA.

Misleading Information (MI) is an integrity event occurring when, being the system declared available, the position error exceeds the PL but not the AL.

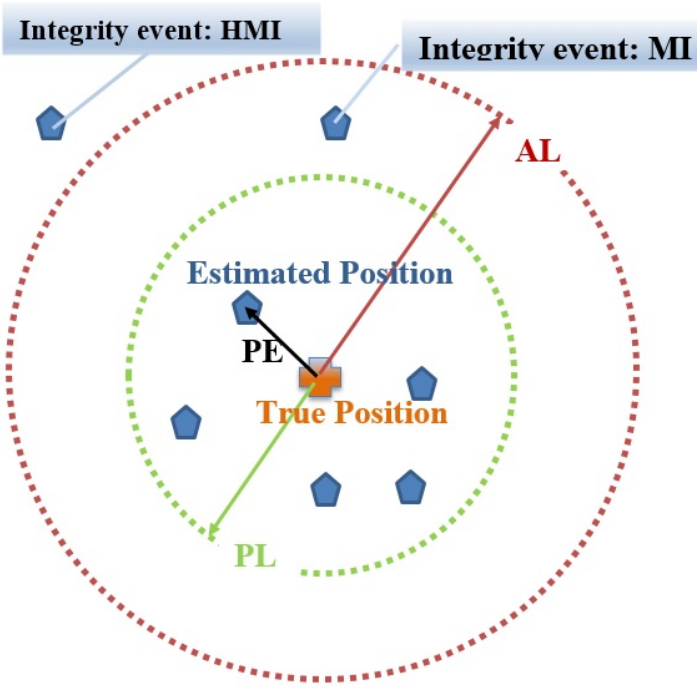

Figure 3.3 – Illustration of relationship between integrity parameters and events: PL, AL, PE and MI, HMI.

Hazardously Misleading Information (HMI) is an integrity event occurring when, being the system declared available, the Position Error (PE) exceeds the AL. Typically, in operating an aircraft, the risk for HMI due to navigation system is budgeted at the level of 10^{-7} to 10^{-9}, which is extremely tight in order to guarantee the safety of operations. But the specification of HMI probability for urban applications has not been set yet.

Fig. 3.3 provides a clearer illustration of the relationship between integrity parameters and each integrity event. Besides, the Stanford diagram (or Stanford plot) is generally used as a handy tool to explain and illustrate most of these integrity events and their relations (as well as to assess positioning performance of systems), which is shown in Fig. 3.4.

The Stanford diagram is plotted in this way: at each epoch, for each sample of a position error and a protection level, a point can be plotted in the Stanford diagram, whose abscissa represents the absolute position error and whose ordinate represents its associated protection level. The diagonal line of the diagram separates the samples in which the position errors are well covered by the computed protection level, i.e., the ones above the diagonal, and the samples in which the computed protection levels fail to bound the position errors, i.e., the ones below the diagonal. If the Alert Limit (AL) is specified according to the targeted applications, the Stanford diagram can be further divided into different zones according to the relationship between Position Error (PE), Protection Level (PL) and the AL. Each zone

represents an integrity events:

- Normal operation: $PE < PL < AL$;
- System Unavailable: $AL < PL$;
- Misleading Information (MI): $PL < PE < AL$;
- Hazardously Misleading Information (HMI): $PL < AL < PE$.

But the disadvantage of Stanford diagram is that the true position error should be known, which is difficult in practice.

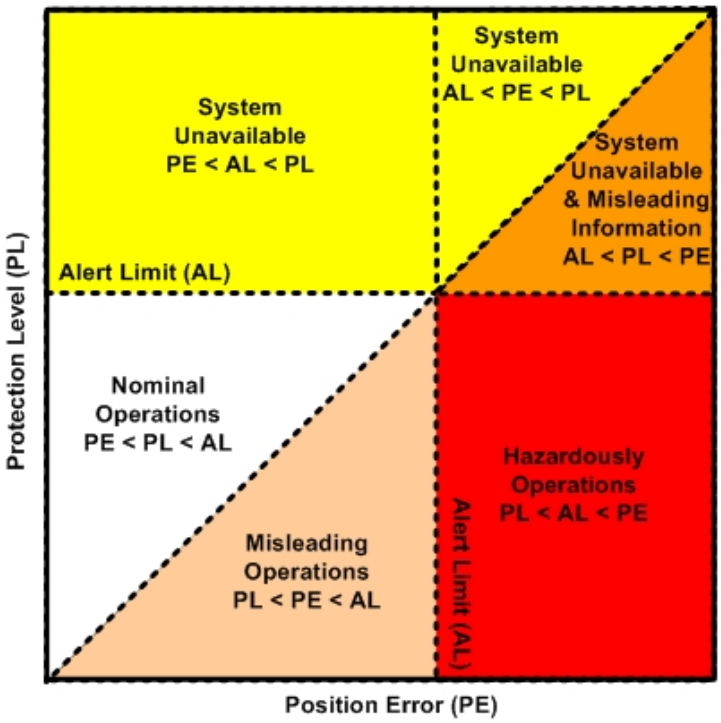

Figure 3.4 – Stanford Diagram (or Stanford plot)

3.3 Classic Integrity Monitoring Approaches for Aviation Applications

Generally, the GNSS integrity information can be obtained from different ways. The most basic is the GNSS navigation messages, which indicate the anomalies related to the system and satellite operations such as satellite clock errors. But this kind of integrity information cannot be used for the real-time applications since the ground control segment can take a few hours to identify and broadcast the satellite service failure [6]. Thus, additional sources have to be used to deal with the integrity control.

In the aviation field, the information of integrity is provided by the three normalized augmentations known under the terms Airborne-Based Augmentation System (ABAS), Ground-Based Augmentation System (GBAS) and Satellite-Based Augmentation System (SBAS) [67]. Among the three architectures, the GBAS and SBAS have to rely on some external aiding devices, such as sensor stations. ABAS can provide integrity information, which is calculated autonomously within the aircraft equipment. These augmentation systems are introduced in Section 2.1.2 of Chapter 2.

Integrity monitoring algorithms developed for land vehicles are mostly based on the principles of the traditional Receiver Autonomous Integrity Monitoring (RAIM). In the following section, the principles of RAIM will be presented.

3.3.1 Overview of Receiver Autonomous Integrity Monitoring (RAIM) Techniques

Receiver Autonomous Integrity Monitoring (RAIM) is a technique based on the consistency check of redundancy of range measurements which is initially investigated in the aviation field since the late 1980s [68–75]. Many different RAIM schemes have been proposed over the past few years, most of which are snapshot algorithms, such as the range comparison RAIM, the parity method RAIM, Least-Squares-Residuals (LS) RAIM and the Separation Solution (SS) RAIM [76–80]. Except for these snapshot algorithms, several Kalman filter based RAIM/FDE schemes are proposed [81, 82], which will be discussed later in Chapter 7.

In fact, the research of RAIM algorithms began since the late 1980s with the publications as [68–70] and [71], which are basics of the further development of RAIM algorithms. As main representatives of this first generation RAIM algorithms, LS RAIM and Weighted RAIM are still used today in aviation field as a classic way to provide low-precision lateral integrity only.

Fig. 3.5 provides an overview of the flowchart of classic RAIM algorithms. Generally speaking, these classic RAIM has following important features:

- The classic RAIM technique mainly aims at detecting and excluding large errors caused by satellite service failure. Since the probability of occurrence of two or more satellite service failures is negligible, classic RAIM detect only one fault each time.
- RAIM may include the function of fault detection and fault exclusion (FDE). It requires at least five (six) pseudo-range measurements to realize the fault detection (fault exclusion).
- The RAIM availability check module does not need to employ current measurements, that is to say, a HPL can be predicted with the satellite/user geometry, the nominal

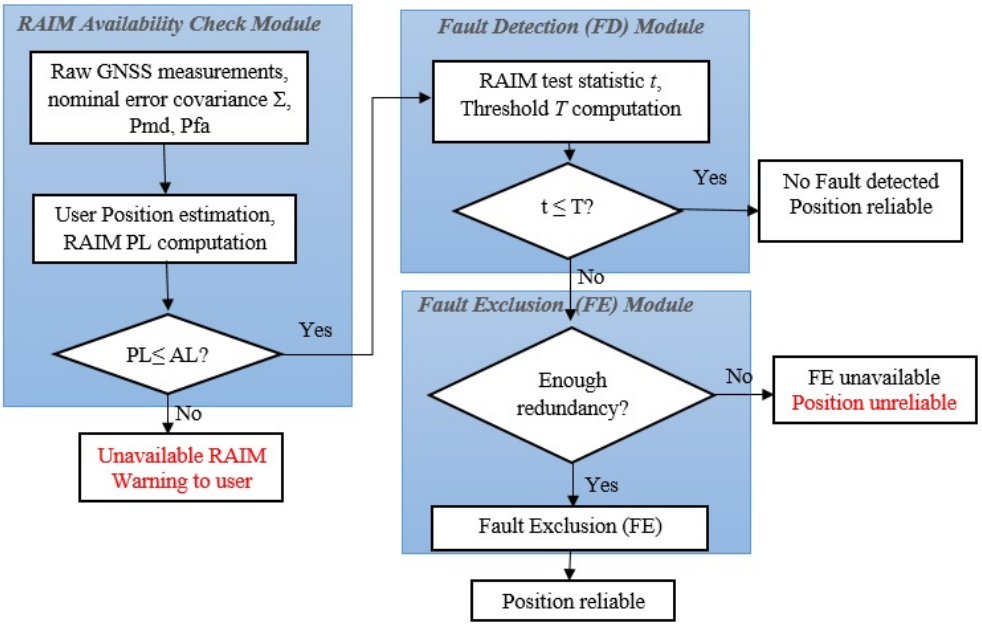

Figure 3.5 – Flowchart of classic RAIM algorithms

error characteristic (error variance) as well as the integrity probability requirements. Only if HPL< HAL can RAIM continue to enter into the FD module. In addition, after the FDE, actual uncertainty level can be calculated with the help of the geometry, the measurements (i.e. the residuals) as well as the error variance. In this case, this level is called the Horizontal Uncertainty Level (HUL) [83].

- Classic RAIM techniques used in the aviation field model the nominal pseudorange error as Gaussian distribution with zero-mean and a known variance.

Till now, no RAIM implementation exists in aviation domain for any flight operations requiring integrity in vertical planes, which has more stringent requirement such as precision approaches. This gave the motivation of developing the second generation of RAIM. Under this context, Advanced RAIM (ARAIM) and Relative RAIM (R-RAIM) are proposed as two parallel candidates for future generation integrity monitoring architectures to support precision approach operations with both lateral and vertical guidance [84, 85]. In fact, as reported in GEAS [85] with updated results, ARAIM with Multiple Hypothesis Separation Solution (MHSS) method was adopted as the major architecture and the position domain RRAIM was only used when ARAIM was not available. Compared to the classic LS RAIM, ARAIM can provide following improvements:

- ARAIM is designed to account for the multi-faults and is possible to exploit the multi-constellation GNSS with dual-frequency observation to remove the first order ionospheric delay [78, 79].

- ARAIM allows explicit computation of the integrity risk allocation while the classic RAIM is mainly based on probability of false alarm and missed detection [86].

Besides, other RAIM architectures exist such as Carrier-Phase-based RAIM (CRAIM) and Extended RAIM (ERAIM). CRAIM is mainly based on the GNSS carrier phase measurements [87, 88]. Although the carrier phase measurement is much more precise compared to the code measurement since a lower level of noise is involved, the ambiguities exists which is difficult to be successfully fixed especially in harsh environments. This is also the reason for which the carrier phase measurements generally cannot be used as an absolute measurement to estimate PVT solutions while they are preferred to be used to estimate the users' dynamic in GNSS-based relative navigation and positioning. ERAIM uses the hybridization of GNSS and INS measurements to realize the integrity monitoring [89–92], which is generally based on the EKF filter. Table 3.1 makes a summary about the classification of the RAIM techniques.

Table 3.1 – Classification of RAIM techniques

Architecture	Measurement	Algorithms	FDE Capability	References
Classic RAIM	GNSS Code	LS / WLS Residual-based method or parity-based method	FDE for single fault	[68–70] [71, 76, 93] [77]
ARAIM	GNSS Code	Solution Separation (SS) method (Single alternative hypothesis or Multiple hypothesis) or Classic Residual-based method	FDE possible for multiple faults	[78, 86, 94] [79, 80, 95] [84, 85, 96] [97, 98]
RRAIM (Range RRAIM or Position RRAIM)	GNSS Code and Time-Differenced Carrier Phase (TDCP)	MHSS or Classic Single alternative hypothesis method	FDE possible for multiple faults	[96, 99, 100] [84, 85, 101]
CRAIM	GNSS Carrier Phase	EKF innovation-based method & ambiguity resolution methods (*e.g.*, LAMBDA [102])	Only FD is possible	[87, 88]
ERAIM	GNSS Code and INS	EKF innovation-based MHSS or EKF innovation-based parity method	FDE possible for multiple faults	[89–92]

3.4 GNSS Integrity Monitoring In Urban Environments

3.4.1 Limitations of the Classic Integrity Concepts in Urban Context

The classic integrity concept employed in aeronautic domain can not be transported straightforwardly into the urban vehicular context because of the limitations due to the stringent

environment. More precisely, following constraints exist.

First of all, integrity control techniques in the aviation field such as RAIM, suppose that the distribution of the range and position domain error is Gaussian with zero-mean and a known variance in the nominal case, while just a single bias is added in the faulty case [72, 73]. The effects of multipath, limited satellite visibility, NLOS due to obstacles are not taken into consideration, which is also the case for the EGNOS [103]. These augmentation systems such as EGNOS can help the low cost commercial receivers to get a better accuracy in open sky conditions but, in a severe environment, their performances degrade, which is proved by experimental data in [103, 104]. Thus, the error models have to be characterized in order to make them more adapted to the urban GNSS applications. We will further address the error models in Chapter 4.

Secondly, the satellite visibility is badly degraded in urban canyons [105]. The availability of traditional augmentation systems such as SBAS will also be affected due to bad satellite visibility [104]. In addition, SBAS adopts the Gaussian model with zero-mean and a known variance as measurement errors and the HPL computed by SBAS takes into account only the measurement noise without bias. As a result, either the SBAS satellites are not visible or the obtained PLs are not sufficient to bound the PEs. They are not usable for urban applications.

Thirdly, as already mentioned in section 3.3, the RAIM algorithm supposes a scenario of high redundancy and that no more than one failure is detected at a time, which is not true in the urban environment. Because the major errors that threaten the GNSS urban integrity are caused by local effects such as multipath and NLOS. The errors provoked by the local effects can be very large and frequent.

Finally, the typical requirements of integrity risk in aviation are often too conservative for the vehicular applications [106].

These limitations have been proved by several research works. For instance, with real GNSS data, [61] shows that, in the dual-constellation case and a HAL of 50 m, the percentage of epochs in which a RAIM configured with $P_{md} = 5 \times 10^{-5}$ and $P_{fa} = 5 \times 10^{-3}$ is available decreases from almost 100% in the rural environment to approximately 55% in the urban one. In the GPS case, it decreases from 50% to around 7%. Lower P_{md} or P_{fa} would still decrease the availability rate. Similar conclusions are obtained with simulations by [107]. In addition, [5] also proves that the HPL calculated by the classic measurement rejection approach is too big for the urban applications (*e.g.*, for a data set of urban Madrid, only 10% of the measurement epochs have a protection level smaller than 100 meters).

3.4.2 Existing Approaches of Integrity Monitoring in Urban Environments

In recent years, some different possibilities of solutions have been studied in terms of navigation integrity monitoring in urban environments. Often, the hybridization techniques between GNSS and other sensors are used to ensure that the solutions could reach the required performances. For example, [108] proposed an integrity monitoring approach with map-matching techniques for land vehicle applications. [109] proposed a initial concept of integrity monitoring architecture using a fisheye camera which is not completely implemented yet.

Besides, a new concept which implements Vehicular Ad-hoc Network (VANET) infrastructures is currently proposed by [110]. That is to say, different vehicles participating to a VANET can share and combine their observations of GNSS signals so that a collaborative spatial/temporal characterization and prediction of the local degradation of the GNSS signals can be implemented.

For the UAVs, multipath effects associate with their low-level flights but the integrity monitoring techniques for urban environments are still in its infancy. GNSS Aircraft-Based Integrity Augmentation (ABIA) technique [50,111–113] is introduced as the main role to guarantee the integrity performance for the UAVs. The ABIA system delivers integrity caution (predictive) and warning (reactive) flags, as well as steering information to the electronic commands of the UAV flight control system. These features allow real-time avoidance of safety-critical flight conditions and fast recovery of the required navigation performance in case of GNSS data losses. In fact, this is similar to the concept of the ABAS, in which the integrity processing of GNSS data is performed onboard the UAV itself, and can be aided by additional sensors. And cooperation between different UAVs and exchange with UAV Traffic Management station are also possible to make in order to realize integrity control.

However, in terms of autonomous integrity monitoring, that is to say, using standalone GNSS receivers, no methods or techniques exist which are well developed and ready to be implemented. Yet, this approach is more promising and attractive for users since it can reduce the complexity of the on-board equipment as well as the costs. Thus, we will concentrate on the integrity monitoring approaches without any other external equipment.

In current literature, two groups of theoretical approaches for integrity monitoring in urban environment exist: the Measurement Rejection Approach (MRA) and the Error Characterization Approach (ECA) [5].

3.4.2.1 Measurement Rejection Approach (MRA)

The principle of the MRA is to reject faulty range measurements such as the classic concept mentioned previously. This approach not only works well in the open-sky environment but

also can work in other environments if the assumption that only a single fault can occur at a time can be got rid of. Yet, removal of such an assumption is really a big challenge.

If multiple simultaneous faulty range measurements are considered, the threat exists that the error sizes can combine with the satellite geometry in such a way as to produce a large position error but very small residuals, thus passing unnoticed to a conventional Fault Detection and Exclusion (FDE) algorithm [5].

[114] proposed an integrity monitoring approach based on the RANdom SAmple Consensus (RANSAC) algorithm. This method is capable of detecting multiple satellite failures. It calculates position solutions based on subsets of four satellites and compares them with the pseudorange of all the other satellites that do not contribute to the solution. Also, a modified RANSAC algorithm, called P-RANSAC, is proposed. P-RANSAC performs a final range comparison using the state estimate obtained with only the inliers identified by RANSAC. The range measurements identified as outliers from this last comparison will be excluded from the final solution. The number of outliers that this approach can identify is the number of satellites in view minus four for the estimation.

There is no doubt that the RANSAC algorithm is a breakthrough for the MRA approach in the urban scenario since it realizes multiple fault detection. And the improvement in performance by the P-RANSAC algorithm is proven by collected data compared to the classic RAIM and RANSAC algorithm in [114]. But these algorithms (RANSAC or P-RANSAC) are not optimal enough considering their computational cost and the difficulty of implementation since the subset technique requires a great amount of storage space as well as computation time.

However, for some of the liability critical applications such as Electronic Toll Collection (ETC), whose main task is to decide whether a user has driven through a road segment or not and charge him if he has. This decision, which is called geo-object recognition, can be taken as a function of the number of user positions lying inside the geo-object boundaries. Thanks to this particularity, only the number of valid positions are concerned by the system and the continuity of the system is not required. So [61] has proposed a modified Weighted Least Square (WLS) RAIM algorithm based on this point. The main difference between the aviation classic RAIM and the WLS RAIM is that the former provides a time-variant HPL with a constant P_{md} and P_{fa}, while the latter provides a time-variant P_{fa} with a constant P_{md} and a HPL (which is always equal to HAL). This is a special case of road integrity monitoring.

Generally speaking, the main disadvantage of the MRA is that it cannot guarantee the availability of the navigation solution with an associated PL since several range measurements are possibly removed. This point is problematic for GNSS users in the urban environment as the satellite visibility is already degraded, which causes the risk of insufficient range measurements. Fortunately, this situation can be improved by using multiple GNSS constellations.

[115] proposed a modified RAIM algorithm which includes geometry and separability checks. This method allows us to detect and exclude erroneous range measurements with the help of GPS/Galileo multi-constellation. Better performances are achieved compared to the classic mono-constellation RAIM. So, other GNSS constellations may be an added value for integrity monitoring in degraded environments.

Besides, the FDE can also be realized based on the Extended Kalman Filter (EKF) innovations, which is proved to have better global performances especially for dynamic platforms assuming the state and observation models are correct [81,82]. However, the limitation of the EKF-based method is its model dependence. That is to say, it is susceptible to unmodelled errors and when unexpected system dynamics occur, this method is prone to high false alarm.

3.4.2.2 Error Characterization Approach (ECA)

The second group of integrity monitoring approach for GNSS-based urban applications is called Error Characterization Approach (ECA) approach. The main idea of the ECA is to characterize the range measurement errors and be able to compute a PL that actually protects, without the need for identifying and removing degraded range measurements, even if they are contaminated with very large errors [5]. As a result, this approach can possibly lead to large protection levels which cannot suit the requirement of quite particular applications.

Isotropy-Based Protection Level (IBPL) is a patented algorithm of GMV as well as an ECA concept implementation which can provide a PL autonomously [116].

The basis of the IBPL algorithm consists in using the vector of least square estimation residuals as a characterization of the position error. And the only assumption made is that the range measurement error vector has an isotropic distribution in the measurement space [116]. This means the error vector can point in any direction of the measurement space with the same probability. Then the following relationship is used:

$$HPL = k \cdot \|r\| \cdot HDOP \tag{3.1}$$

where, r is the least square residual vector and k is called Isotropic Confidence Ratio (ICR) which depends on the target confidence level $1 - \alpha$ (α is the integrity risk), the number of range measurements m and the number of unknown to estimate n.

The detailed derivation of k's expression as a function of α, m and n is in [116]. Some tables of pre-calculated values of k with different α, m and n are available. Other values not in the table can be obtained by the interpolation method.

The IBPL method can perfectly deal with the problem of single fault assumption in the classic RAIM algorithm. It has been proven to be relatively reliable and robust in certain

degraded environment. But the disadvantage is that the calculated PL depends too closely on the number of range measurements. That is to say, if the visibility of the satellite is not good enough, the performance of the IBPL method will be badly degraded. Thus, for mono-constellation receivers in urban environment, IBPL algorithm is not very interesting due to bad satellite visibility.

Despite the robustness of the ECA approaches such as IBPL, their common problem is that, since neither range measurement is removed, the size of PL has the risk of being too large. So a trade-off should be made between the size of PL and the level of integrity risk.

In order to resolve the problems and the shortages of the existing IBPL method, GMV has lately expanded the IBPL method to support the Kalman filter, which is called the KIPL method. The KIPL can apply to GNSS-standalone or hybrid GNSS/INS navigation system. And the KIPL is able to provide tight integrity bounds in all kinds of environments for virtually any desired confidence level [117].

Except for the IBPL and KIPL methods, [118] has proposed a composite approach for HPL computation in urban environments. The principle of this method is to treat the biases and noises in a separate way. The PL can be formulated as a sum of noise component, PL_n plus a bias component, PL_b:

$$PL = PL_n + PL_b \tag{3.2}$$

And in [118], the bias and noise composites are separated by an autoregressive (AR) model. The noise component of HPL is calculated using the weighting model in [119]. For the additional term which represents the bias, the residuals obtained from the least-square PVT algorithm are used.

The analyses of the performances of HPL computation using this method in urban environments have not been made in detail. But in the open sky, it is proven that its main advantage is a clear final decrease in PL [120]. This is good news for urban integrity controlling with the ECA approach. Thus, further research about this method in urban contexts is needed.

3.5 Fault Detection and Exclusion (FDE)

The techniques of Fault Detection and Exclusion (FDE) is widely used in the industry for system diagnosis problems. FDE techniques belong to the Measurement Rejection Approach (MRA) described previously. For GNSS navigation systems, the FDE algorithms are mainly based on the consistency check with the help of the measurement residuals. As described in Chapter 2, the measurement residuals are defined as the difference between the actual measurements and the predicted noiseless measurement that receiver would have made supposing

its state is the current estimation. Residuals are key symbols of presence or absence of measurement outliers since they can indicate the extent to which the measurements are internally consistent.

As mentioned in the previous sections, the integrity monitoring scheme generally consists of two basic functions: the Fault Detection (FD) and the Fault Exclusion (FE). The goal of fault detection is to detect the presence of positioning failure. Upon detection, proper fault exclusion determines and excludes the source of the failure.

The FDE techniques used in GNSS integrity monitoring are mostly based on the hypothesis test. That is to say, a comparison between a test statistic which depends on the measurement residuals and a threshold will be performed. The threshold is set according to the specified integrity probabilities and the statistical distribution of the test.

In this section, two basic test approaches will be presented: the Global Test, which is mainly used for detecting the presence of faults and the Local Test, which is mainly used for identifying the detected faults. Based on these two test schemes, different strategies of FDE will be introduced, which can be potentially applied for GNSS-based applications in urban environments since they can exclude multiple faults.

3.5.1 Different Test Approaches

The Fault Detection and Exclusion (FDE) procedures employed in the GNSS navigation problems are mainly based on the hypothesis test, which is an essential technique in statistics. A hypothesis test evaluates two mutually exclusive statements about a population to determine which statement is best supported by the sample data.

A null hypothesis H_0 and an alternative hypothesis H_a are defined. The former one denotes a fault-free situation which is a reference level from which the situation represented by the alternative hypothesis is deviated, which is hoped to be detected.

Since the sample number is limited, there is always possibility of making wrong decisions. According to the true situation and the decisions, four statistical events exist as shown in Table 3.2. The test is efficient if the probabilities of Correct Decision and Correct Rejection are maximal and the probabilities of False Alarm and Missed Detection are minimal.

Generally, for GNSS integrity monitoring algorithms, the probability of False Alarm and the probability of Missed Detection should be specified according to corresponding applications. With these pre-defined specifications, the hypothesis test can be conducted.

Table 3.2 – Events of a Hypothesis Test

Decision / True Situation	H_0 accepted	H_0 rejected
H_0 true	Correct Decision	False Alarm
H_0 false	Missed Detection	Correct Rejection

3.5.1.1 Global Test (GT)

Global Test (GT) is generally implemented as the primary stage in the whole FDE scheme. It uses the Normalized Sum of Squared Error (NSSE) as the test statistic, which can be written in following quadratic form:

$$NSSE = \hat{r}^T \Sigma^{-1} \hat{r} \tag{3.3}$$

where,
- $\hat{r}$ represents the residual vector, which is defined as the difference between the measurements made and the predicted noiseless measurements if the user's state is the estimated ones. Its expression can be found in Eq. (2.27);
- Σ denotes Variance Covariance Matrix (VCM) of measurements, which is a diagonal matrix with measurement variances as its diagonal components:

$$\Sigma = \begin{bmatrix} \sigma_1^2 & 0 & \dots & 0 \\ 0 & \sigma_2^2 & \dots & 0 \\ \vdots & \vdots & \ddots & \vdots \\ 0 & 0 & \dots & \sigma_m^2 \end{bmatrix}$$

Denoting Z the test statistic NSSE, the GT is conducted as follows:

- Under fault-free (nominal) cases, each residual $\hat{r}_i$ is supposed to follow a centered Gaussian distribution:

$$\hat{r}_i \sim \mathcal{N}(0, \sigma_i^2) \tag{3.4}$$

Then, Z can be written as in Eq. (3.5), which follows a centered χ^2 distribution with k Degree of Freedom (DoF), i.e., $Z_c \sim \chi_k^2$:

$$Z_c = \sum_{i=1}^{m} \frac{\hat{r}_i^2}{\sigma_i^2} \tag{3.5}$$

The DoF (or redundancy) of the system can be expressed as:

$$k = m - n \tag{3.6}$$

with m the number of measurement and n the number of unknown to estimate which equals to 4 in our case. At least one redundancy is necessary for Fault Detection and at least two redundancies are needed for Fault Exclusion.

The Probability Density Function (PDF) of a centered χ^2_k is defined as:

$$\mathbb{P}(z = Z_c) = \frac{1}{2^{\frac{k}{2}}\Gamma(\frac{k}{2})} z^{\frac{k}{2}-1} e^{-\frac{z}{2}} \tag{3.7}$$

and

$$\Gamma(\frac{k}{2}) = \int_0^\infty t^{\frac{k}{2}-1} e^{-t} dt \tag{3.8}$$

- Under faulty cases, one or several residuals $\hat{r}_i$ are supposed to follow a non-centered Gaussian distribution:

$$\hat{r}_i \sim \mathcal{N}(\mu_i, \sigma_i^2) \tag{3.9}$$

Then, Z can be defined similarly as in Eq. (3.5), which follows a non-centered χ^2 distribution. There are two parameters to fix a non-centered χ^2 distribution: the DoF k and the non-centrality parameter λ, i.e., $Z_{nc} \sim \chi^2_{k,\lambda}$.

The non-centrality parameter λ is related to the mean and variance of each Gaussian distribution:

$$\lambda = \sum_{i=1}^{m} \frac{\mu_i^2}{\sigma_i^2} \tag{3.10}$$

The PDF of the non-centered χ^2 distribution is defined as:

$$\mathbb{P}(z = Z_{nc}) = \sum_{i=0}^{\infty} \frac{e^{-\frac{\lambda}{2}}(\frac{\lambda}{2})^i}{i!} \frac{1}{2^{i+\frac{k}{2}}\Gamma(i+\frac{k}{2})} z^{i+\frac{k}{2}-1} e^{-\frac{z}{2}} \tag{3.11}$$

The two hypothesis can be defined as:

$$\begin{aligned} H_0: &\ \text{(fault-free cases)} \quad Z \sim \chi^2_k \\ H_a: &\ \text{(faulty cases)} \quad Z \sim \chi^2_{k,\lambda} \end{aligned} \tag{3.12}$$

The decision is made with the help of a threshold T, which is used to compare with the test statistic Z, i.e., the $NSSE$:

$$\begin{aligned} H_0: &\ if \quad Z \leq T \\ H_a: &\ if \quad Z > T \end{aligned} \tag{3.13}$$

The threshold T is defined with the help of the P_{fa}, which can be written as:

$$P_{fa} = \mathbb{P}(Z > T | H_0) = \int_T^\infty \frac{1}{2^{\frac{k}{2}}\Gamma(\frac{k}{2})} z^{\frac{k}{2}-1} e^{-\frac{z}{2}} dz \tag{3.14}$$

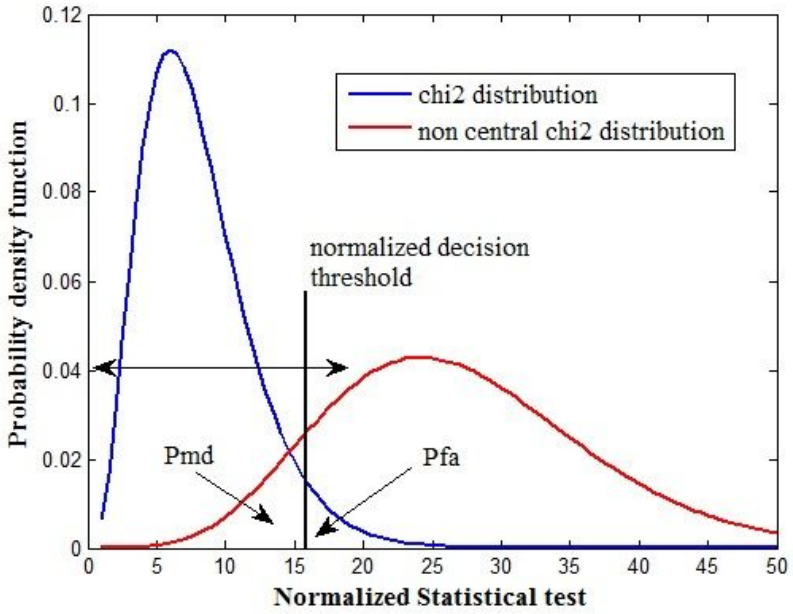

Figure 3.6 – Global Test

Similarly, the probability of missed detection P_{md} can be defined as:

$$P_{md} = \mathbb{P}(Z \leq T|H_a) = \int_0^T \sum_{i=0}^{\infty} \frac{e^{-\frac{\lambda}{2}}(\frac{\lambda}{2})^i}{i!} \frac{1}{2^{i+\frac{k}{2}}\Gamma(i+\frac{k}{2})} z^{i+\frac{k}{2}-1} e^{-\frac{z}{2}} dz \tag{3.15}$$

Fig. 3.6 gives an illustration of the Global Test: a centered χ^2 distribution in blue, a non-centered χ^2 distribution in red, the P_{fa}, P_{md} as well as the threshold T.

In fact, for a FDE problem with GT, a general logic of solution can be as follows:

1) The DoF k is known since the number of measurement m and the number of unknown to be solved n are known: $k = m - n$;

2) Once the Dof k is known, a centered χ^2 distribution can be defined;

3) Set P_{fa} so that the threshold T can be calculated according to the Eq. (3.14);

4) Finally, it remains the P_{md} and the non-centrality parameter λ. One of the two parameters can be pre-defined, according to which, the other will be deduced. If the P_{md} is pre-defined, in this case, the deduced non-centrality parameter can be used to calculate the Minimum Detectable Bias (MDB) or to calculate the Horizontal Protection Level (HPL), which will be detailed in Chapter 6. On the contrary, it is also possible to pre-define the non-centrality parameter in order to predict the P_{md} of a dangerous bias.

Consequently, if the null hypothesis H_0 is rejected and the alternative hypothesis H_a is accepted, this means an inconsistency of the total measurement set is detected. Then, the fault

identification procedure is needed to isolate and exclude the faulty measurement. The LT is one of methods to realize the fault identification.

3.5.1.2 Local Test (LT)

If a fault is detected by Global Test (GT), that means an outlier exists in one or several measurements. A Local Test (LT) can be carried out so as to identify the outlier. The LT uses the normalized residuals as test statistic, which can be written as follows:

$$w_i = |\frac{\hat{r}_i}{\sqrt{(C_{\hat{r}})_{ii}}}| \tag{3.16}$$

where, $(C_{\hat{r}})_{ii}$ represents the ith diagonal element of the covariance matrix of the residuals $C_{\hat{r}}$. The covariance matrix of the residual vector is calculated as follows:

$$C_{\hat{r}} = \Sigma - H(H^T\Sigma^{-1}H)^{-1}H^T \tag{3.17}$$

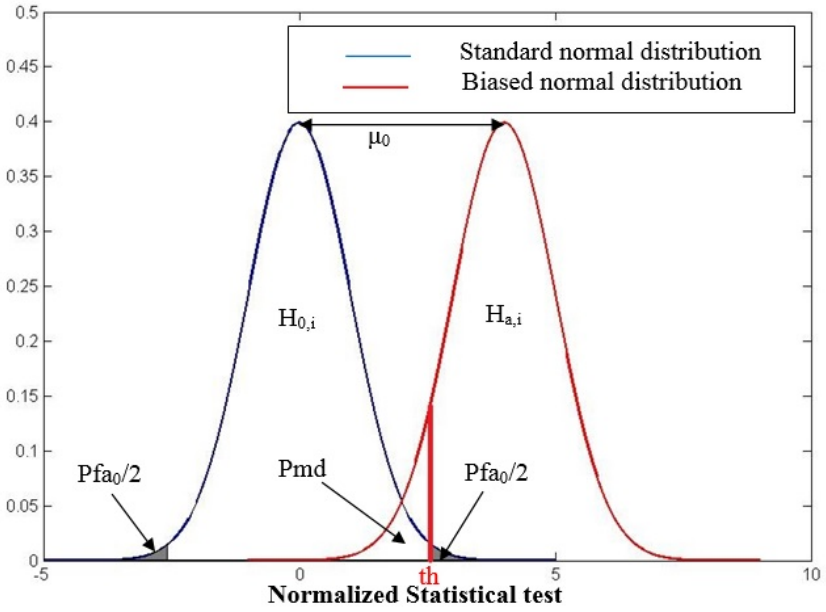

Figure 3.7 – Local Test

If the ith measurement is not an outlier, w_i is supposed to follow a standard normal distribution, which is the local null hypothesis $H_{0,i}$. Otherwise, w_i follows a biased normal distribution with a bias of λ_0, which corresponds to the local alternative hypothesis $H_{a,i}$ as shown in Fig. 3.7. In Fig. 3.7, th denotes the local threshold, which can be calculated with the predetermined local significance level $P_{fa,0}$.

Denoting:
- $\alpha = P_{fa}$, the probability of false alarm or the significance level of the GT;

- $\beta = P_{md}$, the probability of missed detection of GT;
- $\alpha_0 = P_{fa,0}$, the probability of false alarm or the significance level of the LT.

Then, according to Fig. 3.7, we have the following relations:

$$\mathbb{P}(w > th|H_0) = \int_{th}^{\infty} \frac{1}{\sigma\sqrt{2\pi}} exp(\frac{x}{2\sigma^2})dx = \frac{P_{fa,0}}{2} = \frac{\alpha_0}{2} \tag{3.18}$$

$$\mathbb{P}(w < th|H_a) = \int_{th}^{\infty} \frac{1}{\sigma\sqrt{2\pi}} exp(\frac{x-\mu}{2\sigma^2})dx = P_{md} = \beta \tag{3.19}$$

For a real number q with $0 < q < 1$, the q-quantile of a random variable X is defined as the value of x such that:

$$\mathbb{P}(X \leq x) \leq q \tag{3.20}$$

Denoting n_q the q-quantile of a normal distribution, then, by combing the definition above of the quantile and the equations (3.18) and (3.19), we can conclude that:

$$n_{1-\frac{\alpha_0}{2}} = th \tag{3.21}$$

If we denote $n_{1-\beta}$ the $(1-\beta)$-quantile of the normal distribution, by observing the Fig. 3.7, the following equation can be deduced:

$$n_{1-\frac{\alpha_0}{2}} + n_{1-\beta} = \lambda_0 \tag{3.22}$$

where, λ_0 represents the bias of the normal distribution.

In fact, the α and β of the GT and the significance level α_0 of LT are interrelated [121]. That is to say, only two of them can be fixed arbitrarily and the remainder can be deduced. These three parameters have following relationships including the one mentioned in Eq. (3.22):

$$\lambda = \lambda_0^2 = (n_{1-\frac{\alpha_0}{2}} + n_{1-\beta})^2 \tag{3.23}$$

$$\chi^2_{\beta,k,\lambda} = \chi^2_{1-\alpha,k} \tag{3.24}$$

Finally, the LT is realized as follows:

$$\begin{aligned} H_{0,i}: &\quad (i\text{th measurement not an outlier}) && w_i \leq th \\ H_{a,i}: &\quad (i\text{th measurement an outlier}) && (w_i > th) \wedge (w_i > w_k \ \forall k) \end{aligned} \tag{3.25}$$

The measurement with the largest local test statistic w_i exceeding the local threshold will be excluded. This procedure can be repeated several times in a loop until no outlier exists in current measurement set.

What should be highlighted is that, the assumption of a single outlier is made in each iteration of LT. The exclusion of multiple faults can be realized by performing LT in several iterations.

What is more, an additional test of redundancy could be optionally added into the LT procedure, which is concerning the contribution of the examined measurement to the total redundancy. This will be described in the following text.

The redundancy matrix R can be written as [122]:

$$R = C_{\hat{r}}\Sigma^{-1} \tag{3.26}$$

where, $C_{\hat{r}}$ represents the covariance matrix of the residual vector which is defined in Eq. (3.17) and Σ represents the covariance matrix of the measurement errors.

The trace of the matrix R is the redundancy (i.e., the Degree of Freedom) of the system. It can be proven that the diagonal elements r_i are always between 0 and 1, which correspond to the contribution of the ith measurement to the overall redundancy [123, 124]. Ideally, all the diagonal elements of the matrix R should be approximately equal. When r_i is closed to zero, it means that the ith measurement contributes little to the overall redundancy and it is closed to an uncontrolled measurement [124].

Besides, due to the correlation among measurements, a fault of a measurement is possible to spread over all the residuals so as to prevent the detection or even lead to wrong detection. As a result, it is necessary to guarantee that the detected faulty measurement is separated enough with other measurements. That is to say, the following condition can be added into the LT if the ith measurement is detected as faulty one [123]:

$$r_i > |r_{ji}|, \ (j \neq i, j = 1 : m) \tag{3.27}$$

3.5.2 Different Fault Detection and Exclusion (FDE) Methods

Different strategies of Fault Detection and Exclusion (FDE) exist by combining in different ways the basic tests mentioned previously, i.e., Global Test (GT) and Local Test (LT). In this section, five FDE techniques will be introduced: the Classic Test (CT), the Subset Test (ST), the Iterative Local Test, the Forward-Backward (FB) Test and the Danish Method.

3.5.2.1 Classic Test (CT)

One of the most basic FDE techniques is to simply use the GT to detect whether there is a fault. If it is the case, the measurement with the largest normalized residual calculated in Eq. (3.16) will be excluded. This scheme will be called Classic Test since the Fault identification is conducted only by choosing the largest normalized residual. Fig 3.8 shows us the flowchart of this procedure.

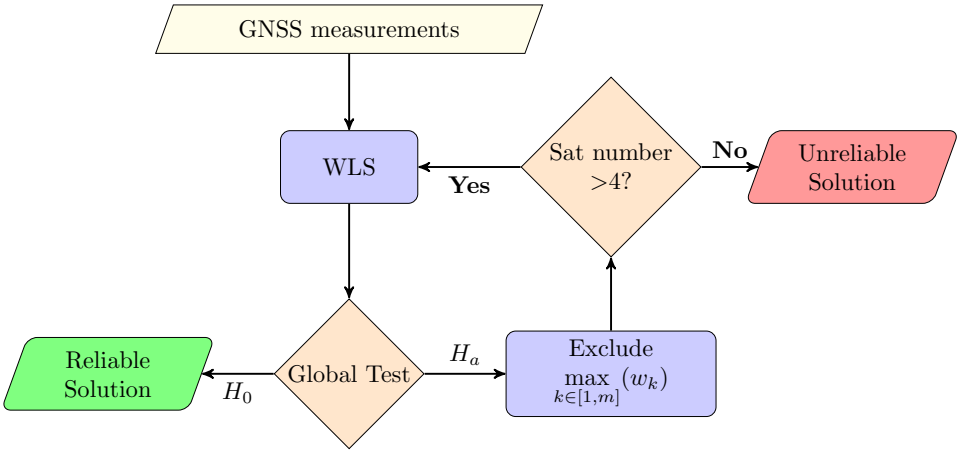

Figure 3.8 – Flowchart of the Classic Test

3.5.2.2 Subset Test (ST)

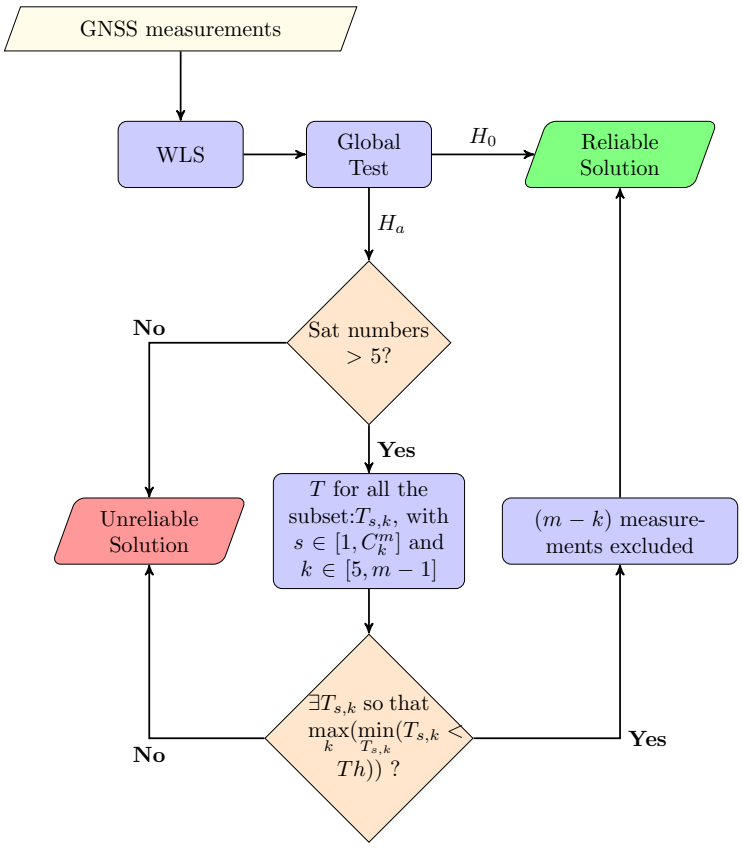

Figure 3.9 – Flowchart of the Subset Test

The principle of the Subset Test (ST) is to perform Global Test (GT) several times while taking out one or several measurements at a time in order to find the right measurement

set excluding the huge errors [123]. More precisely, as shown in Fig. 3.9, the test statistic used in ST is the same as that of the GT. After the initial failure of the GT with all the measurements, if there are enough satellites, that is to say, at least 2 redundancies to realize the fault exclusion, the ST will begin. The test statistics will be calculated for all the possible subsets that include $n+1$ to $m-1$ measurement, where n is the number of unknown to be estimated which is equal to 4 in our case and m is the number of measurements. Thus, all the possible subsets contain the cases of 1 to $m-(n+1)$ measurements excluded. Then, the subset that has the smallest test statistic below the threshold, and at the same time, the largest number of measurement, will be chosen to calculate the position solution.

There is no doubt that the multiple faults can be excluded by the ST. The drawback of ST, however, is the computational complexity especially for the future multi-constellation, which will provide more visible satellites for users. On the contrary, for the mono-constellation in urban environments, the main constraint is that there are often not enough redundancies for the ST, which will badly affect its performance.

3.5.2.3 Iterative Local Test

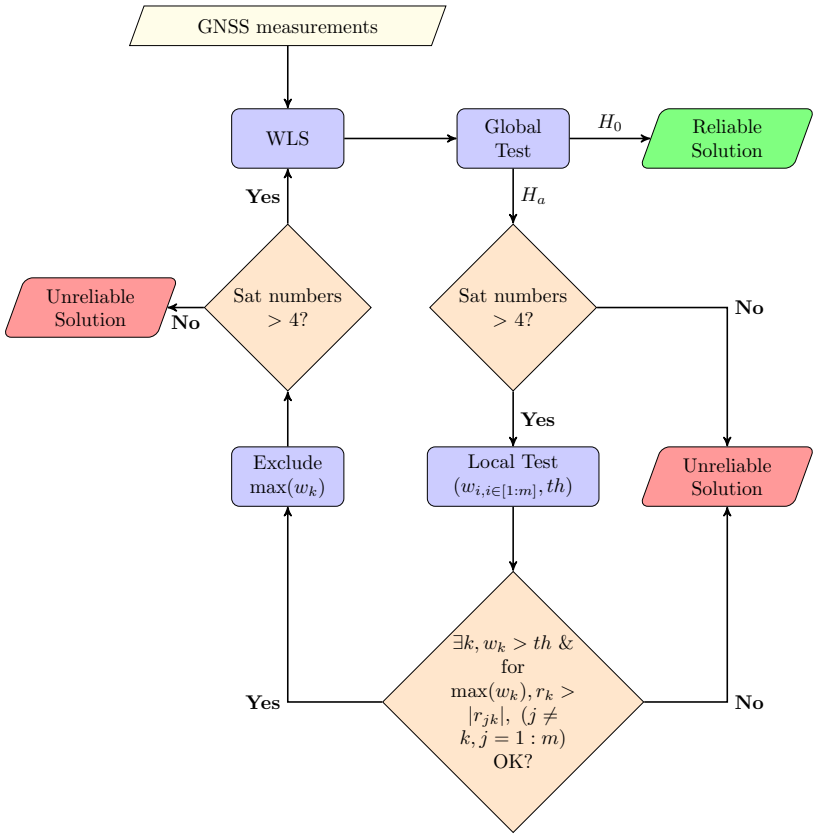

Figure 3.10 – Flowchart of the Iterative Local Test

The principle of the iterative Local Test (LT) is to combine the Global Test (GT) and the Local Test (LT) during each iteration. The GT is used to detect the existence of fault. If the GT is failed and there is enough redundancy, then the LT will be performed individually for each measurement. The measurement with the largest test statistic which is also above the threshold will be examined with the redundancy check. If the redundancy check passes, i.e., the condition in Eq. (3.27) is met, the measurement with the largest test statistic will be excluded. This LT can be continued until there is not enough redundancy or all the actual test statistics are below the threshold. The flowchart of the iterative local test is shown in Fig. 3.10.

The iterative local test is not computationally expensive, especially compared to the previous ST algorithm, since there are not many combinations of cases to do. But the same potential problem of poor redundancy exists in urban canyons.

3.5.2.4 Forward-Backward (FB) Test

Forward-Back (FB) testing is a FDE scheme which uses both global and local tests. The necessity of introducing FB testing is due to the existence of several phenomena in urban environments. First of all, the mutual influence of measurements, that is to say, an error of a measurement which can be absorbed by the residuals of other measurement, will possibly cause erroneous rejection of a good measurement [125]. What is more, the threat of multiple simultaneous failures can induce the risk of Unobservable Multiple Fault (UMF) [5]. That is to say, the error size can combine with the satellite geometry such that a huge position error is produced by very small residual, which make these faulty measurements unobservable by FDE algorithms. Thus, special measure ought to be taken in order to mitigate the mutual influence or even non-observability of the faulty measurements.

Furthermore, at least one redundancy is generally necessary in order to identify an outlier. But the visibility of satellites is usually poor in urban canyons, which means not much redundancy exists. This is also the drawback of the previous algorithms, especially in presence of multiple faults. As a result, FB will include a process of reconsideration of an earlier rejected measurement if more than one observation is excluded.

There are two main parts in the FB testing algorithm: the forward part and the backward part. In the forward part, the GT is firstly carried out to check the measurement consistency. If the GT fails, the LT will be performed in order to identify and exclude the outliers. This forward part will be conducted recursively until no more erroneous measurements are detected and the solution is declared reliable or unreliable. If the GT in the forward part is passed and more than one measurement is excluded, then the backward part will begin, where the excluded measurements will be reintroduced into the measurement set. Fig. 3.11 shows us

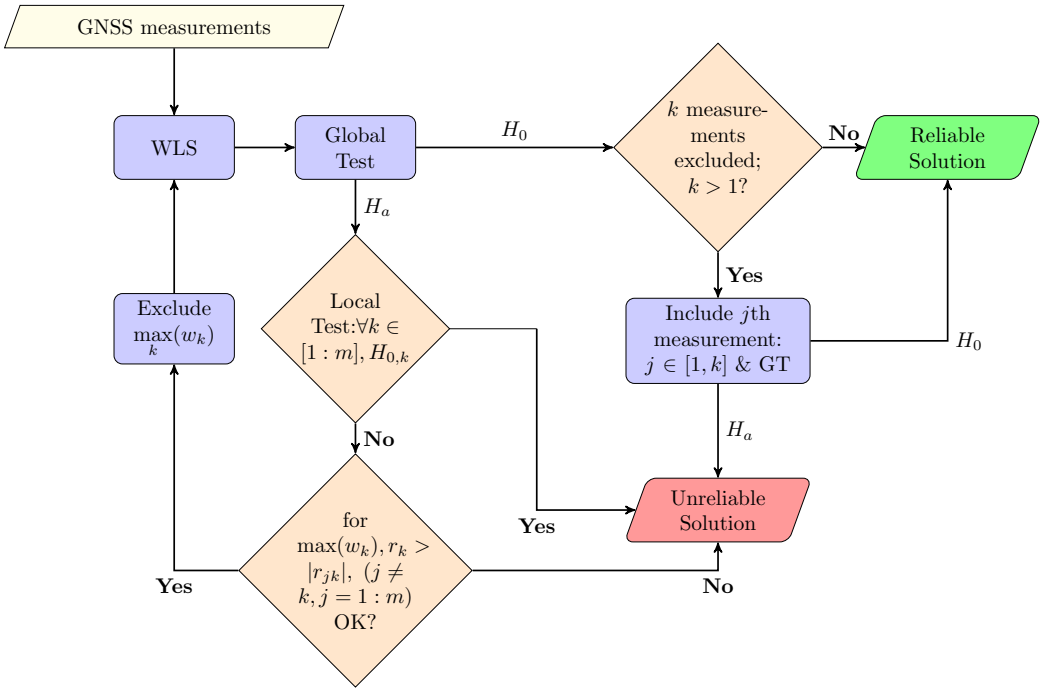

Figure 3.11 – Flowchart of the Forward-Backward Test

the complete scheme of the FB testing.

The main contribution of the FB testing is that the erroneous rejection of the measurement can be mitigated, which can also help to avoid the positioning failure due to the poor redundancy caused by fault exclusion.

3.5.2.5 Danish Method

The Danish method [124] is an iteratively reweighted least square scheme firstly used in the geodetic applications. This method aims at providing consistency among measurements by modifying the *a priori* weights. It is able to reweight the measurements specially to reduce the weights of the suspected outliers.

Here, the Danish method also begins with a Global Test (GT). If the GT is failed, a Local Test (LT) will be carried out in order to identify the faulty measurements. Once the outlier is identified by LT, the exclusion step is replaced by the reweighting scheme. The variance of the suspected measurement will exponentially increase based on the normalized residuals as follows [126]:

$$\sigma^2_{i,j+1} = \sigma^2_{i,0} \cdot \begin{cases} e^{\frac{w_{i,j}}{th}}, & \text{if } w_{i,j} > th \\ 1, & \text{if } w_{i,j} < th \end{cases} \tag{3.28}$$

where,

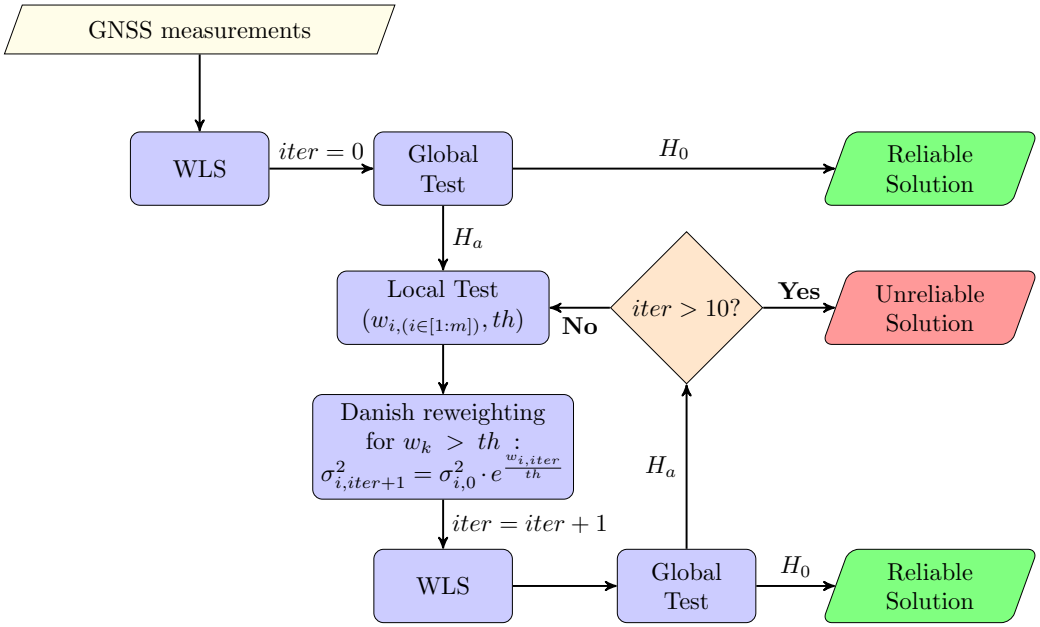

Figure 3.12 – Flowchart of the Danish Method

- $\sigma^2_{i,j+1}$ represents the variance of the ith measurement after $j+1$ iterations;
- $\sigma^2_{i,0}$ represents the a priori variance of the ith measurement error;
- $w_{i,j}$ represents the local test statistic of the ith measurement described in Eq. (3.16) after j iterations.
- th represents the local test threshold.

The Danish method is able to reduce the weight of the measurement with huge errors by increasing their variance instead of excluding them. This process can be iteratively repeated until the solution coverage and the weight no longer need to be changed. Fig. 3.12 gives an illustration of the overall Danish method scheme and here a maximal number of iteration which equals to 10 is added in order to avoid the slow convergence.

In fact, the Danish method replaces the exclusion step by the step of weakening the contribution of the faulty measurement to the overall measurement set. As a result, the problem of non-feasibility due to poor redundancy will be solved, which will be theoretically more adapted to urban environments to some extent.

3.6 Conclusions and Discussions

This chapter deals with the topics concerning GNSS position integrity. After an introduction of the principle terminology and definitions in the domain of GNSS integrity, the limitations and problematics of integrity monitoring in urban environments are analyzed. The difficulty

of integrity monitoring for urban transport applications is firstly to get rid of the one fault assumption made in traditional aeronautic integrity monitoring algorithms. Then the poor satellite visibility in urban canyons is also a limitation.

Different techniques of Fault Detection and Exclusion (FDE) are presented in detail: the Subset Test (ST), the iterative Local Test (LT), the Forward-Backward (FB) Test, the Danish re-weighting method as well as the Classic Test (CT). These FDE algorithms are able to detect and to exclude multiple faults, which can be potentially implemented into the low-cost GNSS commercial receivers. All these FDE techniques discussed in this chapter will be evaluated and compared with real data collected in urban canyons later in Chapter 6.

Part II

CONTRIBUTIONS REGARDING THE ERROR CHARACTERIZATION: ACCURACY IMPROVEMENT

Chapter 4

GNSS Local Error Characterization and Mitigation

Contents

Summary

GNSS performance in challenging environments is one of the most problematic issue for land users. This chapter will mainly discuss about the local effects which degrade the performances of the GNSS positioning and several models allowing to better characterize them.

This chapter will begin by analyzing the harmful local effects (e.g., NLOS receptions and multipath effects) and the way in which they may affect the GNSS positioning performances such as accuracy and integrity. Then, the existing approaches of NLOS/multipath mitigation is summarized. One of approaches adopted in this research work is signal weighting by Weighted Least Squares (WLS) estimator. The WLS can be highly efficient if correct measurement error models are adopted. As a result, several error models are presented, among which, a hybrid model is proposed. These models will be implemented and evaluated later in the chapter 5 with the help of a WLS estimator, which can distribute different weights by considering the real-time local effects.

4.1 Local Effects in Urban Environments and the Approaches of Mitigation

The urban environment presents several challenges to the GNSS signal reception, which could lead to severe degradation of positioning accuracy if no special measures are taken. These complexities can be sorted into two major issues.

First of all, since obstacles in the urban environment can block GNSS Line-of-Sight (LOS) signals, the number of satellites in view will be effectively reduced. Yet this situation can be improved by using a multi-constellation receiver in order to obtain sufficient direct-LOS signals for the computation of a position solution [115, 127]. This effect influences also the geometrical distribution of the satellites around the users, i.e., Dilution of Precision (DOP).

Secondly, due to flat surface reflectors presenting in the urban environment, the problems of multipath interference and NLOS reception arise [53], which are illustrated in Fig. 4.1. In fact, the multipath interference and NLOS reception should be considered as two different phenomena as they can produce different ranging errors. The detailed explanations about these two phenomena are in [128].

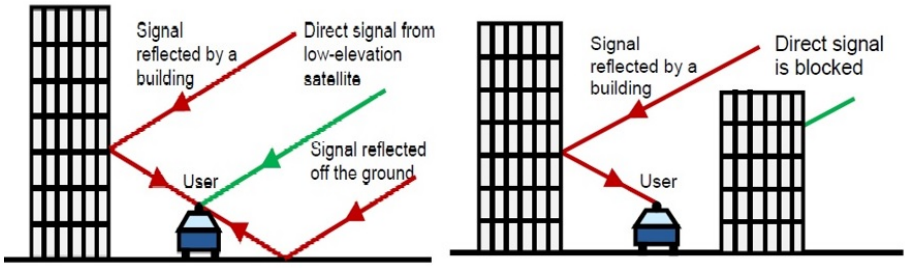

Figure 4.1 – (left)Multipath interference; (right)NLOS reception [128]

The consequences of the two major problems mentioned above are:

1. ***Distort the correlation function of receiver***
   In GNSS received signal processing, correlation is an essential step which helps receivers to estimate Time of Arrival (TOA) Δt of the GNSS signals, which directly links to pseudorange measurements. In fact, by correlating the received satellite Pseudo Random Noise (PRN) code with the replica generated by the local receiver, the TOA Δt can be determined from the maximum of the correlation function as shown in Fig. 4.2 [129]. The reception of a multipath-contaminated signal will effectively distort the correlation function so that the code and carrier phase tracking accuracy will be degraded. This effect can lead to large range errors as well as inaccurate position solutions. Fig. 4.3 gives us an illustration of the effect of multipath interference on the correlation function [7]. The resulting code tracking error depends on the receiver design as well as the direct

and reflected signal strengths, path delay and phase difference, and this error can be up to half a code chip [130, 131].

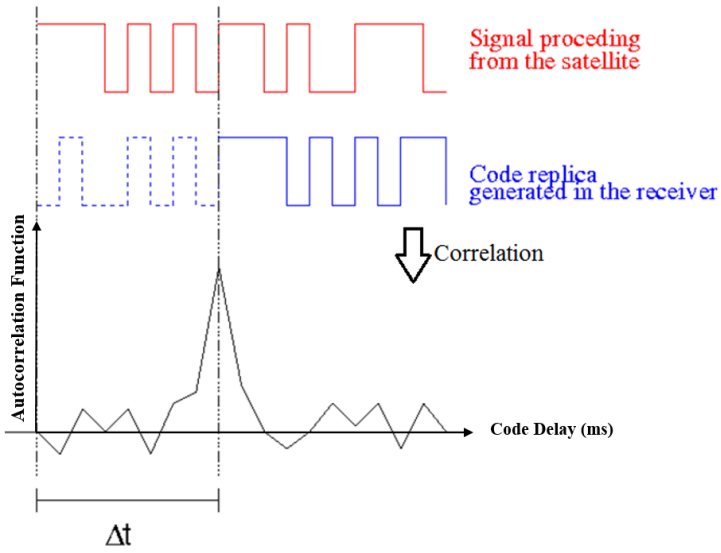

Figure 4.2 – Principle of GNSS code delay tracking [129]

2. ***Increase or decrease the carrier-power-to-noise-density ratio (C/N_0) of the received signals***

   The carrier-power-to-noise-density ratio, *i.e.*, C/N_0, represents the ratio of signal power and noise power per unit of bandwidth. In urban environments, constructive multipath interference leads to an increase in C/N_0, while destructive multipath interference leads to a decrease. The level of C/N_0 will mainly influence the signal tracking performance of GNSS receivers. For instance, the noise of the receivers' tracking loop is directly linked with C/N_0 and the linear domain of the discriminator output is also strongly affected by the level of C/N_0, which will further influence the tracking error [6]. Since the phase of a reflected signal with respect to its directly received counterpart depends on the wavelength, multipath interference may be constructive on one frequency and destructive on another frequency. As a result, these characteristics contribute to new multipath detection technique by comparing the difference in measured C/N_0 between two or multiple frequencies with what is expected for that signal at the elevation angle [53].

3. ***Change the polarization of the signal***

   GNSS signals directly received from satellites have Right-Handed Circular Polarization (RHCP). But after one reflection, the polarization becomes Left-Handed Circular Polarization (LHCP). Thus, most reflected signals have LHCP or mixed polarization. Consequently, multipath mitigation techniques can be developed at antenna design level by differentiating the sensitivity of antenna for RHCP and LHCP [53, 57, 58, 132].

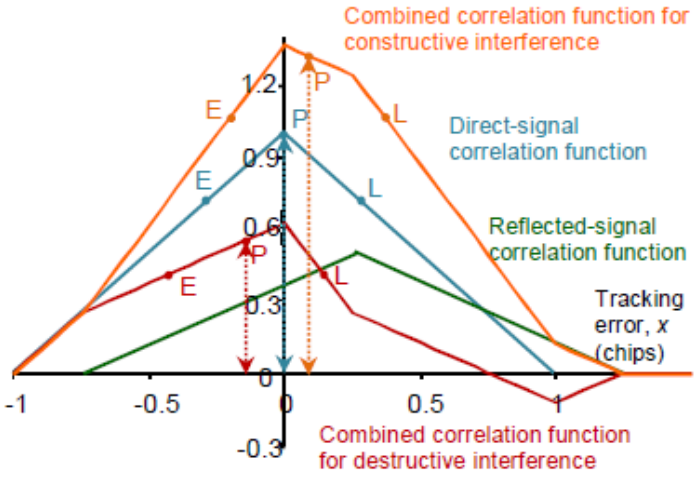

Figure 4.3 – Effect of constructive and destructive multipath interference on the correlation function [7]

4. ***Inconsistent GNSS pseudorange measurements***
   Because of the stringent environment for the GNSS signal reception, it is possible that the pseudorange measurements provided by one or more GNSS satellites are not consistent with other ones. Hence, it is necessary to implement algorithms to ensure that the pseudorange measurements are all consistent. [114] has implemented the RANdom SAmple Consensus (RANSAC) algorithm, developed for computer vision tasks, in the GNSS context. This algorithm is based on consistency checking and it is capable of detecting multiple fault unlike the RAIM technique, which is compatible to a degraded scenario such as urban environment.

The techniques of detecting and mitigating the NLOS receptions and multipath effects exist at different levels. Table 4.1 provides us with a detailed classification of the existing approaches in the literature as well as their main features.

In the framework of this thesis, we will mainly concentrate on the approaches of signal weighting, consistency checking as well as a statistical approach such as the EKF-based filtering. In the next section, several weighting models will be presented, among which, the proposed hybrid model involves also the technique of mapping-aided approach.

Table 4.1 – Classification of the GNSS Multipath Mitigation Approaches

Approaches	Techniques	Features of Techniques	References
Antenna design	① Dual polarization antenna	This method cannot detect all the NLOS, especially those reflected by even times (*e.g.*, twice or 4 times).	[53, 57, 58]
	② Choke Rings	The volume of choke-ring antenna system is too large for most dynamic positioning applications	[132–134]
	③ Controlled Reception Pattern Antenna (CRPA)	Better performance for high elevation signals; large volume and expensive	
	④ Angle of Arrival (AOA) measurement	suitable for NLOS and strong multipath; interference; expensive	
	⑤Multiple Antennas	suitable for large vehicles (*e.g.*ships, trains or large aircraft)	
Receiver Design	① Code Discriminator Design	expensive for manufacturing; huge power consumption	[7, 59]
	② Early-Late Correlator Comparisons	more effective for dynamic applications	[135, 136]
	③ Vector Tracking	Similar mechanism with carrier smoothing	
Weighting model	① C/N_0-based Weighting model ② Satellite elevation-based weighting model	Can improve the positioning accuracy; easy to implement	[137–140]
	③ Danish Reweighting Method	it is an empirical procedure with no valid statistical explanation but perform well in practice	
Signal Processing	① Carrier Smoothing ② Doppler Domain Multipath Mitigation	more adapted to dynamic applications; only multipath interference mitigation, not NLOS mitigation	[141–143]
	③ Multi-frequency C/N_0	reliable for static applications; easy to implement	
Image Processing	① Fisheye Camera	Discrimination between LOS/NLOS	[144–146]
Consistency Checking	① RAIM ② Subset Testing ③ Forward-Back Testing ④ Iterative Local Test	Measurement redundancy required Performance degraded if a large proportion of signals are NLOS	[130, 139, 140]
Mapping-Aided	①2D map-matching (*e. g.*, Urban Trench Model (UTM)) ② 3D environment model	Mapping error exist without knowing true position; computationally intensive; huge work to establish and load 3D city model.	[36, 147, 148]
Statistical Approaches	① Bayesian approaches ② Particle filtering ③ KF-based innovation filtering ④ Maximum likelihood Estimation	latter state is easy to be contaminated by the former one because of the sequential procedures; high processing load is possible	[149–151] [152–154]

4.2 Characterization of the Pseudorange Errors

4.2.1 Estimation of the Pseudorange Errors

GNSS code pseudorange errors come from a variety of sources, which are analyzed in detail in chapter 2. Except errors due to local effects, all the other errors in nominal conditions are well modeled and tested in aeronautic domain for Safety-of-Life (SoL) utilities. The faulty case errors due to GNSS constellation (such as the major satellite failure) or atmosphere (such as the irregular ionospheric delay) occur with low probability: for instance, the probability of occurrence of a major satellite failure is 3 times per year for a 24 GPS satellites constellation.

The pseudorange errors due to local effects, such as multipath, are the most complicated to be modeled because of their variations which strongly depend on the local environments.

And they are frequent and extremely harmful for GNSS receivers since the errors can even be up to several kilometers. In this section, we will present the methodology of estimating the pseudorange (PR) errors in order to understand their behavior in urban canyons and pave the way for the error characterization in the following sections.

The method for computing the PR error in this research work has mainly been developed and employed in the framework of the project named INTURB[1]. It is a post processing procedure with the help of the test trajectories and reference trajectories collected by the navigation systems implemented on the Vehicle for Experimental Research on Trajectories (VERT) of the IFSTTAR. The raw data are collected with a low-accuracy receiver Ublox LEA 6T and the corresponding reference trajectories are provided by an Inertial Navigation System LandINS hybridizing a tactical Inertial Measurement Unit and a high-accuracy dual-frequency GNSS receiver Novatel-DLV3 [155].

The code pseudorange measurement of the ith satellite at epoch k can be written as in Eq.(2.1):

$$P^i(k) = \rho^i(k) + c(\delta t_u(k) - \delta t^i(k)) + d_I^i(k) + d_T^i(k) + D_{mult}^i(k) + n_p^i(k)$$

where,
- ρ^i represents the true geometric distance between the receiver and the satellite i;
- δt_u represents the advance of the receiver clock with respect to system time;
- δt^i represents the advance of the satellite clock with respect to system time;
- d_I^i represents the error due to ionospheric propagation delay;
- d_T^i represents the error due to tropospheric propagation delay;
- D_{mult}^i represents the error due to multipath;
- n_p^i represent measurement noises.

Thus, the PR error can be estimated in this way:

1. The true geometric distances between the receiver and the satellite ρ^i is calculated with the help of the ground truth and the position of ith satellite;
2. The satellite clock offset δt^i is corrected with the broadcast term provided by the system;
3. The atmospheric delay d_I, d_T are corrected by applying the standard models: For the tropospheric delay, the Hopfield model with Essen and Froome coefficients is adopted with standard meteorological parameters defined in [19]. For the ionospheric delay, the GPS broadcast model is used;
4. The receiver clock offset is estimated with the satellite nearest to the zenith, which is theoretically not or the least affected by multipath among all the other satellites in view;

[1]INTURB: positioning INTegrity in URBan environments

5. Finally, by subtracting all the terms estimated in the steps above from the code pseudorange measurement, we can obtain the code pseudorange measurement errors due to multipath, the receiver noise as well as the residual errors which cannot be totally corrected by the error models.

In fact, in the constraint environments, the measurement noises are almost negligible compared to the error caused by local effects, such as multipath error or especially the NLOS reception. We will consider approximately here that the final term obtained in the last step is the error due to local effects, i.e., multipath and NLOS.

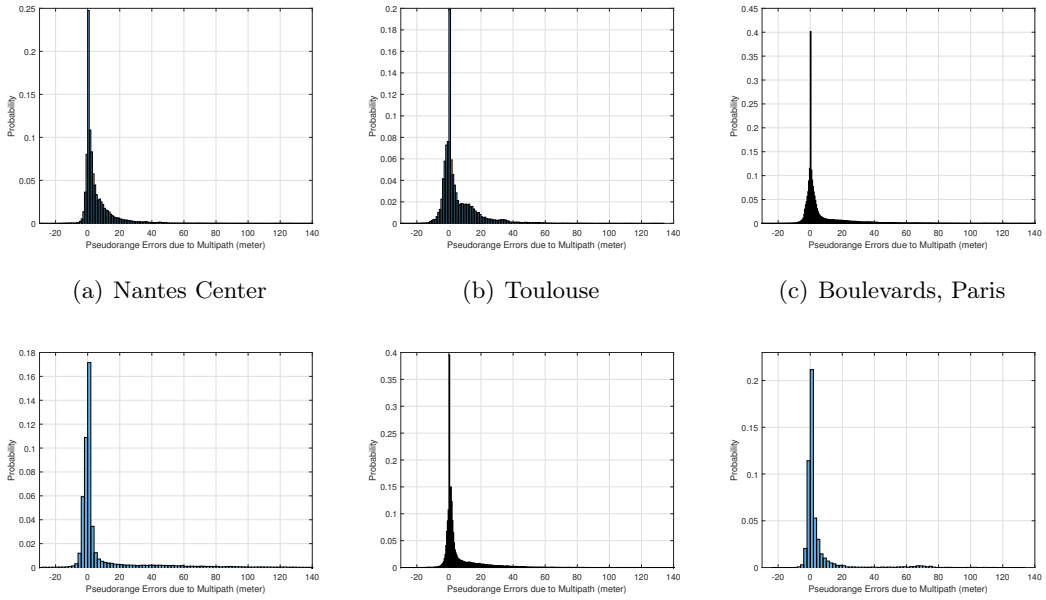

(a) Nantes Center (b) Toulouse (c) Boulevards, Paris

(d) La Défense, Paris (e) Paris XII^{th} (f) Nantes

Figure 4.4 – Histograms of the PR Errors (tails are due to Multipath)

Fig. 4.4 shows the histograms of the estimated PR error with GPS data collected in urban environments of different cities. Table 4.2 reports a summary of the numbers of epochs, the numbers of measurements and the total duration of each dataset. From the histograms we can find that the PR errors have heavy tails especially in the positive part (the largest error reaches more than 100 meters) and the distributions are skew. As expected, this is mainly due to the multipath or NLOS reception since a reflected signal usually travels a longer distance than the direct one. Obviously, the PR errors in urban environments are severely biased by the local effects.

Thus, how to correctly model the PR errors or to properly reduce/exclude the contribution of the severely contaminated signal on the navigation solutions are the main tasks of the following sections.

Table 4.2 – A Summary of Dataset

	Number of Epochs	Number of Observations	Duration
Nantes Center	17903	130073	59min40sec
Toulouse	13779	106568	45min55sec
Boulevards, Paris	80152	585921	4h27min10sec
La Défense, Paris	14776	106413	49min15min
Paris XII^{th}	33567	256141	1h51min53sec
Nantes	3326	24656	11min5sec

4.2.2 Existing Pseudorange Error Models

In a WLS adjustment, the theoretically optimal estimate, which is supposed to be unbiased with minimal variance, can never be achieved unless the correct stochastic measurement error model is applied. The measurement models describe the precision of measurement, which can contribute to improving the positioning accuracy as well as the integrity monitoring process.

The main objective of this section is to present several existing methods that estimate the pseudorange error variance in real time while taking into consideration the local effects in constraint environments. The criteria the most employed to evaluate the signal quality are for example the Carrier-Power-to-Noise-Density Ratio C/N_0 and the satellite elevation. These parameters are easy to be obtained but sometimes cannot correctly reflect the signal quality. The signal reception state, i.e., LOS/NLOS indicator, can be a good criterion of signal quality. But it can only be obtained with the help of other techniques such as the fisheye camera [146] or digital map information. The latter one will be introduced later in the next section.

4.2.2.1 Carrier-Power-to-Noise-Density Ratio (C/N_0) Based Variance Model

The Carrier-Power-to-Noise-Density Ratio C/N_0 is one of the key parameters that determine receiver performance. It is an indicator of GNSS signal tracking quality. For example, tracking loops experience a rapid increase of tracking error for signals with low C/N_0 (e.g., lower than 25dbHz) or even loose lock. In most of the cases, the low C/N_0 are due to multipath, i.e., signal received after reflections/diffractions or a poor satellite geometry.

Fig. 4.5 shows an illustration of the absolute PR errors as a function of C/N_0 with GPS data collected in the urban canyon of Nantes and Toulouse, France. As expected, PR errors increase when the values of C/N_0 decrease.

According to this feature between C/N_0 and the measurement errors, several models of measurement variance exist in the literature as a function of the carrier-power-to-noise-density

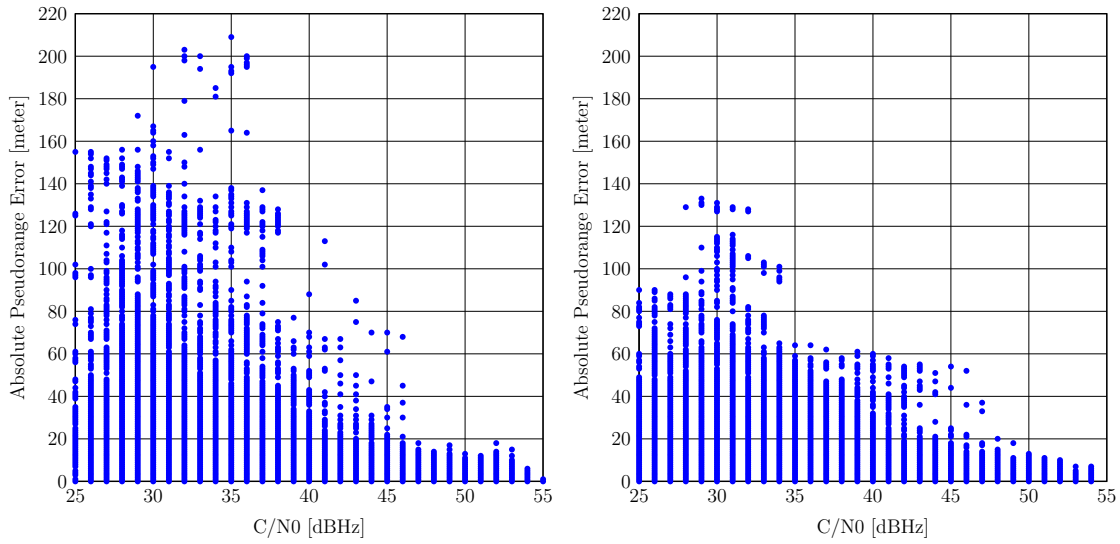

(a) Data Collected in Nantes Urban Canyon (b) Data Collected in Toulouse Urban Canyon

Figure 4.5 – Absolute Pseudorange Errors as a function of C/N_0 in different urban canyons

ratio (C/N_0), such as the sigma-ε model [138] and the sigma-Δ model [156]. Here in this research work, we choose to implement one of the C/N_0 models: sigma-ε model, which is studied in many research work and is proved to be generally efficient.

The sigma-ε model was built up firstly for geodetic receivers by [138], which links the C/N_0 observable to the variance of the GPS phase observation. Then this model is generalized by [137]. A complete formula that goes with all receiver types is proposed, which can be written as:

$$\sigma_i^2 = a + m \times 10^{-\frac{C/N_0}{10}} \tag{4.1}$$

where,
- σ_i^2 (in m^2) represents the variance of the measurement error of the ith satellite;
- a (in m^2) and m (in m^2Hz) are model parameters which depends on the receiver/antenna type and environments.

There are two parameters to calibrate in this sigma-ε model: a and m. They should be chosen according to the particular user equipment as well as the environment. In the current literature, these two parameters are usually calibrated empirically. Once proper parameters are chosen, this model generates little computational load and is well suited for kinematic and real time applications.

4.2.2.2 Satellite Elevation-Based Variance Model

Satellite elevation is another criteria to evaluate signal quality since a satellite with high elevation is generally less impacted by the local effects. Fig. 4.6 shows the absolute PR error as a function of satellite elevation with GPS data collected in the urban canyons of Nantes and Toulouse. Similar trend with the previous C/N_0-PR error can be observed, the PR errors decrease when satellite elevations increase.

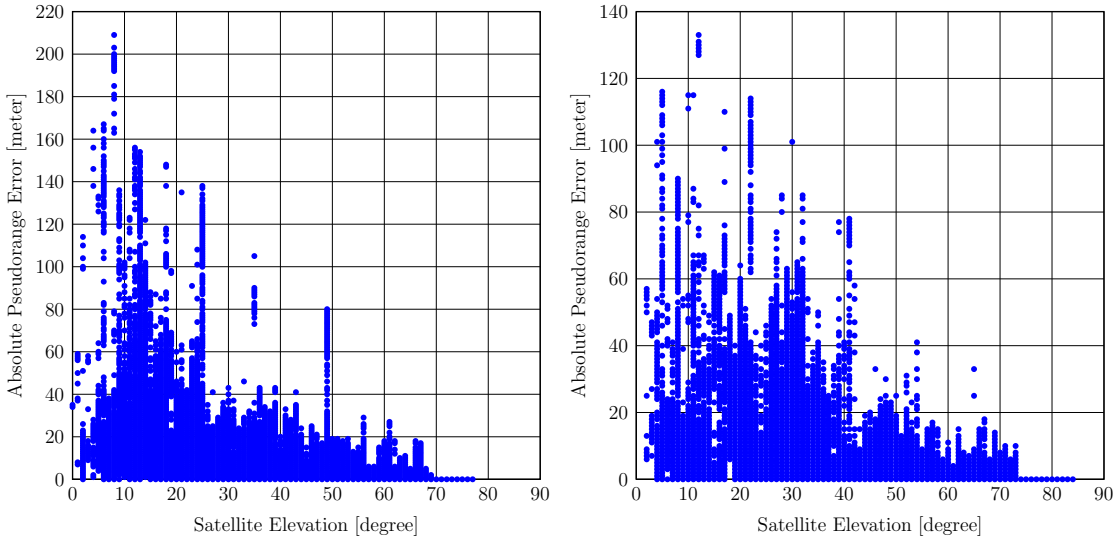

(a) Data Collected in Nantes Urban Canyon (b) Data Collected in Toulouse Urban Canyon

Figure 4.6 – Absolute Pseudorange Errors as a function of Satellite Elevation in different urban canyons

In many GNSS analysis software packages (such as *Gamit* [157]), the elevation-dependent measurement error models are implemented because of their simplicity of implementation and the global efficiency.

Several elevation dependent PR error variance exist in the literature, such as the *sin* type one in Eq. (4.2) and the *exponent* type one in Eq. (4.3) [119, 158]:

$$\sigma_i^2 = c_1^2 / sin^2(\theta_i) \tag{4.2}$$

$$\sigma_i^2 = c_2^2 + c_3^2 \times exp(-\frac{2\theta_i}{\theta_0}) \tag{4.3}$$

where,
-θ_i represents the elevation of the ith satellite;
-c_1, c_2, c_3 and θ_0 are model parameters which depend on the receiver and environment.

The model parameters should fit the receiver equipment used for data collecting as well as the traveled environments. There is not yet a methodology in the literature to efficiently choose these model parameters except empirically calibrating.

4.2.2.3 Dirichlet Process Mixture (DPM) Model

The Dirichlet Process Mixture (DPM) model is a flexible density modeling based on a Bayesian nonparametric approach [159]. It is adapted into the context of GNSS by the PhD research work of N. Viandier in [160]. DPM can get rid of the drawback of the Jump Markov System (JMS). That is to say, instead of using a limit number of Gaussian, DPM can generate an infinite Gaussian mixture. Moreover, not like the JMS, which has to allocate the time of sliding window length for initialization, DPM can start immediately at the time of acquisition [161] .

The basis of the DPM is the Dirichlet Process (DP) [162], which is a distribution over distributions, i.e., each component draw from a Dirichlet process is itself a distribution. Distributions draw from a Dirichlet process are discrete, but cannot be described using a finite number of parameters, thus it is classified as a nonparametric model.

The general principle of the DPM is to model a set of observations $\{y_1, \cdots, y_n\}$ using a set of latent parameters or also called cluster $\{\theta_1, \cdots, \theta_n\}$. The preliminary theory of DPM begins from the Bayesian non-parameter density estimation problem.

* **Preliminary Knowledges of Bayesian Non-Parametric Density Estimation** Denoting F the distribution of the observations y_k. The nonparametric model allowing to estimate F can be written as:

$$F(y) = \int_{\theta} f(y|\theta) d\mathbb{G}(\theta) \tag{4.4}$$

where,
- $\theta \in \Theta$ is the latent parameters or cluster;
- $f(\cdot\,|\theta)$ is a mixed Probability Density Function (PDF) representing the likelihood function;
- $\mathbb{G}$ is a Random Probability Measure (RPM) distributed according to a prior distribution.

For the DPM, the DP is selected as a RPM prior for $\mathbb{G}$. There are two parameters to determine a DP: a base distribution $\mathbb{G}_0$ and a positive scaling parameter α. Since the DP is a distribution over distributions (i.e., a measure on measures), we can randomly draw a distribution $\mathbb{G}$ from a DP and then independently draw n random variables θ_k for $\mathbb{G}$. That is to say,

$$\theta_k|\mathbb{G} \sim \mathbb{G} \tag{4.5}$$

where,

$$\mathbb{G} \sim DP(\mathbb{G}_0, \alpha) \tag{4.6}$$

Moreover, an important property of the DP is that $\mathbb{G}$ is discrete with probability which equals to one. Consequently, the stick breaking representation can be introduced as an infinite sum of Dirac measures [163]:

$$\mathbb{G} = \sum_{k=1}^{\infty} \pi_k \delta_{\theta_k} \tag{4.7}$$

where,
- $\theta \sim \mathbb{G}_0$;
- $\pi_k = \beta_k \prod_{j-1}^{k-1}(1-\beta_j)$;
- $\beta_k \sim B(1, \alpha)$ and B is the standard Beta distribution;
- δ_{θ_k} is a Dirac measure located in θ_k.

What is more, it is proven in [164] that, by marginalizing out G, the predicted distribution of θ_{n+1} knowing cluster $\{\theta_1, \cdots, \theta_n\}$ follows a Polya urn scheme:

$$\theta_{n+1}|\theta_{1:n} \sim \frac{1}{\alpha+n}\sum_{k=1}^{n}\delta_{\theta_k} + \frac{\alpha}{\alpha+n}\mathbb{G}_0 \tag{4.8}$$

This means that, the new sample θ_{n+1} can take the value of a previous sample with the probability $\frac{n}{\alpha+n}$ or can take a random value from $\mathbb{G}_0$ with the probability $\frac{\alpha}{\alpha+n}$.

Finally, the unknown distribution of observation F can be estimated as follow:

$$F(y) = \sum_{k=1}^{\infty} \pi_k f(y|\theta_k) \tag{4.9}$$

* **Dirichlet Process Mixture (DPM) and Its Adaptation in the Context of GNSS**

With the preliminary knowledges described in the previous text, we can now enter into the Dirichlet Process Mixture (DPM), which is based on the Dirichlet Process (DP) in the framework of Bayesian non parametric approaches.

Fig. 4.7(a) provides an hierarchical representation of the DPM models. The DP is mainly used to specify the latent distribution. The core part of the DPM can be seen as a simple Bayesian problem with the likelihood function $y_i \sim p_{\theta_i}(y_i)$ and the prior $\theta_i \sim \mathbb{G}(\theta_i)$. The prior $\mathbb{G}$ is not fixed, which is a random distribution generated by the DP described previously. They can be summarized as:

$$\begin{aligned} &y_i \sim p_{\theta_i}(y_i),\ i = 1, \ldots, m \\ &\theta_i \sim \mathbb{G}(\theta_i) \\ &\mathbb{G} \sim DP(\mathbb{G}_0, \alpha) \end{aligned} \tag{4.10}$$

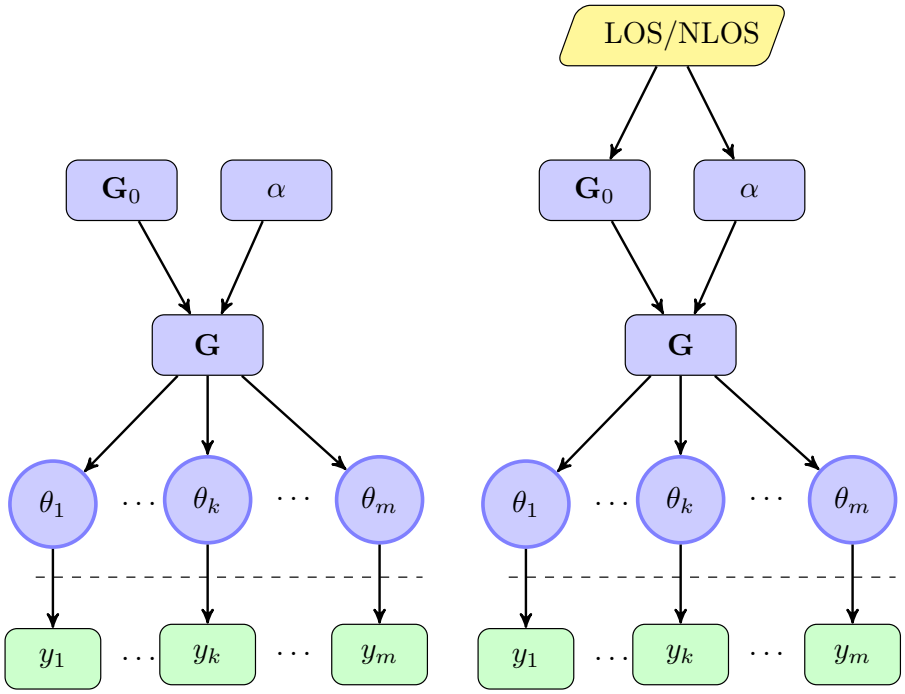

(a) DPM [161] (b) DPM with Signal Reception States [160]

Figure 4.7 – Hierarchical representation of DPM models

A special case of the DPM is that the prior likelihood function is chosen as a Gaussian distribution. That is to say, if we choose the latent parameters θ_i as the couple of mean and variance of the PR errors:

$$\theta_i = \{\mu_i, \Sigma_i\} \tag{4.11}$$

the mean and the $p_{\theta_i}(y_i)$ in the equation above can be written as:

$$p_{\mu_i,\Sigma_i}(y_i) = \mathcal{N}(y_i; \mu_i, \Sigma_i) \tag{4.12}$$

Under this condition, the base distribution is a Normal Inverse-Wishart (IW) Distribution since the IW distribution represents positive definite matrices, which can serve as a prior for any covariance matrix Σ. So, we have:

$$\mathbb{G}_0(\mu, \Sigma) = \mathcal{N}(\mu; m, B) \times \mathcal{W}^{-1}(\Sigma^{-1}; R, r) \tag{4.13}$$

where,
- m and B are respectively the mean and the variance-covariance matrix of the normal distribution;
- R and r are respectively the scale matrix and the degree of freedom of the IW Distribution.

The DPM can now be adapted to the context of GNSS applications with the steps above. The PhD research of [160] has improved this version of DPM by adding another level at the top of the DPM hierarchical representation as shown in Fig. 4.7(b). That is to say, the signal reception states LOS/NLOS are considered to help construct the base distribution $\mathbb{G}_0$ and the strength parameter α of the DP.

The variables of the DPM will change according to the signal reception state LOS/NLOS. This means, for LOS reception, we have:

$$\begin{cases} \mathbb{G} \sim DP(\mathbb{G}_0, \alpha_1) \\ \sigma_k \sim \mathcal{W}^{-1}(\Sigma_1, dof1) \\ \mu_k \sim \mathcal{N}(\mu_0, \frac{\sigma_k}{k_1}) \end{cases} \tag{4.14}$$

For NLOS reception, we have:

$$\begin{cases} \mathbb{G} \sim DP(\mathbb{G}_0, \alpha_2) \\ \sigma_k \sim \mathcal{W}^{-1}(\Sigma_2, dof2) \\ \mu_k \sim \mathcal{N}(\mu_0 + \hat{r}_k, \frac{\sigma_k}{k_2}) \end{cases} \tag{4.15}$$

where,
- α_1 and α_2 are DP strength scaling factors, where $\alpha_1 << \alpha_2$;
- Σ_1 and Σ_2 are scale matrix of the IW distribution, where $\Sigma_1 < \Sigma_2$;
- dof_1 and dof_2 are Degree of Freedom of the IW distributions, where $dof_1 < dof_2$;
- μ_0 represents the mean of the normal distribution, which is to be fixed;
- k_1 and k_2 are scale factors and $k_1 > k_2$;
- $\hat{r}_k$ is the estimated PR errors, which can be taken as the estimated residual.

In fact, according to Eq. (4.8), the fact of choosing DP strength parameter as $\alpha_1 << \alpha_2$ means that the latent parameter for a NLOS signal reception has a high probability of being drew from the base distribution $\mathbb{G}_0$ rather than being equal to the previous clusters. This procedure is essential since it can better follow the parameter (error mean an error variance) jumps caused by the NLOS receptions.

As a result, at each epoch for each satellite, the final mean μ and variance σ of the mixture error distribution estimated by DPM are obtained with the weighted sum of N particles as follows:

$$\mu = \sum_{k=1}^{N} w_k \mu_k \tag{4.16}$$

$$\sigma^2 = \sum_{k=1}^{N} w_k (\sigma_k^2 + \mu_k^2) - \mu^2 \tag{4.17}$$

where,

- w_k represent the weight of the kth particle, which can be calculated according to the Sequential Importance Sampling (SIS) algorithm or Rao-Blackwellisation particle filter [165].

The research work of [160] adopts thresholds on C/N_0 or estimated residuals in order to distinguish the signal reception state (LOS/NLOS). But these criteria are not exactly suitable in face of complex dense urban canyons. This is because C/N_0 values can possibly increase due to constructive multipath interference. And the estimated residuals are probably small with the presence of the correlated measurement faults, which is also mentioned as Unobservable Multiple Fault (UMF). As a result, these criteria may induce erroneous estimation from the beginning of the DPM hierarchical level.

The DPM has several advantages compared to the traditional models since it can estimate dynamically the mean and variance at each epoch for each satellite according to their state of reception. But the choice of parameters is always complicated and not yet a methodology exists in the literature.

The choices of parameters include the number of particle N, the strength parameter of the DP under LOS and NLOS $\alpha_{1,2}$, the parameters for IW distribution under LOS/NLOS as well as their degree of freedom, the scale factors $k_{1,2}$ as well as the prior distribution initialization parameters. These parameters should be chosen carefully since they will influence on the final estimations.

Furthermore, the complexity of algorithm implementation and parameter calibration prevent DPM from being employed as real-time algorithm for GNSS applications.

4.2.3 A Proposed Hybrid Model: Contribution of the Urban Multipath Model (UMM)

4.2.3.1 Starting from the Urban Trench Model (UTM)

The Urban Trench Model (UTM) is proposed in [35]. It is based on the exploitation of a *2D+1* digital map containing simplified features of urban environment as well as the corresponding building height information in real time. By geometric modeling, the UTM can provide signal reception states by separating the satellites which are in direct visibility from the ones which are hidden or in indirect visibility. Moreover, the additional distance traveled by the NLOS signals can be calculated by UTM and further corrected from the pseudorange measurements.

The map information is from the BD TOPO® of the IGN[2], which can be registered as a set

[2]Institut National de l'Information Géographique et Forestière

of attributes applicable to the standard polyline structure of digital maps. For instance, the street are made of links between nodes (i.e., segments) and shape points; the buildings are made of polygons. An illustration of the BD TOPO® layers is shown in Fig. 4.8(a).

The first step of the UTM is to characterize the street segment, on which is located the vehicle, with several parameters as follows:
- The segment ID;
- The direction angle;
- The point coordinates at two sides of the segment;
- The neighbor's id list (for a fast map-matching process);
- W: Width of the street;
- H: Height of buildings;
- P: Position of the vehicle, which is a normalized indicator and takes the value zero for the extreme left side of the street and the value one for the extreme right side.

This step can pave the way for the following step of satellite mask computation. An important assumption of UTM is that, the urban streets are approximately considered as trenches with constant width and homogeneous heights at each side and the length of each trench is infinite, where comes from the model name "Urban Trench". Fig. 4.8(b) provides a street view of a typical urban trench.

Then, with the previous triplet parameters, the geometric model of the street can be established as shown in Fig. 4.8(c). The algorithm for calculating the critical elevations can be carried out as an illustration shown in Fig. 4.8(c). And the mask of visibility can be constructed by exploring each direction of the vehicle as an example shown in Fig. 4.8(d).

The elevation of each satellite will be compared with the critical elevation in the visibility mask. If the satellite elevation is lower than the critical elevation, the signal reception state is NLOS, otherwise, the signal is received as LOS.

Finally, the additional distances traveled by the NLOS signals can be calculated according to the geometry relations, which can be later corrected in the calculation of navigation solutions.

The basic version of UTM is a deterministic one. And a later version has been expanded to a probabilistic one in [36] by taking into consideration the distribution of the pseudorange errors. In the following part of the research work, we will only consider the deterministic UTM.

In terms of the computation of the additional distances for the NLOS signals, the initial version of the deterministic UTM considers that the number of reflections that may occur is supposed not to exceed 3 and the opposite buildings are always high enough to reflect the

(a) The BD TOPO ® layers

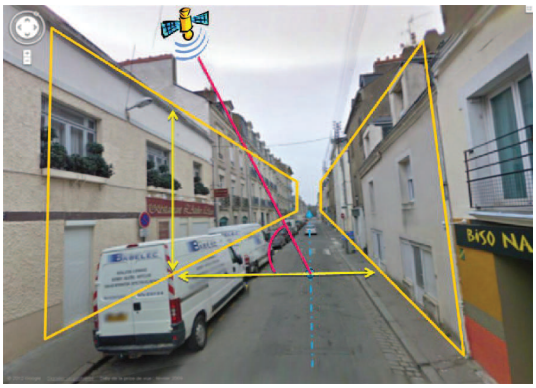

(b) A typical uban trench (corresponding to the red line in (a))

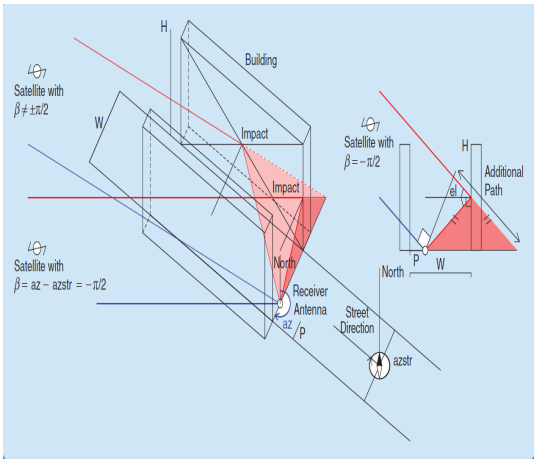

(c) The geometric model

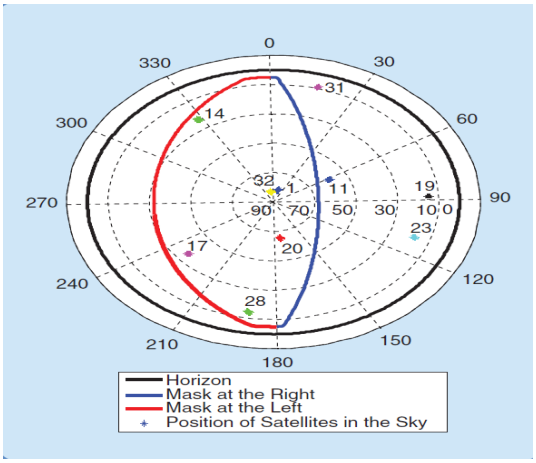

(d) Mask of Visibility

Figure 4.8 – Urban Trench Model Illustration [35]

NLOS signals. This version is further improved by taking into consideration the height of the opposite building. That is to say, if the opposite building is not high enough to reflect the signal, the additional distance will not be calculated by the specular reflection law. In these situations, the signals are potentially received by diffractions. Due to the complexity of fixing the diffraction direction of the received signal, the additional distance will be considered as zero.

The two versions of UTM will be further implemented and evaluated with real data in the chapter 5.

4.2.3.2 From Urban Trench Model (UTM) to Urban Multipath Model (UMM)

As mentioned in the previous section, an important hypothesis of UTM is that, the length of the streets is infinite and the buildings at each side of the street are of the same height. In fact, this hypothesis is an approximation of the map geometry. It fits well the reality when the vehicle is inside the homogeneous streets which have approximately the same geometric features at each side. An example of a typical urban trench is shown in Fig. 4.9(a). However, this assumption is no longer true especially in the non-homogeneous streets or the intersections as illustrated in Fig. 4.9(b).

(a) Inside a homogeneous street: a typical urban trench

(b) At an intersection area

Figure 4.9 – Example of two kinds of streets

In order to avoid the drawback of the UTM, the Urban Multipath Model (UMM) is proposed while getting rid of the infinite length street assumption, which allows improving the robustness of the model. The UMM uses the same BD TOPO road layers as UTM. A simplified ray tracing approach is adopted by UMM while taking into consideration the geometric features of the surrounding environments.

The process is first to detect if any facade exists in every satellite azimuth, with a height high enough to occult the corresponding satellite elevation. This initial step will identify LOS/NLOS satellites. Fig. 4.10 shows an example of this step at a crossroad in the *Chaussée de la Madeleine* of Nantes. Fig. 4.10(a) is an illustration with the information of digital map, where the polygons represent upside view of buildings. The red lines represent the directions of each received satellite azimuth. Fig. 4.10(b) is the street view of the same location provided by Google Earth®.

The next step is to examine every facade locally, to detect whether it could make a specular reflection with the occulted satellite previously identified. In this case, the final step is to check that no other facade may occult the reflected ray, whether in between the antenna and the impact point, or whether in between the impact point and the satellite. In case several facades exist with reflected rays, the one with the largest grazing angle (i.e., the smallest

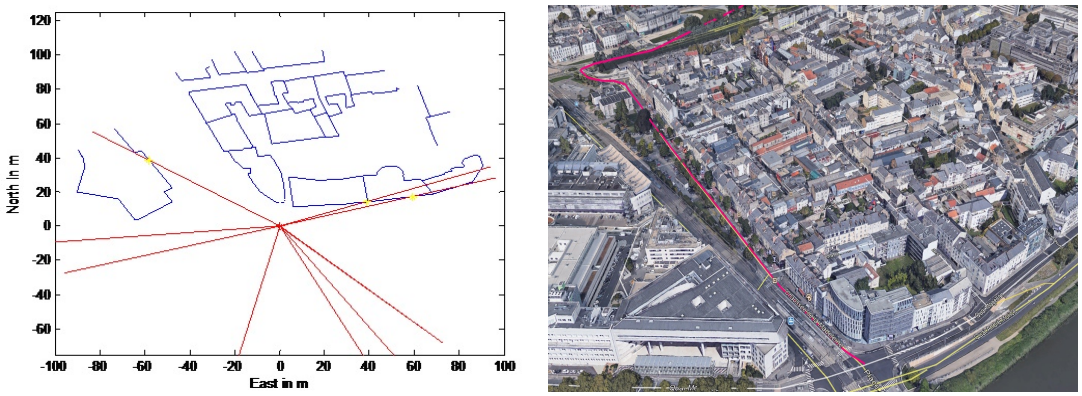

(a) (b)

Figure 4.10 – An illustration of the first step of the UMM

angle of incidence) is preferred. Facades are regarded as vertical planes, with the height of the polygon they belong to. Fig. 4.11 shows an illustration of this step provided respectively by digital map (Fig. 4.11(a)) and the same location provided by Google Earth® (Fig. 4.11(b)). The green line represents a NLOS satellite signal which is reflected by a facade (in blue) and then received by the user.

Finally, the additional distances will be calculated for all the NLOS receptions according to the geometrical rules of specular reflection.

Algorithm 1 provides the complete procedure of the LOS/NLOS identification and the computation of the additional distance by the Urban Multipath Model (UMM).

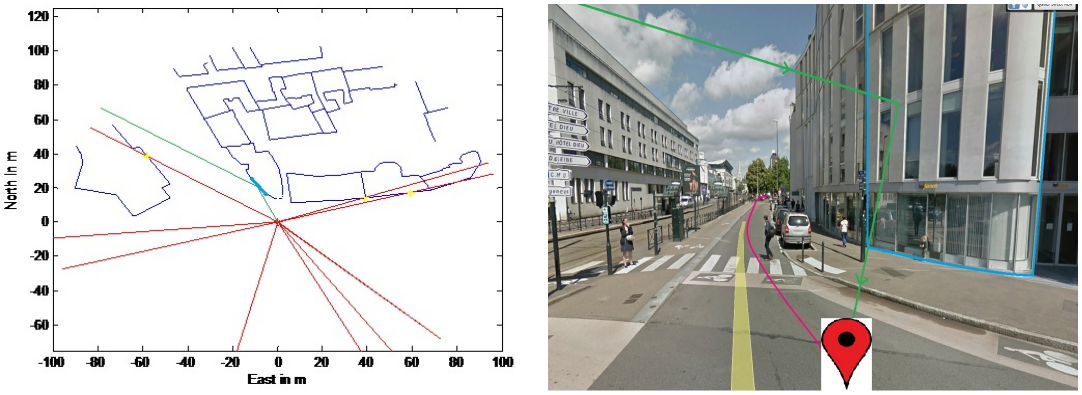

(a) (b)

Figure 4.11 – An illustration of the second step of the UMM

Algorithm 1 Urban Multipath Model (UMM) LOS/NLOS Identification and Computation of the Additional Distances

Require: BD TOPO® road layers: ID of road links, segments, polygons representing the buildings, height of each building, height of the receiver antenna

procedure LOS/NLOS Identification

Step 1: Prepare the ray segments R^i at each direction of azimuth $Azim^i$ for each visible satellite i, with $\|R^i\| = L$, $i \in [1, m]$; ▷ L=100 m in this research work

Step 2:

for $i = 1$ to m **do**

Explore the ray segment R^i to see if there exists intersection points with the line segments of polygons (vertical projection of buildings on the plan);

if $\exists$ intersection points P_i **then**

Choose the nearest intersection point and calculate the critical elevation angle θ_c by taking into consideration the height of the building;

if $\theta_i \geq \theta_c$ **then** ▷ θ_i is the elevation angle of the ith satellite

return ith Satellite is LOS

else if $\theta_i \leq \theta_c$ **then**

return ith Satellite is NLOS

end if

end if

end for

end procedure

procedure Additional Distance Computation

if ith Satellite is NLOS **then**

Explore every local facade in a circle zone centered at the user with a radius of l meters in order to find the possible reflection facades ▷ $l = 50m$ in this research work

if Several facades can make specular reflections **then**

Choose the facade with the largest grazing angle

end if

Calculate the additional distance AD_i according to the geometric rules of specular reflection.

end if

end procedure

4.2.3.3 A Proposed Hybrid Error Model

Despite their non-complicated implementation, the C/N_0 dependent and satellite elevation dependent error models mentioned previously present some drawbacks especially in dense urban canyons.

In terms of C/N_0-dependent error model, constructive multipath interference leads to an increase in C/N_0, while destructive multipath interference leads to a decrease. Thus all signals with high $C/N0$ do not possess high quality. And concerning the satellite elevation-dependent error model, it is possible that a signal with high elevation is received from multipath while on the contrary, a low-elevation signal is received in direct way. It strongly depends on the local environment especially the geometry of the traveled street.

As a result, only one indicator, such as C/N_0 or satellite elevation, cannot correctly model the measurement errors in dense urban. Thus it is necessary to consider several criteria at the same time in order to increase the probability of correctly indicating the signal quality.

Inspired by [119], a hybrid model, which combines both C/N_0, satellite elevation as well as the contribution of the Urban Multipath Model (UMM), is proposed. Here, the UMM is involved to provide the signal reception state as well as the additional distance correction for the NLOS signals. For each code pseudorange measurement, the hybrid model can be written as:

$$\sigma^2 = k \times \frac{m \cdot 10^{-0.1 \times C/N_0}}{sin^2(\theta)} \tag{4.18}$$

where,
- m is a parameter for model calibration, which depends on receivers and environments.
- k is an multiplier which differentiates the LOS signals from NLOS signals in this way:

$$k = \begin{cases} k_1 & if \quad LOS \\ k_2 & if \quad NLOS \end{cases}$$

and $k1 < k2$.

This hybrid model takes into consideration not only the C/N_0, satellite elevation but also the signal reception state (LOS/NLOS) as well as the correction of the additional distance at the pseudorange measurement level. The latter two information are provided by the UMM. The indicator k is used here as a spring in order to amplify the error of the NLOS signals so that the weight of NLOS signals will decrease in the total contribution of the navigation solution estimation.

The additional term a in Eq. (4.1) is not necessary in the numerator of hybrid model since its impact is proved to be very low in practice.

4.3 Conclusions and Discussions

This chapter begins by a detailed analysis of local effects existing in urban environments as well as the approaches to mitigate the local effects. Different techniques of local effects mitigation exist at different levels. In this research work, error characterizations, consistency check and statistic-based filtering will be adopted as main approaches. And this chapter mainly deals with the error characterization.

Several models existing in the literature which allow modeling GNSS measurement error variances are introduced: the C/N_0-based error model, the satellite elevation-based error model as well as the Dirichlet Process Mixture (DPM).

The C/N_0-based model and the satellite elevation-based model are easy to be implemented and are possible to be used in real-time. But they cannot perfectly reflect signal qualities. Because all the healthy signals do not have high C/N_0 values and the signals with high C/N_0 can be produced by constructive multipath interferences. Similarly, satellites with high elevations are more probable to be received as LOS but this is not absolute since it strongly depends on the local environment configurations.

DPM can dynamically estimate the measurement error variance and mean. But its complexity of implementation prevents it from being employed in real time. And the choice for the parameters of DPM is also extremely sophisticated.

Under this context, a new hybrid model is proposed by considering simultaneously several information: the C/N_0, the satellite elevation, the signal reception state LOS/NLOS as well as the range corrections for the NLOS signals. The last two pieces of information are provided by the proposed Urban Multipath Model (UMM) with the help of a *2D+1* digital map (containing simplified plan features of urban environments as well as the corresponding building height information). This model is an improved version of the Urban Trench Model (UTM) proposed in [35]. UMM is based on a simplified ray-tracing approach to distinguish signal reception state LOS/NLOS and at the same time it can calculate the additional distances traveled by the NLOS signal. These additional distances are removed when applying the hybrid model.

The hybrid model can be implemented into common commercial receivers once a digital map is integrated. It is not computational expensive so that it is possible to be employed in real time.

All the error models introduced in this chapter will be implemented and evaluated with real data in Chapter 5. The model calibrations and the choices of parameters will also be addressed. They will be embedded into a Weighted Least Squares (WLS) estimator in which signals will be re-weighted according to the error variances estimated by the corresponding error models.

Chapter 5

Accuracy Performance Comparison and Evaluation

Contents

Summary

This chapter aims at evaluating the error models described in Chapter 4 with real GPS data collected in urban canyons. The GPS dataset used in this PhD research work is collected during the project named INTURB (positioning INTegrity in URBan environments) in urban canyons of three cities: Paris, Nantes and Toulouse. The error models are mainly calibrated and analyzed in detail with the data of Nantes city center and then applied on the total dataset. Different error models are compared and evaluated with the Weighted Least Squares (WLS) estimator.

This chapter will begin by an introduction of the GPS data, which is used for evaluating the error models. Then, the model calibration will be described. Finally, the main results about the accuracy improvement are presented.

Part of results presented in this section is the subject of the author's publication in [139].

5.1 Introduction of the GPS Dataset

The GPS dataset used in this PhD research work is collected by the Geoloc team of the IFSTTAR during the data campaign of the project INTURB (positioning INTegrity in URBan environments) in 2013. The data are collected in the urban environments of Nantes, Paris and Toulouse in France. The receiver under test is an ublox-LEA-6T, which is a typical low-cost car navigation equipment. Its measurement update rate is 5 Hz. The reference trajectories corresponding to the test trajectories are provided by the Reference Trajectory Measurement System (RTMeS). This RTMeS includes a LandINS inertial unit and a dual frequency Novatel-DL3 receiver, which is a high accuracy GNSS receiver enabling PPK with the French network of permanent local stations. The accuracy with the RTMeS can achieve less than 10 cm.

The test receiver and the RTMeS are both installed at the roof of the Vehicle for Experimental Research on Trajectories (VERT) of the IFSTTAR as shown in Fig. 5.1 [155].

Figure 5.1 – VERT, the vehicle of IFSTTAR used to collect GPS data [155]

The data are collected in three cities of France: Nantes, Toulouse and Paris. There are six data sets as shown previously in Table 4.2, which gives a detailed report about each data set concerning the total number of epochs, the number of measurements as well as the total duration of each data campaign. Fig. 5.2 shows the reference trajectories of the six datasets.

These data are collected in urban environments of each city (part of data in sub-urban is also included) as an example of trajectory of Nantes center shown in Fig. 5.3 by Google Earth®. The traveled streets were in deep urban with medium height buildings, and various width. It is a typical urban environment of French (European) city center of the 19th and 20th

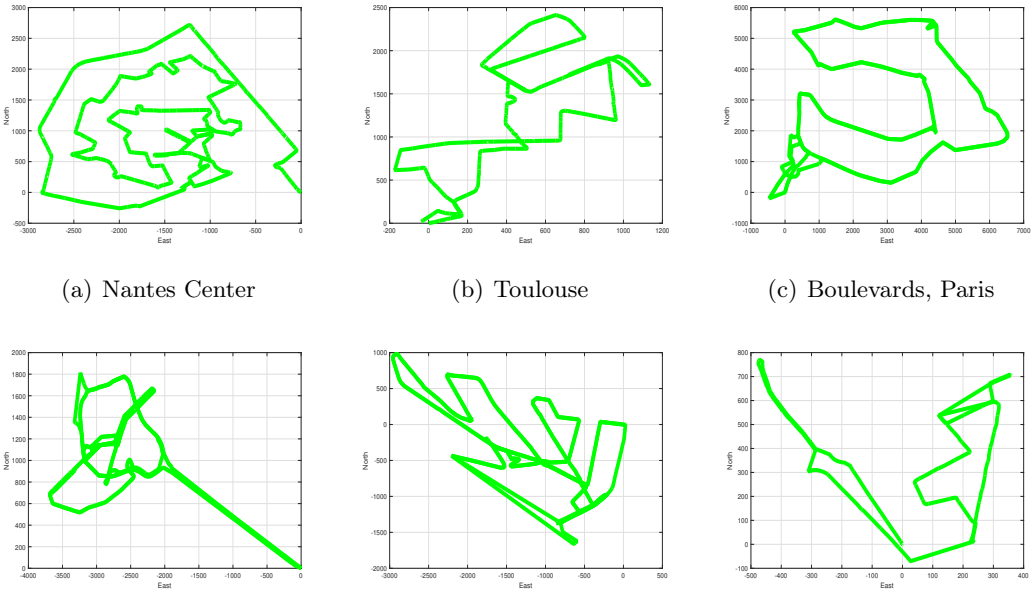

(a) Nantes Center (b) Toulouse (c) Boulevards, Paris

(d) La Défense, Paris (e) Paris XII^{th} (f) Nantes

Figure 5.2 – Reference trajectories of the six datasets

centuries. Besides, the dataset of *La Défense, Paris* and *Boulevards, Paris* include part of severely degraded data collected in deep urban canyons or with skyscrapers at each side.

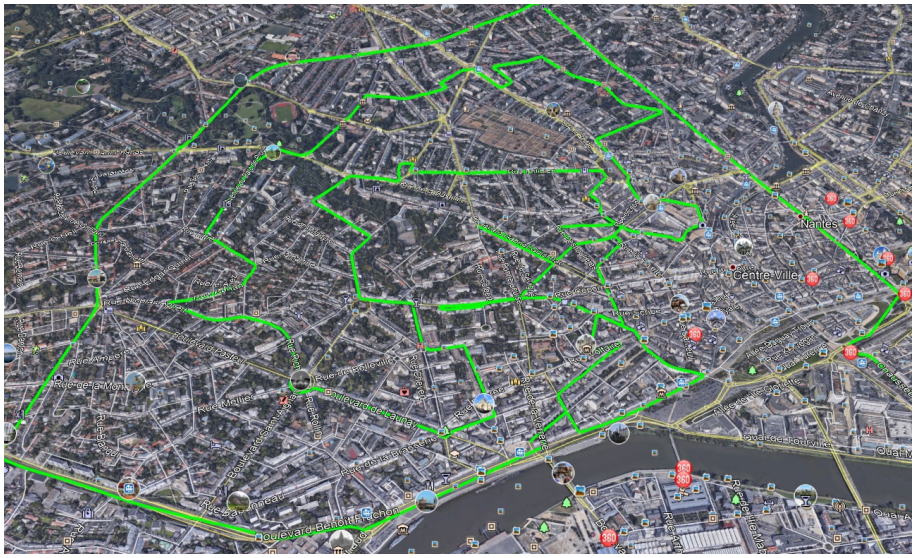

Figure 5.3 – An overview of the trajectory in the city center of Nantes, France

5.2 Calibration and Test with Real GPS Data

5.2.1 Model Calibration

Except the Dirichlet Process Mixture (DPM), the other three error models described in Chapter 4 provide the error information by error variance characterization. The utilities of these error variances are twofold, as explained in the following:

- Firstly, these error variances will be used in the Weighted Least Squares (WLS) estimator in order to distribute different weights for different measurements. According to the navigation equation of the WLS described in Chapter 2, the estimation of the navigation solution vector $\Delta\hat{X}_{WLS}$ including the user 3D position and the user clock offset can be written as:

$$\Delta\hat{X}_{WLS}(k) = (H^T W H)^{-1} H^T W \times \Delta Y(k)$$

  where, the weighting matrix W is defined as the inverse matrix of the measurement error variance-covariance matrix Σ, that is to say:

$$W = \Sigma^{-1} = \begin{bmatrix} \frac{1}{\sigma_1^2} & 0 & \dots & 0 \\ 0 & \frac{1}{\sigma_2^2} & \dots & 0 \\ \vdots & \vdots & \ddots & \vdots \\ 0 & 0 & \dots & \frac{1}{\sigma_m^2} \end{bmatrix}$$

  Since each weight is inversely proportional to each error variance respectively, measurements with small error variances will contribute to large weights in the estimation. On the contrary, measurements with large error variances, such as NLOS signals, will get small weights or even approximately canceled from the measurement set by a nearly zero weight.

  Due to this concern, one of the strategies of the error model calibration is to enlarge the difference between the error of the healthy signals and the unhealthy signals in order to distribute larger weights to the former ones and small weights to the latter ones. The criteria for distinguishing healthy and unhealthy signals (or LOS/NLOS signals if possible) are as discussed in the error models such as C/N_0, satellite elevation or directly the LOS/NLOS indicators provided by the map-based models (Urban Trench Model (UTM) or Urban Multipath Model (UMM)).

- Secondly, these error variances will be used further in the integrity monitoring procedures. More precisely, they will be involved in the computation of the test statistics - Normalized Sum of Squared Error (NSSE) as well as the calculation of the Horizontal Protection Level (HPL).

Special attention should be payed to the error model calibration, that the errors should not be too "over-bounded". That is to say, ideally, the error variances obtained from the models should only well cover the nominal signal errors.

If the measurement errors are over-estimated by the error models, the integrity monitoring procedures, especially the Fault Detection and Exclusion (FDE) algorithms, will give more tolerance to the measurement faults, i.e., they are less selective. This is because the test statistic - NSSE, will be possibly too small since the residuals are normalized by over-bounded error variances. Moreover, if the error variances are over estimated, the sizes of HPLs will be too huge which leads to conservative position error bounds. The size of HPL is one of criteria to evaluate the quality of integrity monitoring especially fo urban transport applications. The HPLs with huge sizes have not much meaning if they are much larger than the road configurations.

As a result, from an integrity monitoring point of view, the estimated error should not be too conservative, otherwise, they will prevent huge errors from being detected and will provide too huge HPLs.

Of course, the choice of the model parameters is also application-dependent. If the targeted applications attach more importance to the navigation continuity instead of a strong liability, i.e., integrity, the error models can be calibrated to have a high coverage ratio for both nominal and faulty errors.

Since our target applications are liability-critical ones, we will take into consideration the two strategies analyzed above in order to make the calibration for the models described in Chapter 4.

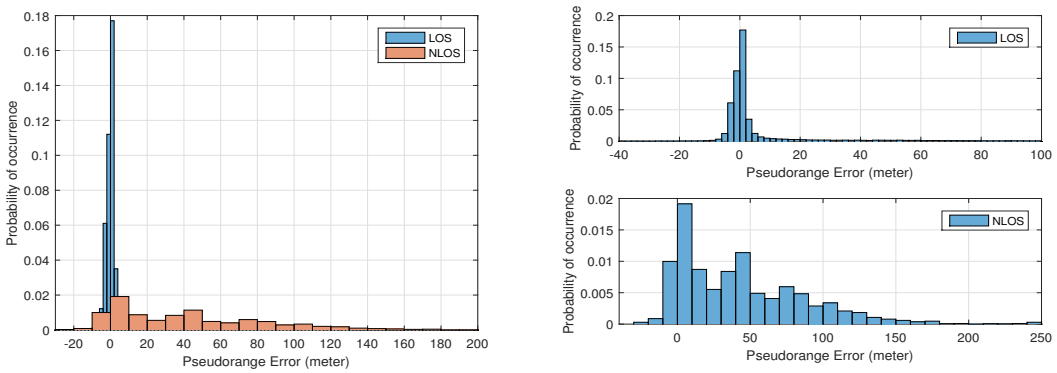

(a) (b)

Figure 5.4 – PR Error Histogram of LOS/NLOS (La Défense)

With the help of the Urban Multipath Model (UMM), the LOS/NLOS signal can be distinguished. Before calibrating, let us observe the PR error distribution of LOS and NLOS signals

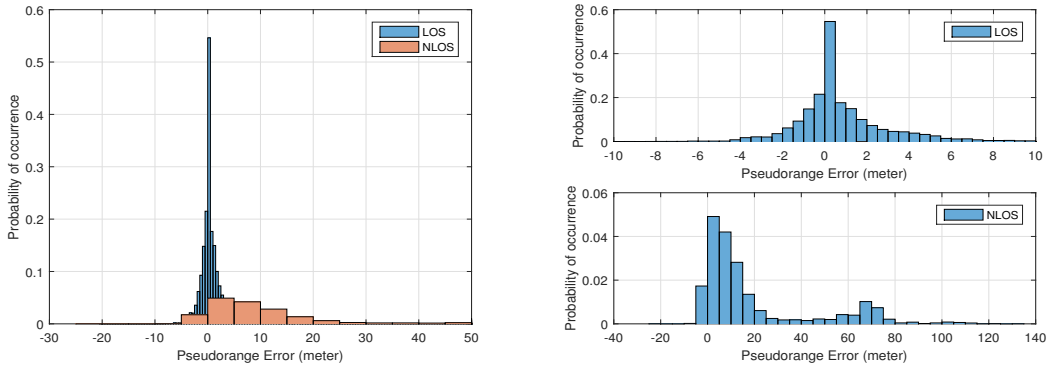

(a) (b)

Figure 5.5 – PR Error Histogram of LOS/NLOS (Nantes)

according to the UMM.

Fig. 5.4 - Fig. 5.7 show the histograms of the PR error of LOS and NLOS in different cities. The sub-figures at left side are the histograms of LOS/NLOS superposed together and the sub-figures at the right sides are the corresponding histograms with separated figure windows.

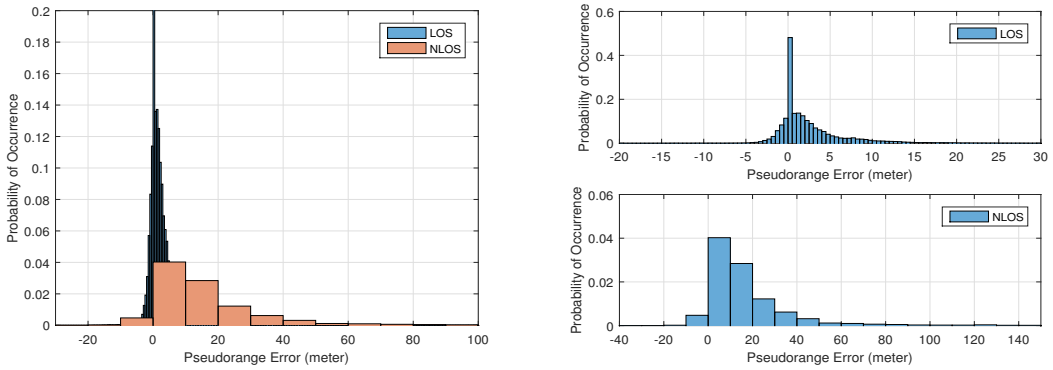

(a) (b)

Figure 5.6 – PR Error Histogram of LOS/NLOS (Nantes Center)

We can find that the PR errors of LOS signals are mostly centered around zero (e.g., as shown in the top figures of Fig. 5.5(b)), while that of the NLOS signals are biased with multiple peaks (e.g., the bottom figure of the Fig. 5.7(b)) and more extended with heavy tail (e.g., the bottom figure of the Fig. 5.4(b)), which are caused by the multipath reception.

Fig. 5.8 shows the quantile-quantile (Q-Q) plot of the PR error of Nantes dataset with respect to a normal distribution. Q-Q plot is a graphical tool to help check the coherence between data samples and a theoretical distribution, which is a normal distribution here. If the sample

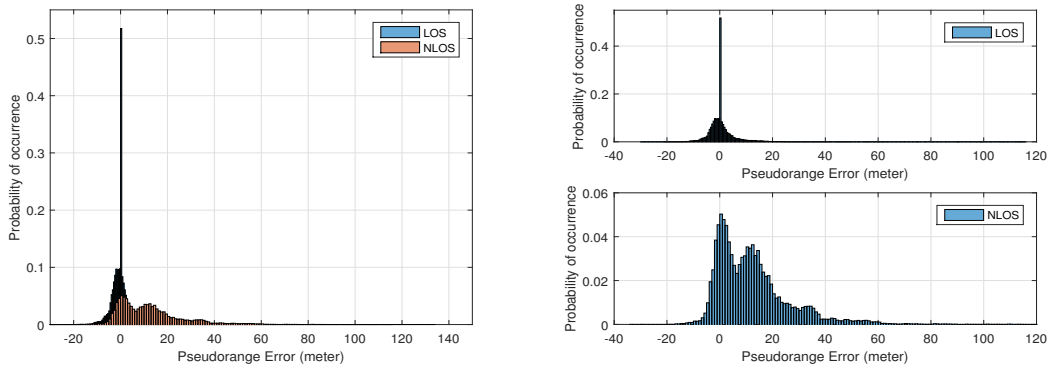

(a) (b)

Figure 5.7 – PR Error Histogram of LOS/NLOS (Toulouse)

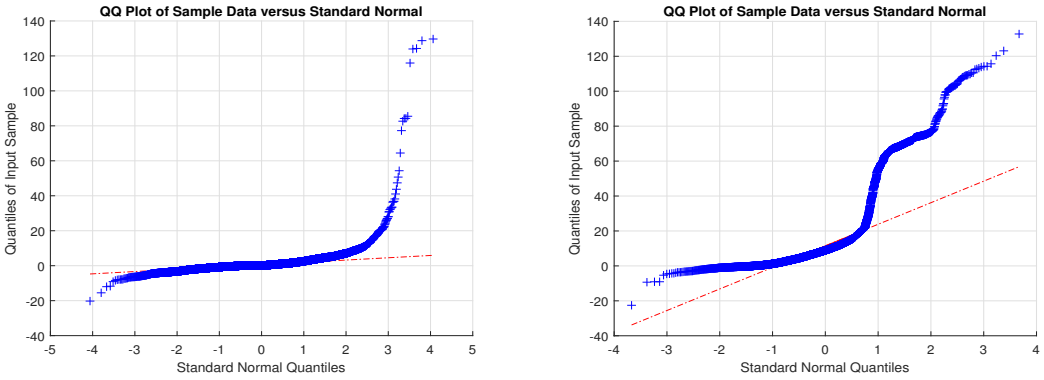

(a) LOS signals (b) NLOS signals

Figure 5.8 – Quantile-quantile plot of the PR errors with a normal distribution (Nantes)

data follow exactly the theoretical distribution, they will have a linear pattern in the Q-Q plot, otherwise, they are not linear. We can see from the Fig. 5.8 that the PR error of the LOS signals have a large coherence with the normal distribution but the errors of the NLOS signals have not, which follow a strongly nonlinear pattern. This proves again that the PR error of NLOS signals are strongly biased.

5.2.1.1 The carrier-power-to-noise-density ratio (C/N_0)-based variance model

The objective of this sub-section is to calibrate the C/N_0-based model in order to find suitable model parameters for GNSS-based applications in urban environments. These parameters should be suitable not only for position estimation but also for integrity monitoring.

This model can be written as:

$$\sigma_i^2 = a + m \times 10^{-\frac{C/N_0}{10}} \tag{5.1}$$

where, a and m are model parameters to be calibrated.

In the literature, the two parameters in this model are usually fixed empirically. There is not yet a well-developed methodology for calibrating the two parameters. According to [166], the choice of the two parameters can be made by empirically fitting the model variance curve with the pseudorange error as a function of C/N_0. We will also employ this strategy while taking into consideration the two precautions mentioned previously.

In order to further analyze the role of the two parameters, the formula above can be re-written as:

$$\sigma_i^2 = m \times (10^{-\frac{C/N_0}{10}} + \gamma) \tag{5.2}$$

where, $\gamma = \dfrac{a}{m}$.

We can consider that there are still two parameters to be fixed: m and γ. In fact, according to the Eq. (5.2), the multiplier m will not impact on the weights of the measurements since it can be factorized out of the weighting matrix:

$$W = \Sigma^{-1} = \frac{1}{m} \begin{bmatrix} \frac{1}{\sigma_{0,1}^2} & 0 & \dots & 0 \\ 0 & \frac{1}{\sigma_{0,2}^2} & \dots & 0 \\ \vdots & \vdots & \ddots & \vdots \\ 0 & 0 & \dots & \frac{1}{\sigma_{0,m}^2} \end{bmatrix}$$

where, $\sigma_{0,k} = 10^{-\frac{C/N_{0,k}}{10}} + \gamma$.

Despite the fact that m does not impact on the weight distribution for the measurements, it plays an important role to decide the magnitude of the measurement error level. So, it will be involved into the integrity monitoring procedure.

In terms of the factor γ, it is important to properly calibrate it since together with the C/N_0, it helps to differentiate the weights between each measurement. If we take into consideration the first strategy of calibration mentioned previously, i.e., to enlarge the difference between the healthy and the unhealthy signal, we can consider:

$$\lim_{C/N_0 \to C/N_{0,max}} f(C/N_0) \to 0 \tag{5.3}$$

where,

$$f: \quad C/N_0 \mapsto m \times (10^{-\frac{C/N_0}{10}} + \gamma) \tag{5.4}$$

The maximal value of the C/N_0 of out total dataset equals to 54 dBHz. As a result, we will fix the factor γ as follow in order to decrease the error variance for high C/N_0 values so that they will contribute large weights for navigation solution estimation:

$$\gamma = -10^{-\frac{55}{10}} = -3.16 \times 10^{-6} \tag{5.5}$$

On the other hand, the multiplier m is calibrated empirically with LOS signals identified *a priori* using UMM due to the concerns discussed in Section 5.2.1. Sub urban or landscape testing can also be used for the calibration. Then the calibrated parameters are applied to all the other dataset in order to validate the model calibration while not loosing the generalization.

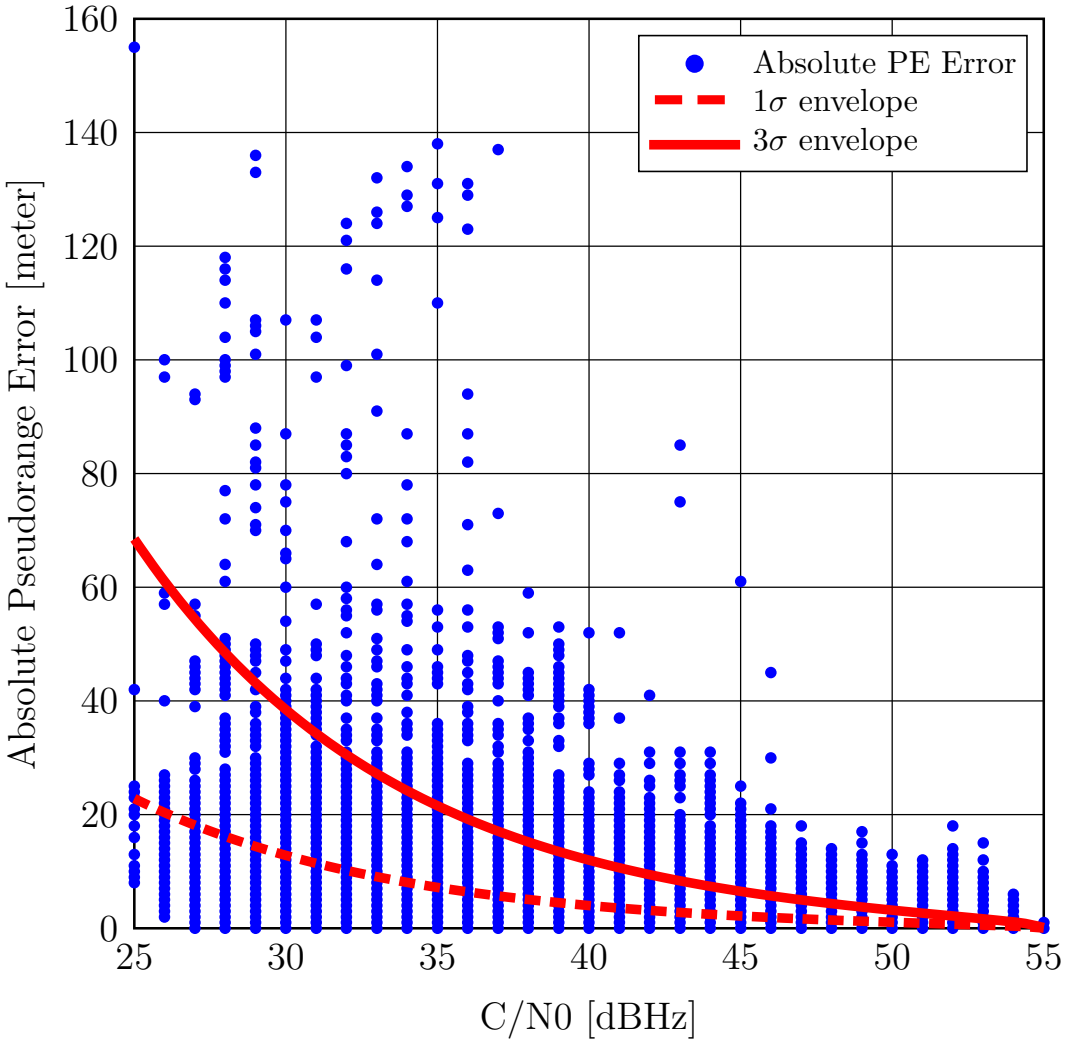

Figure 5.9 – 1-σ and 3-σ error envelope of the calibrated model *vs* the absolute PR errors with respect to the C/N_0 (Nantes Center)

The final choice for the two parameters are as follow:

$$\begin{cases} m = 165000 \\ \gamma = -3.16 \times 10^{-6} \end{cases} \Longleftrightarrow \begin{cases} m = 165000 \\ a = -0.52 \end{cases} \tag{5.6}$$

Table 5.1 – C/N_0-based Error Model Coverage Ratio

	$1-\sigma$ **coverage ratio (%)**	$3-\sigma$ **coverage ratio (%)**
Nantes Center	61.42	92.73
Toulouse	80.39	94.60
Boulevards, Paris	73.94	93.63
La Défense, Paris	75.66	89.86
Paris XII^{th}	71.99	95.35
Nantes	77.30	97.45

Fig. 5.9 provides the 1-σ and 3-σ error envelopes of the calibrated model as well as the absolute PR errors with respect to the C/N_0 (Nantes Center). Table 5.1 reports the C/N_0-based error model coverage ratio when applied with all the other dataset. The 1-σ error envelope coverage ratio is around 61%-77% and the 3-σ error envelope coverage ratio is around 90%-97%. Since the measurement errors should not be over-estimated for the reason of integrity monitoring issue, this coverage ratio is considered satisfactory.

In the following sections, we will thus apply this model calibration on the Weighted Least Squares (WLS) estimator and further on the integrity monitoring module in Chapter 6.

5.2.1.2 The elevation-based variance model

The following elevation-based model is chosen to be implemented [158]:

$$\sigma_i^2 = c_1^2 / sin^2(\theta_i) \tag{5.7}$$

where, θ_i is the elevation angle of the ith satellite and c_1 is the model parameter to be calibrated.

Similarly, as discussed in the C/N_0-based model, the multiplier c_1^2 has no impact on weights of the measurements. It is only involved into the procedure of the integrity monitoring. Thus, the model will be calibrated ideally to cover most of the nominal errors.

After trials, the parameter $c_1^2 = 5$ is chosen for this elevation-dependent model. Fig. 5.10 provides the 1-σ and 3-σ error envelopes of the calibrated model as well as the absolute PR errors of LOS signals with respect to the satellite elevations (Nantes Center). The coverage ratios of the 1-σ and 3-σ error envelopes are respectively 85% and 98%.

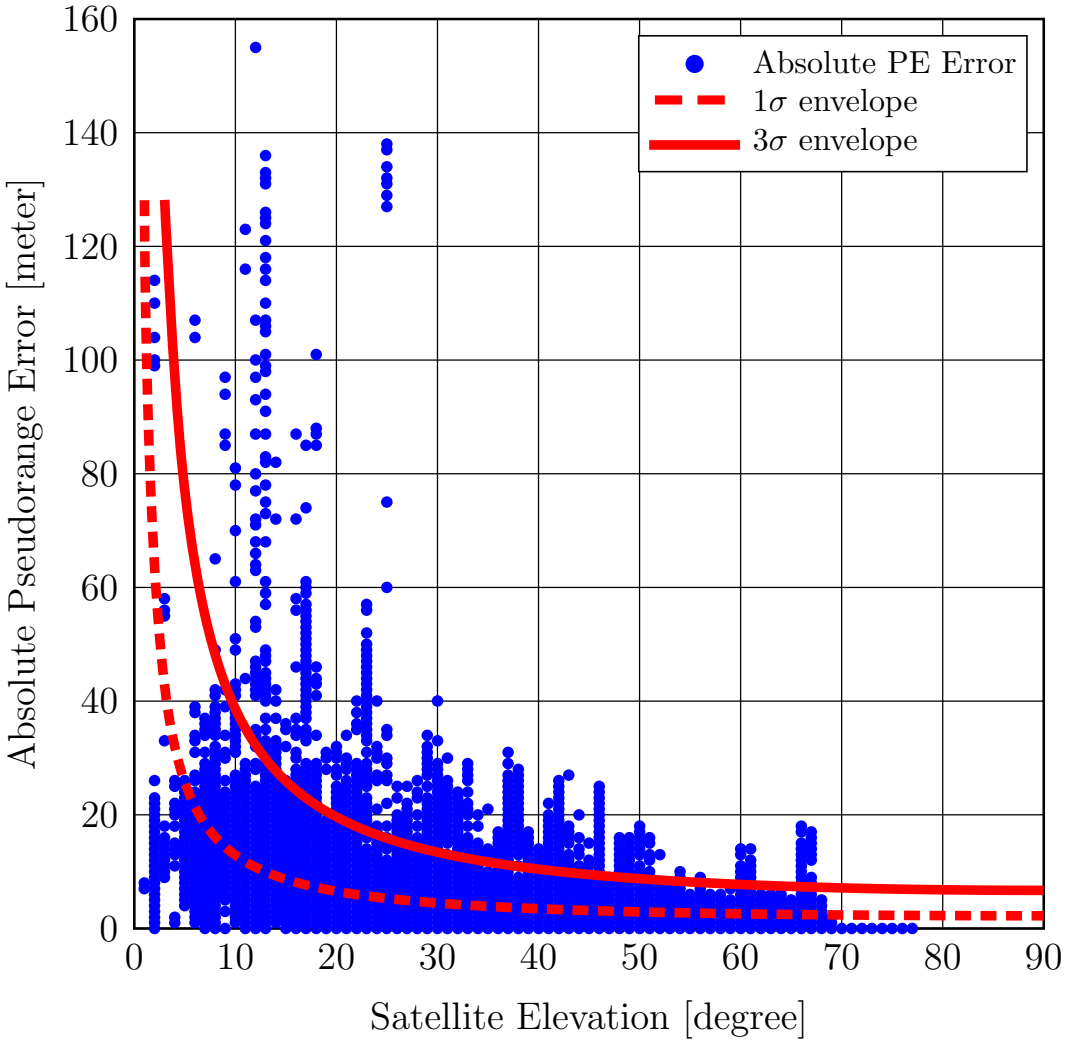

Figure 5.10 – 1-σ and 3-σ error envelope of the calibrated model *vs* the absolute PR errors with respect to the satellite elevation (Nantes Center)

Table 5.2 – Elevation-based Error Model Coverage Ratio

	$1-\sigma$ **coverage ratio (%)**	$3-\sigma$ **coverage ratio (%)**
Nantes Center	84.58	98.08
Toulouse	88.89	98.26
Boulevards, Paris	88.82	98.20
La Défense, Paris	81.90	88.21
Paris XII^{th}	90.07	98.09
Nantes	96.87	99.81

Table 5.2 reports the elevation-based error model coverage ratio with all the other dataset. The 1-σ error envelope coverage ratio is around 81%-96% and the 3-σ error envelope coverage

ratio is around 88%-99%.

5.2.1.3 The Dirichlet Process Mixture (DPM)

The DPM in the context of GNSS applications described in Chapter 4 can be briefly summarized as follows:

- For LOS receptions:

$$\begin{cases} \mathbb{G} \sim DP(\mathbb{G}_0, \alpha_1) \\ \sigma_k \sim \mathcal{W}^{-1}(\Sigma_1, dof1) \\ \mu_k \sim \mathcal{N}(\mu_1, \frac{\sigma_k}{k_1}) \end{cases} \tag{5.8}$$

- For NLOS receptions:

$$\begin{cases} \mathbb{G} \sim DP(\mathbb{G}_0, \alpha_2) \\ \sigma_k \sim \mathcal{W}^{-1}(\Sigma_2, dof2) \\ \mu_k \sim \mathcal{N}(\mu_2, \frac{\sigma_k}{k_2}) \end{cases} \tag{5.9}$$

The DPM parameters employed in [160] for GNSS-based applications in urban or sub-urban environments will be used in this research work. The particle number N is fixed equal to 20 as a result of a compromise between computational complexity and performance. Table 5.3 provides the list of values for the other parameters.

Table 5.3 – DPM Parameters

Parameters	$\alpha_{1,2}$	$k_{1,2}$	$dof_{1,2}$	$\Sigma_{1,2}$	$\mu_{1,2}$
LOS	500	0.1	10	1	$\hat{r_k}$
NLOS	3000	1	5	10	$\hat{r_k}$

where, $\hat{r}_k$ is the estimated residual.

5.2.1.4 The Hybrid Model

The Hybrid model can be written in the following form:

$$\sigma^2 = k \times \frac{m \cdot 10^{-0.1 \times C/N_0}}{sin^2(\theta)} \tag{5.10}$$

where,

- m is a parameter for model calibration, which depends on receivers and environments.

- k is a multiplier which differentiates the LOS signals from NLOS signals in this way:

$$k = \begin{cases} k_1 & if \quad LOS \\ k_2 & if \quad NLOS \end{cases}$$

and $k1 < k2$.

Recall that the signal reception state is distinguished with the help of the map-based model Urban Trench Model (UTM) proposed in [35,36] or Urban Multipath Model (UMM) proposed in this PhD research work.

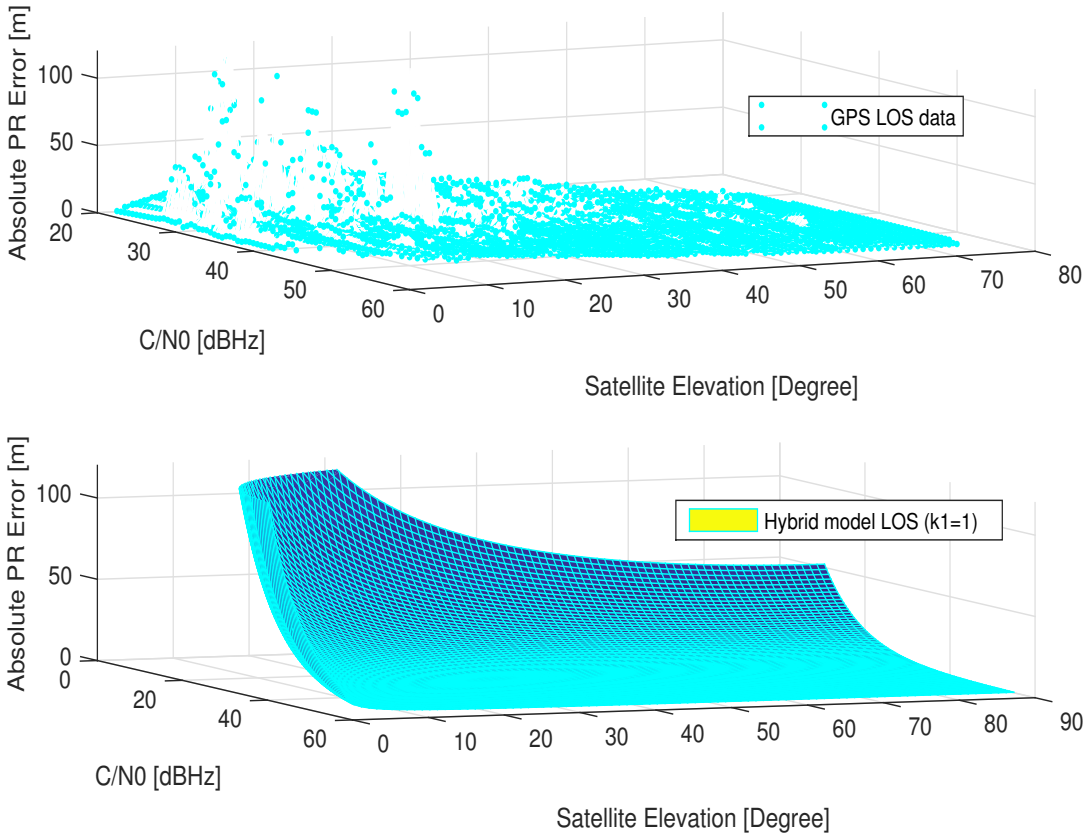

Figure 5.11 – Absolute PR error, C/N_0 and Satellite elevation of **LOS signals** with: Real GPS data (upper figure) *vs* Hybrid model (bottom figure)

A similar analysis is made for the choice of m and k with the help of the PR errors with respect to the C/N_0 and the satellite elevations. The factor k is used to amplify the weight differences between the LOS signals and the NLOS, which will be fixed as:

$$\begin{cases} k_1 = 1 & if \quad LOS \\ k_2 = 10 & if \quad NLOS \end{cases} \tag{5.11}$$

And the factor m is empirically tested with different values in the interval of $[3 \times 10^4, 4 \times 10^4]$ and is finally be fixed as:

$$m = 30375 \tag{5.12}$$

Fig. 5.11 and Fig. 5.12 show the behavior of absolute PR error as a function of C/N_0 and the satellite elevations, which are made respectively with LOS and NLOS signals. The upper figures are drawn with real GPS data and the bottom figures are with the hybrid model with the calibrations described above.

We can see that the absolute PR errors increase when the C/N_0 and satellite elevations decrease for both LOS and NLOS signals, which is as expected. Yet for the NLOS signals, the global inclination of the surface is steeper than that of the LOS signals. This phenomenon is better modeled by the factor k. This can be observed more clearly in Fig. 5.13, where absolute PR errors of both LOS and NLOS signal modeled by the Hybrid model are illustrated.

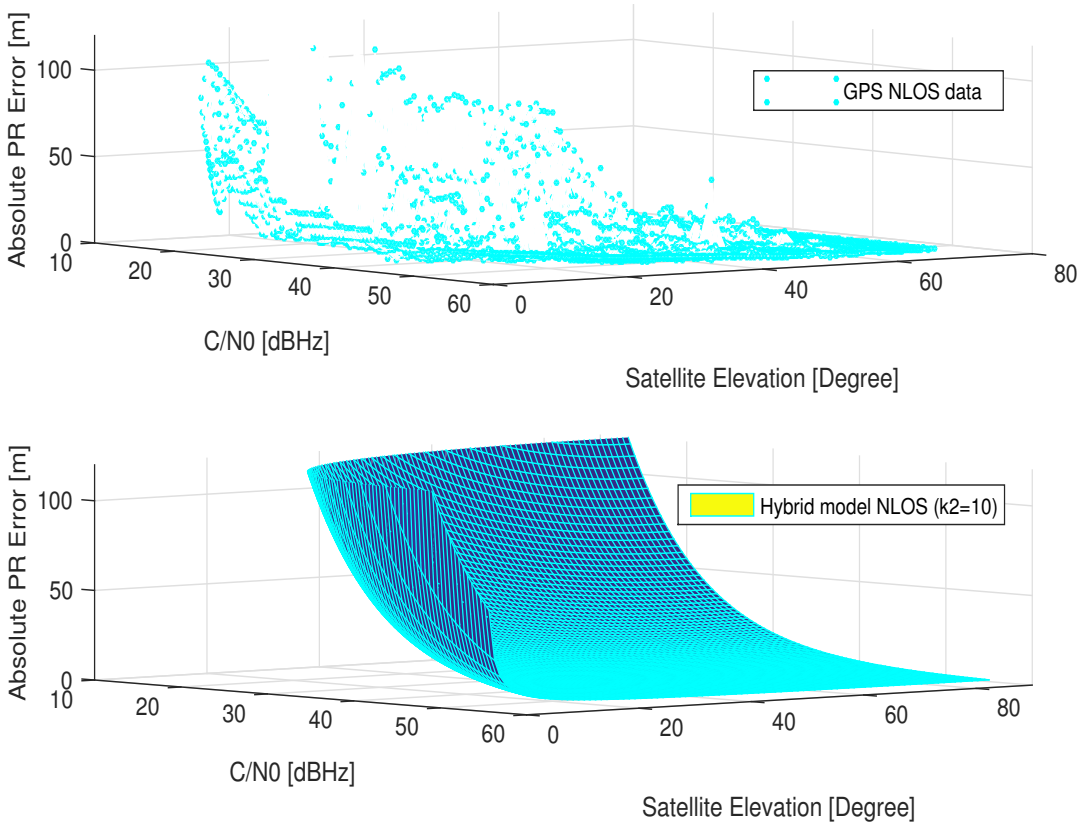

Figure 5.12 – Absolute PR error, C/N_0 and Satellite elevation of **NLOS signals** with: Real GPS data (upper figure) *vs* Hybrid model (bottom figure)

In fact, this model takes into consideration both information of the C/N_0 and the satellite

elevations. This will enhance the probability of correctly modeling the signal quality compared to the C/N_0-dependent model and the satellite elevation-dependent model. At the same time, the factor k helps improve the contribution of the healthy signals on the final navigation solution and decrease that of the unhealthy signals.

Besides the digital map-based Urban Multipath Model (UMM) used in this research work, there exists other possible means to distinguish the signal reception states. For example, several research works in literature use a simple threshold of C/N_0 (such as, the signals with $C/N_0 > 40dBHz$ will be considered as LOS) to distinguish the signal reception states. And the use of a fisheye camera is also possible to help distinguish the LOS/NLOS signals as in [146].

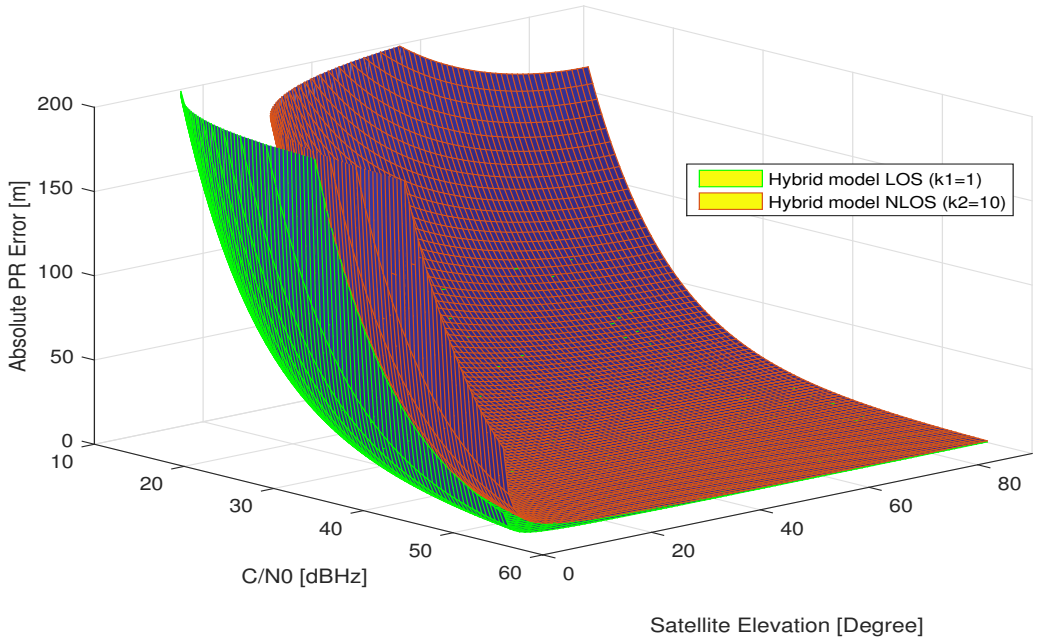

Figure 5.13 – Hybrid model: LOS and NLOS

5.2.2 Analysis of Accuracy Performance

In the previous section, we have calibrated all the necessary parameters of each error model presented in Chapter 4. Then they will be implemented into the Weighted Least Squares (WLS) estimator with real data presented at the beginning of this chapter. The performance of accuracy will be evaluated and compared.

The evaluation of accuracy performance will begin with a comparison between the Urban Multipath Model (UMM) and the two versions of Urban Trench Model (UTM). Then all the error models presented previously will be compared and their accuracy gain will be ranked.

A final sub-section contributes to testing and discussing the performance of Dirichlet Process Mixture (DPM).

5.2.2.1 The Improvement of Urban Multipath Model (UMM) Compared to Urban Trench Model (UTM)

As described in the Section 4.2.3.1 of Chapter 4, in the framework of the deterministic Urban Trench Model (UTM), there are two versions in the development history of this model. These two versions are mainly different in terms of the additional distance computations for the NLOS signals.

The initial version of the deterministic UTM considers that the number of reflections that may occur is supposed not to exceed 3 and the opposite buildings are always high enough to reflect the NLOS signals. This initial version is further improved by taking into consideration the height of the opposite building, which is the second version. That is to say, if the opposite building is not high enough to reflect the signal, the additional distance will not be calculated by the specular reflection law. In these situations, the signals are potentially received by diffractions or other situations. Due to the complexity of fixing the direction of the received signal, the additional distance will be considered as zero.

The Urban Multipath Model (UMM) proposed here, in fact, is still an improved version of the previous UTM in terms of the additional distance computation. The UMM uses a simplified ray tracing approach to distinguish the signal reception state and to calculate the additional distances, which can get rid of the assumption of infinite-length street of UTM and can also take into consideration the heights of opposite buildings.

In this sub-section, we will mainly evaluate and compare the accuracy performance of the two versions of deterministic UTM and the UMM. In summary, they are:

- **UTM v1**: Urban Trench Model (UTM) without taking into consideration the height of the opposite buildings, i.e., the opposite buildings are always high enough to reflect the signals;
- **UTM v2**: Urban Trench Model (UTM) with taking into consideration the heights of the opposite buildings. If the opposite building is not high enough to reflect the signal, the additional distance will be considered as zero;
- **UMM**: Urban Multipath Model (UMM), which is a simplified ray tracing approach to distinguish the signal reception state and to calculate the additional distance for NLOS signals.

Fig. 5.14 shows the Cumulative Distribution Function (CDF) of the Horizontal Position Error

(HPE) using Weighted Least Squares (WLS) estimator with the total dataset (163503 epochs). The hybrid model is used to estimate the measurement error variance with the help of the UTM v1, UTM v2 as well as the UMM, which are described in the text above. Besides, the CDF of HPE estimated with the Ordinary Least Squares (OLS) estimator (i.e., each measurement has the same weight for the navigation estimation) is also drawn in the same figure for comparison purpose.

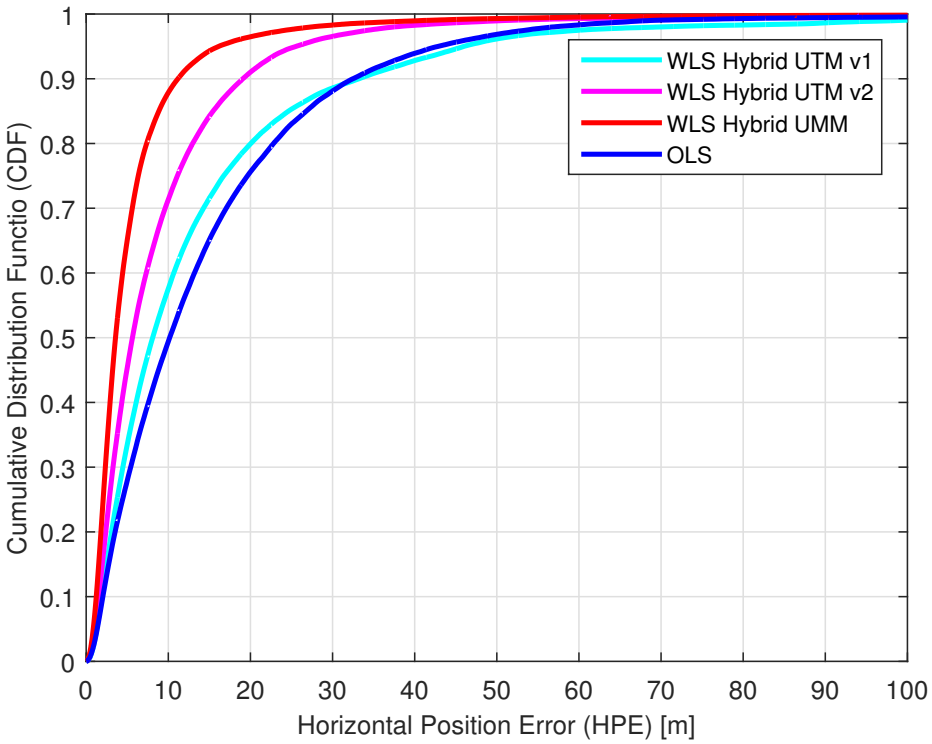

Figure 5.14 – Cumulative Distribution Function (CDF) of the Horizontal Position Error (HPE) with the total dataset (163503 epochs)

Table 5.4 – Accuracy Performances (Total Data)

Position Estimator	**HPE (meter)**		
	50%	***75%***	***95%***
Ordinary Least Squares (OLS)	10.17	19.64	42.87
WLS Hybrid model with UTM v1	8.10	16.74	45.97
WLS Hybrid model with UTM v2	5.63	11.11	25.54
WLS Hybrid model with UMM	3.57	6.34	16.10

As expected, the hybrid model with the UMM achieves the best performance in terms of accuracy. And the second version of UTM, which takes into consideration of the heights of

the opposite buildings, performs better than the first version of UTM.

Table 5.4 reports the accuracy of HPE at 50%, 75% and 95% quantile with the four solvers illustrated in the Fig. 5.14. The WLS with Hybrid UMM model can improve the median HPE by 65% compared to the OLS. This ratio for the two versions of UTM is respectively 20% (UTM v1) and 45% (UTM v2).

In conclusion, in terms of the proposed hybrid model combined with respectively the three digital map-based model: UTM v1 (without taking into consideration the opposite building heights), UTM v2 (taking into consideration the opposite building heights) and the UMM (using a simplified ray tracing approach), the ranking of accuracy performance from best to worst is:

1. WLS Hybrid UMM;
2. WLS Hybrid UTM v2;
3. WLS Hybrid UTM v1.

This proves that the Urban Multipath Model (UMM) effectively provides better accuracy than the other two versions of Urban Trench Model (UTM). What about their performances compared to the other error models, such as C/N_0-dependent error variance model and the satellite elevation-based error variance model. This will be analyzed in the following section.

5.2.2.2 Accuracy Comparison of Error Models

This section will mainly compare the accuracy performance of the C/N_0-dependent error variance model, the satellite elevation-based error variance model as well as the hybrid model. The Dirichlet Process Mixture (DPM) will be analyzed separately in Section 5.2.2.3.

Table 5.5 – Accuracy Performances Summary (Total Dataset)

Position Estimator	**HPE (meter)**			
	50%	***75%***	***95%***	***Accuracy Ranking***
WLS Hybrid model with UMM	3.57	6.34	16.10	1
WLS C/N_0-based model	4.41	8.36	21.84	2
WLS Hybrid model with UTM v2	5.63	11.11	25.54	3
WLS Elevation-based model	6.89	13.86	30.04	4
WLS Hybrid model with UTM v1	8.10	16.74	45.97	5
Ordinary Least Squares (OLS)	10.17	19.64	42.87	6

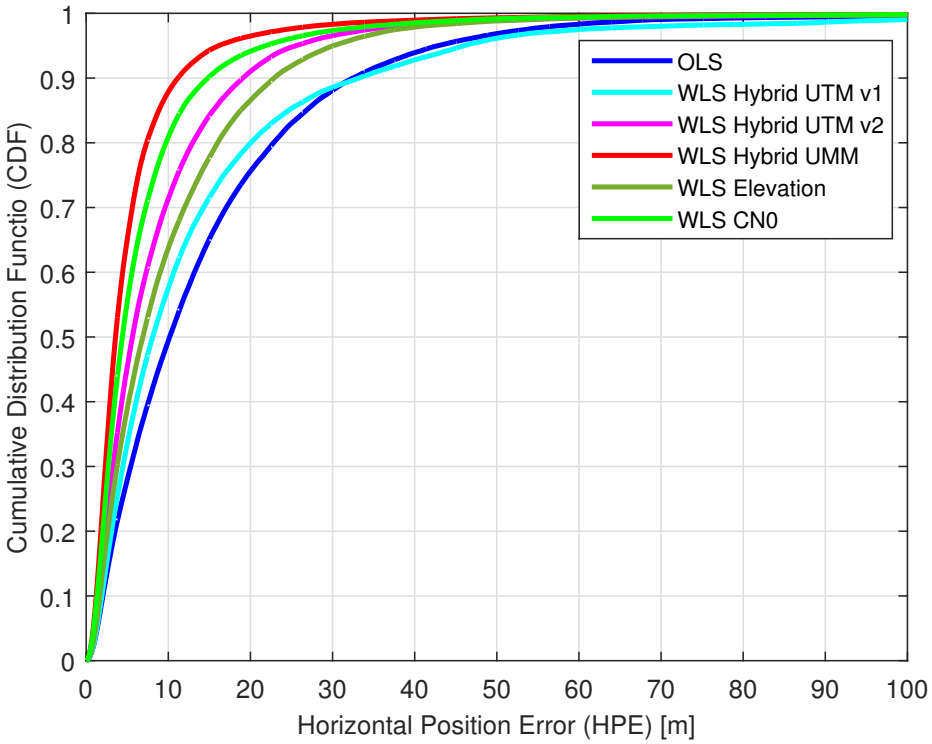

Figure 5.15 – Cumulative Distribution Function (CDF) of HPE (Total Dataset)

Fig. 5.15 shows the CDF of the HPE of different error models obtained with the total dataset (163503 epochs). We can see that the hybrid model combined with UMM always remains the first place concerning the accuracy among all the other solvers.

The C/N_0-based error variance model has the second best accuracy performance. This is no doubt a good news since the C/N_0-based model is convenient for the low-cost commercial GNSS receivers thanks to its simplicity of implementation and its ease of access. Table 5.5 provides quantitative analysis about the accuracy performance with the six solvers shown in the figure as well as their ranking of accuracy. This ranking only takes into account the global accuracy performance.

Table 5.6 – Accuracy Performances Summary (Nantes Center Dataset)

Position Estimator	**HPE (meter)**			
	50%	***mean***	***75%***	***95%***
Ordinary Least Squares (OLS)	5.66	10.14	11.51	30.70
WLS Elevation-based model	3.81	6.12	7.86	17.52
WLS C/N_0-based model	2.64	4.81	4.84	13.78
WLS Hybrid model with UMM	2.32	3.61	3.87	10.83

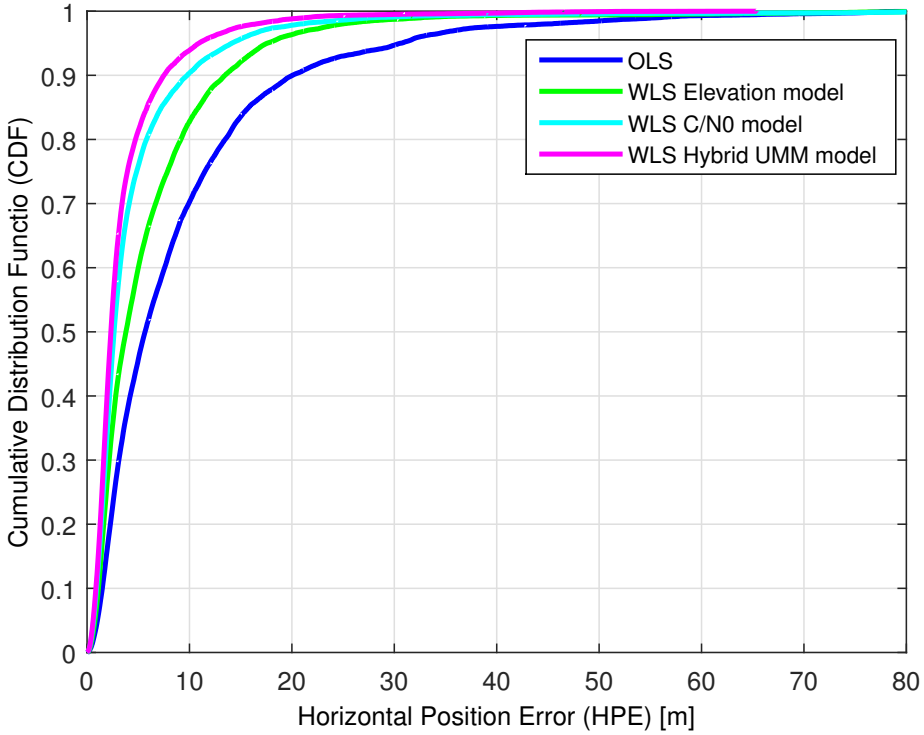

Figure 5.16 – Cumulative Distribution Function (CDF) of the HPE (Nantes Center dataset)

Since the two versions of deterministic UTM model cannot provide better accuracy performance than the UMM in the framework of hybrid model, we will only implement the UMM model hereafter in the following research work.

After analyzing the error models with the total dataset, let's take one of the datasets, the Nantes center, to analyze in detail the accuracy performance of these error models.

Fig. 5.16 shows the CDF of the HPE estimated respectively with the Ordinary Least Squares (OLS) and the Weighted Least Squares (WLS), in which three error models are employed: the elevation-dependent model, the C/N_0-dependent model and the Urban Multipath Model (UMM). Fig. 5.17 shows the reference trajectory, the estimated trajectories with different solvers as well as the comparison of the HPE in certain period of time. The same accuracy performance trend is observed with the results obtained with total dataset. Table 5.6 reports the quantitative results about the HPE accuracy. The hybrid model can achieve 2.32 meters in median, which improves significantly compared to the OLS estimator, which has 5.66 meters in median for HPE. The C/N_0-based error variance model is better than the satellite elevation-based model in terms of the accuracy performance.

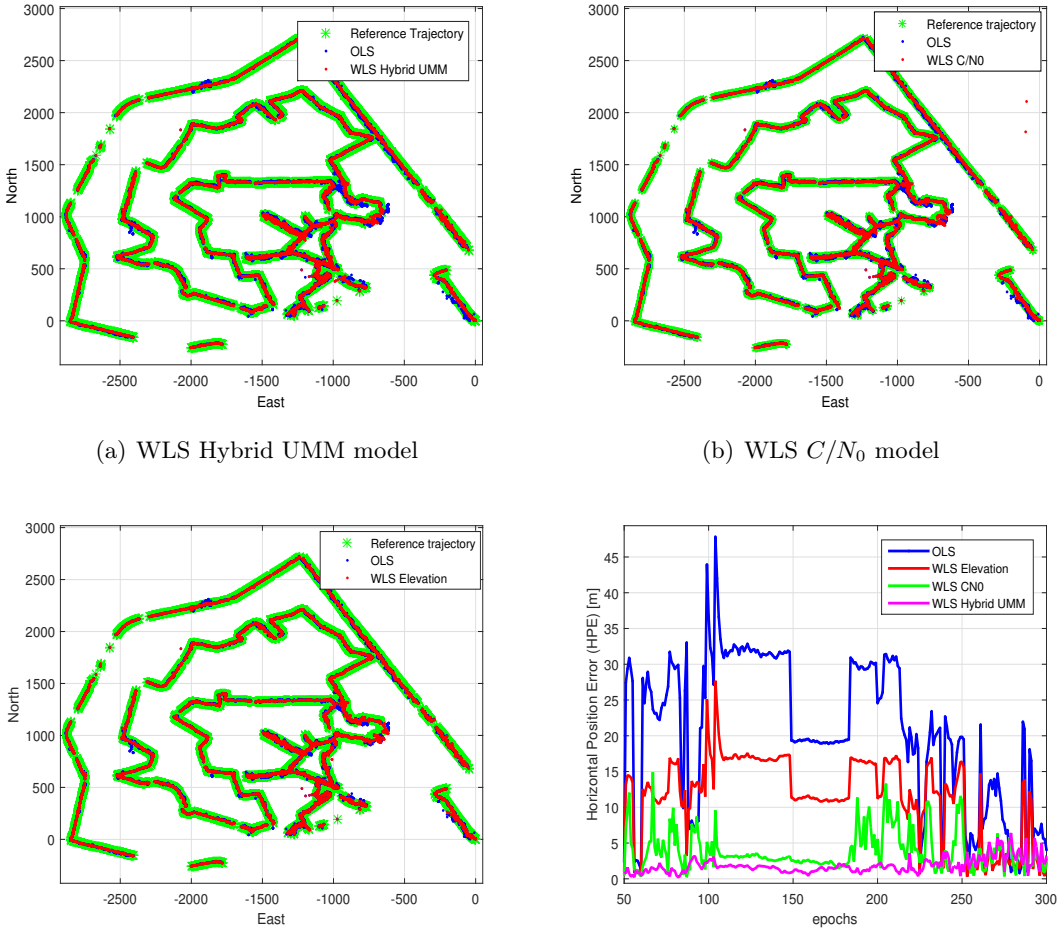

(a) WLS Hybrid UMM model

(b) WLS C/N_0 model

(c) WLS Elevation model

(d) Comparison of HPE

Figure 5.17 – Reference Trajectory (in green) and Estimated Trajectories (Ordinary Least Squares (OLS) (in blue) and Weighted Least Squares (WLS) in red) as well as their HPE comparison (Nantes Center Dataset)

5.2.2.3 Concerning the Dirichlet Process Mixture (DPM)

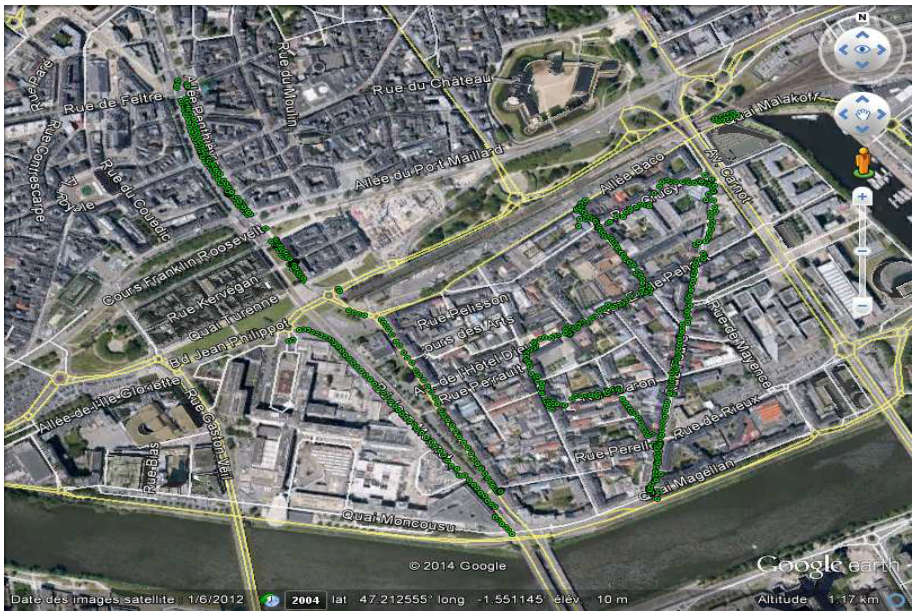

Figure 5.18 – An overview Nantes dataset trajectory

The implementation of the Dirichlet Process Mixture (DPM) is much more complicated than the other models described previously. And this model is computationally expensive since a particle filter is integrated, which is essentially a Monte Carlo method.

Due to these limitations, the Dirichlet Process Mixture (DPM) is not suitable to be implemented in real-time navigation system. But it is still interesting to take a look at its performance compared to other error models described above. As a result, we will implement the DPM with the dataset of Nantes, which includes 3326 epochs. The traveled streets were also in deep urban as shown in Fig. 5.18.

Table 5.7 – Accuracy Performances Summary (Nantes)

Position Estimator	**HPE (meter)**		
	50%	***75%***	***95%***
Ordinary Least Squares (OLS)	5.40	14.18	59.89
WLS Elevation-based model	4.27	11.71	38.31
WLS Dirichlet Process Mixture (DPM)	3.77	9.52	24.65
WLS C/N_0-based model	3.06	6.46	18.37
WLS Hybrid model with UMM	2.33	3.59	7.76

Fig. 5.19 provides the CDF of the HPE with the OLS as well as the WLS with four different error models: the satellite elevation-based error model, the C/N_0-based error model, the

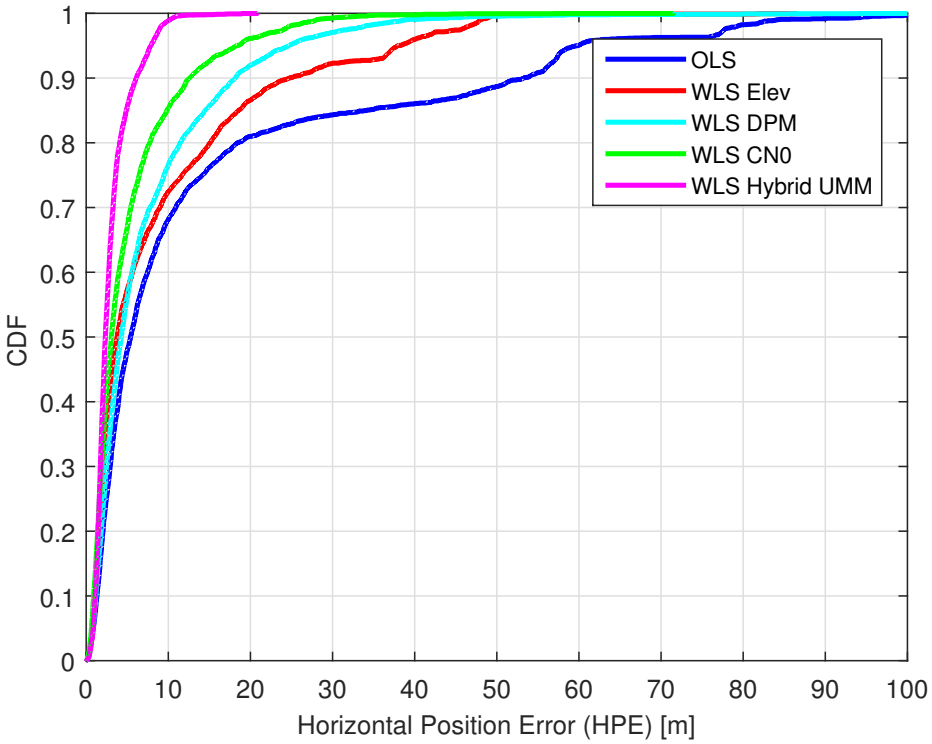

Figure 5.19 – Cumulative Distribution Function (CDF) of the Horizontal Position Error (HPE) with Nantes dataset

hybrid model with UMM and the DPM. Table 5.7 reports the statistical HPE results with all the solvers.

The WLS with DPM model implemented here does not provide a performance as good as expected in the theory. Its accuracy performance, with 3.77 m median HPE, is only better than the OLS estimator (median HPE: 5.40 m) and the WLS with elevation-based error model (median HPE: 4.27 m); it is worse than the C/N_0-based model (median HPE: 3.06 m) and the hybrid model with UMM (median HPE: 2.33 m). In order to find the reason, let us take a look into the variance and mean values estimated by DPM compared to the PR errors estimated in Section 4.2.1, which will be considered as true PR error, and the estimated residuals.

Fig. 5.20 provides a skyplot of the initial epoch of Nantes dataset. Here, we will choose two most representative satellites to make the analysis: the satellite 32 (SAT 32) and the satellite 31 (SAT 31). SAT 32 is near to the zenith, which is theoretically less contaminated by the multipath and NLOS, as it is declared as LOS during 96% of its visible time in the Nantes dataset according to the UMM. On the contrary, the SAT 31 has a low elevation and it is declared as LOS only during 37% of its visible time. As a result, SAT 32 can be considered as a typical LOS satellite and SAT 31 can be considered as a typical NLOS satellite.

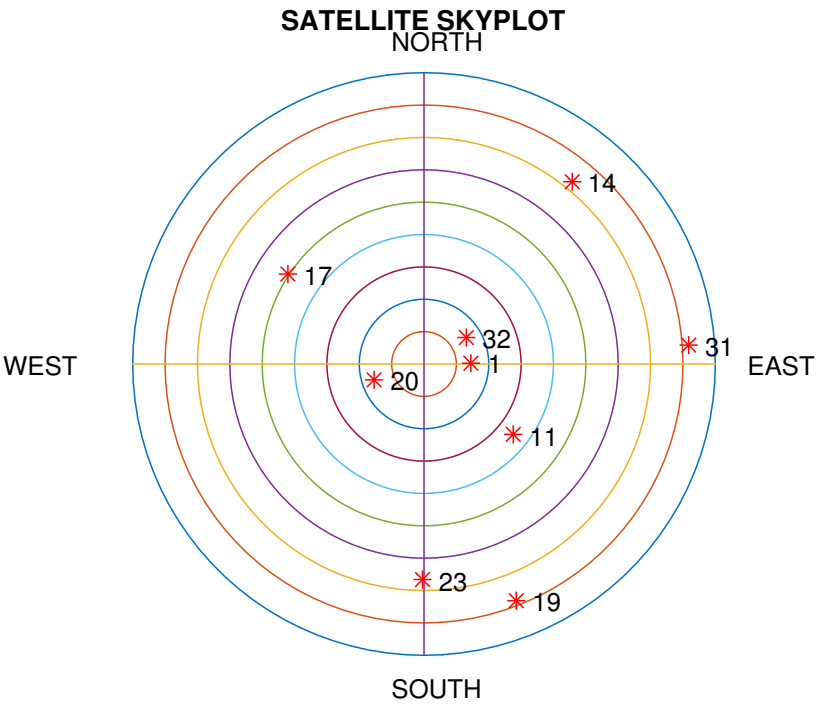

Figure 5.20 – A skyplot of the initial epoch of Nantes dataset

Fig. 5.21 and Fig. 5.22 show the 1-σ and 3-σ error bounds with respect to the true PR errors estimated in Section 4.2.1 as well as the estimated measurement residuals with WLS DPM estimator. We can observe that for SAT 32, i.e., in the case of LOS signals, the DPM error bound for the true PR error is still satisfactory. The 1-σ error can bound 54% of the true PR error (Fig. 5.21(a)) and the 3-σ error can bound 81% of the true PR error (Fig. 5.21(b)). Detailed zooms are shown in Fig. 5.21(e). For the SAT 31, i.e., in the case of NLOS signals, however, the DPM error bound can hardly well bound the true PR error. The 1-σ error can only bound 19% of the true PR error (Fig. 5.22(a)) and the 3-σ error can bound 48% of the true PR error (Fig. 5.22(b)). Fig. 5.22(e) shows a zoom of 1-σ error bound, where, huge errors appear but the error bounds do not well follow.

However, the DPM error bounds can almost perfectly bound the estimated residuals both in LOS cases and NLOS cases as shown in Fig. 5.21(c), Fig. 5.21(d), Fig. 5.22(c) and Fig. 5.22(d). The 1-σ error bound has already achieved 97% for SAT 32 and 99.7% for SAT 31.

It is not difficult to observe that, the mean estimated by DPM has too much dependence on the residual. As mentioned several times in the previous chapters, since the residuals are possible "absorbed" by Unobservable Multiple Fault (UMF), the strong dependence of DPM on the residual may cannot correctly reflect the signal quality.

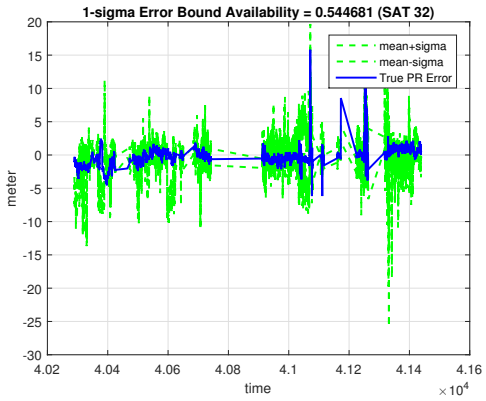

(a) 1-σ error bound for true PR errors

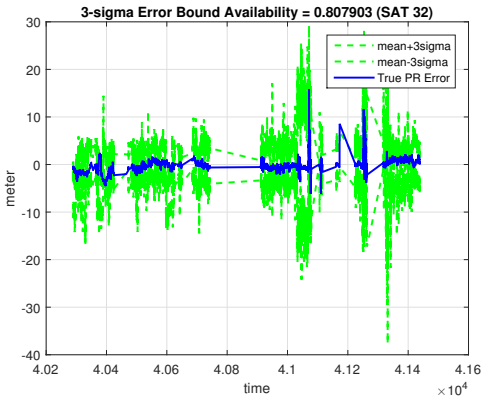

(b) 3-σ error bound for true PR errors

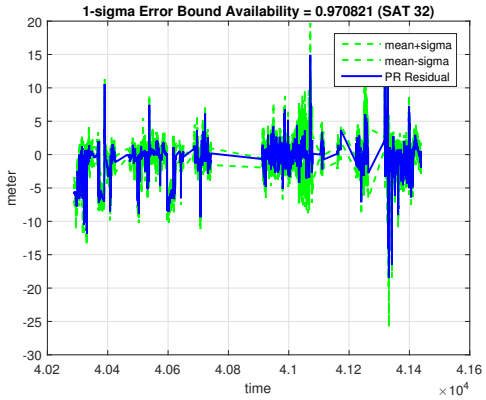

(c) 1-σ error bound for estimated residuals

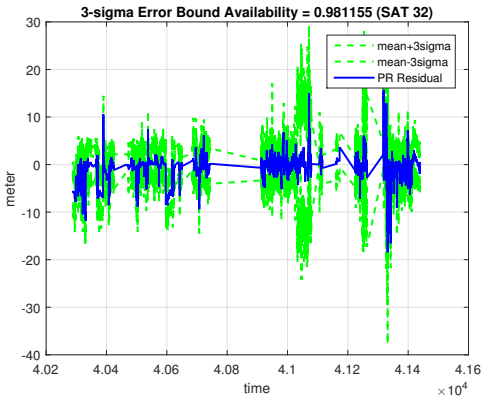

(d) 3-σ error bound for estimated residuals

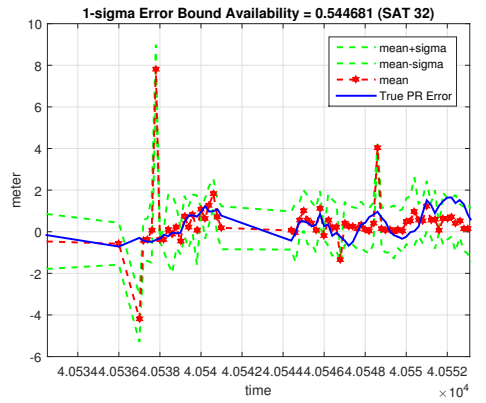

(e) a zoom of 1-σ error for true PR errors

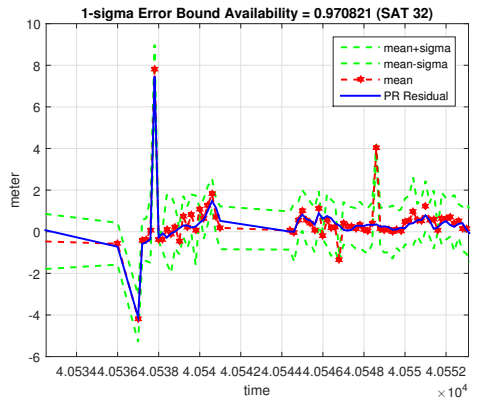

(f) a zoom of 1-σ error for estimated residuals

Figure 5.21 – DPM Error Bound Availability for SAT 32, a typical LOS satellite

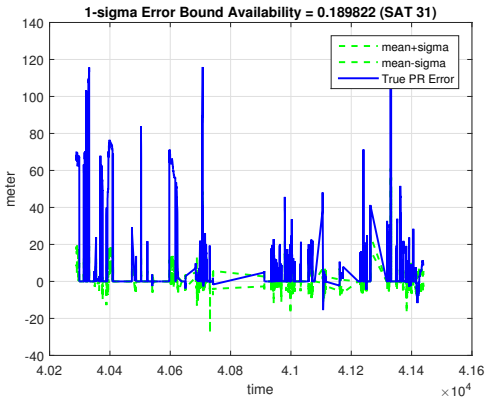

(a) 1-σ error bound for true PR errors

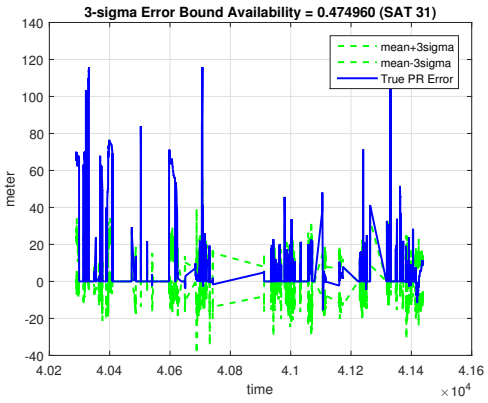

(b) 3-σ error bound for true PR errors

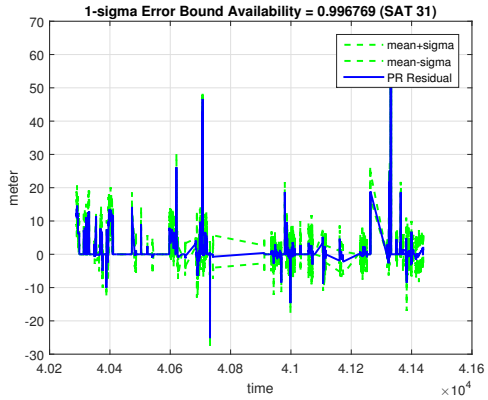

(c) 1-σ error bound for estimated residuals

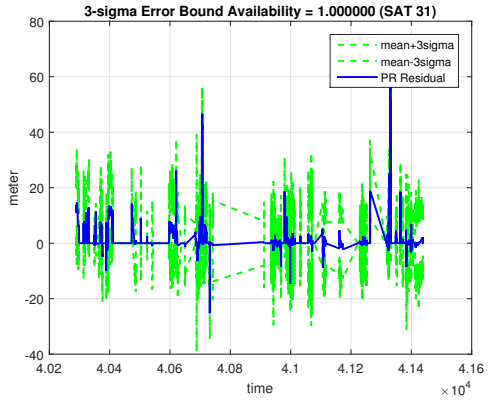

(d) 3-σ error bound for estimated residuals

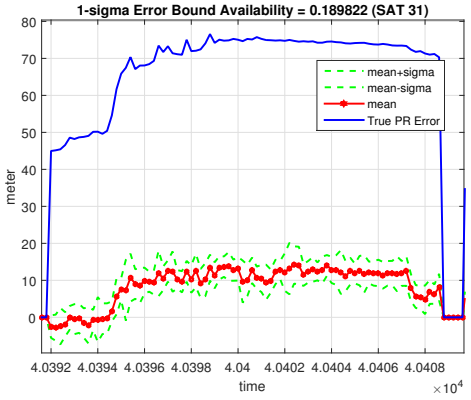

(e) a zoom of 1-σ error for true PR errors

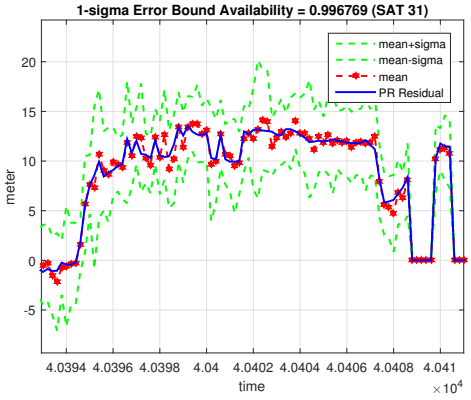

(f) a zoom of 1-σ error for estimated residuals

Figure 5.22 – DPM Error Bound Availability for SAT 31, a typical NLOS satellite

Also, the parameter adaptation of the DPM is always a huge work to do. A better performance is possible to achieve by adapting different DPM parameters.

5.3 Conclusion and Discussion

This chapter aims at evaluating and comparing the accuracy performance of the following error models in the framework of the Weighted Least Squares (WLS) estimator:

- The C/N_0-based variance error model;
- The satellite elevation-based variance error model;
- The Dirichlet Process Mixture (DPM);
- The proposed hybrid model combined with the following three map-based error model in order to distinguish the signal reception state and to correct the additional distances for the NLOS signals:
    * Urban Trench Model (UTM) v1: not taking into consideration the heights of the opposite buildings, i.e., the opposite buildings are always hight enough to reflect the signals;
    * Urban Trench Model (UTM) v2: taking into consideration the heights of the opposite buildings. If the opposite building is not high enough to reflect the signal, the additional distance will be considered as zero;
    * Urban Multipath Model (UMM): a simplified ray tracing approach to distinguish the signal reception state and to calculate the additional distance for NLOS signals.

Generally speaking, all the weighting schemes can provide better accuracy performance than the Ordinary Least Squares (OLS), in which all the measurements have the same weight.

Among all these solvers, the WLS with the hybrid model combined with UMM achieves the best accuracy performance. This solver improve the median Horizontal Position Error (HPE) from 10.17 m to 3.57 m compared to the OLS with the total dataset. With the Nantes center dataset, the median HPE can achieve 2.32 m. The main advantages of this solver is that it is not complicated to be implemented once a digital map is integrated in the receiver. Moreover, its computational charge is not heavy, which open the possibility of real-time implementation. However, the dependence of the map information is at the same time a limitation for this solver despite of its best accuracy performance. The digital map accuracy and the need of update are also important to be taken into consideration if this model will be implemented into commercial GNSS receivers. But it is also possible to use other methods to distinguish

the signal reception state, such as a simple C/N_0 threshold or the use of fisheye camera with image processing. This may be a perspective for future research.

The WLS with the C/N_0 model provides the second best accuracy performance among all these solvers. The median HPE with the total dataset is 4.41 m. Its simplicity of implementation and the ease access of C/N_0 information make it popular to be implemented in the GNSS receivers. However, its limitation is that, on the one hand, it cannot properly indicate the signal quality especially in dense urban environments since constructive multipath interference leads to an increase in C/N_0, while destructive multipath interference leads to a decrease. On the other hand, the model parameter depends not only on the receivers but also the traveled environment and it is possible to make slight adaptations according to the targeted applications. A better methodology to calibrate the parameters of this model is still an issue to be discussed.

The Dirichlet Process Mixture (DPM) is at the third place concerning the accuracy among all the solvers mentioned. This model is able to provide a mean and a variance of measurement error at each epoch for each visible satellite with the help of a set of cluster. Compared to the C/N_0-based error model, it seems not really profitable to use the DPM due to its complexity of implementation and the high computational cost. The choice of the model parameters is also a huge work for the use of DPM. The performance of this model can be expected better with other parameters but this is not the main objective of this research work.

Then it comes the elevation-based variance error model, whose accuracy performance is only better than the OLS but worst than all the other WLS solvers mentioned previously. Satellites near to the zenith have less possibility to be contaminated by local effects but this is not absolute due to the complexity of street geometry. Thus, it is better to use the elevation as an auxiliary information to indicate signal quality.

In the following chapter concerning GNSS integrity, we will focus on the WLS estimator with the two best error models analyzed above: the hybrid model with UMM and the C/N_0-based model.

Part III

CONTRIBUTIONS REGARDING THE INTEGRITY MONITORING IN URBAN ENVIRONMENTS

Chapter 6

Snapshot Residual-Based Integrity Monitoring

Contents

Summary

Based on the error models analyzed in Chapter 5, this chapter will construct a complete snapshot residual-based integrity monitoring system by adding the FDE techniques in Chapter 3 at the next step of the Weighted Least Squares (WLS) estimator. And the Horizontal Protection Level (HPL) is also calculated.

This chapter begins with an overview of the complete system, including an accuracy enhancement module, an integrity enhancement module as well as the computation of HPL. The HPL computation will be analyzed in detail. Then follows the integrity performance evaluation and comparison with real GPS data collected in urban canyons. Finally, the conclusion will be addressed.

Part of the results presented in this section is the subject of the author's publication in [167].

6.1 Introduction

For the liability or safety critical applications, it is of utmost importance to ensure not only high accuracy but also the required integrity performance for the specific applications. Yet urban environments present great challenges for GNSS positioning performances due to the existence of local effects such as multipath and NLOS reception. To overcome the urban environment constraints and to guarantee a satisfactory level of trust for the final PVT solution, we propose here a complete integrity monitoring scheme for GNSS-based low-cost urban transport receivers.

This scheme consists of two main modules highlighting respectively the positioning accuracy and integrity. The accuracy enhancement model relies mainly on better characterizations of the measurement errors and the integrity module employs FDE techniques in order to eliminate measurements with huge errors.

In fact, the two metrics, GNSS accuracy and integrity, are not completely independent. They are related between each other. This means, if an estimator is optimal in integrity monitoring, that is to say, the FDE algorithms can correctly detect and exclude the faulty measurements, this will no doubt help improve the positioning accuracy. On the contrary, an estimator which is suboptimal in integrity monitoring can possibly further degrade the accuracy performance due to the erroneous exclusion of healthy measurements. This latter phenomenon can occur for example in the presence of strongly correlated multiple faults. They can be absorbed in error residuals, preventing the detection of the faulty measurements, which is called Unobservable Multiple Fault (UMF).

Moreover, if the number of faulty measurements is more than half the total measurement number, certain FDE algorithms will have difficulty in properly detecting the faulty measurements, especially the ones depending on the consistency check among total measurement set. In constraint environments, such as urban canyons, this phenomenon can often happen, which is a great challenge for integrity monitoring procedure implemented for land users.

In this section, different possibilities of combination between the Weighted Least Squares (WLS) solvers presented in the Chapter 5 and the FDE techniques presented in Chapter 3 will be tested in order to find the optimal one for urban integrity monitoring. Different HPL computations will be also discussed and evaluated with real GPS data collected in urban environments.

6.2 Overview of the System Design

Fig. 6.1 shows an overview of the complete system. There are two main modules in this integrity monitoring system:

- An accuracy enhancement module, in which, the two best Weighted Least Squares (WLS) solvers evaluated in Chapter 5 are selected: the WLS with Hybrid Urban Multipath Model (UMM) and the WLS with C/N_0-based model;
- An integrity enhancement module, in which, five FDE techniques are implemented: the Classic Test (CT), the Subset Test (ST), the iterative Local Test (LT), the Forward-Backward (FB) Test as well as the Danish re-weighting method. These FDE techniques are described in detail in Section 3.5.

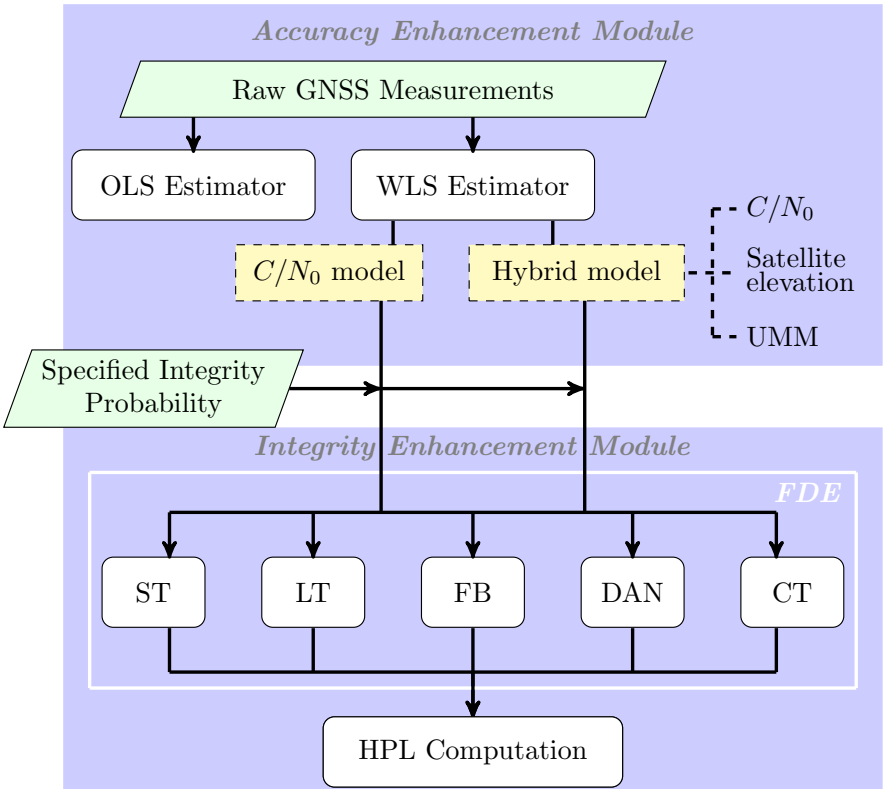

Figure 6.1 – An overview of the complete integrity monitoring scheme

The Ordinary Least Squares (OLS) solver is also implemented in purpose of performance comparison.

The justifications of this proposed scheme come from the required performances for the navigation system: to provide accurate positioning information accompanied with certainty. That is to say, the final navigation solution should be not only accurate but also with trust. As a

result, starting from inaccurate positions contaminated by multipath or NLOS reception, the accuracy enhancement module will help improve the positioning accuracy by better characterizing the measurement errors. The output of the accuracy enhancement module should be relatively accurate positioning informations but without certainty.

Then the integrity enhancement module will further eliminate the faulty measurements by FDE algorithms and a HPL will be calculated in order to provide a statistical error bound for users. In fact, the main functionalities expected from a FDE technique are twofold:

- On the one hand, the non reliable positions with huge errors should be flagged so that a warning can be sent to the users to inform them of the non credible information. This is important in an original integrity point of view in that the integrity monitoring techniques are designed to provide timely warnings for users in case of non reliable navigation information. The prevention of the huge errors is essential for liability-critical applications;
- On the other hand, the reliable positions obtained after applying FDE, are expected to have better accuracy performance thanks to the exclusion of the faulty measurements. But the accuracy improvement is not the main task of the FDE algorithms. If the huge error prevention is correctly done, the accuracy improvement can be considered as an added value.

Except the computation of HPL, all the other techniques in the complete system are introduced in the previous chapters. So in the following section, we will discuss about the computation of HPL.

6.3 Horizontal Protection Level (HPL) Discussion and Computation

6.3.1 Derivation of the HPL Computation

Protection Level (PL) is an important output of integrity monitoring procedures, which plays a role of a statistical tool to bound the position error. For users, it is a factor that quantifies the certainty of the positioning information. It is also a parameter to evaluate the external reliability of the system.

Let us recall the definition of the PL and HPL, which is briefly mentioned in the Chapter 3:

PL *is a statistical error bound computed so as to guarantee that the probability of the absolute position error exceeding the said number is smaller than or equal to the target integrity risk [3].*

HPL *is the radius of a circle in the horizontal plane (the local plane tangent to the WGS-84 ellipsoid), with its center being at the true position, that describes the region assured to contain the indicated horizontal position. It is a horizontal region where the missed detection and false alert requirements are met for the chosen set of satellites when autonomous fault detection is used [18].*

As more and more GNSS-based applications emerged in different domains, the meaning of PL has been assigned with more variations. Fig. 6.2 shows an illustration of the xPL (x: *Vertical* or *Horizontal*) under the context of the aeronautic, the automobile as well as the train domains. This figure also presents the integrity events according to the relationship among the PE, AL and the PL, which is described in Chapter 3.

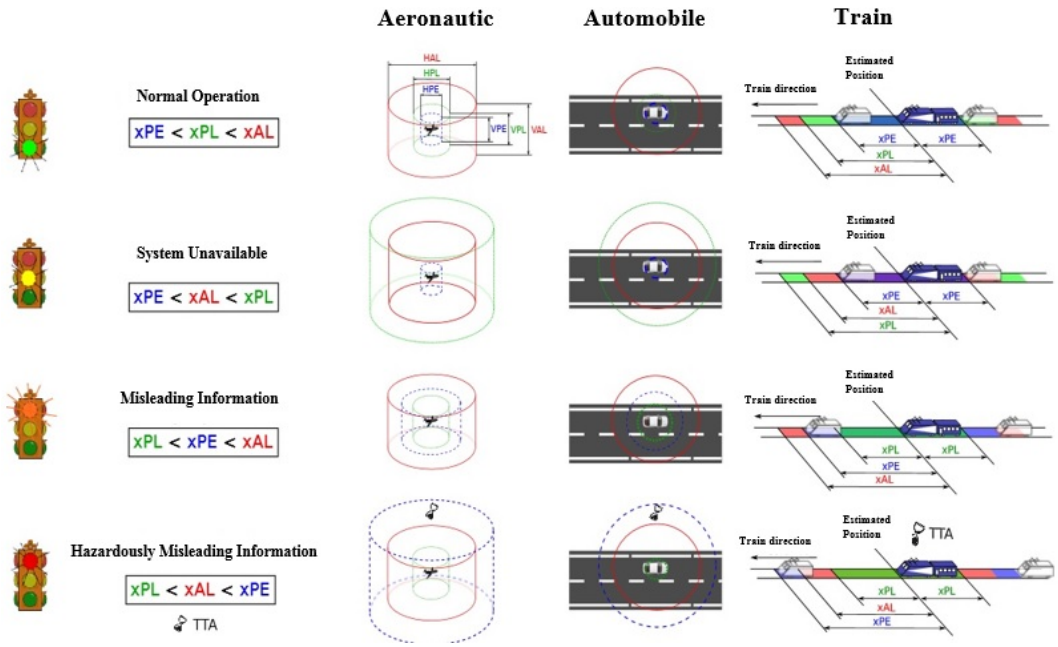

Figure 6.2 – An illustration of Position Error (PE), Alert Limit (AL), Protection Level (PL) in different domains [168]

The computation of xPL is originally developed for aeronautic users, for whom, both HPL and VPL are required. The VPL is usually more stringent than the HPL for the aircraft especially during the precision-approach with vertical guidance. Then the concept of PL is expanded into the automobile domain. Here, the HPL is attached more importance than the VPL since the vertical movement of a vehicle is negligible compared to the horizontal one. And the needs are more in the horizontal plan such as the guidances, the anti-collision, etc. Thus, the PL estimation problem can be simplified from 3D to 2D under the context of automobile. Moreover, for applications requiring lane-level accuracy, it is also possible to introduce the Cross-Track (CT) PL and the Along-Track (AT) PL. This is similar for trains: once the railway track is fixed, the AT PL is enough to bound the position error. So the PL

estimation problem can be simplified to only one dimension for railway applications. In this research work, we will concentrate on the HPL in the framework of automobile applications.

The objective of HPL is to bound the estimated position errors, i.e., the difference between the estimated positions and the true (unknown) position of the receiver, while taking into consideration the impact of measurement errors and bias on the estimated position error. Thus the design of HPL computation begins from deducing the expression of the estimated position error as a function of measurement error and bias.

In Chapter 2, we have obtained the following relationship with WLS estimator:

$$\Delta\hat{X} = (H^T\Sigma^{-1}H)^{-1}H^T\Sigma^{-1} \times \Delta Y \tag{6.1}$$

with,

$$\begin{aligned} \Delta Y &= H\Delta X + E \\ &= H\Delta X + B + \varepsilon \end{aligned} \tag{6.2}$$

where, B represents the measurement bias vector and ε represent the measurement error vector.

Denoting $H^+ = (H^T\Sigma^{-1}H)^{-1}H^T\Sigma^{-1}$, the left pseudo-inverse matrix of H, i.e., $H^+H = I$, then:

$$\begin{aligned} \Delta\hat{X} &= H^+\Delta Y \\ &= H^+(H\Delta X + E) \\ &= \Delta X + H^+E \end{aligned} \tag{6.3}$$

So that,

$$\Delta\hat{X} - \Delta X = H^+(B + \varepsilon) \tag{6.4}$$

Since $\Delta\hat{X} - \Delta X = (\hat{X} - \hat{X}_0) - (X - \hat{X}_0) = \hat{X} - X$, with $\hat{X}_0$ the point of linearization, we obtain the final expression of the position error as a function of measurement error and bias:

$$\boxed{\hat{X} - X = H^+(B + \varepsilon)} \tag{6.5}$$

In a normal use of the positioning solutions, the true position errors are not observable. In an integrity monitoring problem, the estimated residual $\hat{r}$ is an observable quantity which allows checking the consistency of measurements. If we can find the relationship between the residual and the estimated position error or at least between the residual and the measurement error, this will no doubt help bound the estimated position error.

As is defined previously in chapter 2, the measurement residual represents the deviation between the measurements made and the predicted noiseless measurements that the receiver

would have made if its state is the estimated one:

$$\begin{aligned}\hat{r} &= \Delta Y - H \times \Delta\hat{X} \\ &= \Delta Y - H \times H^{+}\Delta Y \\ &= (I - HH^{+})\Delta Y \\ &\triangleq S\Delta Y\end{aligned} \tag{6.6}$$

where, the matrix S is idempotent, i.e., $SS = S$. This means S is singular so not invertible.

From Eq. (6.6), we can continue the derivation by substituting ΔY with its expression in Eq. (6.2):

$$\begin{aligned}\hat{r} &= S(H\Delta X + B + \varepsilon) \\ &= (I - HH^{+})H\Delta X + S(B + \varepsilon)\end{aligned} \tag{6.7}$$

Since $(I - HH^{+})H = 0$, we obtain the following expression of the estimated measurement residual as a function of measurement error and bias:

$$\boxed{\hat{r} = S(B + \varepsilon)} \tag{6.8}$$

According to the two important equations framed above, we can observe that the impacts of measurement error and bias on the position error and the residual are transfered respectively by the matrix H^{+} and S. Since the matrix S is non invertible, we cannot directly link the residual, which is an observable quantity, with the estimated position error, which is our objective to bound.

In fact, the calculation of HPL should always take into consideration two sources of impacts on the position error: the impacts of measurement noise and the impacts of the measurement bias. In other words, the position error $(\hat{X} - X)$ should be bounded while taking into consideration the measurement noise ε and the measurement bias B. The relationship would be better expressed as a function of the observable quantities.

We will begin by firstly looking for the impact of the measurement bias on the position error. Supposing there is only one biased measurement, that is to say:

$$B = \begin{bmatrix} 0 \cdots & b_j & \cdots 0 \end{bmatrix} \tag{6.9}$$

According to Eq. (6.5), we have[1]:

$$(\hat{X}-X)_b = H^+ \times \begin{bmatrix} 0 \\ \vdots \\ b_j \\ \vdots \\ 0 \end{bmatrix} = \begin{bmatrix} \cdots & H^+_{E,j} & \cdots \\ \cdots & H^+_{N,j} & \cdots \\ \cdots & H^+_{U,j} & \cdots \\ \cdots & H^+_{T,j} & \cdots \end{bmatrix} \times \begin{bmatrix} 0 \\ \vdots \\ b_j \\ \vdots \\ 0 \end{bmatrix} \tag{6.10}$$

So the Horizontal Position Error (HPE) can be expressed in a local ENU frame as following:

$$\begin{aligned} HPE_b &= \sqrt{(\hat{X}-X)^2_E + (\hat{X}-X)^2_N} \\ &= \sqrt{(H^+_{E,j})^2 + (H^+_{N,j})^2} \times b_j \end{aligned} \tag{6.11}$$

The bias at the jth measurement b_j can be bounded from two different points of view:

- If we start from the test statistic $NSSE$, which is defined as:

$$NSSE = \hat{r}^T \Sigma^{-1} \hat{r} \tag{6.12}$$

Taking into consideration the bias of jth measurement, according to Eq. (6.8) and Eq. (6.9), we have:

$$NSSE = B^T S^T \Sigma^{-1} S B = \frac{S_{j,j} b_j^2}{\sigma_j^2} \tag{6.13}$$

As a result:

$$|b_j| = \sqrt{\frac{NSSE}{S_{j,j}}} \sigma_j \tag{6.14}$$

By substituting the equation above into the Eq. (6.11), we can finally obtain:

$$HPE_b = \sqrt{(H^+_{E,j})^2 + (H^+_{N,j})^2} \times \sqrt{\frac{NSSE}{S_{j,j}}} \sigma_j \tag{6.15}$$

Denoting:

$$HSLOPE_j = \frac{\sqrt{(H^+_{E,j})^2 + (H^+_{N,j})^2}}{\sqrt{S_{j,j}}} \tag{6.16}$$

The horizontal position error can be bounded by the worst-case satellite, so that:

$$HPE_b \leq \max_i (HSLOPE_i \times \sigma_i) \sqrt{NSSE} \tag{6.17}$$

[1] the sub-index 'b' hereafter means 'bias'

In fact, the term $HSLOPE_i$ represents the sensitivity of HPE to the bias of i^{th} satellite. That is to say, the satellite with the largest $HSLOPE$ is the most difficult to detect because given the same HPE, it yields the smallest test statistic. Also, given the same test statistic, the satellite with the highest $HSLOPE$ produces the largest HPE.

- Similar with the previous derivation but starting from the non-centrality parameter, which is defined in Eq. (3.10) as:

$$\lambda = \sum_{i=1}^{m} \frac{\mu_i^2}{\sigma_i^2}$$

Under the assumption of only-one bias present in the jth measurement, the expression above can be simplified as:

$$\lambda = \frac{\mu_j^2}{\sigma_j^2} \tag{6.18}$$

where, μ_j and σ_j represent the mean and standard deviation of the jth residual: $\hat{r}_j \sim \mathcal{N}(\mu_j, \sigma_j^2)$.

According to Eq. (6.8), the mean of jth residual can be written as:

$$\mu_j = S_{j,j} b_j \tag{6.19}$$

As a result,

$$\lambda = \frac{S_{j,j} b_j^2}{\sigma_j^2} \tag{6.20}$$

So,

$$|b_j| = \frac{\sqrt{\lambda}}{\sqrt{S_{j,j}}} \sigma_j \tag{6.21}$$

By substituting the equation above into the Eq. (6.11), we can finally obtain:

$$\begin{aligned} HPE_b &= \sqrt{(H_{E,j}^+)^2 + (H_{N,j}^+)^2} \times \sqrt{\frac{\lambda}{S_{j,j}}} \sigma_j \\ &= HSLOPE_j \times \sigma_j \sqrt{\lambda} \end{aligned} \tag{6.22}$$

By assuming the bias occurs on the worst-case satellite, we finally obtain:

$$HPE_b \leq \max_i (HSLOPE_i \times \sigma_i) \sqrt{\lambda} \tag{6.23}$$

Then, it remains the impact of the measurement noise ε on the position error. According to the Eq. (6.5), the impact of noise on the position error can be written as[2]:

$$\|(\hat{X} - X)_n\| = \|H^+ \varepsilon\| \tag{6.24}$$

[2]the sub-index 'n' hereafter means 'noise'

The term at the right side of the equation can be bounded by calculating its covariance matrix, which is a quality matrix for position error denoted as Q_X:

$$\begin{aligned} Q_X &= H^{+} Cov(\varepsilon) H^{+T} \\ &= H^{+} \Sigma \; H^{+T} \\ &= (H^T \Sigma^{-1} H)^{-1} H^T \Sigma^{-1} \Sigma ((H^T \Sigma^{-1} H)^{-1} H^T \Sigma^{-1})^T \end{aligned} \tag{6.25}$$

Since the measurement error covariance matrix Σ is diagonal, i.e., $\Sigma^T = \Sigma$ and $(\Sigma^{-1})^T = \Sigma^{-1}$, the equation above can be simplified as:

$$Q_X = (H^T \Sigma^{-1} H)^{-1} \tag{6.26}$$

As defined in [18], the matrix Q_X can be reformed as:

$$Q_X = \begin{bmatrix} d_E^2 & d_{EN} & d_{EU} & d_{ET} \\ d_{EN} & d_N^2 & d_{NU} & d_{NT} \\ d_{EU} & d_{NU} & d_U^2 & d_{UT} \\ d_{ET} & d_{NT} & d_{UT} & d_T^2 \end{bmatrix} \tag{6.27}$$

The position error uncertainty along the semi-major axis of the error ellipse, which is shown in Fig. 6.3 in green, can be calculated as:

$$d_{major} = \sqrt{\frac{d_E^2 + d_N^2}{2} \sqrt{(\frac{d_E^2 - d_N^2}{2})^2 + d_{EN}^2}} \tag{6.28}$$

As a result, the impact of measurement noise on the position error can be estimated by multiplying an inflation factor k, which can be deduced from the specified probability of missed detection and the corresponding degree of freedom:

$$\|(\hat{X} - X)_n\| \leq k \cdot d_{major} \tag{6.29}$$

Finally, by summing up the impact of measurement error and that of the bias, or taking into consideration only one of them, we can find different expressions of HPL proposed in the literature, which will be listed as follows. One can also find the use of Horizontal Uncertainty Level (HUL) to bound the horizontal position errors. The difference between the HPL and the HUL will be discussed later in this section.

The HPL proposed in [74], which will be denoted as HPL1 hereafter in this chapter:

$$HPL1 = \max_i (HSLOPE_i \times \sigma_i) \sqrt{T} + k \cdot d_{major} \tag{6.30}$$

where, T is the threshold defined in Eq. (3.14).

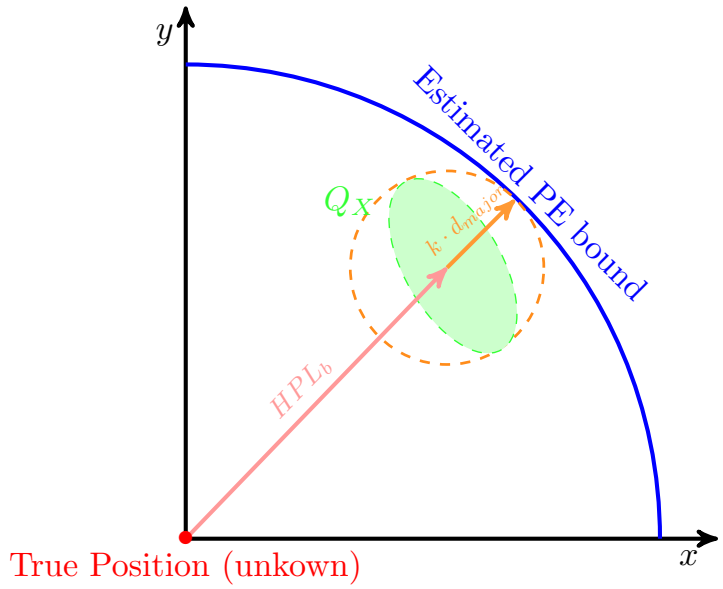

Figure 6.3 – Composition of the Estimated Position Error Bound

The HUL proposed in [83]:

$$HUL = \max_i(HSLOPE_i \times \sigma_i)\sqrt{NSSE} + k \cdot d_{major} \tag{6.31}$$

The HPL proposed in [75], which will be denoted as HPL2 hereafter in this chapter:

$$HPL2 = \max_i(HSLOPE_i \times \sigma_i)\sqrt{\lambda} + k \cdot d_{major} \tag{6.32}$$

And the HPL calculated in SBAS consider only the impact of measurement noise on the position error [18]:

$$HPL_{SBAS} = k \cdot d_{major} \tag{6.33}$$

The main difference between the HPL and the HUL is the predictability. HPL is predictable with the help of the satellite geometry information, the expected measurement error characteristics as well as the specified probability requirements (e.g., P_{md}, P_{fa}). Yet the HUL is not predictable and requires the real-time measurements. This is the reason why the threshold T is present in the expression of HPL in Eq. (6.30) but the $NSSE$ is present in the expression of HUL in Eq. (6.31).

One important metric to evaluate a HPL is that it can properly bound the errors with a reasonable size which depends strongly on the targeted application. Usually, a compromise should be found between the size of the HPL (the smaller the better) and the error bounding capability.

6.3.2 HPL evaluation with the total dataset

To evaluate the potential of the HPL in urban environment, the four methods of HPL computation described previously (i.e., the HPL1 in Eq. (6.30), the HPL2 in Eq. (6.32), the HPL_{SBAS} in Eq. (6.33) and the HUL in Eq. (6.31)) will be tested with the total dataset. The total number of epoch is 163503, among which 161724 epochs (near 9h) are available to realize HPL computations (since it is impossible to compute a HPL if the visible satellite number is strictly smaller than 5). In this research work, we will fix $P_{md} = P_{fa} = 10^{-2}$.

Fig. 6.4 and Fig. 6.5 provide the Stanford diagram for the four HPLs with respectively the C/N_0-based WLS estimator and the Hybrid Urban Multipath Model (UMM) WLS estimator (without applying any FDE).

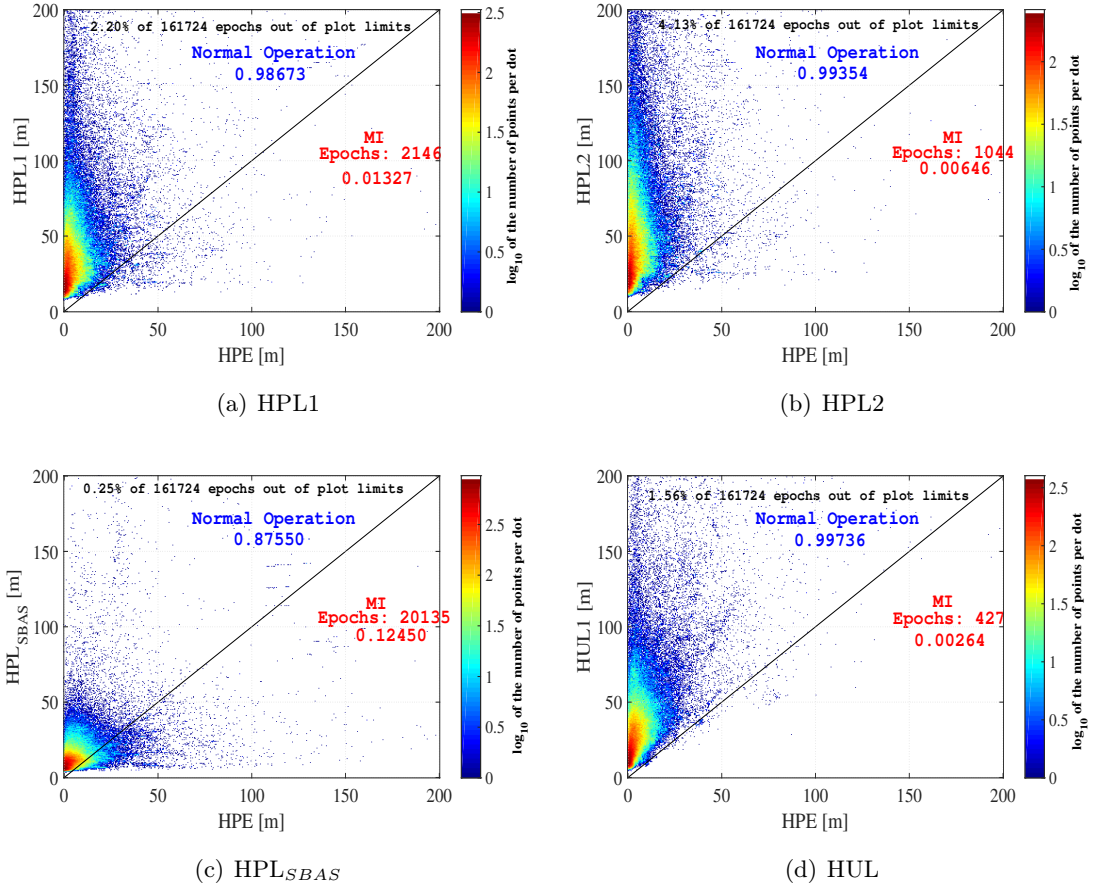

(a) HPL1

(b) HPL2

(c) HPL_{SBAS}

(d) HUL

Figure 6.4 – Stanford Diagram for Four Different HPLs Obtained with C/N_0-based WLS estimator without FDE (161724 epochs)

What should be highlighted is that the FDE algorithms are not yet applied in this section since we will firstly evaluate the HPLs in order to choose one most fitted for urban transport applications. In the following sections, this optimal HPL will be implemented in the

complete integrity monitoring scheme together with the FDE techniques. Moreover, the size of Horizontal Alert Limit (HAL) is not specified here. This is because the HAL is strongly application dependent and there are not yet any specifications concerning the size of HAL for urban transport GNSS integrity monitoring.

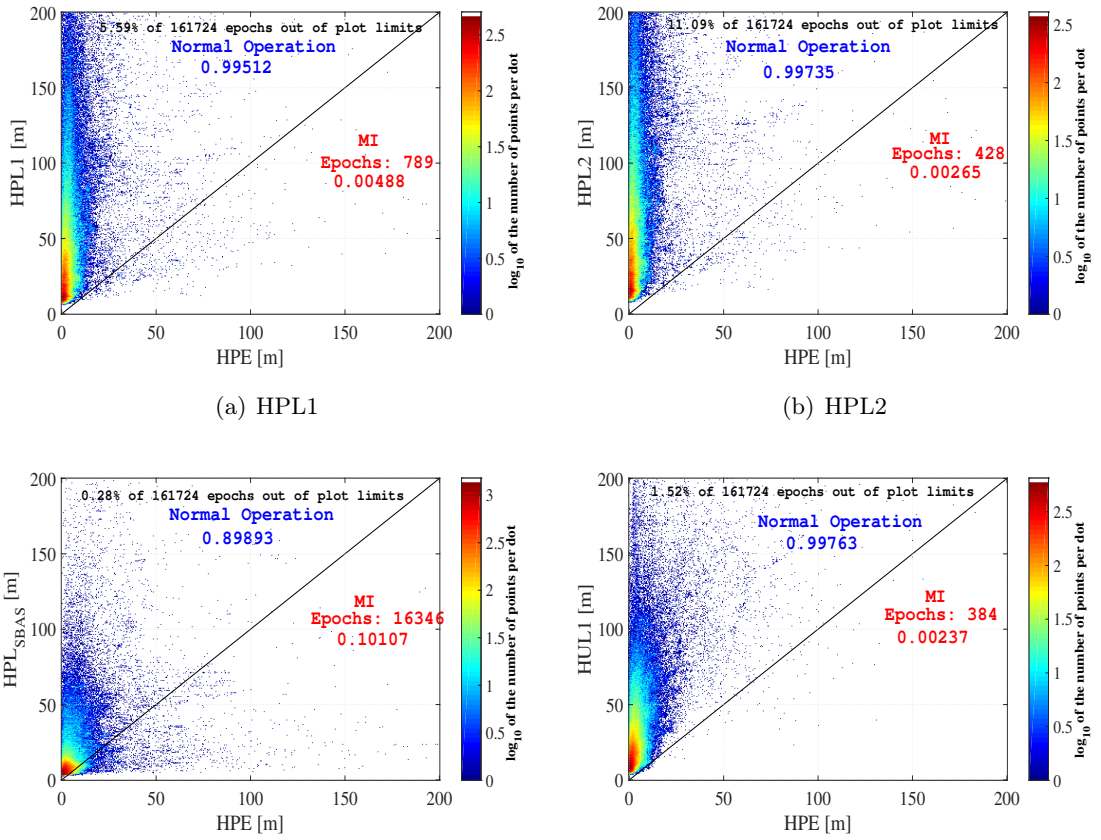

(a) HPL1

(b) HPL2

(c) HPL_{SBAS}

(d) HUL

Figure 6.5 – Stanford Diagram for Four Different HPLs Obtained with Hybrid UMM WLS estimator without FDE (161724 epochs)

Fig. 6.6 plots the Cumulative Distribution Function (CDF) of the four different HPLs with the two weighting models and the Table 6.1 summarizes the HPL size statistics and the probability of Misleading Information (MI) events.

From the Stanford diagram and the statistics, we can conclude that the HPL2 is the most "conservative" one. That is to say, it has the biggest size compared to the other three methods (median(HPL2) = 42.11 m with C/N_0 model and median(HPL2)=50 m with Hybrid UMM model). Putting apart HUL, HPL2 can better bound the position errors than the HPL1 and the HPL_{SBAS} ($P_{mi} = 0.65\%$ with C/N_0 model and $P_{mi} = 0.27\%$ with hybrid UMM model).

Then the HPL1 is the second conservative. Its size is reduced compared to the HPL2 (me-

Table 6.1 – Statistics of the Four Different HPLs

HPL	**C/N_0-based WLS (m)**				**Hybrid UMM WLS (m)**			
Type	***5%***	***50%***	***95%***	***P_{mi}(%)***	***5%***	***50%***	***95%***	***P_{mi}(%)***
HPL1	13.40	30.92	109.53	1.33	10.45	34.84	214.36	0.49
HPL2	17.45	42.11	170.60	0.65	13.78	50.00	328.85	0.27
HPL_{SBAS}	5.30	10.91	31.35	12.45	3.99	8.11	50.36	10.11
HUL	9.36	27.24	95.95	0.26	7.18	21.16	107.43	0.24

dian(HPL1) = 30.92 m with C/N_0 model and median(HPL1) = 34.84 m with Hybrid UMM model) but it produces more MI events (P_{mi} = 1.33% with C/N_0 model and P_{mi} = 0.49% with hybrid UMM model).

Concerning the HPL_{SBAS}, it can hardly well bound the estimated position errors with such small sizes (median(HPL_{SBAS}) = 10.91 m with C/N_0 model and median(HPL_{SBAS}) = 8.11 m with Hybrid UMM model). This is expected since the HPL_{SBAS} considers only the impact of the measurement noises on the estimated position error as discussed in the previous section, which is far from sufficient in urban environments. So it produces a high probability of MI events (P_{mi} = 12.45% with C/N_0 model and P_{mi} = 10.11% with hybrid UMM model). This is why the HPL provided by SBAS cannot be employed directly for urban GNSS-based transport applications.

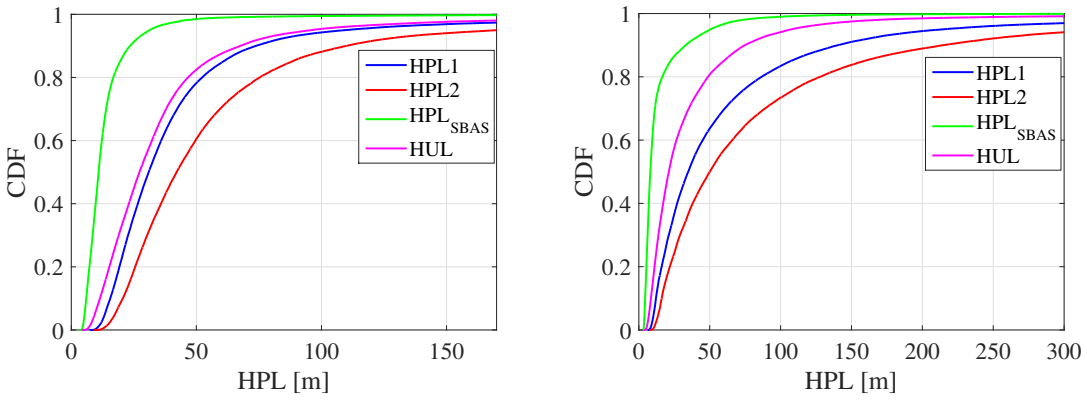

(a) C/N_0-based WLS Estimator (b) Hybrid UMM WLS Estimator

Figure 6.6 – CDF of the Four Different HPLs with Two Weighting Models (161724 epochs)

Finally, the HUL can reach a compromise between the size and the error bounding capability among all these four methods. Its size is smaller than the HPL1 and HPL2 (median(HUL) = 27.24 m with C/N_0 model and median(HUL) = 21.16 m with Hybrid UMM model) so that it is less conservative. It is capable of providing the lowest probability of MI events

($P_{mi} = 0.26\%$ with C/N_0 model and $P_{mi} = 0.24\%$ with hybrid UMM model).

The same conclusions can be drawn by analyzing the Horizontal Safety Index (HSI), which is proposed in [5] and is defined as follow:

$$HSI = \frac{HPL - HPE}{HPL} \tag{6.34}$$

HSI is a factor to evaluate the performance of HPL computation algorithm. The more conservative the algorithm, the closer the HSI is to one. The MI events are represented by negative values of HSI. Ideally, the HSI index should be positive, which means no MI events, and near to zero, which means its size is not too large compared to that of HPE.

Fig. 6.7 shows the curves of CDF for HSI with two weighting schemes. Obviously, the HPL_{SBAS} has a large part of negative HSI index, which is a proof of its poor error bounding capability. The HPL2 and HPL1 have more values of HSI index close to one so that they are conservative. HUL is able to provide the best compromise among these four methods.

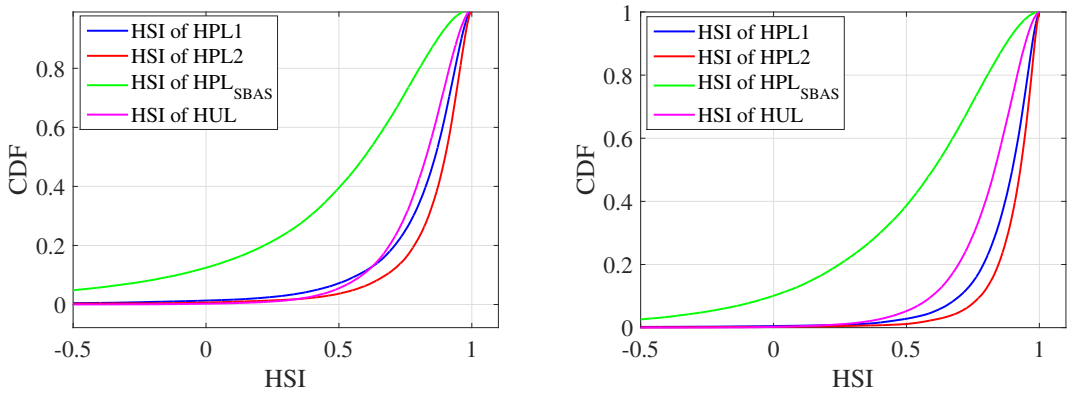

(a) C/N_0-based WLS Estimator

(b) Hybrid UMM WLS Estimator

Figure 6.7 – HSI of the Four Different HPLs with Two Weighting Models (Total Dataset)

In short, the HUL can reach a compromise between the size and the error bounding capability, which is the most suitable for integrity monitoring of GNSS-based urban transport applications. Consequently, in the following sections of this chapter, we will choose this method in order to provide a bound for the estimated position errors.

6.4 Analysis of the Integrity Performance of the Complete Scheme

The following performances of the complete proposed scheme (Weighted Least Squares (WLS) + Fault Detection and Exclusion (FDE)) shown in Fig. 6.1 will be evaluated in this section:

- Horizontal positioning accuracy;
- The size of the HPL;
- The probability of misleading information P_{mi};
- The Ratio of Reliable Positions (RRP) declared by FDE: if there is not enough redundancy to realize the FDE or to exclude all the faulty measurements, the solutions will be flagged as unreliable. Otherwise, the positions are flagged as reliable. In the case without FDE, the RRP represents the percentage of epochs where enough redundancy (at least one) exists to compute a HPL.

Here, we fix $P_{fa} = P_{md} = 10^{-2}$.

6.4.1 Results with Nantes center Dataset

Let's begin by analyzing the results with the Nantes center dataset, which includes 17903 epochs (near 1h). The complete overview of the trajectory is shown previously in Fig. 5.3.

Table 6.2 and Table 6.3 summarize the system performances before and after applying the FDE techniques with respectively C/N_0-based WLS estimator and the Hybrid UMM WLS estimator.

Table 6.2 – Performances Summary for **C/N_0-based** WLS with FDE (Nantes Center)

FDE	**Accuracy: HPE (m)**				**Integrity**		
Type	***50%***	***mean***	***95%***	***std***	***50% HPL (m)***	***P_{mi}(%)***	***RRP(%)***
None	2.64	4.81	30.74	26.79	19.46	0.28	98.68
ST	2.45	4.61	14.44	8.02	18.26	0.76	98.58
LT	2.38	3.56	9.56	4.41	17.76	0.11	93.55
FB	2.32	3.43	9.90	4.36	17.46	0.14	95.01
DAN	2.50	4.13	11.18	6.17	19.21	0.28	94.81
CT	2.46	4.55	13.61	8.07	18.29	0.75	98.57

Concerning the C/N_0-based WLS estimator, the accuracy performance is again improved by FDE techniques especially huge errors are removed since the standard deviations of HPE are much reduced. For example, the iterative Local Test (LT) can reduce the 95% HPE from 30.74 m to 9.56 m compared to the solver without FDE. The sizes of HPLs can be also reduced especially by Forward-Backward (FB) Test and the iterative LT. What has to be highlighted concerning these two FDE techniques is that, their probabilities of Misleading Information (MI) events P_{mi} are also reduced at the same time with their size reductions. This is a proof of strong enhancement of integrity performance. The performances of the Subset Test (ST)

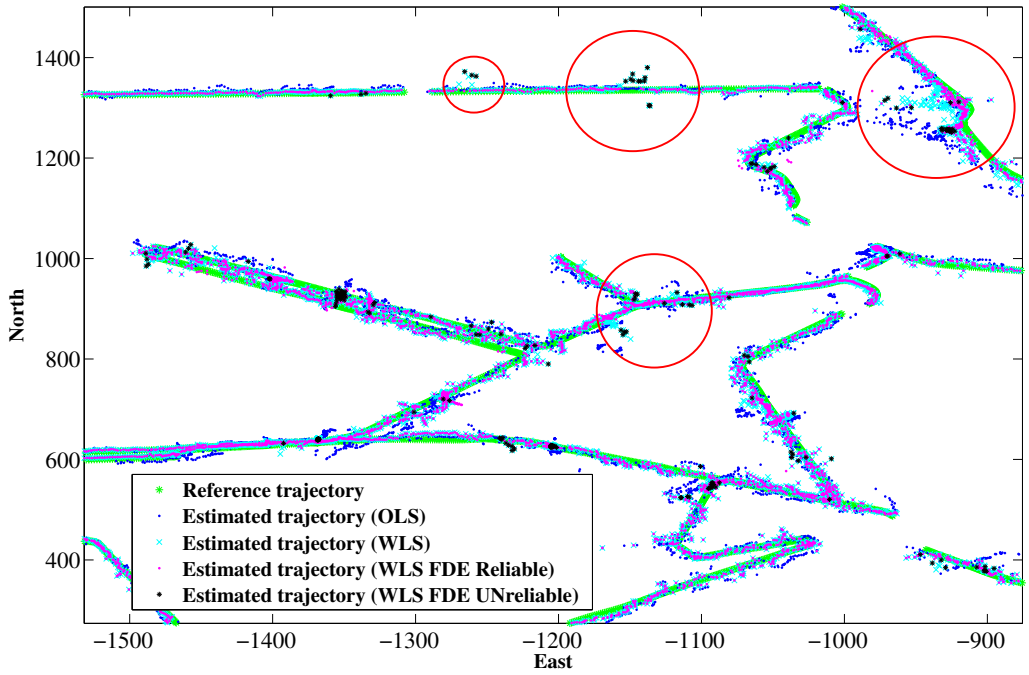

Figure 6.8 – Zoomed trajectories: Reference Trajectory (in green), Trajectory estimated by Ordinary Least Squares (OLS) (in blue), Trajectory estimated with C/N_0-based WLS (in sky blue), Trajectory estimated with C/N_0-based WLS with Forward-Backward (FB) (Reliable positions in magenta and UNreliable in black)

and the Classic Test (CT) are similar on both accuracy and integrity. But they are relatively worse than the other three FDE techniques. They can only exclude huge faults but are not very effective for small faults since the low percentiles HPE have very small improvement compared to the solver without FDE. The Ratio of Reliable Positions (RRP) of the five FDE techniques varies from 93.55% to 98.58%.

Fig. 6.8 presents some details about an example with the FB test. Several zoomed trajectories are drawn: the reference trajectory (in green), the trajectory estimated by Ordinary Least Squares (OLS) (in blue), the trajectory estimated with C/N_0 WLS (in sky blue) as well as the trajectory estimated with WLS C/N_0 and FB (the reliable positions are in magenta and unreliable positions are in black). Especially in the red circles, the huge HPEs are either reduced or flagged as unreliable, which provides a strong integrity monitoring capability.

In terms of the Hybrid UMM WLS estimator with FDE, its global performances on accuracy and integrity are generally better than the C/N_0-based WLS with FDE, if a comparison is made between Table 6.2 and Table 6.3. The best accuracy can be obtained by applying the iterative LT on the Hybrid UMM WLS estimator, where the median HPE achieves 2.29 m with

Table 6.3 – Performances Summary for **Hybrid UMM** WLS with FDE (Nantes Center)

FDE	**Accuracy: HPE (m)**				**Integrity**		
Type	***median***	***mean***	***95%***	***std***	***50% HPL (m)***	P_{mi} ***(%)***	***RRP(%)***
None	2.32	3.61	10.83	4.43	15.92	0.05	98.68
ST	2.33	3.76	11.27	5.49	15.49	0.17	98.59
LT	2.29	3.46	10.55	4.04	15.40	0.06	96.56
FB	2.30	3.48	10.59	4.09	15.44	0.07	96.78
DAN	2.31	3.59	10.70	4.64	15.83	0.04	98.31
CT	2.33	3.74	11.13	5.39	15.48	0.17	98.59

$std = 4.04m$. Concerning integrity performance, the position errors can be better bounded with smaller HPL while producing less MI events by the Hybrid UMM WLS estimator with FDE compared to the C/N_0-based WLS with FDE. The RRP with the five FDE varies from 96.56% to 98.59%, which is also slightly higher than the C/N_0-based WLS with FDE.

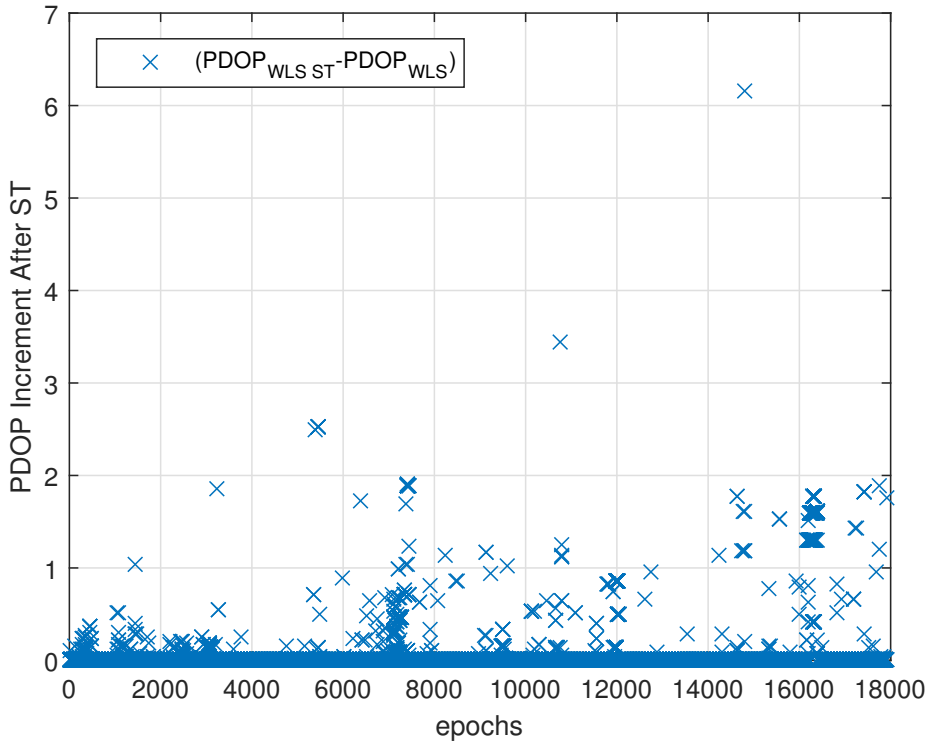

Figure 6.9 – PDOP Increments After Subset Test (Nantes Center)

Then a comparison will be made inside Table. 6.3, i.e., to compare the effects of FDE techniques on the Hybrid UMM WLS estimator. The improvements on accuracy are slight by iterative LT, FB test and the Danish method. However, by ST and CT, the accuracy is de-

graded. This is because the effects of satellite geometry degradation is predominant compared to the effects of fault elimination.

In fact, the GNSS positioning accuracy depends not only on the range measurement quality but also the user/satellite geometry, i.e., Dilution of Precision (DOP). For a FDE method, correct exclusions of faulty measurements will ameliorate the range measurement quality but will also inevitably degrade the satellite geometry due to a decrease of available satellite measurements. If the former effect is predominant against the latter one, the final accuracy can be improved. But if the latter one is predominant, the final accuracy will be degraded. Moreover, heavy correlations among measurements in urban canyons can also possibly lead to erroneous exclusion of healthy satellites.

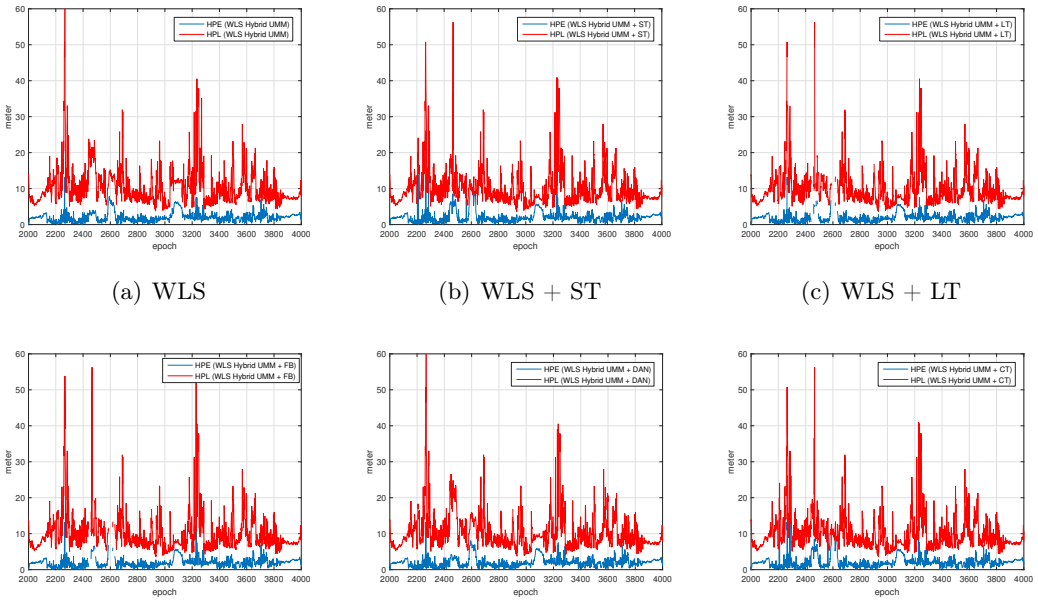

(a) WLS (b) WLS + ST (c) WLS + LT

(d) WLS + FB (e) WLS + DAN (f) WLS + CT

Figure 6.10 – HPL and HPE by Hybrid UMM without and with FDE techniques

Here, with the Hybrid UMM WLS estimator, huge bias are corrected at a first level by UMM model, in which the calculated additional distances are removed. The ST and CT is generally efficient only for huge bias as results shown previously with the C/N_0-based WLS estimator. Consequently, the DOP degradation is predominant against the effects of measurement quality improvement. Fig. 6.9 shows an example of Position Dilution of Precision (PDOP) increment after applying the ST, which is a proof of severe satellite geometry degradation.

The overall integrity performances of the Hybrid UMM WLS applied with different FDE techniques are satisfactory: the P_{mi} varies from 0.04% to 0.17%. This can be further observed in Fig. 6.10, which shows the HPL and HPE over a certain period of time window with Hybrid

UMM WLS estimator as well as that applied with the five FDE techniques.

6.4.2 Results with the total Dataset

The complete system presented in Section 6.2 is then applied on the total dataset, which includes 163503 epochs (near 9h) collected in urban canyons of three different cities as described in Section 5.1.

Before analyzing the performance in detail, Table 6.4 summarizes the test situations before entering into each FDE technique. Among the 163503 epochs in the total dataset, there are 1779 epochs with zero redundancy. That is to say, FDE is impossible to be carried out for 1.09% of the total data due to lack of redundancy. An initial Global Test (GT) failure means a fault is detected and it will be isolated later by each FDE technique. In the framework of C/N_0-based WLS estimator, 32% of epochs detect a fault and this ratio is lower with Hybrid UMM WLS estimator, which is 14%.

Table 6.4 – Test Situation Summary (Total Dataset)

Test Situation	**C/N_0 WLS**		**Hybrid UMM WLS**	
	Number of Epochs	***(%)***	***Number of Epochs***	***(%)***
Zero Redundancy	1779	1.09	1779	1.09
Initial GT failure	51936	31.76	22960	14.04

Table 6.5 and Table 6.7 present the performance summary of the five FDE techniques in the framework of two weighting solvers: the C/N_0-based WLS and the Hybrid UMM WLS. Table 6.6 and Table 6.8 present refined statistical results of reliable positions declared by each FDE technique with two weighting solvers. That is to say, in these two latter tables, the statistical analysis is made by keeping the same epoch samples (i.e., the epochs declared as reliable) for WLS solutions and WLS with FDE. Fig. 6.11 and Fig. 6.12 provide the corresponding Stanford diagrams.

Huge errors exist in the total dataset, which are possibly due to badly degraded measurements caused by local effects and losses of lock of the receiver. These huge errors can reach several kilometers with only WLS estimators as observed in the tables: $std(HPE) = 9.48$ km for C/N_0-based WLS and $std(HPE) = 2.62$ km for Hybrid UMM WLS. Fortunately, they can be effectively detected by the FDE techniques since the standard deviation of the errors are all reduced to smaller than 20 m. This proves the efficiency of the FDE on huge errors.

In the framework of C/N_0-based WLS estimator, as shown in Table 6.5, the accuracy is globally improved while applying the FDE techniques. Among all the FDE, the iterative Local Test (LT) has the best performance on accuracy and integrity. It improves the median

Table 6.5 – Performances Summary for C/N_0-based WLS with FDE (Total Dataset)

FDE	Accuracy: HPE (m)			Integrity		
Type	*50%*	*95%*	*std*	*50% HPL (m)*	P_{mi} *(%)*	*RRP(%)*
None	4.41	21.84	9.48×10^3	27.24	0.26	98.91
ST	4.12	28.78	13.60	23.32	2.26	98.21
LT	3.62	15.66	7.17	21.70	0.34	84.61
FB	3.72	16.75	7.97	22.50	0.42	89.66
DAN	3.98	19.50	9.31	24.93	0.19	90.32
CT	4.12	28.05	17.51	23.34	1.98	98.17

HPE from 4.41 m to 3.62 m and the median HPL is 21.70 m while guarantees a probability of Misleading Information (MI) P_{mi} at 0.34%. The Forward-Backward (FB) Test has the second best performance after LT, whose RRP is slightly higher than that of the LT because of the backward loop. The Danish method is not as good as the latter two FDE on accuracy but it performs well on integrity since it reduces the size of HPL and P_{mi} at the same time compared to the WLS estimator. The Ratio of Reliable Positions (RRP) declared by the FDE techniques with C/N_0-based WLS varies from 85% to 98%. The integrity performance can be observed more clearly with the help of the Stanford diagram in Fig. 6.11.

Table 6.6 – Refined Analysis on Reliable Positions: C/N_0-based WLS with FDE (Total Dataset)

Reliable	*RRP*	Accuracy: HPE (m)				Integrity	
Positions	*(%)*	*50%*	*mean*	*95%*	*std*	*50% HPL (m)*	P_{mi} *(%)*
WLS	98.21	4.37	97.04	21.63	6.80×10^3	27.08	0.26
ST		4.12	8.12	28.78	13.60	23.32	2.26
WLS	84.61	3.99	36.48	17.95	3.97×10^3	25.06	0.25
LT		3.62	5.51	15.66	7.71	21.70	0.34
WLS	89.66	4.15	6.79	19.43	29.55	26.08	0.25
FB		3.72	5.78	16.75	7.97	22.50	0.42
WLS	90.32	4.20	6.88	20.83	9.91	26.26	0.26
DAN		3.98	6.46	19.50	9.31	24.93	0.19
WLS	98.17	4.37	97.07	21.60	6.81×10^3	27.07	0.26
CT		4.12	7.98	28.05	17.51	23.34	1.98

If we take a look at the performance summary on the reliable epochs declared by each FDE in Table 6.6, the effectiveness of the FDE technique is clearer. In this table, each couple of

WLS and FDE has the same epoch samples, which are the ones declared as reliable by the corresponding FDE. The accuracy improvement is obvious especially in mean values and the standard deviation of HPE. For example, the mean HPE is reduced from 97.04 m to 8.12 m for the epochs declared as reliable by ST. This means huge errors are "corrected" by FDE since faulty measurements are excluded. The Danish method has the smallest size of HPL with the lowest P_{mi} among its

Table 6.7 – Performances Summary for **Hybrid UMM** WLS with FDE (Total Dataset)

FDE	**Accuracy: HPE (m)**			**Integrity**		
Type	***50%***	***95%***	***std***	***50% HPL (m)***	***P_{mi} (%)***	***RRP(%)***
None	3.57	16.45	2.62×10^3	21.16	0.24	98.91
ST	3.63	19.53	11.18	20.00	0.92	98.63
LT	3.42	14.67	7.00	19.48	0.33	90.34
FB	3.46	15.09	8.03	19.75	0.36	92.21
DAN	3.52	15.48	8.24	20.77	0.23	96.44
CT	3.63	19.08	10.17	20.02	0.80	98.61

Table 6.8 – Refined Analysis on Reliable Positions: **Hybrid UMM** WLS with FDE (Total Dataset)

Reliable	***RRP***	**Accuracy: HPE (m)**				**Integrity**	
Positions	***(%)***	***50%***	***mean***	***95%***	***std***	***50% HPL (m)***	***P_{mi} (%)***
WLS	98.63	3.56	30.42	16.28	2.62×10^3	21.11	0.23
ST		3.63	6.40	19.53	11.18	20.00	0.92
WLS	90.34	3.46	22.62	14.87	1.27×10^3	20.20	0.24
LT		3.42	5.22	14.67	7.00	19.48	0.33
WLS	92.21	3.49	10.17	15.26	622.23	20.49	0.24
FB		3.46	5.42	15.09	8.03	19.75	0.36
WLS	96.44	3.54	5.65	15.87	8.56	21.01	0.24
DAN		3.52	5.57	15.48	8.24	20.77	0.23
WLS	98.61	3.56	30.42	16.27	2.62×10^3	21.10	0.23
CT		3.63	6.27	19.08	10.17	21.02	0.80

In terms of the Hybrid UMM WLS estimator, as shown in Table 6.7, the global performance of accuracy and integrity are better than the former C/N_0-based WLS estimator. That is to say, the size of HPL are smaller but covers in a correct way the HPE as seen that the P_{mi} is lower. The overall HPE have been reduced by the use of our estimator. Especially

with the iterative LT, the median HPE can achieve 3.42 m and the P_{mi} can be guaranteed at 0.33% with a median HPL at 19.48 m. The RRP varies from 90% to 99% for the five FDE techniques, which is also slightly higher than the previous C/N_0-based WLS with FDE. Fig. 6.12 shows the corresponding Stanford diagrams.

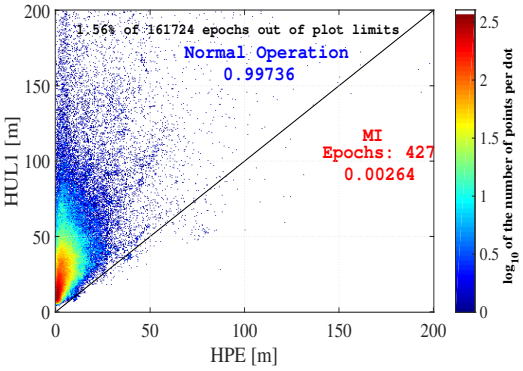

(a) WLS Only

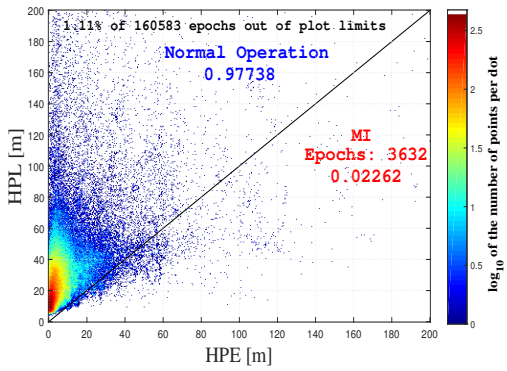

(b) WLS + ST

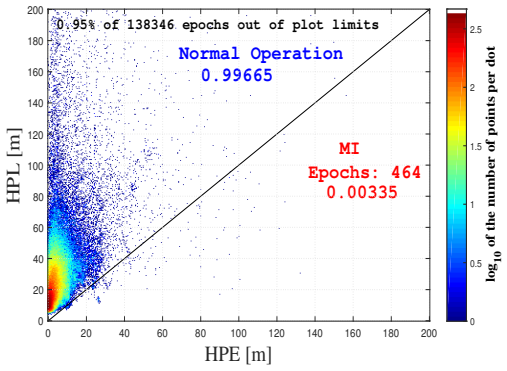

(c) WLS + LT

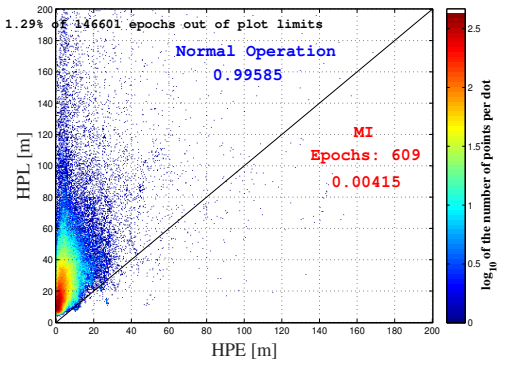

(d) WLS + FB

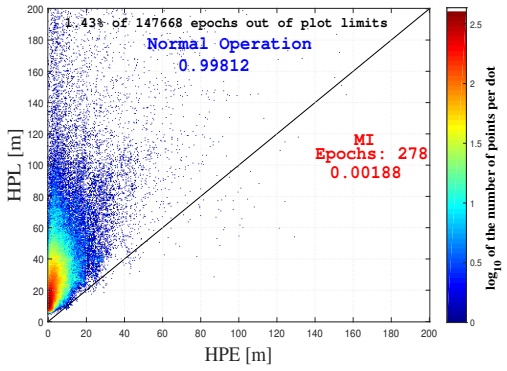

(e) WLS + DAN

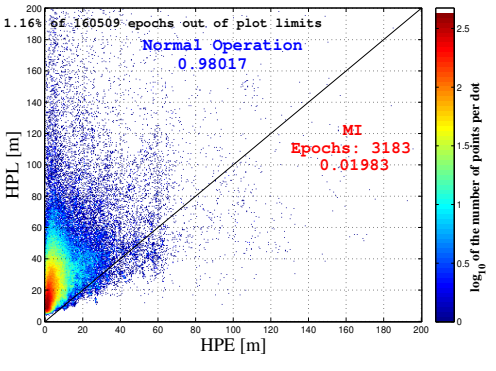

(f) WLS + CT

Figure 6.11 – Stanford Diagram by $\boldsymbol{CN_0}$**-based** WLS estimator without and with FDE (Total Dataset)

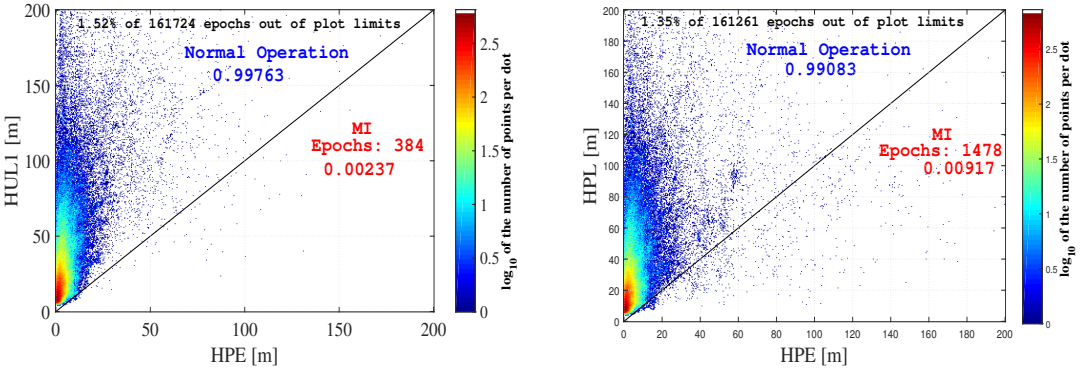

(a) WLS Only

(b) WLS + ST

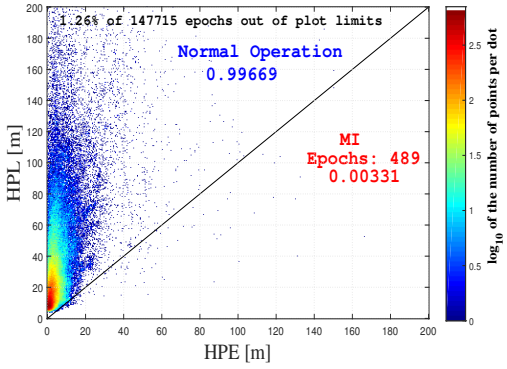

(c) WLS + LT

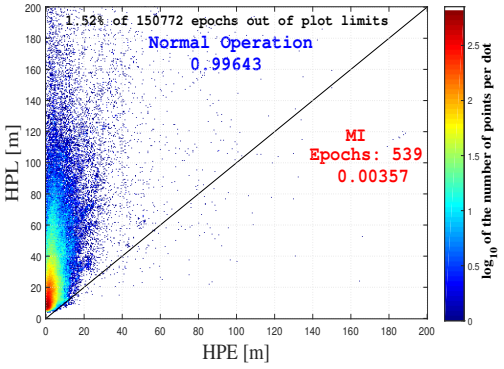

(d) WLS + FB

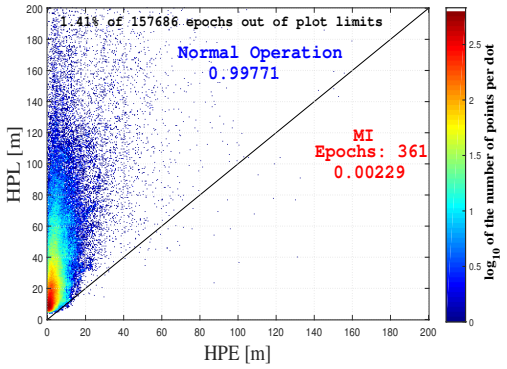

(e) WLS + DAN

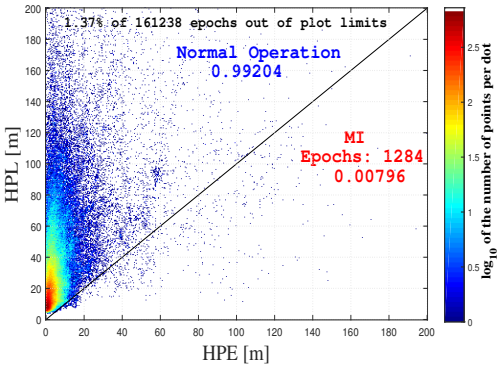

(f) WLS + CT

Figure 6.12 – Stanford Diagram by **Hybrid UMM** WLS estimator without and with FDE (Total Dataset)

Table 6.8 reports the performance summary for reliable epochs declared by each FDE technique. Similar trends are observed: huge position errors are repaired by the FDE techniques thanks to the exclusion of the faulty measurements.

6.5 Conclusion and Discussion

This chapter firstly introduced the proposed scheme of integrity monitoring system, which can be potentially applied on the GNSS-based urban transport applications. This system includes two main modules: an accuracy enhancement module and an integrity monitoring module.

The accuracy enhancement module employs two different weighting solvers: the C/N_0-based Weighted Least Squares (WLS) and the Hybrid Urban Multipath Model (UMM) WLS. The integrity enhancement module includes five different FDE techniques for purpose of comparison: the Subset Test (ST), the iterative Local Test (LT), the Forward-Backward (FB) Test, the Danish re-weighting method as well as a Classic Test (CT). Finally, a Horizontal Protection Level (HPL) is calculated in order to provide a statistical error bound.

After the introduction of the complete integrity monitoring system, several methods of HPL computation existing in the current literature are derived in detail. Four HPL computation methods are tested and evaluated with the total dataset described in Section 5.1, which are collected in urban canyons of three different cities in France (near 9h). The one most adapted to GNSS-based urban applications is chosen to be implemented into the complete integrity system.

Finally, the complete system is tested with the dataset of Nantes center and the total dataset. The Hybrid UMM WLS estimator with FDE has a better performance of accuracy and integrity than the C/N_0-based WLS estimator. Among all the combinations of weighting solvers and the FDE techniques, the Hybrid UMM WLS estimator with the LT can achieve the best performance of accuracy and integrity with the total dataset: median(HPE)= 3.42 m and median(HPL)=19.48 m while guaranteeing the probability of Misleading Information (MI) $P_{mi} = 0.33\%$.

The Subset Test (ST) and the Classic Test (CT) has similar performances. These two methods can eliminate huge errors. But special attention should be payed while using these two methods especially after applying the range corrections, such as the Hybrid UMM model. Since the small quantile of HPE can be degraded with these two FDE techniques. This is because a correct elimination of faulty measurement can help improve accuracy but also degrade the satellite geometry due to a reduction of the satellite number. If the former phenomenon is predominant against the latter, the overall accuracy can be improved. Otherwise, the accuracy, especially the small-quantile one, will be degraded. An additional satellite geometry control can be added after ST and CT by simply choosing a threshold for Dilution of Precision (DOP).

The Ratio of Reliable Positions (RRP) declared by the five FDE techniques varies from 85%

to 98% in the framework of the C/N_0-based WLS scheme and it varies from 90% to 99% with the Hybrid UMM WLS. The non-reliable positions are flagged due to a lack of redundancy to realize or to accomplish the FDE. The lack of redundancy to realize the FDE is mainly because of a limited satellite visibility while the lack of redundancy to accomplish the FDE may occur especially with the presence of multiple heavily degraded measurements. This latter means, despite the exclusion of several faulty measurements, the remaining measurements still cannot provide a reliable position but their is no longer enough redundancy to continue the FDE.

In fact, the lack of redundancy is a limitation of the snapshot-based integrity monitoring. This situations is expected to be improved by multi-constellation or the use of a sequential integrity monitoring scheme in order to increase the degree of freedom of the complete system. The latter will be analyzed in detail in the next chapter.

The proposed integrity monitoring system can be potentially implemented in the low-cost GNSS receivers for the purpose of eliminating huge errors. The overall performances can be further improved by hybridizing other sensors, which is not in the framework of this PhD research work.

Chapter 7

Extended Kalman Filter (EKF) Innovation-Based Integrity Monitoring

Contents

Summary

As a parallel class of approach with the snapshot residual-based integrity monitoring, the sequential integrity monitoring approach recently attracts more and more attention in this research domain. The main estimator employed in this approach is an Extended Kalman Filter (EKF), which is widely used in different domain. It can provide optimal estimations of navigation parameters if the system dynamic motions and the observation are properly modeled.

This chapter begins by introducing the basic theories of EKF innovation-based integrity monitoring approach especially the corresponding FDE techniques. Then the HPL computation in the framework of innovation-based quality control is discussed, in which, a novel HPL computation method is proposed. Finally, the complete system is evaluated and tested with real GPS data collected in urban canyons. The final results are compared with the results obtained in Chapter 6.

Part of results in this chapter is the subject of the author's publication in [169].

7.1 Extended Kalman Filter (EKF) Innovation-Based Integrity Monitoring System Design

7.1.1 Introduction

Kalman Filter (KF) and Extended Kalman Filter (EKF) are tools widely used in different domains for estimation problems. By optimally weighting the current measurements and the dynamic model, the KF can provide recursive estimations for state vector. It is possible to implement KFs at different levels of navigation information processing procedures, for example, at a preliminary level to process physical measurements provided by sensors, at an intermediate level to hybridize measurements from different sensors, or at a final level to optimize the position information estimated by different systems.

The EKF-based integrity monitoring approach has attracted more and more attention recently thanks to its possibility of hybridizing other sensors with GNSS [170–173]. Besides, one important advantage of the sequential approach compared to the snapshot one is that the Degree of Freedom (DoF) of the system is exactly equal to the number of observations, this being not decreased by the number of unknown parameters (i.e. the dimension of the state vector).

As described in Section 2.4.2 concerning the theory of the EKF, the main difference between the EKF and the Least Squares (LS) method is the involvement of the dynamic model, which allows the system to make the prediction according to the dynamic model. The predicted state introduce additional redundancy for the integrity monitoring problem.

For the snapshot residual-based method, the Degree of Freedom (DoF) of the system is $m-n$ (m is the number of measurements, and n is the number of states to estimate, i.e., $n = 4$ in this research work). Thus, at least $n+1$ measurements are needed to realize the Fault Detection and at least $n+2$ measurements are needed to realize the Fault Exclusion. While in the case of the innovation-based FDE with EKF, thanks to the presence of the n-dimensioned predicted states, the DoF of system is m. If there are always n states to estimate, only one measurement is sufficient to realize the same FD test and only 2 measurements are needed for the FDE. Table 7.1 makes the summary of the system DoF and redundancy in the two classes of integrity monitoring approach.

Since in urban environments satellite visibility is often poor, the fact that less measurements are required for KF innovation-based FDE will make the integrity monitoring system more robust.

In the following sections, an EKF innovation-based integrity monitoring scheme will be designed and then implemented. Its performance will be evaluated with real data collected in

urban canyons of three different cities in France as described in Section 5.1.

Table 7.1 – Summary of System DoF and Redundancy

Integrity Monitoring Approach	The Number of			Minimal Number of measurements	
	measurement	unknown	DoF	for FD	for FDE
Snapshot Residual	m	n	$m-n$	$n+1$	$n+2$
Sequential Innovation	m	n	m	1	2

7.1.2 Extended Kalman Filter (EKF) Implementation

7.1.2.1 Basic Implementation

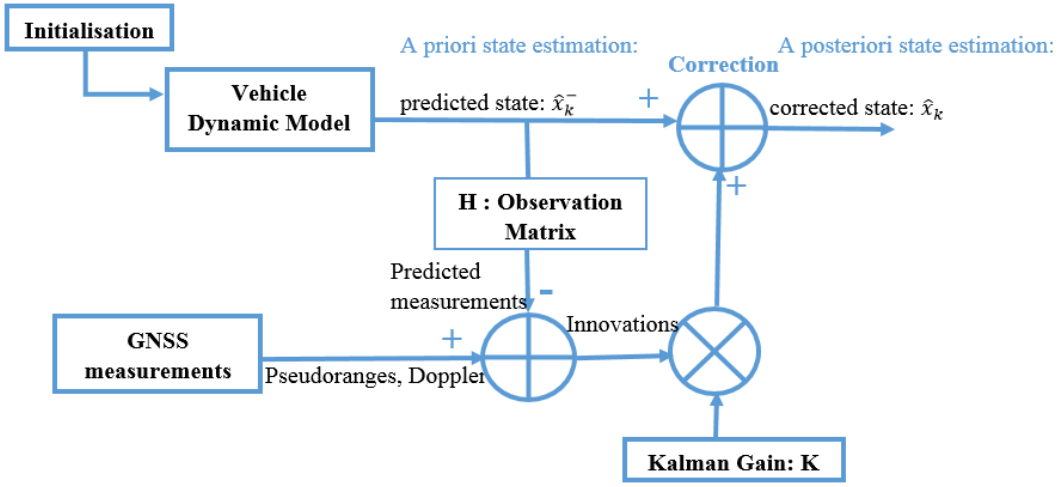

Figure 7.1 – Flowchart of Extended Kalman Filter (EKF)

The basic theories of Extended Kalman Filter (EKF) is presented previously in Section 2.4.2.2 of Chapter 2. Fig. 7.1 shows the flowchart of the EKF implemented in this research work. Here, the EKF is designed to estimate the vehicle position (e, n, u), velocity (v_e, v_n, v_u) as well as the user clock offset δt and user clock drift $d\delta t$. The state vector consists of:

$$x_k = [e \quad v_e \quad n \quad v_n \quad u \quad v_u \quad c\delta t \quad cd\delta t]^T \tag{7.1}$$

where, c is the speed of light.

A constant velocity dynamic model described in [174] is employed. That is to say, the state

transition matrix F can be simply expressed as:

$$F = \begin{bmatrix} \phi & 0 & 0 & 0 \\ 0 & \phi & 0 & 0 \\ 0 & 0 & \phi & 0 \\ 0 & 0 & 0 & \phi \end{bmatrix} \quad \text{where,} \quad \phi = \begin{bmatrix} 1 & \Delta t \\ 0 & 1 \end{bmatrix} \tag{7.2}$$

in which, Δt is the time interval between subsequent measurement samples.

So the vehicle motion can be modeled as follows:

$$x_k = F x_{k-1} + w_{k-1} \tag{7.3}$$

where, w_k denotes the zero-mean Gaussian process model noise with covariance matrix Q.

The matrix Q is designed as follow [174]:

$$Q = \begin{bmatrix} Q_{PV} & 0 & 0 & 0 \\ 0 & Q_{PV} & 0 & 0 \\ 0 & 0 & Q_{PV} & 0 \\ 0 & 0 & 0 & Q_T \end{bmatrix} \tag{7.4}$$

where,

$$Q_{PV} = \begin{bmatrix} \frac{S_p \Delta t^3}{3} & \frac{S_p \Delta t^2}{2} \\ \frac{S_p \Delta t^2}{2} & S_p \Delta t \end{bmatrix} \quad \text{and} \quad Q_T = \begin{bmatrix} S_f \Delta t + \frac{S_g \Delta t^3}{3} & \frac{S_g \Delta t^2}{2} \\ \frac{S_g \Delta t^2}{2} & S_g \Delta t \end{bmatrix}$$

and S_p, S_g, S_f are the spectral densities associated with the white noise [174].

The calibration of the three spectral density values are made with the help of a time-window mask on GNSS measurements. That is to say, during this time window (i.e., 10 seconds in this research work), there is no GPS measurements to feed the EKF and the state estimations are carried out only according to the system dynamic model. Under this configuration, the estimated Horizontal Position Errors (HPEs) are roughly compared with an estimated error bound, which is the *a posteriori* estimated horizontal position error covariance multiplied by an inflation factor k (i.e., $k = 3$ in this research work). If the divergence of the HPEs inside time window mask can be mostly covered by the estimated error bounds, this means the spectral densities are satisfactory. These parameters are finally be fixed as in Table 7.2 for each dataset.

The research in this PhD aims at studying the performances of a standalone GNSS receiver, hence, measurement vector z_k is composed of GNSS code pseudorange and Doppler measurements, which will be used to feed the EKF. The linearized measurement vector can be written as:

$$z_k = H_k x_k + \nu_k \tag{7.5}$$

Table 7.2 – Spectral Density Parameter Values for Each Dataset

	S_p	S_g	S_f
Nantes Center	70	70	70
Toulouse	200	200	200
Boulevards, Paris	300	300	300
La Défense, Paris	350	350	350
Paris XII^{th}	200	200	200
Nantes	70	70	70

where, H_k denotes the observation matrix and ν_k represents the measurement noise at the epoch k, which is assumed to follow a zero-mean Gaussian distribution with covariance matrix R:

$$\nu_k \sim \mathcal{N}(0, R_k)$$

The design of the matrix R_k will be described in the next section.

7.1.2.2 EKF Measurement Error Covariance Matrix Design: Weighted EKF (WEKF) Scheme

The covariance matrix of the measurement noise R_k plays an important role to guarantee the performance of the EKF. Traditionally, the matrix R_k is diagonal and supposed as time-invariant. Its diagonal components are variances of measurement errors. However, in urban environments, the GNSS signals are severely degraded and measurement errors vary frequently depending on local effects. Thus, a time-variant R_k instead of a fixed one is preferred.

Recall that the error models described and proposed in Chapter 4 can take into consideration the real-time signal quality by modeling the pseudo-range measurement error variances with different criteria. As a result, we propose here a Weighted Extended Kalman Filter (WEKF) scheme, in which the measurement error covariance matrix R_k will be scaled by error models. The two error models, the C/N_0-based one and the Hybrid UMM, which are evaluated as the best ones in Chapter 5, will be implemented in the matrix R_k in the WEKF scheme.

The measurement error covariance matrix at the kth epoch $R_k \in \mathbb{R}^{2m \times 2m}$ can be written as[1]:

$$R_k = \begin{bmatrix} \Sigma_{PR} & 0 \\ 0 & \Sigma_{Dop} \end{bmatrix} \tag{7.6}$$

where, Σ_{PR} and Σ_{Dop} are respectively the measurement covariance matrix of the pseudorange measurements and the Doppler measurements.

[1] m is the number of visible satellites

The two error variance models, i.e., the C/N_0 model and the Hybrid UMM model, calibrated in Chapter 5 will be only implemented for the pseudorange measurements error covariance matrix, i.e., Σ_{PR}. The Doppler error covariance Σ_{Dop} will adopt a fixed value as its diagonal components, which varies from $(2\ m/s)^2$ to $(6\ m/s)^2$ for different datasets in this research work.

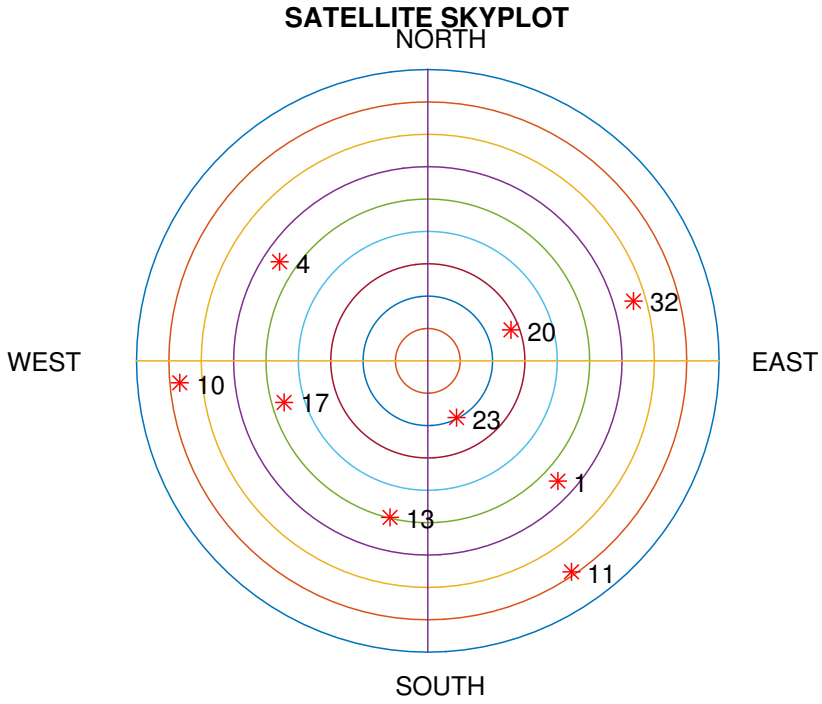

Figure 7.2 – A skyplot of the initial epoch of the Nantes Center dataset

The justifications for this choice are as follows. The Doppler measurements are generally less affected by the local effects compared to the pseudorange measurements. Fig. 7.2 shows a skyplot of the initial epoch of Nantes center dataset and Fig. 7.3 shows the PR errors as well as the Doppler errors for each visible satellite present in the skyplot. The PR errors and the Doppler errors are estimated with the method described in Section 4.2.1 of Chapter 4.

Fig. 7.3 shows that the Doppler measurements are less affected compared to the PR measurements. For instance, if we look into the satellite 11, whose elevation is the lowest in the skyplot, its Doppler errors are much smaller and more stable than its pseudorange errors.

Of course, it is possible to implement the same error models for Doppler error covariances. But the model parameters should be carefully re-calibrated. Considering that the Doppler measurements are less affected by the local effects, the fixed Doppler measurements covariance will be adopted in this research work.

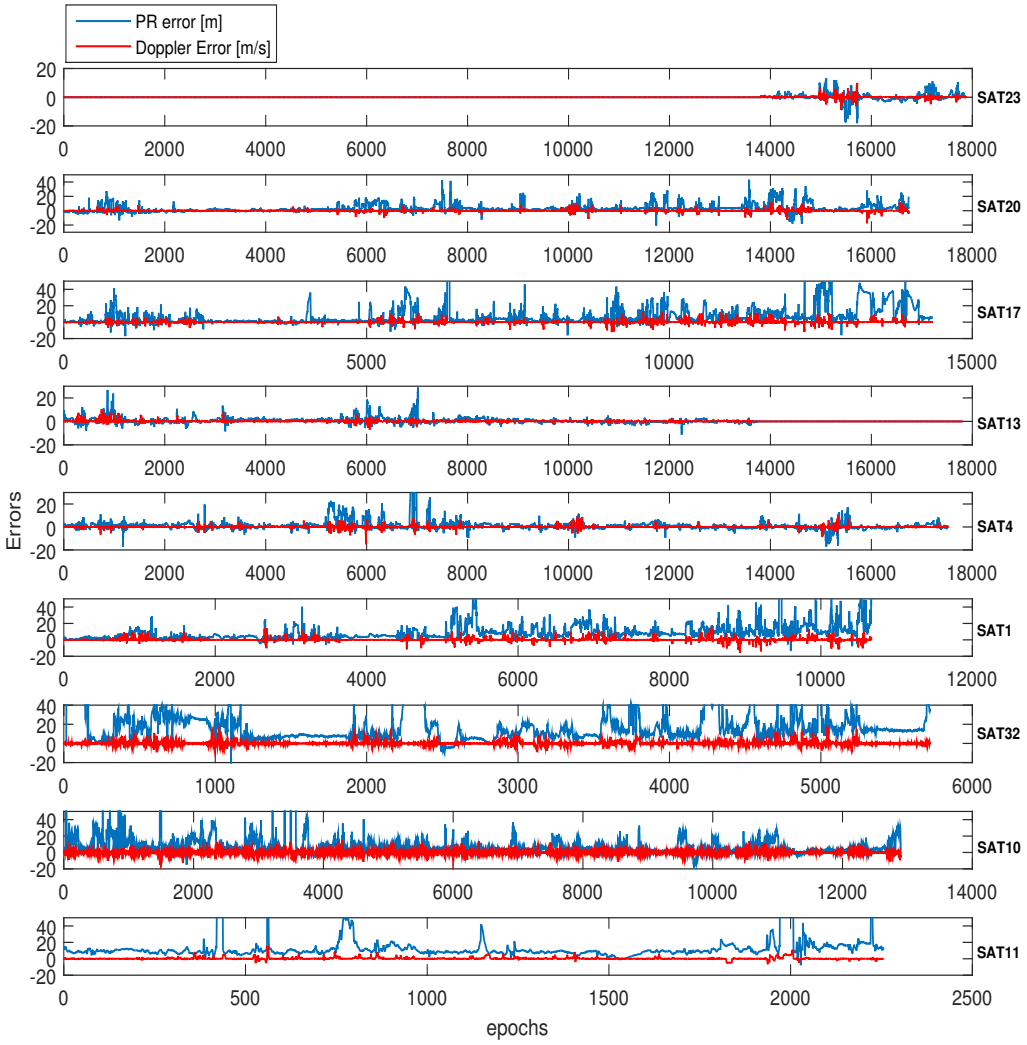

Figure 7.3 – Pseudorange Error and Doppler Error (Nantes Center dataset)

7.1.3 EKF Innovation-based Fault Detection and Exclusion (FDE)

The innovation γ_k at instant k is defined as the difference between the measurement and its prediction at time k:

$$\gamma_k = z_k - H_k \hat{x}_k^- \tag{7.7}$$

where, H_k denotes the observation matrix and $\hat{x}_k^-$ represents the *a priori* state estimation at instant k.

As a result, the covariance matrix S_k of the innovation vector can be derived as:

$$S_k = H_k P_k^- H_k^T + R_k \tag{7.8}$$

where, P_k^- denotes the covariance matrix of the EKF predicted state and R_k represents the covariance matrix of measurement errors.

Similar with the residual in the snapshot method, the innovation is supposed to follow a centered Gaussian distribution in nominal cases and to follow a non-central Gaussian distribution in faulty cases [172].

For the EKF innovation-based FDE, the Normalized Innovation Squared (NIS) is used as the test statistic to realize the initial Global Test (GT) for the purpose of fault detection. With Eq. (7.7) and Eq. (7.8), the NIS at instant k q_k can be computed as:

$$q_k = \gamma_k^T S_k^{-1} \gamma_k \tag{7.9}$$

The two hypotheses of the test are:

- Under fault-free conditions, q_k follows a central chi-squared distribution with m_k degree of freedom, where m_k is the number of visible satellite at instant k. With a specified probability of false alarm P_{fa}, a threshold T_k can be defined as follow:

$$P_{fa} = \int_{T_k}^{\infty} \frac{1}{2^{\frac{m_k}{2}} \Gamma(\frac{m_k}{2})} z^{\frac{m_k}{2}-1} e^{-\frac{z}{2}} dz \tag{7.10}$$

- Under faulty conditions, q_k follows a non-central chi-squared distribution with m_k degree of freedom and a non-centrality parameter λ_k^2 [172]:

$$\lambda_k^2 = \mathbb{E}[\gamma_k^T] S_k^{-1} \mathbb{E}[\gamma_k] \tag{7.11}$$

The system will declare a detection of fault if the GT fails:

$$q_k > T_k \tag{7.12}$$

If a fault is detected, the Fault Exclusion procedure will start in order to isolate the faulty measurements. Different fault isolation techniques exist. The general ideas of these FDE techniques are similar but some details should be adapted in accordance with the EKF innovation-based sequential method. The main difference between the innovation-based FDE and the snapshot-based FDE is mainly in the step of re-adaptation after each exclusion, that is to say:

- For the snapshot-based FDE, after each exclusion, a new position solution will be calculated with the remaining measurements. Then the new test statistic, i.e., Normalized Sum of Squared Error (NSSE), will be constructed from the residual with the help of this new position solution;

- While for the innovation-based FDE, after identifying the faulty measurement, the exclusion will be made directly from the innovation vector γ_k, its covariance matrix R_k as well as the geometry matrix H_k. Then, the new test statistic, i.e., Normalized Innovation Squared (NIS), can be calculated. The predicted state vector remains the same after the exclusion. As a result, the final exclusion effect of the innovation-based FDE only affects on the Kalman gain and the innovation vector.

As a result, the effects of the innovation-based FDE is less stronger than that of the snapshot residual-based FDE. We propose here to introduce the Classic Test and the Danish re-weighting method presented in the snapshot residual-based integrity monitoring scheme into the innovation-based scheme. In fact, it is also possible to adapt the Subset Test (ST), the iterative Local Test (LT) as well as the Forward-Backward (FB) Test. But our preliminary results (not presented in this PhD thesis) show that their performances are not better than the Classic Test and the Danish re-weighting method. This issue can be an axis of future research.[2]

7.1.3.1 Innovation-based Classic Test (IBCT) Scheme

In case of a fault detected, the EKF Innovation-based Classic Test (IBCT) scheme excludes the measurement with the biggest normalized innovation. But the difference with the snapshot-based method is that the innovations cannot be normalized simply by dividing the corresponding diagonal term of its covariance matrix S. This is because the matrix S involves the cross correlations of the state components.

One possible solution is to apply the Cholesky decomposition as in [175]. Since the matrix S is proved to be positive semi-definite, its inverse matrix S^{-1} is also positive semi-definite. Hence it is possible to apply the Cholesky decomposition to S^{-1} in order to remove correlations. This means that S^{-1} can be written as follows:

$$S^{-1} = M^T M \tag{7.13}$$

where, the matrix M is lower triangular, which can be used to normalize the innovation.

Finally, the normalized innovation used to identify the fault is:

$$\tilde{\gamma} = M\gamma \tag{7.14}$$

$\tilde{\gamma}$ is a vector of size $2m \times 1$ with m the number of visible satellite. The first m terms in $\tilde{\gamma}$ represent the normalized innovations of pseudorange measurements and the last m terms represent that of the Doppler measurements.

[2] in the following text, the sub-index k, which represents the epoch number, will be omitted for the purpose of simplicity.

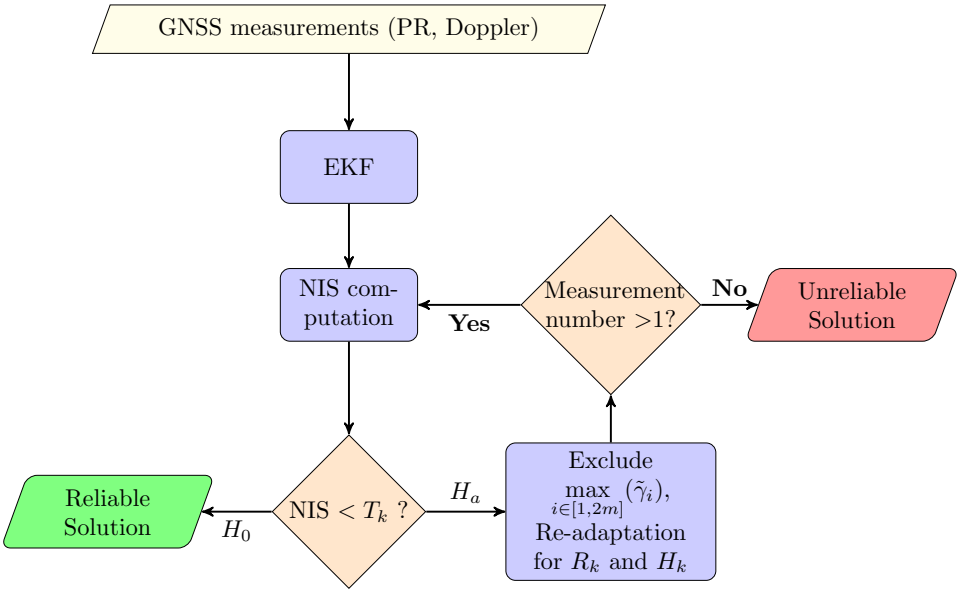

Figure 7.4 – Flowchart of the Innovation-based Classic Test (IBCT)

Fig. 7.4 presents the flowchart of the Innovation-based Classic Test (IBCT). Once a fault is detected by the initial Global Test, the measurement with the biggest normalized innovation will be excluded. This procedure can be repeated several times in a loop until there is no fault detected or there is no longer redundancy existing to continue the fault isolation. In the latter case, the estimated position will be flagged as unreliable.

7.1.3.2 Innovation-based Danish (IBDAN) Re-weighting Scheme

Danish method aims at providing consistency among measurements by re-weighting the measurement variances. In the literature, it is often used with the Least Squares (LS) solver or its variance Weighted Least Squares (WLS). Here, we proposed to adapt this method in the context of the innovation-based integrity monitoring scheme. A flowchart of the Innovation-based Danish (IBDAN) re-weighting scheme is shown in Fig. 7.5.

If a fault is detected during the jth iteration, the Danish method will firstly calculate the normalized innovation vector $\tilde{\gamma}$ as in Eq. (7.14). At the same time, a local threshold th is also calculated in the same way as the snapshot approach, which is described in Section 3.5.1.2. Then the re-weighting approach will be applied on the measurement error covariance matrix R in this way:

$$\sigma^2_{i,j+1} = \sigma^2_{i,0} \cdot \begin{cases} e^{\frac{\tilde{\gamma}_{i,j}}{th}}, & \text{if } \tilde{\gamma}_{i,j} > th \\ 1, & \text{if } \tilde{\gamma}_{i,j} < th \end{cases} \tag{7.15}$$

where, $\sigma^2_{i,0}$ represents the *a priori* error variance of the ith measurement during the jth

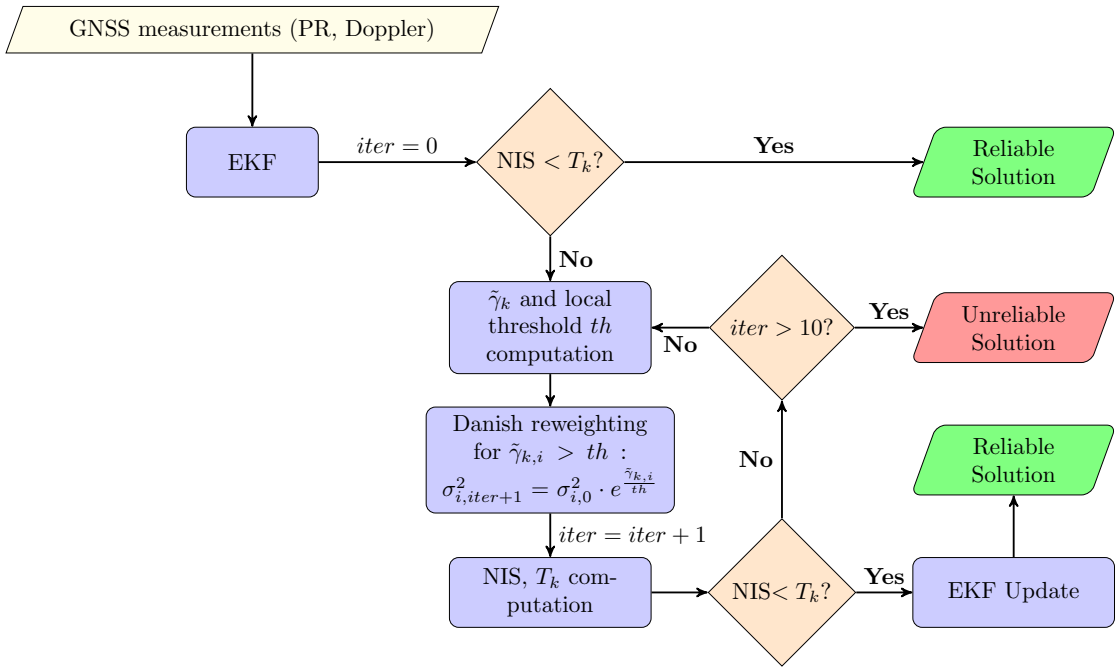

Figure 7.5 – Flowchart of the Innovation-based Danish method

iteration and the $\sigma^2_{i,j+1}$ represents the re-weighted error variance for the ith measurement in the $(j+1)$th iteration.

This re-weighted measurement error covariance matrix R will be involved in the computation of the innovation covariance matrix S as in Eq. (7.8). So a new Normalized Innovation Squared (NIS) and a new threshold can be calculated in order to realize a new Global Test (GT). In the case that GT succeeds, the EKF update procedure will be conducted by taking into consideration the re-weighted measurement error covariance matrix R.

7.1.4 EKF Innovation-Based HPL

7.1.4.1 Derivation of the Innovation-based HPL

A large body of research work contributes to the computation of the HPL for the snapshot residual-based integrity monitoring algorithm [18, 73–75, 83] while very few papers can be found dealing with the EKF innovation-based HPL [172, 173, 176].

Similar with the residual-based snapshot integrity monitoring approach, the EKF innovation-based HPL can also take the slope-based form [74, 83] as described in Chapter 6:

$$HPL = \max_i (Hslope_i \sigma_i)\sqrt{p_{bias}} + K(P_{md}) d_{major} \tag{7.16}$$

where,

- $Hslope_i$ represents the sensitivity of HPE to a bias of i^{th} satellite;
- σ_i denotes the standard deviation of the i^{th} measurement error;
- p_{bias} represents the bias in the space of test statistic, which can take the following values according to how much conservative one will be:
  * The Test Threshold T_k;
  * The non centrality parameter λ_k;
  * The Normalized Innovation Squared (NIS).
- $K(P_{md})$ is an inflation factor in order to meet specified integrity risk;
- d_{major} denotes the position error uncertainty along the semi-major axis of the error ellipse.

In the case of EKF, the d_{major} can be deduced with the help of the estimated state variance matrix P:

$$d_{major} = \sqrt{P_{ee} + P_{nn}} \tag{7.17}$$

where, P_{ee} and P_{nn} are respectively the position variances in the East and North directions.

Now we will make the derivation of the $Hslope$ for EKF innovation-based integrity monitoring. According to [173], the failure-mode slope ρ_k^2 can be formulated as:

$$\rho_k^2 = \frac{\mathbb{E}[\varepsilon_k]^2}{\lambda_k^2} \tag{7.18}$$

where, ε_k denotes the error between state vector estimation and the true value at the instant k, i.e., $\varepsilon_k = \hat{x}_k - x_k$.

Keeping the same notions as in Section 2.4.2 of Chapter 2 where addresses the EKF principles, the measurement model can be written as:

$$z_k = H_k x_k + v_k \tag{7.19}$$

with v_k the measurement noise. If we substitute the measurement z_k into the following EKF state update equation:

$$\hat{x}_k = \hat{x}_k^- + K_k(z_k - H_k\hat{x}_k^-) \tag{7.20}$$

We have:

$$\hat{x}_k = \hat{x}_k^- + K_k(H_k x_k + v_k - H_k\hat{x}_k^-) \tag{7.21}$$

Then, with the help of the EKF state prediction equation, Eq. (7.21) can be written as:

$$\hat{x}_k = K_k^{'} F\hat{x}_{k-1} + K_k H_k x_k + K_k v_k \tag{7.22}$$

where, $K_k^{'} = I - K_k H_k$.

If we subtract x_k at two sides of Eq. (7.22), and substitute Eq. (7.3) into it at the same time, the following expression can be obtained:

$$\varepsilon_k = K_k^{'} F \varepsilon_{k-1} + K_k v_k - K_k^{'} w_{k-1} \tag{7.23}$$

So that,

$$\mathbb{E}[\varepsilon_k] = K_k^{'} F \mathbb{E}[\varepsilon_{k-1}] + K_k \mathbb{E}[v_k] \tag{7.24}$$

since the process model noise w_k is supposed to be zero-mean, i.e., $\mathbb{E}[w_k] = 0$.

Assuming there is no prior fault, i.e., all the faults at the previous epochs are instantaneously detected and correctly excluded, we have:

$$\mathbb{E}[\varepsilon_{k-1}] = 0 \tag{7.25}$$

So under faulty conditions, we have $\mathbb{E}[v_k] = f_k$, with f_k the fault profile vector, thus:

$$\mathbb{E}[\varepsilon_k] = K_k f_k \tag{7.26}$$

Concerning the denominator of the slope term ρ_k^2, the non-centrality parameter λ_k^2 can be written as:

$$\lambda_k^2 = \mathbb{E}[\gamma_k^T] S_k^{-1} \mathbb{E}[\gamma_k] \tag{7.27}$$

Similarly, with the help of the EKF state prediction equation, Eq. (7.3) and Eq. (7.19), the innovation can be written as:

$$\begin{aligned} \gamma_k &= z_k - H_k \hat{x}_k^- \\ &= -H_k F \varepsilon_{k-1} + H_k w_{k-1} + v_k \end{aligned} \tag{7.28}$$

So,

$$\mathbb{E}[\gamma_k] = -H_k F \mathbb{E}[\varepsilon_{k-1}] + H_k \mathbb{E}[w_{k-1}] + \mathbb{E}[v_k] \tag{7.29}$$

Thus, under fault conditions and without prior fault, we have:

$$\mathbb{E}[\gamma_k] = f_k \tag{7.30}$$

Finally, the $Hslope_{k,i}$ at the instance k for the i^{th} measurement can be derived as [176]:

$$\begin{aligned} Hslope_{k,i} &= \sqrt{\frac{\mathbb{E}[\varepsilon_{e,k}]^2 + \mathbb{E}[\varepsilon_{n,k}]^2}{\mathbb{E}[\gamma_k^T] S_k^{-1} \mathbb{E}[\gamma_k]}} \\ &= \sqrt{\frac{f_i^T K_k^T \tau_e^T \tau_e K_k f_i + f_i^T K_k^T \tau_n^T \tau_n K_k f_i}{f_i^T S_k^{-1} f_i}} \end{aligned} \tag{7.31}$$

where, τ is a vector allowing to select the desired state from the full state vector and f_i is a fault profile vector containing zeros except for the corresponding satellite under evaluation.

7.1.4.2 Discussion about the Innovation-based Hslope

In this research work, the main differences between the implemented Extended Kalman Filter (EKF) and the Weighted Least Squares (WLS) are the involvement of the system dynamic model and the measurements of Doppler. Let us take a look at the impacts of these differences on the *Hslope*.

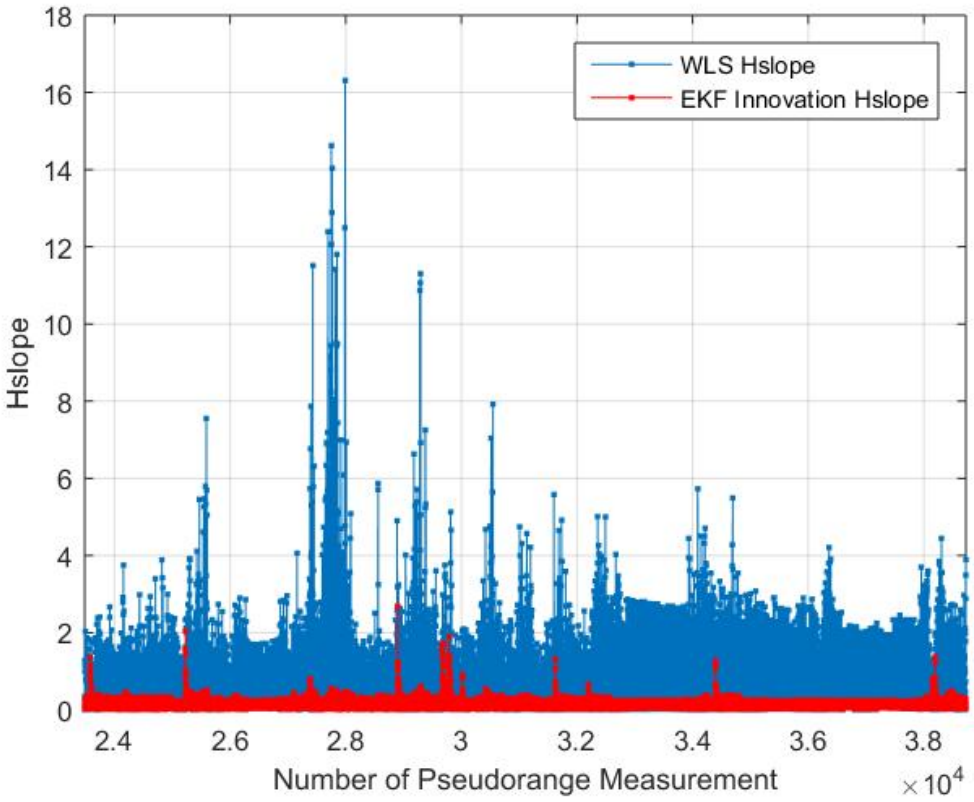

Figure 7.6 – A comparison of snapshot WLS residual-based *Hslope* and the EKF innovation-based *Hslope* (Nantes Center Dataset)

Fig. 7.6 shows the *Hslope* calculated respectively by the snapshot residual-based approach (blue curve) and the sequential innovation-based approach (red curve). The latter is calculated according to Eq. (7.31). The measurement error variance model used for both two approaches is the C/N_0-based model.

What can be observed is that the EKF sequential innovation-based *Hslopes* are generally much smaller than the WLS residual-based *Hslopes*. This means, theoretically, given the same size of bias, the EKF innovation-based approach yields a smaller position error than the snapshot residual-based approach. At the same time, for a same level of HPE, the EKF innovation-based approach can provide a larger test statistic which makes the fault easier to

be detected.

Recall that, however, the assumption of no prior fault is made for this innovation-based slope in Eq. (7.31). This means, if the prior faults are all correctly detected and excluded, the theoretical advantages of the innovation-based HPL mentioned in the previous paragraph can be true. Otherwise, if the prior faults remain, because of the sequential feature of the EKF, this innovation-based HPL can lead to a high P_{mi} due to its non sufficient size. This will be proved with our real dataset in the next section.

7.1.4.3 A Proposed Innovation-based HPL Computation

The analysis in the previous section shows the potential risk of non sufficient HPL size by taking into account the non prior fault assumption. As a result, a compromise should be found between the optimal assumption [176], i.e., non prior fault assumption, and the worst-case assumption [172], i.e., all the history fault exist. The optimal assumption can possibly lead to too small HPLs since one or several prior faults, which are not detected or excluded instantaneously, can impact the estimation of current epoch. The worst-case assumption can potentially lead to too huge HPLs since all the historical faults are considered. This latter one is used to find the worst case fault of spoofing attacks in [172].

Motivated and inspired by this analysis, we propose here a new innovation-based HPL, especially a new *Hslope* computation, by taking into consideration the fault of the last epoch. That is to say, if a fault was detected at the last epoch, the *Hslope* in the HPL will be computed according to the following proposed method. Otherwise, the assumption of no prior fault will be made so that Eq. (7.31) will be used.

Begin from the following slope expression in Eq. (7.18):

$$\rho_k^2 = \frac{\mathbb{E}[\varepsilon_k]^2}{\lambda_k^2}$$

In Section 7.1.4.1, what have been have already obtained under faulty cases are:

$$\begin{aligned} \mathbb{E}[\varepsilon_k] &= K_k^{'} F \mathbb{E}[\varepsilon_{k-1}] + K_k \mathbb{E}[v_k] \\ &= K_k^{'} F \mathbb{E}[\varepsilon_{k-1}] + K_k f_k \\ &= K_k^{''} \mathbb{E}[\varepsilon_{k-1}] + K_k f_k \end{aligned} \tag{7.32}$$

where, $K_k^{''} = K_k^{'} F$.

and,

$$\begin{aligned} \mathbb{E}[\gamma_k] &= -H_k F \mathbb{E}[\varepsilon_{k-1}] + H_k \mathbb{E}[w_{k-1}] + \mathbb{E}[v_k] \\ &= -H_k F \mathbb{E}[\varepsilon_{k-1}] + f_k \end{aligned} \tag{7.33}$$

Only the fault of the last epoch, i.e., $(k-1)$th epoch, will be taken into account. As a result, a particular solution to Eq. (7.32) as a function of fault profile of the two epochs $f_{k-1|k}$ can be written as:

$$\begin{aligned}\mathbb{E}[\varepsilon_k] =& \underbrace{\begin{bmatrix} K_k'' K_{k-1} & K_k \end{bmatrix}}_{A_k} \underbrace{\begin{bmatrix} f_{k-1} \\ f_k \end{bmatrix}}_{f_{k-1|k}} \\ =& A_k f_{k-1|k}\end{aligned} \tag{7.34}$$

Substituting Eq. (7.34) into Eq. (7.33), the following expression can be obtained:

$$\begin{aligned}\mathbb{E}[\gamma_k] =& - H_k F K_{k-1} f_{k-1} + f_k \\ =& \underbrace{\begin{bmatrix} -H_k F K_{k-1} & I \end{bmatrix}}_{B_k} \underbrace{\begin{bmatrix} f_{k-1} \\ f_k \end{bmatrix}}_{f_{k-1|k}} \\ =& B_k f_{k-1|k}\end{aligned} \tag{7.35}$$

As a result, the proposed *Hslope*, denoted as $Hslope^{+}_{k,i}$ at the instance k for the i^{th} measurement can be derived as:

$$\begin{aligned}Hslope^{+}_{k,i} &= \sqrt{\frac{\mathbb{E}[\varepsilon_{e,k}]^2 + \mathbb{E}[\varepsilon_{n,k}]^2}{\mathbb{E}[\gamma_k^T] S_k^{-1} \mathbb{E}[\gamma_k]}} \\ &= \sqrt{\frac{f^T_{(k-1|k),i} A_k^T \tau_e^T \tau_e A_k f_{(k-1|k),i} + f^T_{(k-1|k),i} A_k^T \tau_n^T \tau_n A_k f_{(k-1|k),i}}{f^T_{(k-1|k),i} B_k^T S_k^{-1} B_k f_{(k-1|k),i}}}\end{aligned} \tag{7.36}$$

where, τ is a vector allowing to select the desired state from the full state vector and $f_{(k-1|k),i}$ a fault profile vector containing zeros except for the ith satellite under evaluation.

In summary, the proposed innovation-based HPL at instant k will be computed in this way:

$$\begin{aligned}HPL =& K(P_{md}) \sqrt{P_{ee} + P_{nn}} \\ &+ \sqrt{\lambda_k^2} \cdot \begin{cases} \max\limits_i (Hslope_{k,i} \sigma_i), & \text{if no fault detected at } (k-1)\text{th epoch} \\ \max\limits_i (Hslope^{+}_{k,i} \sigma_i), & \text{if fault detected at } (k-1)\text{th epoch} \end{cases}\end{aligned} \tag{7.37}$$

The non-centrality term is chosen here in the expression of the HPL for purpose of conservative due to the analysis made in Section 7.1.4.2.

7.2 Test Results and Performance Analysis

Similarly with the Chapter 6, the following performances of the proposed sequential innovation-based integrity monitoring scheme (Extended Kalman Filter (EKF) + Fault Detection and

Exclusion (FDE)) will be evaluated in this section:

- Horizontal positioning accuracy;
- The size of the HPL. The following two HPL are implemented for comparison:
  * The one under the assumption of no prior fault:

$$HPL1 = \max_i(Hslope_i\sigma_i)\sqrt{\lambda_k^2} + K(P_{md})\sqrt{P_{ee}+P_{nn}} \tag{7.38}$$

  * The proposed one:

$$\begin{aligned} HPL2 =& K(P_{md})\sqrt{P_{ee}+P_{nn}} \\ &+\sqrt{\lambda_k^2}\cdot\begin{cases} \max_i(Hslope_{k,i}\sigma_i), & \text{if no fault detected at } (k-1)\text{th epoch} \\ \max_i(Hslope^+_{k,i}\sigma_i), & \text{if fault detected at } (k-1)\text{th epoch} \end{cases} \end{aligned} \tag{7.39}$$

- The probability of misleading information P_{mi};
- The Ratio of Reliable Positions (RRP) declared by the complete system.

Here, we also fix $P_{fa} = P_{md} = 10^{-2}$, which are the same as in Chapter 6.

A special detection for the receiver clock jump phenomenon, which occurs usually in the low-cost receivers, is added in order to deal with the potential EKF divergence. Once a clock jump is detected, the EKF will be reset. In this case, the estimated positions will also be considered as unreliable.

7.2.1 Results with Nantes Center Dataset

The Nantes center dataset (17903 epochs) will be used in this section to evaluate the EKF innovation-based integrity monitoring system.

First of all, in order to prove the benefit of Weighted Extended Kalman Filter (WEKF), a classic EKF with time-invariant measurement error covariance matrix R is also implemented, in which $\sigma_{\text{pseudorange}} = 8\text{m}$ and $\sigma_{\text{Doppler}} = 2\text{m/s}$.

Fig. 7.7 shows the Cumulative Distribution Function (CDF) curves with the six solvers in two classes of approaches (without FDE applied): the dashed lines are with the snapshot approach (the Ordinary Least Squares (OLS), the Weighted Least Squares (WLS) with the C/N_0-based model and the WLS with the Hybrid UMM model) and the solid lines are with the sequential EKF approach (the EKF with fixed R, the WEKF with C/N_0-based model and WEKF with the Hybrid UMM model). Table 7.3 summarizes the statistical performance of accuracy.

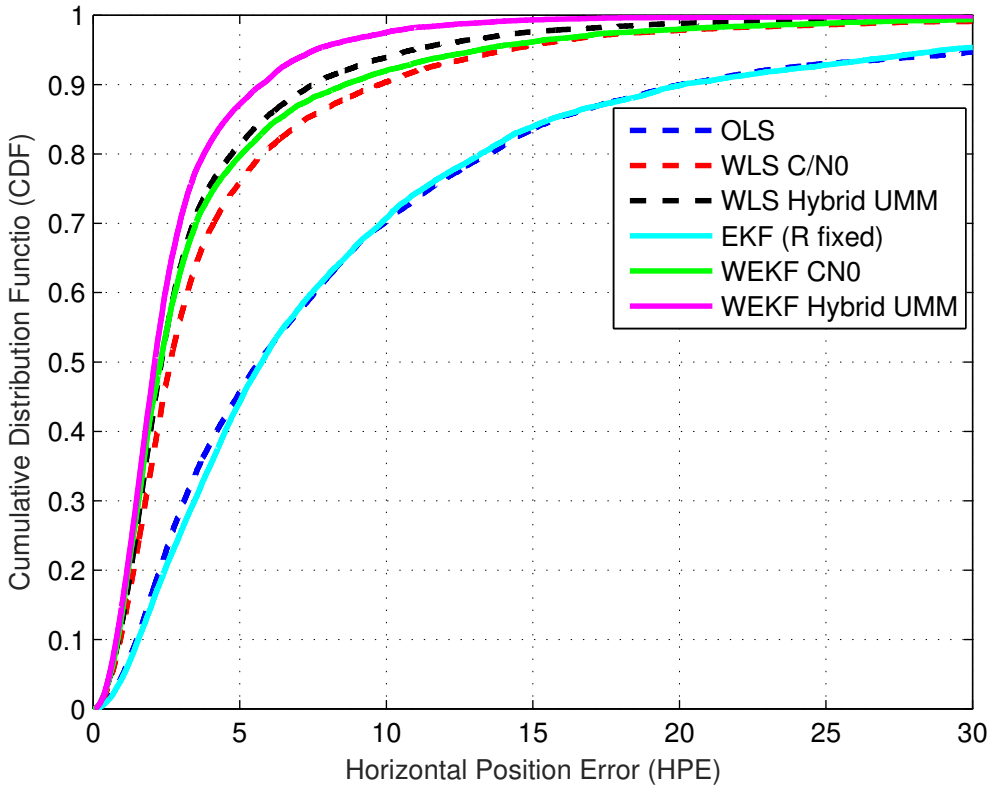

Figure 7.7 – HPE Comparison with the Six Solvers without FDE (Nantes Center Dataset)

Table 7.3 – Summary of Accuracy with Six Solvers no FDE Applied (Nantes Center)

Estimator Type		**Accuracy: HPE (m)**		
		50%	***75%***	***95%***
OLS		5.66	11.51	30.70
EKF		5.76	11.26	29.21
WLS	C/N_0	2.64	4.84	13.78
	Hybrid UMM	2.32	3.87	10.83
WEKF	C/N_0	2.30	4.13	13.21
	Hybrid UMM	2.09	3.29	7.54

The accuracy with the OLS and the classic EKF is almost at the same level. They are both much worse than the weighted solvers. This proves the advantages of implementing the weighting models. Concerning the two weighting models, the accuracy with the Hybrid UMM model is better than the C/N_0-based model both in snapshot approach and sequential approach. The median HPE can achieve 2.09 m with the WEKF Hybrid UMM estimator, which improves 63% compared to the OLS estimator. In terms of the two classes of approaches,

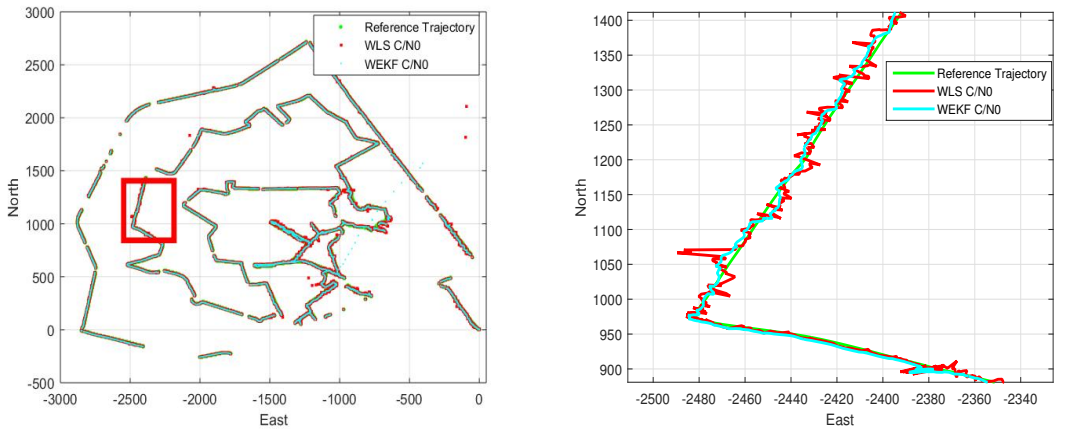

(a) Complet Trajectories (b) Zoomed Trajectories of the red squared zone

Figure 7.8 – Smoother trajectory by the filtering effects (Nantes Center Dataset)

the EKF sequential one is better than the snapshot one thanks to the involvement of system dynamic model. This effect is more obvious between the WEKF and the WLS.

The fact that the sequential approach performs better than the snapshot approach is mainly due to the presence of the dynamic model and the filtering effects which make the estimated trajectory smoother than the one with the snapshot approach. This effect can be observed more clearly in Fig. 7.8. Fig. 7.8(b) shows the zoomed trajectories in the red squared zone of the Fig. 7.8(a). The estimated trajectories are obtained respectively by the WLS and WEKF with the C/N_0-based weighting model. The trajectory with the WEKF is much smoother than the one with the WLS, which produces the accuracy gain.

Table 7.4 – Performances Summary for $\boldsymbol{C/N_0}$**-based** WEKF with FDE (Nantes Center)

FDE	**Accuracy**				**Integrity**				
	HPE (m)				**50% HPL (m)**		P_{mi}(%)		**RRP**
Type	***50%***	***mean***	***95%***	***std***	***HPL1***	***HPL2***	P_1	P_2	(%)
None	2.32	4.44	13.21	20.42	12.76	–	1.71	–	99.99
IBCT	2.32	3.40	9.89	3.78	10.79	11.49	0.98	0.49	99.99
IBDAN	2.31	3.28	9.39	3.45	11.12	11.41	0.45	0.44	96.69

Then, the FDE techniques, i.e., the Innovation-based Classic Test (IBCT) and the Innovation-based Danish (IBDAN) re-weighting method, will be applied on the WEKF estimator with the two error models, i.e., the C/N_0-based model and the Hybrid UMM model. Table 7.4 and Table 7.5 summarize the accuracy and the integrity performance of the complete EKF innovation-based integrity monitoring system. What should be mentioned is that, the HPL

Table 7.5 – Performances Summary for **Hybrid UMM** WEKF with FDE (Nantes Center)

FDE	Accuracy HPE (m)				Integrity 50% HPL (m)		P_{mi}(%)		RRP
Type	***50%***	***mean***	***95%***	***std***	***HPL1***	***HPL2***	P_1	P_2	(%)
None	2.09	2.81	7.54	2.61	8.28	–	1.03	–	99.99
IBCT	2.09	2.77	7.26	2.54	8.30	8.39	0.74	0.53	99.99
IBDAN	2.08	2.78	7.19	2.74	8.35	8.40	0.62	0.51	99.18

is calculated with the two methods described at the beginning of this section in Eq. (7.38), i.e., without prior faults, and Eq. (7.39), i.e., with prior fault of the last epoch, for purpose of comparison. The proposed one, i.e., HPL2, is only computed when the FDE techniques are applied due to its designed feature.

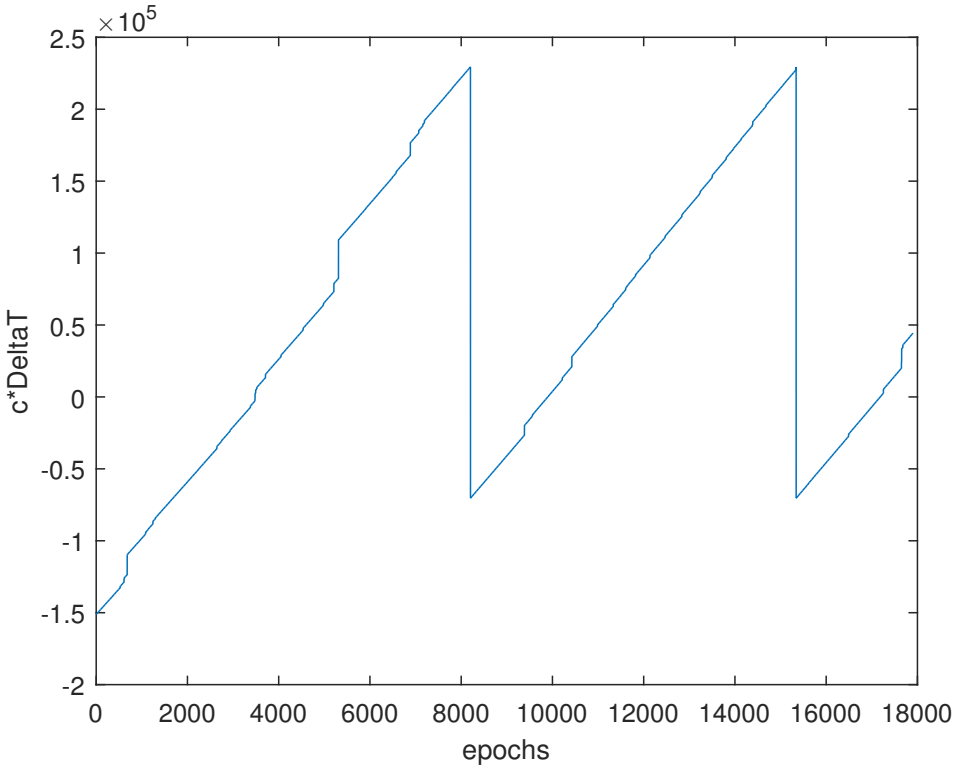

Figure 7.9 – Receiver Clock Jump (Nantes Center Dataset)

Generally speaking, the global performance of accuracy and integrity with the WEKF innovation-based integrity monitoring scheme are better than the snapshot residual based approach. This is because the sizes of HPE and HPL are both reduced. There is an augmentation of P_{mi}, which can be guaranteed however under 2%. Moreover, thanks to the redundancy gain of the EKF sequential approach, the FDE is more available since the Ratio of Reliable Posi-

tions (RRP) declared by the system is higher than the snapshot approach. This can be an advantage especially in face of the poor satellite visibility in urban canyons. The RRP of the WEKF with the two error models without FDE both achieve 99.99%. The lack of 0.01% is due to the detection of the clock jump (2 epochs) as shown in Fig. 7.9.

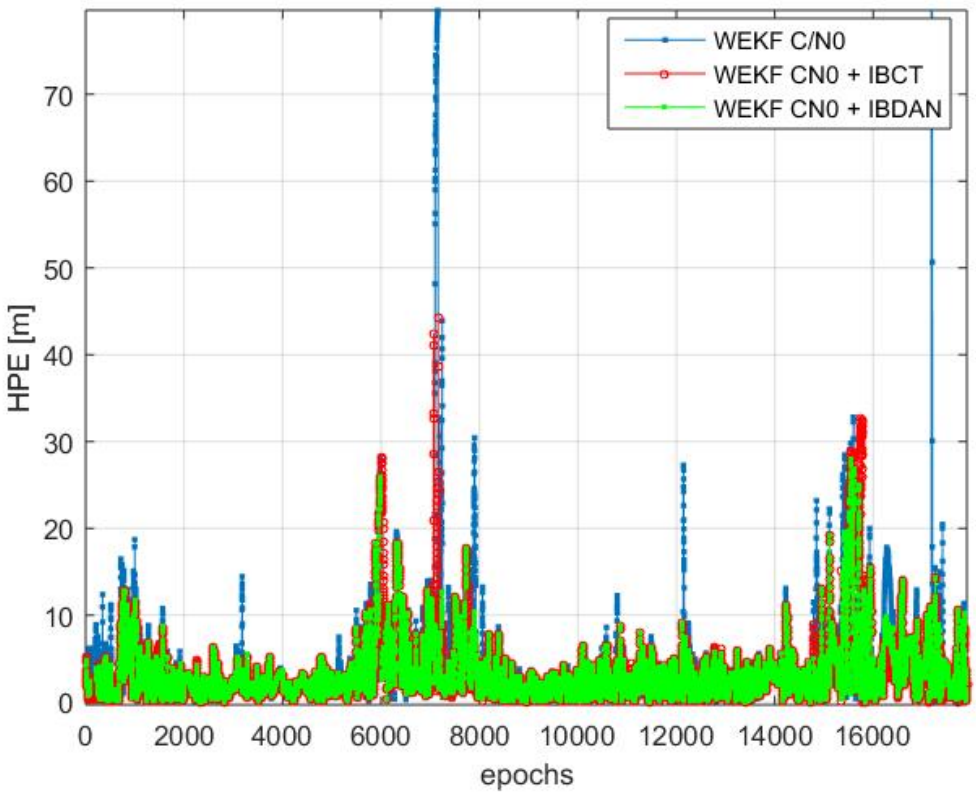

Figure 7.10 – Horizontal Position Error (HPE) Comparison Before vs After Applying FDE techniques on WEKF with C/N_0 model (Nantes Center Dataset)

Concerning the C/N_0-based WEKF, the improvement of accuracy by the two FDE techniques is obvious. Especially with the IBDAN re-weighting method, the high-quantile errors are effectively removed, for example, the 90% accuracy is reduced from 13.21 m to 9.39 m and the standard deviation is reduced from 20.42 m to 3.45 m. Fig. 7.10 shows the HPE with only WEKF C/N_0 solver and this one applied with the two FDE techniques, i.e., IBCT and IBDAN. The huge errors are reduced especially at the time intervals of [0,2000], [6000,8000], as well as [14000,17000].

The median sizes of both HPLs for both FDE techniques vary around 10 m$\sim$13 m and the P_{mi} varies from 0.44% to 1.71%. What should be highlighted is that, the proposed HPL, i.e., HPL2, performs better than the HPL1 especially with the IBCT: with an increase of median HPL by less than 1 m, the P_{mi} is reduced by 50%. Fig. 7.11 shows the Stanford diagrams of

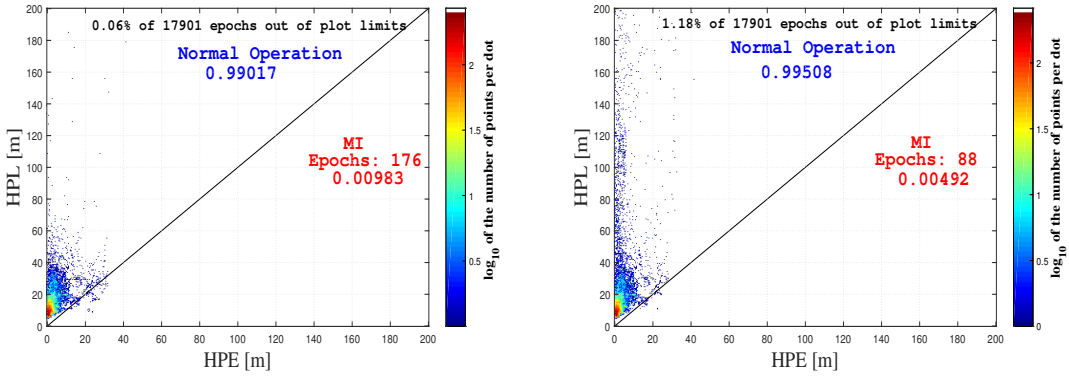

(a) HPL1

(b) HPL2

Figure 7.11 – Stanford Diagram of WEKF C/N_0 + IBCT (Nantes Center Dataset)

the WEKF C/N_0 with IBCT. The HPL is calculated respectively with HPL1 (Fig. 7.11(a)) and HPL2 (Fig. 7.11(b)). HPL2 is more conservative compared to the HPL1 since its size is bigger but produces significantly lower P_{mi}. As a result, when choosing the method of HPL, a compromise should be found between the size and the ratio of P_{mi} according to the targeted applications.

The IBDAN can provide better integrity performances with the Hybrid UMM WEKF than the IBCT except its RRP is slightly lower.

In terms of the Hybrid UMM WEKF, its global performance is still better than the C/N_0-based approach as shown in Table 7.5. Compared to the C/N_0-based model analyzed in the previous text, its accuracy is better and the size of HPL is smaller with generally lower ratios of P_{mi}, which proves a better error bounding capability. Concerning the proposed HPL2, similar conclusions as in C/N_0-based approach can be drawn under the framework of WEKF with Hybrid UMM. Fig. 7.12 shows the Stanford diagrams of the WEKF Hybrid UMM with the IBCT. The HPL is calculated respectively with HPL1 (Fig. 7.12(a)) and HPL2 (Fig. 7.12(b)).

For the Hybrid UMM based WEKF, the accuracy improvement by the FDE techniques is not so obvious as in the C/N_0-based WEKF. This is because, firstly, the pseudorange errors are already corrected at a first level by the UMM model based on the geometry of the digital map. Secondly, the number of epochs where faults are detected is more in the C/N_0-based WEKF than in the Hybrid UMM-based WEKF. Table 7.6 reports the situation of initial Global Test (GT) failures by the two weighting models. As shown in Table 7.6, the measurements possess more consistency with the Hybrid UMM WEKF so that only 2.66% of epochs are detected with faults thanks to the range error corrections by the UMM. This ratio is higher in C/N_0-based WEKF, i.e., 9.35%.

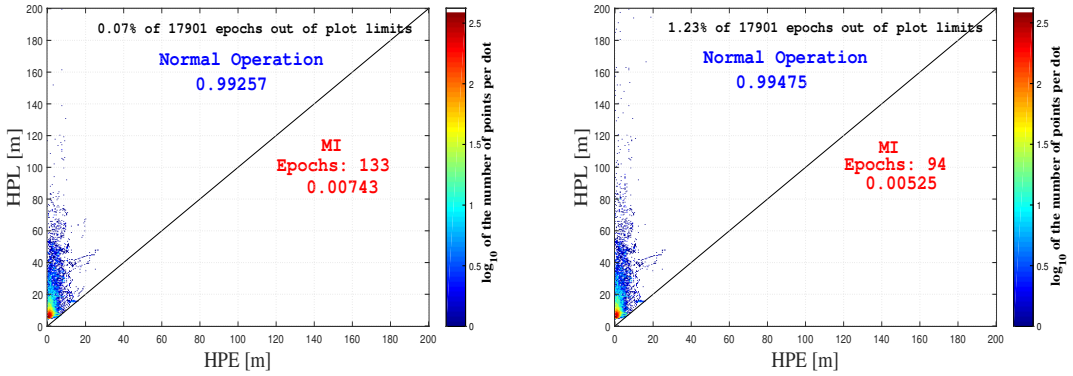

(a) HPL1 (b) HPL2

Figure 7.12 – Stanford Diagram of WEKF Hybrid UMM + IBCT (Nantes Center Dataset)

Table 7.6 – Test Situation Summary (Nantes Center Dataset)

Test Situation	C/N_0 **WEKF**		**Hybrid UMM WEKF**	
	Number of Epochs	***(%)***	***Number of Epochs***	***(%)***
Initial GT failure	1674	9.35	476	2.66

Moreover, among these epochs where the initial GT fails, the number of excluded measurements (pseudorange measurements or Doppler measurements) in C/N_0-based approach is more than that of the Hybrid UMM WEKF. Fig. 7.13 shows a comparison of the number of excluded measurements by IBCT with respectively C/N_0-based WEKF and the Hybrid UMM-based WEKF. For the Hybrid UMM-based WEKF, the IBCT excludes 3 measurements maximum but for the C/N_0-based WEKF, the maximum number of excluded measurements reaches 10.

7.2.2 Results with the Total Dataset

In this section, the complete EKF Innovation-based integrity monitoring scheme will be evaluated with the total dataset described in Section 5.1, in which the total number of epoch is 163503 (near 9h).

Table 7.7 – Test Situation Summary (Total Data)

Test Situation	C/N_0 **WEKF**		**Hybrid UMM WEKF**	
	Number of Epochs	***(%)***	***Number of Epochs***	***(%)***
Initial GT failure	28394	17.37	15237	9.32

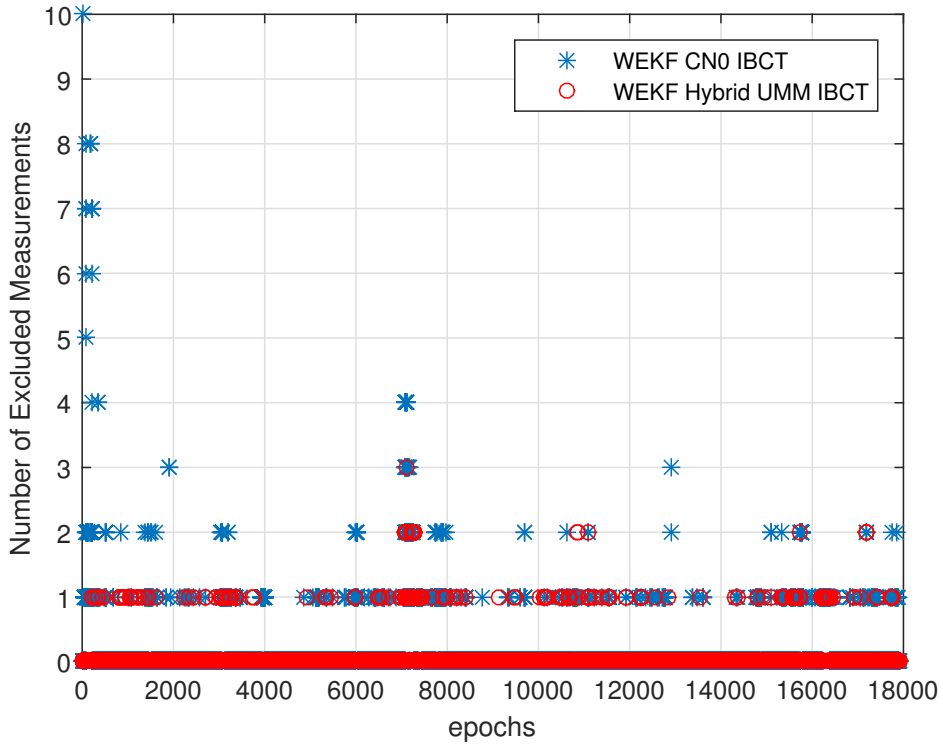

Figure 7.13 – Number of Excluded Measurements (Nantes Center Dataset)

Table 7.7 summarizes the number of the initial Global Test (GT) failure respectively in the framework of the two Weighted Extended Kalman Filter (WEKF) schemes with the two weighting models. 17.37% of epochs have the initial GT failure with the C/N_0-based WEKF while this ratio is only 9.32% with the Hybrid UMM WEKF. This means less epochs are involved by the FDE techniques with the Hybrid UMM model because it produces smaller EKF innovations thanks to the range corrections.

Table 7.8 – Performances Summary for $\boldsymbol{C/N_0}$**-based** WEKF with FDE (Total Dataset)

FDE	**Accuracy**			**Integrity**				
	HPE (m)			**50% HPL (m)**		P_{mi}(%)		**RRP**
Type	***50%***	***95%***	***std***	***HPL1***	***HPL2***	P_1	P_2	(%)
None	4.14	20.89	22.95	18.69	–	1.86	–	99.90
IBCT	3.86	19.53	21.66	18.43	20.43	1.71	0.67	99.89
IBDAN	3.67	15.39	20.38	15.59	16.53	1.13	1.02	92.37

Table 7.8 gives a summary about the accuracy and integrity performances of the C/N_0-based WEKF with and without the FDE techniques. The HPLs are calculated respectively with the two methods mentioned at the beginning of this section. If a comparison is made between the

snapshot and sequential approaches without FDE with the C/N_0 model, the accuracy with the WEKF is better. Especially the huge errors are directly removed by filtering since the standard deviation of HPE with the WLS C/N_0 is 9.48 km (in Table 6.5) and here is 22.95 m. The sequential EKF innovation-based approach has tendency to provide tighter HPL bound compared to the snapshot-based approach since the sizes of HPL are smaller and the P_{mi} is generally higher.

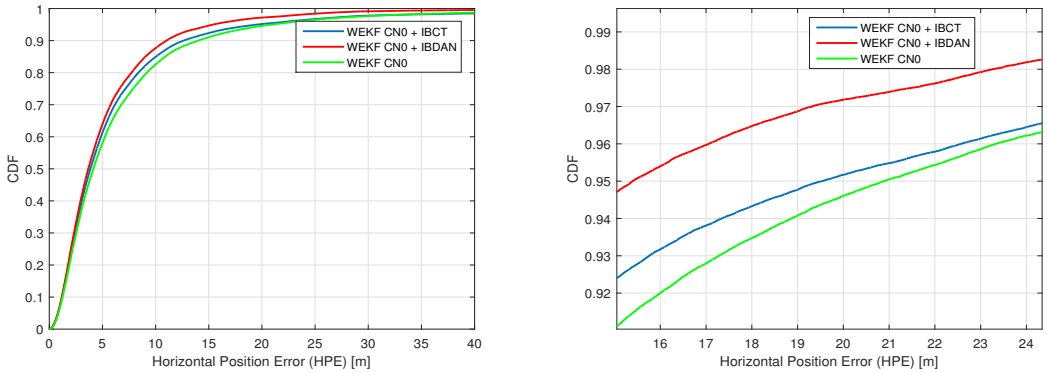

(a) Complet CDF curves

(b) Zoomed CDF curves on 95% accuracy

Figure 7.14 – Cumulative Distribution Function (CDF) of HPE with C/N_0-based WEKF (Total Dataset)

The Innovation-based Danish (IBDAN) re-weighting method performs globally better than the Innovation-based Classic Test (IBCT) in terms of accuracy and error bounding capability. Fig. 7.14 shows the Cumulative Distribution Function (CDF) of the HPE under the context of C/N_0-based WEKF. The best accuracy is obtained with the IBDAN method especially the huge tail errors are effectively removed (e.g., the zoomed CDF curved on 95% accuracy are shown in Fig. 7.14(b)).

But the Ratio of Reliable Positions (RRP) declared by the IBDAN is lower than the IBCT, which is due to difficulties of convergence. But this ratio, i.e., 92.37%, is still higher than the parallel WLS approach with Danish method, i.e., 90.32%, thanks to the redundancy gain of the EKF innovation-based approach.

The proposed HPL2 can better bound the HPE despite of its conservative nature. For example, with IBCT, a gain of 10.85% in median size compared to HPL1 can reduce the P_{mi} by 60.83%. Fig. 7.15 plots the Stanford Diagrams of the C/N_0-based WEKF with the two FDE (i.e., IBCT and IBDAN) and the two HPL computation methods. The HPL1 has a smaller size but a higher P_{mi} and the HPL2 has the opposite features, which are more conservative. A compromise should be made according to the applications when choosing these two HPL computations.

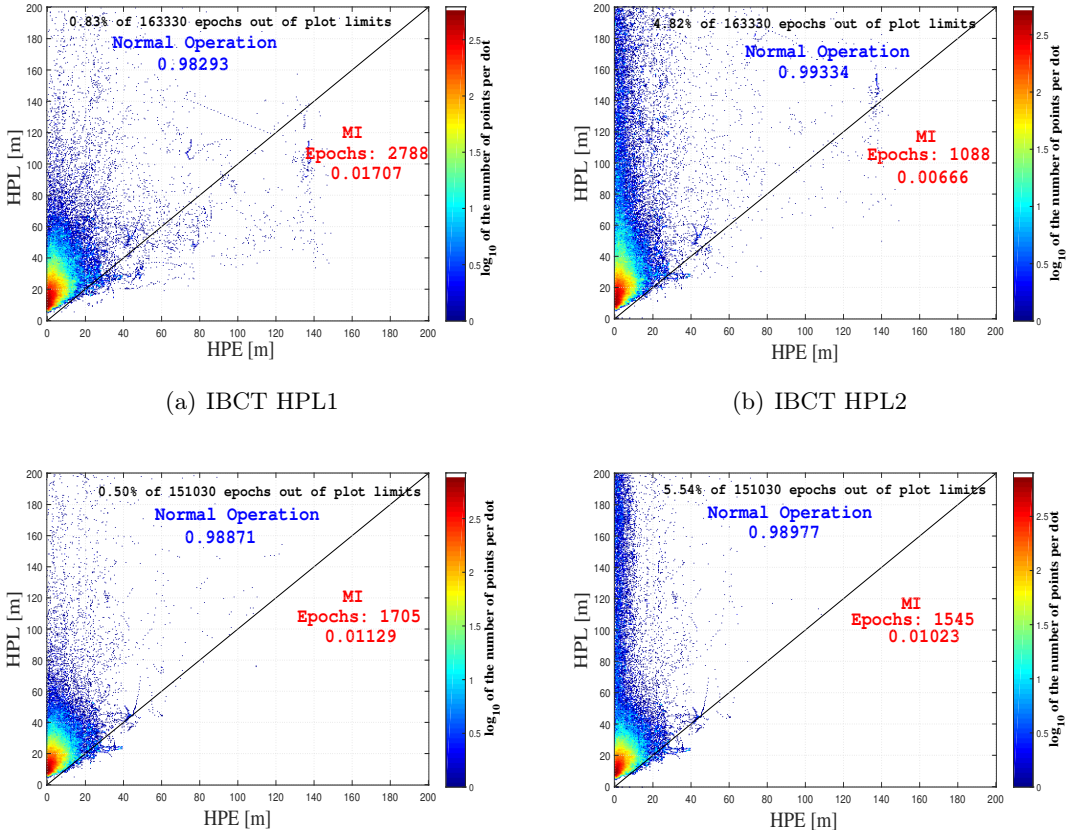

(a) IBCT HPL1

(b) IBCT HPL2

(c) IBDAN HPL1

(d) IBDAN HPL2

Figure 7.15 – Stanford Diagram of WEKF C/N_0 with FDE (Total Dataset)

Table 7.9 – Performances Summary for **Hybrid UMM** WEKF with FDE (Total Dataset)

FDE	**Accuracy**			**Integrity**				
	HPE (m)			**50% HPL (m)**		P_{mi}(%)		**RRP**
Type	***50%***	***95%***	***std***	***HPL1***	***HPL2***	P_1	P_2	(%)
None	3.85	20.71	12.30	19.04	–	2.26	–	99.90
IBCT	3.74	19.96	29.09	19.53	20.95	1.37	0.73	99.89
IBDAN	3.60	16.52	12.21	16.38	17.17	1.55	1.36	95.51

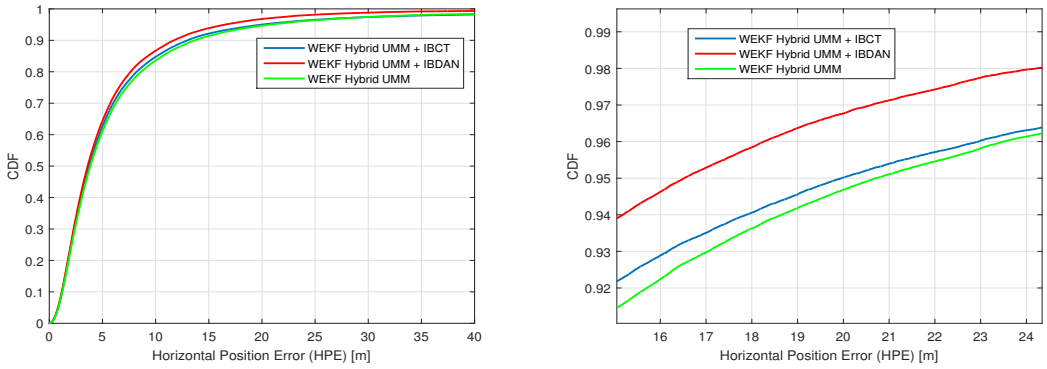

(a) Complet CDF curves

(b) Zoomed CDF curves on 95% accuracy

Figure 7.16 – Cumulative Distribution Function (CDF) of HPE with Hybrid UMM-based WEKF (Total Dataset)

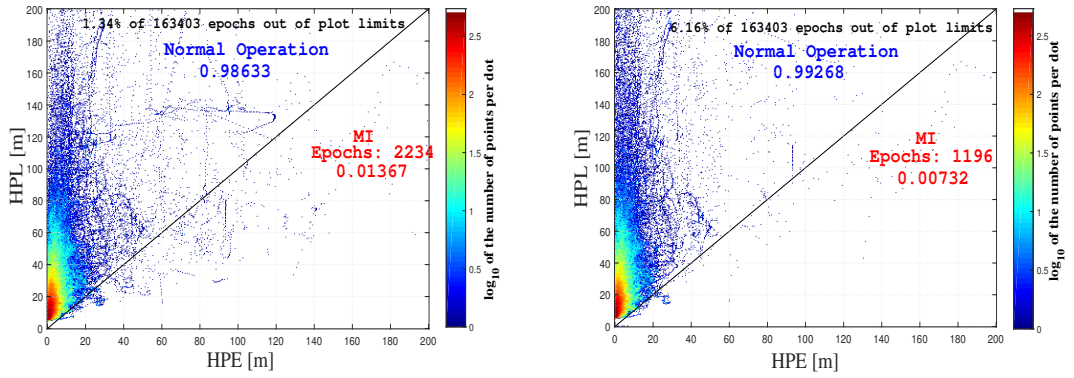

(a) IBCT HPL1

(b) IBCT HPL2

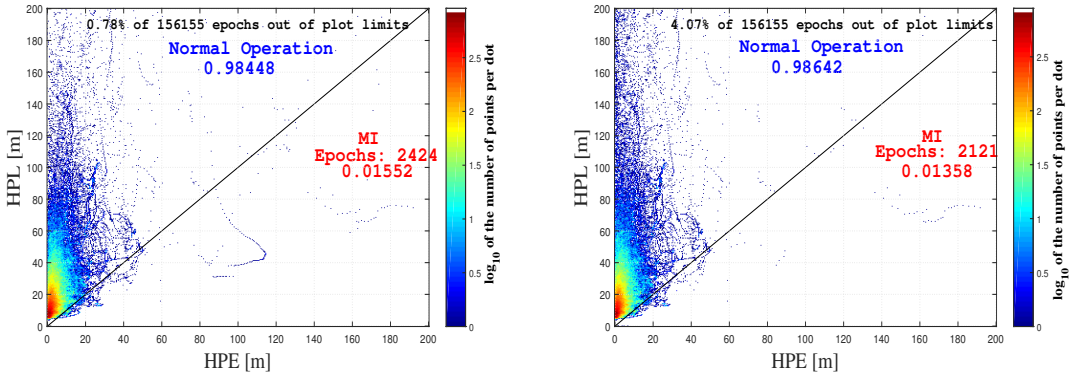

(c) IBDAN HPL1

(d) IBDAN HPL2

Figure 7.17 – Stanford Diagram of WEKF Hybrid UMM with FDE (Total Dataset)

Concerning the Hybrid UMM-based WEKF, Table 7.9 makes a summary about the accuracy and integrity performances and Fig. 7.16 shows the corresponding CDF curves. Fig. 7.16 proves that the global accuracy performance can be improved by both of the two FDE especially the IBDAN re-weighting method.

Concerning the two HPL computation methods, similar conclusions can be drawn as previously with C/N_0-based model. Fig. 7.17 plots the Stanford diagrams with the two FDE and two HPL in the framework of the Hybrid UMM-based WEKF. The proposed HPL2 has a better error bounding capability compared to the HPL1 even though its size is bigger. The RRP declared by IBCT is higher than the parallel method in the snapshot approach. But the RRP declared by IBDAN is slightly lower than this one in the snapshot approach due to difficulties of convergence.

7.3 Conclusion and Discussion

This chapter aims at designing and implementing a complete Extended Kalman Filter (EKF) innovation-based integrity monitoring scheme. The following points concerning some conclusions and discussions can be addressed:

- Firstly, the accuracy with the EKF estimator is globally better than that with the WLS estimator. In particularly, the concept of Weighted Extended Kalman Filter (WEKF) is proposed and tested here by implementing two error models evaluated in the previous chapters (i.e., the C/N_0-based model and the Hybrid Urban Multipath Model (UMM)) into the measurement error covariance matrix of the EKF. The results with the real data collected in urban canyons prove that the accuracy can still be significantly improved by the WEKF compared to the classic EKF.

- Secondly, as a parallel approach with the snapshot residual-based integrity monitoring scheme, the innovation-based scheme has the advantage of redundancy gain thanks to the prediction states. This advantage can be observed obviously with the IBCT. There are no longer unreliable positions due to initial zero redundancy. Receivers can benefit from the redundancy gain especially in face of poor satellite visibility.

- Thirdly, two FDE techniques existing in the snapshot approach are adapted in the sequential innovation-based integrity monitoring approach, i.e., the Innovation-based Classic Test (IBCT) and the Innovation-based Danish (IBDAN) re-weighting method. Of course, other FDE techniques discussed in Chapter 6, such as the Local Test (LT) and the Forward-Backward (FB) Test, are also possible to be adapted into the EKF innovation-based approach. But for EKF, without re-calculation of a new solution after each exclusion, these two approaches cannot provide better performances compared to

the IBCT, which is proved by our preliminary results. This can be a perspective for future research.

- Under the assumption of no prior fault, the EKF innovation-based approach produces lower fault *slopes* compared to the WLS residual-based snapshot approach. This means tighter HPLs can be provided by the EKF-based approach. Theoretically, this means the position errors are less sensitive to the measurement bias and faults are easier to be detected. However, with the results of the real data, the HPL computed under this assumption is not big enough to bound the HPE. As a result, a new method of HPL computation is proposed by taking into consideration the fault of the last epoch. With the results of the real data, the proposed HPL can better bound the position error with a slight augmentation of size.

- Concerning the final performances with the complete EKF innovation-based scheme, it is sophisticated to conclude in one sentence. In terms of the FDE technique, the IBDAN method can provide better accuracy improvement compared to the IBCT with both of the two error models. And the IBDAN can provide tighter HPL compared to the IBCT. But the IBCT possess a lower P_{mi} and a higher Ratio of Reliable Positions (RRP). The choice of the method can be made according to the requirement of the targeted applications. For example, applications requiring high integrity can choose the IBCT while applications requiring high continuity can choose the IBDAN.

Part IV

CONCLUSION

Chapter 8

Conclusions and Perspectives

Contents

Summary

This chapter summarizes the research work conducted in the framework of this PhD Thesis and draws the conclusions from the results obtained from the previous chapters. Some perspectives for future work will also be addressed.

8.1 Conclusions

The research work of this PhD is carried out in the context of an increasing number of the Global Navigation Satellite Systems (GNSS)-based applications in constraint environments. The performances of GNSS can be severely degraded by the local effects, such as the multipath and the Non-Line-of-Sight (NLOS) reception. The main objective of this research is to improve the positioning service quality of a GNSS receiver for the applications in constraint environments. The targeted performances are mainly GNSS positioning accuracy and integrity for low-cost GNSS receivers.

Firstly, an overview on GNSS positioning principles and a survey on GNSS integrity monitoring techniques in urban environments are made. The survey regarding the GNSS integrity monitoring in urban environments corresponds to the author's publication of [45]. Then, the main research work is conducted around two axis: accuracy enhancement and integrity enhancement.

The accuracy enhancement is mainly realized by the use of more realistic error models, which are presented and tested in Chapter 4 and Chapter 5. These error models can reflect the real-time signal quality by taking into consideration different criteria, such as the C/N_0 (carrier-power-to-noise-density ratio), the satellite elevation, the signal reception states LOS/NLOS, etc. Under this axis of work, a new hybrid model is proposed. This model combines the information of C/N_0, the satellite elevations, the signal reception state LOS/NLOS as well as the range corrections. The last two informations are obtained with the help of a *2D+1* map (2D building features with building heights) by geometric approach. A novel model named Urban Multipath Model (UMM) is proposed with a simplified ray-tracing approach, which is an improved version of the existing Urban Trench Model (UTM) [36]. The UMM can distinguish the signal reception state LOS/NLOS and can provide the range corrections for NLOS signals, which are used for the proposed hybrid error model.

Then, all these error models are embedded with the help of a Weighted Least Squares (WLS) estimator, in which, measurements with large errors will contribute low weights to the final position solutions and measurements with small errors will contribute more. The results with real GPS data collected in urban canyons in Chapter 5 show that, among all these error models, the best accuracy is obtained by the Hybrid UMM-based WLS estimator.

The Hybrid UMM-based WLS is not complicated to be implemented once a digital map is integrated in the receiver. But the main constraint is that its performance strongly depends on the map accuracy and availability. The current results with Hybrid UMM can be still improved with a high accurate map while it can be possibly degraded if a low-quality map is used since additional errors will be involved. Moreover, the necessity of updating is also an important issue to be considered.

Except the Hybrid UMM, the C/N_0-based model performs better than all the other error models evaluated in this thesis, as shown in Chapter 5. The main advantage of this model is the easy access of the C/N_0 information. It does not depend on other aiding techniques. However, the model calibration is sophisticated since the two parameters are environment-dependent and receiver-dependent. The parameters used in this research work can be considered as reference values for similar low-cost receivers in urban environments especially for applications required high integrity.

After the accuracy enhancement, the two best error models, i.e., the $C/N0$-based model and the Hybrid UMM, are chosen to help construct the complete integrity monitoring schemes. The integrity monitoring schemes are designed in the framework of two classes of approaches: the snapshot residual-based integrity monitoring and the Extended Kalman Filter (EKF) innovation-based integrity monitoring. These two classes of integrity monitoring methods are presented and evaluated respectively in Chapter 6 and Chapter 7, which are respectively the subjects of the author's publications of [139, 167] and [169, 177].

The snapshot residual-based integrity monitoring scheme designed in Chapter 6 consists of two main modules: an accuracy enhancement module, in which weighting models discussed previously are implemented with a WLS estimator, and an integrity enhancement module. In the integrity enhancement module, following five Fault Detection and Exclusion (FDE) techniques are evaluated for purpose of comparison: the Classic Test (CT), the Subset Test (ST), the iterative Local Test (LT), the Forward-Backward (FB) Test as well as the Danish re-weighting method. Finally, the Horizontal Protection Level (HPL) is calculated and the Probability of Misleading Information P_{mi} is evaluated.

As a result, different combinations of weighting solvers and FDE techniques are tested as in author's publications of [139] and [167]. The results show that huge errors can be removed by most of the FDE techniques so that the GNSS performance reliability is improved. The Hybrid UMM-based WLS estimator with FDE has better global performances than the C/N_0-based WLS with FDE. In particular, the Hybrid UMM WLS with the LT performs the best among all these combinations in terms of positioning accuracy, the size of HPL as well as its error bounding capability. But due to lack of redundancy before or during the FDE, the Ratio of Reliable Positions (RRP) declared by this complete system after LT is only 90.34% with the total dataset (163503 epochs). This situation is hoped to be further improved by the use of multi-constellation or the involvement of other sensors.

In the framework of the EKF innovation-based integrity monitoring presented in Chapter 7, the two error models are implemented in the proposed Weighted Extended Kalman Filter (WEKF) in order to enhance the accuracy at the first level. Here, a classic dynamic model with constant velocity is implemented for the EKF. Results show that, with the help of more realistic error models, the WEKF can effectively provide better accuracy than the classic

EKF, where the measurement errors are considered as invariant. This part of research is partly published in [169].

Then, two of the FDE techniques implemented in the snapshot approach are adapted for the EKF innovation-based approach, i.e., the Innovation-based Classic Test (IBCT) and the Innovation-based Danish (IBDAN) re-weighting method. One important advantage of the innovation-based integrity monitoring is the gain on redundancy thanks to the predicted states. As a result, the FDE availability can be improved especially in face of the poor satellite visibility in dense urban canyon. This feature can be proved by comparing the RRP declared by the IBCT (i.e., 99.89%) and that declared by the CT in the snapshot approach (i.e., 98.17%) with the total dataset. Since the Danish re-weighting method does not exclude measurements, there is no problem of redundancy lack. But difficulties can be found in the procedure of convergence for the Danish re-weighting method, which is the cause of unreliable positions.

Concerning the HPL computation, the innovation-based HPL provides too tight bound under the assumption of no prior fault. Thus, a new method of HPL computation is proposed by taking into account of the fault detected at the last epoch. This choice is a compromise between the HPL size and its error bounding capability. Results show that, this proposed HPL is more conservative since it can better bound the position errors with a slight gain of size compared to the one with the assumption of no prior fault.

The Hybrid UMM-based WEKF integrity monitoring scheme performs better than the one based on C/N_0 in terms of the accuracy and integrity. And the IBDAN method has a global better performance than the IBCT in both of the two weighting EKF in terms of accuracy and HPL size. But the IBCT is able to provide lower P_{mi} and higher availability despite of larger sizes of HPL. The choice of the FDE method can be made according to the requirement of the targeted applications. For example, applications requiring high integrity can choose the IBCT while applications requiring high continuity prefer to choose the IBDAN.

Finally, the comparisons are made between the two parallel integrity monitoring schemes: the snapshot residual-based scheme and the EKF innovation-based scheme, as in author's publication of [177] (which is under review actually). In the framework of the C/N_0-based error model, the EKF innovation-based scheme is globally better than the snapshot residual-based scheme especially in terms of accuracy and availability. But the snapshot-based approach can provide lower P_{mi} with bigger HPL. On the contrary, for the Hybrid UMM-based error model, the best accuracy is obtained with the snapshot WLS solver. The erroneous range corrections made by UMM can induce huger impacts with EKF due to its sequential feature. Thus, the UMM hybridizes better with the snapshot approach. And the overall performance of the Hybrid UMM is still better than the C/N_0-based approach.

8.2 Perspectives

As more and more GNSS constellations will be ready to be operational, such as the European Galileo and the Chinese Beidou, the integrity monitoring techniques studies in this research work can be extended with Multi-Constellation Multi-Frequency (MCMF). With multi-constellations, satellite visibility will be significantly improved in urban environments so that the issue of lack of redundancy for FDE will be solved. If multi-frequency is used, the ionospheric error will be better corrected and the accuracy can still be improved.

Moreover, all the schemes proposed in this research work can also be applied with multiple sensor hybridization, such as the Inertial Navigation System (INS). The hybrid system can breakthrough the drawbacks of the standalone GNSS since the can provide accurate short term measurements with high rate which can be used to interpolate the GNSS measurements and to cover unavailable areas of GNSS. But it will also introduce additional errors and sensor faults.

More realistic dynamic models for system motion can be implemented into the EKF in order to replace the classic one in this research work. If the dynamic model is more coherent with the true system motion, better performance can be expected for both accuracy and integrity.

Other filters, which are more robust in face of measurement outliers, can be used instead of the classic one. For example, the Outlier Robust Kalman Filter (ORKF) proposed in [178, 179] which is able to detect the measurement outliers in real-time. This kind of robust filtering can get rid of the assumption of Gaussian distribution for measurement noises and it can be used especially for non-Gaussian and heavy-tailed noises. Moreover, all the parameters of the ORKF can be learned in a completely unsupervised manner, which much simplifies the calibration procedures compared to the classic EKF.

Concerning the Urban Multipath Model (UMM), better performance can be expected with high accuracy maps. And the Hybrid UMM weighting model will no doubt performs better.

The GNSS integrity monitoring for urban transport applications is a challenging and promising topic. Corresponding integrity specifications for road applications are being finalized. And in the railway sector, where some track-side equipments are envisaged to be replaced by GNSS-based solutions for signaling purpose, integrity specifications will also be mandatory. The integrity monitoring control techniques are hopefully to be implemented into the GNSS receivers for personal navigation systems or railway signaling systems in the near future.

Bibliography

[1] European Global Navigation Satellite Systems Agency (GSA), "GNSS Market Report," *Issue 5*, May 2017. (Cited in page 2.)

[2] J. Marais, J. Beugin, and M. Berbineau, "A survey of GNSS-based research and developments for the european railway signaling," *IEEE Transactions on Intelligent Transportation Systems*, vol. 18, no. DOI: 10.1109/TITS.2017.2658179, pp. 2602–2618, 2017. (Cited in page 2.)

[3] International Civil Aviation Organization, *International Standards and Recommended Practices*. Annex 10 to Convention on International Civil Aviation, volume 1, sixth ed., July 2006. Radio Navigation Aids. (Cited in pages 3, 39, 41, 42 and 124.)

[4] MOPS LAAS, "Minimum Operational Performance Standards for Global Positioning System/Local Area Augmentation System airborne equipment," *RTCA SC-159, DO-253A*, 2001. (Cited in page 3.)

[5] J. Cosmen-Schortmann, M. Azaola-Saenz, M. Martínez-Olagüe, M. Toledo-Lopez, *et al.*, "Integrity in urban and road environments and its use in liability critical applications," in *Proc. Position, Location and Navigation Symposium, 2008 IEEE/ION*, pp. 972–983, IEEE, 2008. (Cited in pages 5, 37, 48, 49, 50, 51, 62 and 135.)

[6] E. Kaplan and C. Hegarty, *Understanding GPS: principles and applications*. Artech house, 2005. (Cited in pages 13, 20, 21, 27, 44 and 71.)

[7] P. D. Groves, *Principles of GNSS, inertial, and multisensor integrated navigation systems*. Artech house, 2013. (Cited in pages xii, 13, 22, 70, 72 and 73.)

[8] B. W. Parkinson and J. Spilker, J. J., *Progress in Astronautics and Aeronautics: Global Positioning System: Theory and Applications*, vol. 2. Washington, DC: AIAA, 1996. (Cited in page 13.)

[9] M. M. Hoque and N. Jakowski, "Ionospheric propagation effects on gnss signals and new correction approaches," in *Global Navigation Satellite Systems: Signal, Theory and Applications*, InTech, 2012. (Cited in page 17.)

[10] D. Have, "Reference set of parameters for raim availability simulations," *working paper Sofreavia*, pp. 8–9, 2003. (Cited in page 20.)

[11] Y. C. Lee and M. P. McLaughlin, "Feasibility analysis of raim to provide lpv-200 approaches with future gps," in *ION GNSS 20th International Technical Meeting of the Satellite Division*, pp. 2898–2919, 2007. (Cited in page 20.)

[12] C. Hernández, C. Catalán, and M. Martínez, "Galileo integrity concept and its applications to the maritime sector," *Marine Navigation and Safety of Sea Transportation*, p. 117, 2009. (Cited in page 20.)

[13] S. Andrés and C. Daniel, *Integrity monitoring applied to the reception of GNSS signals in urban environments*. PhD thesis, Institut Natinal Polytechnique de Toulouse, 2012. (Cited in page 20.)

[14] J. A. Klobuchar, "Ionospheric time-delay algorithm for single-frequency gps users," *IEEE Transactions on aerospace and electronic systems*, no. 3, pp. 325–331, 1987. (Cited in page 21.)

[15] European Union, "European GNSS (Galileo) Open Servic - Ionospheric Correction Algorithm for Galileo Single Frequency Users," 2016. (Cited in page 21.)

[16] European Union, "European GNSS (Galileo) Open Servic - Signal In Space Interface Control Document," *OD SIS ICD*, no. Issue 1, 2010. (Cited in page 21.)

[17] M. M. Hoque and N. Jakowski, "Higher order ionospheric effects in precise GNSS positioning," *Journal of Geodesy*, vol. 81, no. 4, pp. 259–268, 2007. (Cited in page 21.)

[18] RTCA/DO-229D, "Minimum Operational Performance Standards for Global Positioning System/Wide Area Augmentation System airborne equipment," *RTCA SC-159*, 2006. (Cited in pages 21, 37, 42, 125, 130, 131 and 158.)

[19] RTCA/DO-229D, "Minimum Operational Performance Standards for Global Positioning System/Wide Area Augmentation System airborne equipment," *RTCA SC-159*, 2006. (Cited in pages 22 and 74.)

[20] J. W. Betz and K. R. Kolodziejski, "Extended theory of early-late code tracking for a bandlimited gps receiver," *Navigation*, vol. 47, no. 3, pp. 211–226, 2000. (Cited in page 22.)

[21] S. Stephens and J. Thomas, "Controlled-root formulation for digital phase-locked loops," *IEEE Transactions on Aerospace and Electronic Systems*, vol. 31, no. 1, pp. 78–95, 1995. (Cited in page 22.)

[22] P. Misra and P. Enge, *Global Positioning System: Signals, Measurements and Performance Second Edition*. Lincoln, MA: Ganga-Jamuna Press, 2006. (Cited in page 22.)

[23] Y. C. Lee, "Performance of receiver autonomous integrity monitoring (raim) in the presence of simultaneous multiple satellite faults," in *Proceedings of the 60th Annual Meeting of the Institute of Navigation*, pp. 687–697, 2001. (Cited in page 23.)

[24] Department of Defense USA, "Global positioning service standard positioning service performance standard," 2001. (Cited in page 23.)

[25] K. Van Dyke, K. Kovach, J. Kraemer, J. Lavrakas, J. Fernow, J. Reese, N. Attallah, and B. Baevitz, "Gps integrity failure modes and effects analysis," in *Proceedings of the 2003 National Technical Meeting of The Institute of Navigation*, pp. 689–703, 2001. (Cited in page 23.)

[26] N. Sokolova, A. J. Morrison, J. Curran, and M. Petovello, "Do modern multi-frequency civil receivers eliminate the ionospheric effect?," 2017. (Cited in page 23.)

[27] T. Söderström and P. Stoica, "System identification," 1989. (Cited in page 28.)

[28] R. E. Kalman, "A new approach to linear filtering and prediction problems," *Journal of basic Engineering*, vol. 82, no. 1, pp. 35–45, 1960. (Cited in page 28.)

[29] P. S. Maybeck, *Stochastic models, estimation, and control*, vol. 3. Academic press, 1982. (Cited in page 30.)

[30] R. G. Brown, P. Y. Hwang, *et al.*, *Introduction to random signals and applied Kalman filtering*, vol. 3. Wiley New York, 1992. (Cited in pages xi, 30 and 31.)

[31] O. L. R. Jacobs and O. Jacobs, *Introduction to control theory*. Clarendon Press Oxford, 1974. (Cited in page 30.)

[32] J. Farrell, *Aided navigation: GPS with high rate sensors*. McGraw-Hill, Inc., 2008. (Cited in page 32.)

[33] M. G. Petovello, *Real-time integration of a tactical-grade IMU and GPS for high-accuracy positioning and navigation*. Citeseer, 2003. (Cited in page 33.)

[34] M. A. Quddus, W. Y. Ochieng, and R. B. Noland, "Current map-matching algorithms for transport applications: State-of-the art and future research directions," *Transportation research part c: Emerging technologies*, vol. 15, no. 5, pp. 312–328, 2007. (Cited in page 33.)

[35] D. Bétaille, F. Peyret, M. Ortiz, S. Miquel, and L. Fontenay, "A new modeling based on urban trenches to improve gnss positioning quality of service in cities," *IEEE Intelligent transportation systems magazine*, vol. 5, no. 3, pp. 59–70, 2013. (Cited in pages xii, 33, 83, 85, 90 and 103.)

[36] D. Bétaille, F. Peyret, M. Ortiz, S. Miquel, and F. Godan, "Improving accuracy and integrity with a probabilistic urban trench modeling," *Navigation*, vol. 63, no. 3, pp. 283–294, 2016. (Cited in pages 33, 73, 84, 103 and 180.)

[37] J. S. Greenfeld, "Matching gps observations to locations on a digital map," in *81th annual meeting of the transportation research board*, vol. 1, pp. 164–173, 2002. (Cited in page 33.)

[38] D. Bernstein and A. Kornhauser, "An introduction to map matching for personal navigation assistants," 1998. (Cited in page 33.)

[39] M. Yu, *Improved positioning of land vehicle in ITS using digital map and other accessory information*. PhD thesis, The Hong Kong Polytechnic University, 2006. (Cited in page 33.)

[40] C. Blazquez and A. Vonderohe, "Simple map-matching algorithm applied to intelligent winter maintenance vehicle data," *Transportation Research Record: Journal of the Transportation Research Board*, no. 1935, pp. 68–76, 2005. (Cited in page 33.)

[41] W. Y. Ochieng, M. Quddus, and R. B. Noland, "Map-matching in complex urban road networks," *Revista Brasileira de Cartografia*, vol. 2, no. 55, 2003. (Cited in page 33.)

[42] S. K. Honey, W. B. Zavoli, K. A. Milnes, A. C. Phillips, M. S. White Jr, and G. E. Loughmiller Jr, "Vehicle navigational system and method," Jan. 3 1989. US Patent 4,796,191. (Cited in page 33.)

[43] D. Obradovic, H. Lenz, and M. Schupfner, "Fusion of map and sensor data in a modern car navigation system," *Journal of VLSI signal processing systems for signal, image and video technology*, vol. 45, no. 1-2, pp. 111–122, 2006. (Cited in page 33.)

[44] F. Gustafsson, F. Gunnarsson, N. Bergman, U. Forssell, J. Jansson, R. Karlsson, and P.-J. Nordlund, "Particle filters for positioning, navigation, and tracking," *IEEE Transactions on signal processing*, vol. 50, no. 2, pp. 425–437, 2002. (Cited in page 33.)

[45] N. Zhu, J. Marais, D. Bétaille, and M. Berbineau, "GNSS Position Integrity in Urban Environments: A Review of Literature," *IEEE Transactions on Intelligent Transportation Systems*, vol. PP, no. DOI: 10.1109/TITS.2017.2766768, pp. 1–17, 2018. (Cited in pages 36 and 180.)

[46] P. B. Ober, *Integrity prediction and monitoring of navigation systems*, vol. 1. Integricom Publishers Leiden, 2003. (Cited in page 37.)

[47] European Global Navigation Satellite Systems Agency, "GNSS Market Report," *Issue 4*, March 2015. (Cited in page 37.)

[48] T. Beech, M. Martinez-Olague, and J. Cosmen-Schortmann, "Integrity: A key enabler for liability critical applications," in *Proceedings of the US ION 61st Annual Meeting, 27–29 June, Cambridge, MA*, pp. 1–10, 2005. (Cited in page 37.)

[49] S. Lo, S. Pullen, J. Blanch, P. Enge, A. Neri, V. Palma, M. Salvitti, and C. Stallo, "Projected performance of a baseline high integrity gnss railway architecture under nominal and faulted conditions," in *Proceedings of the 30th International Technical Meeting of the Satellite Division of the Institute of Navigation, Portland*, pp. 25–29, 2017. (Cited in page 37.)

[50] S. Bijjahalli, S. Ramasamy, and R. Sabatini, "Masking and multipath analysis for unmanned aerial vehicles in an urban environment," in *Digital Avionics Systems Conference (DASC), 2016 IEEE/AIAA 35th*, pp. 1–9, IEEE, 2016. (Cited in pages 37 and 49.)

[51] "COST Action TU1302. SaPPART White paper: Better use of Global Navigation Satellite Systems for safer and greener transport. IFSTTAR, 2015. Technique et Méthodes," no. ISBN 978-2-85782-706-1. (Cited in pages xi, 37 and 39.)

[52] L. Wang, P. D. Groves, and M. K. Ziebart, "Multi-constellation gnss performance evaluation for urban canyons using large virtual reality city models," *Journal of Navigation*, vol. 65, no. 03, pp. 459–476, 2012. (Cited in page 38.)

[53] P. D. Groves, Z. Jiang, M. Rudi, and P. Strode, "A portfolio approach to NLOS and multipath mitigation in dense urban areas," *The Institute of Navigation*, 2013. (Cited in pages 38, 70, 71 and 73.)

[54] M. S. Braasch, "Multipath effects," in *Global Positioning System: Theory and Applications, Volume I* (B. W. Parkinson and J. Spilker, J. J., eds.), ch. 14, pp. 547–568, Washington DC: AIAA, 1996. (Cited in page 38.)

[55] J. J. Spilker Jr, "Foliage attenuation for land mobile users," in *Global Positioning System: Theory and Applications, Volume I* (B. W. Parkinson and J. J. Spilker Jr, eds.), ch. 15, pp. 569–583, Washington DC: AIAA, 1996. (Cited in page 38.)

[56] J. J. Spilker Jr and F. D. Natali, "Interference effects and mitigation techniques," in *Global Positioning System: Theory and Applications, Volume I* (B. W. Parkinson and J. J. Spilker Jr, eds.), ch. 20, pp. 717–771, Washington DC: AIAA, 1996. (Cited in page 38.)

[57] P. D. Groves, Z. Jiang, B. Skelton, P. A. Cross, L. Lau, Y. Adane, and I. Kale, "Novel multipath mitigation methods using a dual-polarization antenna," 2010. (Cited in pages 38, 71 and 73.)

[58] O. Leisten and V. Knobe, "Optimizing small antennas for body-loading applications," *GPS World*, vol. 23, no. 9, pp. 40–44, 2012. (Cited in pages 38, 71 and 73.)

[59] O. M. Mubarak and A. G. Dempster, "Analysis of early late phase in single-and dual-frequency gps receivers for multipath detection," *GPS solutions*, vol. 14, no. 4, pp. 381–388, 2010. (Cited in pages 38 and 73.)

[60] P. D. Groves and Z. Jiang, "Height aiding, C/N0 weighting and consistency checking for GNSS NLOS and multipath mitigation in urban areas," *Journal of Navigation*, vol. 66, no. 05, pp. 653–669, 2013. (Cited in page 38.)

[61] D. Salos, A. Martineau, C. Macabiau, B. Bonhoure, and D. Kubrak, "Receiver autonomous integrity monitoring of GNSS signals for electronic toll collection," *Intelligent Transportation Systems, IEEE Transactions on*, vol. 15, no. 1, pp. 94–103, 2014. (Cited in pages 38, 48 and 50.)

[62] CEN-CENELEC, "Space - Use of GNSS-based positioning for road Intelligent Transport system (ITS)- Part 1: Definitions and system engeneering procedures for the establishment and assessment of performance," in *prEN 16803-1*, 2015. (Cited in page 39.)

[63] J. Rife and S. Pullen, "Aviation applications," (Cited in pages 39 and 41.)

[64] M. Monnerat, "Integrity monitoring for road applications," in *presentation at Positioning with Confidence Workshop, CNES CCT PDS, ENAC, Toulouse, France*, 2013. (Cited in page 40.)

[65] R. T. Ioannides, T. Pany, and G. Gibbons, "Known vulnerabilities of global navigation satellite systems, status, and potential mitigation techniques," *Proceedings of the IEEE*, vol. 104, no. 6, pp. 1174–1194, 2016. (Cited in page 40.)

[66] D. Salós, C. Macabiau, A. Martineau, B. Bonhoure, and D. Kubrak, "Analysis of gnss integrity requirements for road user charging applications," in *Satellite Navigation Tech-*

nologies and European Workshop on GNSS Signals and Signal Processing (NAVITEC), 2010 5th ESA Workshop on, pp. 1–8, IEEE, 2010. (Cited in page 42.)

[67] A. Martineau, *Performance of Receiver Autonomous Integrity Monitoring (RAIM) for Vertical Guided Approaches*. PhD thesis, Institut Natinal Polytechnique de Toulouse, 2008. (Cited in page 45.)

[68] Y. C. Lee, "Analysis of range and position comparison methods as a means to provide gps integrity in the user receiver," in *Proceedings of the 42nd Annual Meeting of the Institute of Navigation*, pp. 1–4, 1986. (Cited in pages 45 and 47.)

[69] G. BROWN and P. Y. Hwang, "GPS failure detection by autonomous means within the cockpit," *Navigation*, vol. 33, no. 4, pp. 335–353, 1986. (Cited in pages 45 and 47.)

[70] R. G. Brown and P. McBurney, "Self-Contained GPS Integrity Check Using Maximum Solution Separation," *Navigation*, vol. 35, no. 1, pp. 41–53, 1988. (Cited in pages 45 and 47.)

[71] M. Brenner, "Implementation of a RAIM Monitor in a GPS Receiver and an Integrated GPS/IRS," *ION GPS-90*, pp. 397–406, 1990. (Cited in pages 45 and 47.)

[72] R. Grover Brown, "Receiver autonomous integrity monitoring," in *Global Positioning System: Theory and Applications, Volume II* (B. W. Parkinson and J. J. Spilker Jr, eds.), ch. 5, pp. 143–165, Washington DC: AIAA, 1996. (Cited in pages 45 and 48.)

[73] R. G. Brown, "A baseline GPS RAIM scheme and a note on the equivalence of three RAIM methods," *Navigation*, vol. 39, no. 3, pp. 301–316, 1992. (Cited in pages 45, 48 and 158.)

[74] T. Walter and P. Enge, "Weighted RAIM for precision approach," in *PROCEEDINGS OF ION GPS*, vol. 8, pp. 1995–2004, Institute of Navigation, 1995. (Cited in pages 45, 130 and 158.)

[75] R. G. Brown, *GPS RAIM: Calculation of Thresholds and Protection Radius Using Chi-square Methods; a Geometric Approach*. Radio Technical Commission for Aeronautics, 1994. (Cited in pages 45, 131 and 158.)

[76] M. Joerger, S. Stevanovic, S. Langel, and B. Pervan, "Integrity Risk Minimisation in RAIM Part 1: Optimal Detector Design," *Journal of Navigation*, vol. 69, no. 03, pp. 449–467, 2016. (Cited in pages 45 and 47.)

[77] M. Joerger, S. Langel, and B. Pervan, "Integrity Risk Minimisation in RAIM Part 2: Optimal Estimator Design," *Journal of Navigation*, vol. 69, no. 04, pp. 709–728, 2016. (Cited in pages 45 and 47.)

[78] J. A. Blanch, T. F. Walter, P. K. Enge, S. Wallner, F. A. Fernandez, R. Dellago, R. Ioannides, B. Pervan, I. F. Hernandez, B. Belabbas, *et al.*, "A proposal for multi-constellation advanced raim for vertical guidance," 2011. (Cited in pages 45, 46 and 47.)

[79] J. Blanch, T. Walter, P. Enge, Y. Lee, B. Pervan, M. Rippl, and A. Spletter, "Advanced raim user algorithm description: Integrity support message processing, fault detection,

exclusion, and protection level calculation," in *Proceedings of the 25th International Technical Meeting of The Satellite Division of the Institute of Navigation (ION GNSS 2012)*, pp. 2828–2849, 2012. (Cited in pages 45, 46 and 47.)

[80] J. Blanch, T. Walter, and P. Enge, "Optimal positioning for advanced RAIM," *Navigation*, vol. 60, no. 4, pp. 279–289, 2013. (Cited in pages 45 and 47.)

[81] A. Grosch, O. G. Crespillo, I. Martini, and C. Günther, "Snapshot residual and kalman filter based fault detection and exclusion schemes for robust railway navigation," in *Navigation Conference (ENC), 2017 European*, pp. 36–47, IEEE, 2017. (Cited in pages 45 and 51.)

[82] S. Hewitson and J. Wang, "Gnss receiver autonomous integrity monitoring with a dynamic model," *The Journal of Navigation*, vol. 60, no. 2, pp. 247–263, 2007. (Cited in pages 45 and 51.)

[83] R. S. Young, G. A. McGraw, and B. T. Driscoll, "Investigation and comparison of horizontal protection level and horizontal uncertainty level in fde algorithms," in *ION GPS-96*, pp. 1607–1614, 1996. (Cited in pages 46, 131 and 158.)

[84] FAA, "GNSS Evolutionary Architecture Study: Phase I-Panel Report," *GNSS Evolutionary Architecture Study Panel*, 2008. (Cited in pages 46 and 47.)

[85] FAA, "GNSS Evolutionary Architecture Study: Phase II-Panel Report," *GNSS Evolutionary Architecture Study Panel, Feb*, 2010. (Cited in pages 46 and 47.)

[86] B. S. Pervan, S. P. Pullen, and J. R. Christie, "A multiple hypothesis approach to satellite navigation integrity," *Navigation*, vol. 45, no. 1, pp. 61–71, 1998. (Cited in page 47.)

[87] S. Feng, W. Ochieng, T. Moore, C. Hill, and C. Hide, "Carrier phase-based integrity monitoring for high-accuracy positioning," *GPS solutions*, vol. 13, no. 1, pp. 13–22, 2009. (Cited in page 47.)

[88] A. Jokinen, S. Feng, W. Ochieng, C. Hide, T. Moore, and C. Hill, "Fixed ambiguity precise point positioning (PPP) with FDE RAIM," in *Position Location and Navigation Symposium (PLANS), 2012 IEEE/ION*, pp. 643–658, IEEE, 2012. (Cited in page 47.)

[89] W. Y. Ochieng, S. Feng, T. Moore, C. Hill, and C. Hide, "User Level Integrity Monitoring and Quality Control for High Accuracy Positioning using GPS/INS Measurements," *Positioning (POS) Journal Information*, p. 14, 2010. (Cited in page 47.)

[90] S. Hewitson and J. Wang, "Extended receiver autonomous integrity monitoring (ERAIM) for GNSS/INS integration," *Journal of Surveying Engineering*, vol. 136, no. 1, pp. 13–22, 2010. (Cited in page 47.)

[91] J. L. Farrell, "Full integrity testing for gps/ins," *Navigation*, vol. 53, no. 1, pp. 33–40, 2006. (Cited in page 47.)

[92] P. Y. Hwang, "Applying nioraim to the solution separation method for inertially-aided aircraft autonomous integrity monitoring," in *Proceedings of the 2005 National Technical Meeting of The Institute of Navigation*, pp. 992–1000, 2001. (Cited in page 47.)

[93] A. Rakipi, B. Kamo, S. Cakaj, V. Kolici, A. Lala, and I. Shinko, "Integrity Monitoring in Navigation Systems: Fault Detection and Exclusion RAIM Algorithm Implementation," *Journal of Computer and Communications*, vol. 3, no. 06, p. 25, 2015. (Cited in page 47.)

[94] J. Blanch, T. Walter, and P. Enge, "A simple algorithm for dual frequency ground monitoring compatible with araim," in *Proceedings of the 21st International Technical Meeting of the Satellite Division of The Institute of Navigation (ION GNSS 2008)*, pp. 1911–1917, Citeseer, 2008. (Cited in page 47.)

[95] M. Joerger and B. Pervan, "Fault detection and exclusion using solution separation and chi-squared ARAIM," *IEEE Transactions on Aerospace and Electronic Systems*, vol. 52, no. 2, pp. 726–742, 2016. (Cited in page 47.)

[96] Y. Jiang and J. Wang, "A-RAIM and R-RAIM Performance using the Classic and MHSS Methods," *Journal of Navigation*, vol. 67, no. 01, pp. 49–61, 2014. (Cited in page 47.)

[97] M. Choi, J. Blanch, T. Walter, and P. Enge, "Advanced RAIM Demonstration using Four Months of Ground Data," *Proceedings of ION ITM 2011*, 2011. (Cited in page 47.)

[98] C. Milner and W. Ochieng, "ARAIM for LPV-200: the ideal protection level," in *Proceedings of the 23rd International Technical Meeting of The Satellite Division of the Institute of Navigation (ION GNSS 2010)*, pp. 3191–3198, 2001. (Cited in page 47.)

[99] T. Walter, P. Enge, J. Blanch, and B. Pervan, "Worldwide vertical guidance of aircraft based on modernized GPS and new integrity augmentations," *Proceedings of the IEEE*, vol. 96, no. 12, pp. 1918–1935, 2008. (Cited in page 47.)

[100] Y. C. Lee, "A position domain relative RAIM method," *IEEE Transactions on Aerospace and Electronic Systems*, vol. 47, no. 1, pp. 85–97, 2011. (Cited in page 47.)

[101] L. Gratton, M. Joerger, and B. Pervan, "Carrier phase relative RAIM algorithms and protection level derivation," *Journal of Navigation*, vol. 63, no. 02, pp. 215–231, 2010. (Cited in page 47.)

[102] P. Teunissen and S. Verhagen, "Gnss carrier phase ambiguity resolution: challenges and open problems," in *Observing our Changing Earth*, pp. 785–792, Springer, 2009. (Cited in page 47.)

[103] K. Ali, F. Dovis, and M. Pini, "Characterizing Local Effects on Protection Level Concept in Urban Environments," 2012. (Cited in page 48.)

[104] K. Ali, M. Pini, and F. Dovis, "Measured performance of the application of EGNOS in the road traffic sector," *GPS solutions*, vol. 16, no. 2, pp. 135–145, 2012. (Cited in page 48.)

[105] J. Marais, M. Berbineau, and M. Heddebaut, "Land mobile GNSS availability and multipath evaluation tool," *Vehicular Technology, IEEE Transactions on*, vol. 54, no. 5, pp. 1697–1704, 2005. (Cited in page 48.)

[106] S. Pullen, T. Walter, and P. Enge, "SBAS and GBAS Integrity for Non-Aviation Users: Moving Away from Specific Risk," *Proc. ION ITM 2011*, pp. 24–26, 2011. (Cited in page 48.)

[107] A. Nowak and C. Specht, "Snapshot raim algorithms availability in urban areas," *Annual of Navigation*, pp. 73–88, 2006. (Cited in page 48.)

[108] N. R. Velaga, M. A. Quddus, A. L. Bristow, and Y. Zheng, "Map-aided integrity monitoring of a land vehicle navigation system," *Intelligent Transportation Systems, IEEE Transactions on*, vol. 13, no. 2, pp. 848–858, 2012. (Cited in page 49.)

[109] E. Shytermeja, A. Garcia-Pena, and O. Julien, "Proposed architecture for integrity monitoring of a GNSS/MEMS system with a fisheye camera in urban environment," in *Localization and GNSS (ICL-GNSS), 2014 International Conference on*, pp. 1–6, IEEE, 2014. (Cited in page 49.)

[110] D. Margaria and E. Falletti, "A novel local integrity concept for GNSS receivers in urban vehicular contexts," in *Position, Location and Navigation Symposium-PLANS 2014, 2014 IEEE/ION*, pp. 413–425, IEEE, 2014. (Cited in page 49.)

[111] R. Sabatini, T. Moore, and C. Hill, "A new avionics-based gnss integrity augmentation system: Part 1–fundamentals," *Journal of Navigation*, vol. 66, no. 03, pp. 363–384, 2013. (Cited in page 49.)

[112] R. Sabatini, T. Moore, and C. Hill, "A new avionics-based gnss integrity augmentation system: Part 2–integrity flags," *Journal of Navigation*, vol. 66, no. 04, pp. 501–522, 2013. (Cited in page 49.)

[113] R. Sabatini, T. Moore, C. Hill, and S. Ramasamy, "Investigation of gnss integrity augmentation synergies with unmanned aircraft systems sense-and-avoid," (Cited in page 49.)

[114] G. Castaldo, A. Angrisano, S. Gaglione, and S. Troisi, "P-RANSAC: an integrity monitoring approach for GNSS signal degraded scenario," *International Journal of Navigation and Observation*, vol. 2014, 2014. (Cited in pages 50 and 72.)

[115] D. Borio and C. Gioia, "Galileo: The added value for integrity in harsh environments," *Sensors*, vol. 16, no. 1, p. 111, 2016. (Cited in pages 51 and 70.)

[116] S. Azaola, "Method for autonomous determination of protection levels for GNSS positioning based on navigation residuals and an isotropic confidence ratio," Nov. 2009. EP Patent App. EP20,080,380,133. (Cited in page 51.)

[117] P. Navarro *et al.*, "Computing meaningful integrity bounds of a low-cost kalman-filtered navigation solution in urban environments," in *ION GNSS*, 2015. (Cited in page 52.)

[118] K. A. Bin Ahmad, M. Sahmoudi, and C. Macabiau, "A composite approach for HPL computation of GNSS positioning confidence in urban environments," (Cited in page 52.)

[119] S. Tay and J. Marais, "Weighting models for GPS pseudorange observations for land transportation in urban canyons," in *6th European Workshop on GNSS Signals and Signal Processing*, p. 4p, 2013. (Cited in pages 52, 78 and 89.)

[120] D. Bruckner, F. van Graas, and T. Skidmore, "Statistical characterization of composite protection levels for GPS," *GPS solutions*, vol. 15, no. 3, pp. 263–273, 2011. (Cited in page 52.)

[121] W. Baarda, "A testing procedijre for use in ge, odetic ne, tworks," 1968. (Cited in page 58.)

[122] B. Schaffrin, "Reliability measures for correlated observations," *Journal of Surveying Engineering*, vol. 123, no. 3, pp. 126–137, 1997. (Cited in page 59.)

[123] S. Kuang, *Geodetic network analysis and optimal design: concepts and applications*. Ann Arbor PressInc, 1996. (Cited in pages 59 and 61.)

[124] A. Leick, L. Rapoport, and D. Tatarnikov, *GPS satellite surveying*. John Wiley & Sons, 2015. (Cited in pages 59 and 63.)

[125] G. Lu, *Quality control for differential kinematic GPS positioning*. University of Calgary, 1992. (Cited in page 62.)

[126] P. Jorgensen, "Ah, robust estimation!," *Aust. J. Geod. Photo. Surv.*, vol. 42, pp. 19–32, 1985. (Cited in page 63.)

[127] N. Viandier, A. Rabaoui, J. Marais, and E. Duflos, "Enhancement of galileo and multi-constellation accuracy by modeling pseudorange noises," in *Intelligent Transport Systems Telecommunications,(ITST), 2009 9th International Conference on*, pp. 459–464, IEEE, 2009. (Cited in page 70.)

[128] P. D. Groves, Z. Jiang, L. Wang, and M. K. Ziebart, "Intelligent urban positioning using multi-constellation GNSS with 3D mapping and NLOS signal detection," 2012. (Cited in pages xi and 70.)

[129] J. Sanz Subirana, J. Juan Zornoza, and M. Hernandez-Pajares, *GNSS Data Processing, Vol.1: Fundamentals and Algorithms*. ESA Communications, 2013. (Cited in pages xi, 70 and 71.)

[130] Z. Jiang, P. D. Groves, W. Y. Ochieng, S. Feng, C. D. Milner, and P. G. Mattos, "Multi-constellation GNSS multipath mitigation using consistency checking," in *Proceedings of the 24th International Technical Meeting of The Satellite Division of the Institute of Navigation (ION GNSS 2011)*, pp. 3889–3902, Institute of Navigation, 2011. (Cited in pages 71 and 73.)

[131] D. A. Braasch, Y. Liu, and D. R. Corey, "Multipath effects," in *Global positioning system: theory and applications*, Citeseer, 1996. (Cited in page 71.)

[132] Z. Jiang and P. D. Groves, "NLOS GPS signal detection using a dual-polarisation antenna," *GPS solutions*, vol. 18, no. 1, pp. 15–26, 2014. (Cited in pages 71 and 73.)

[133] A. Brown, N. Gerein, *et al.*, "Test results from a digital p (y) code beamsteering receiver for multipath minimization," in *ION 57th Annual Meeting, Albuquerque, NM*, 2001. (Cited in page 73.)

[134] M. H. Keshvadi, A. Broumandan, and G. Lachapelle, "Analysis of gnss beamforming and angle of arrival estimation in multipath environments," in *Proceedings of the Institute of Navigation 2011 International Technical Meeting (ION ITM), San Diego, CA, USA*, pp. 24–26, 2011. (Cited in page 73.)

[135] M. Irsigler and B. Eissfeller, "Comparison of multipath mitigation techniques with consideration of future signal structures," in *Proceedings of the International Technical Meeting of the Institute of Navigation (ION-GPS/GNSS?03)*, pp. 2584–2592, 2003. (Cited in page 73.)

[136] L.-T. Hsu, P. D. Groves, and S.-S. Jan, "Assessment of the multipath mitigation effect of vector tracking in an urban environment," Institute of Navigation Publications, 2013. (Cited in page 73.)

[137] A. Wieser and F. K. Brunner, "An extended weight model for gps phase observations," *Earth, planets and space*, vol. 52, no. 10, pp. 777–782, 2000. (Cited in pages 73 and 77.)

[138] H. Hartinger and F. Brunner, "Variances of gps phase observations: the sigma-ε model," *GPS solutions*, vol. 2, no. 4, pp. 35–43, 1999. (Cited in pages 73 and 77.)

[139] N. Zhu, J. Marais, D. Bétaille, and M. Berbineau, "Evaluation and comparison of GNSS navigation algorithms including FDE for urban transport applications," *Proceedings of Institute of Navigation (ION) International Technical Meeting (ITM), Monterey, CA, USA*, 2017. (Cited in pages 73, 91 and 181.)

[140] H. Kuusniemi, A. Wieser, G. Lachapelle, and J. Takala, "User-level reliability monitoring in urban personal satellite-navigation," *IEEE Transactions on Aerospace and Electronic Systems*, vol. 43, no. 4, 2007. (Cited in page 73.)

[141] M. Bahrami and M. Ziebart, "Instantaneous doppler-aided rtk positioning with single frequency receivers," in *Position Location and Navigation Symposium (PLANS), 2010 IEEE/ION*, pp. 70–78, IEEE, 2010. (Cited in page 73.)

[142] A. Soloviev and F. van Graas, "Utilizing multipath reflections in deeply integrated gps/ins architecture for navigation in urban environments," in *Position, Location and Navigation Symposium, 2008 IEEE/ION*, pp. 383–393, IEEE, 2008. (Cited in page 73.)

[143] P. Xie, M. G. Petovello, and C. Basnayake, "Multipath signal assessment in the high sensitivity receivers for vehicular applications," in *Proceedings of the ION GNSS*, 2011. (Cited in page 73.)

[144] J.-i. Meguro, T. Murata, J.-i. Takiguchi, Y. Amano, and T. Hashizume, "Gps multipath mitigation for urban area using omnidirectional infrared camera," *IEEE Transactions on Intelligent Transportation Systems*, vol. 10, no. 1, pp. 22–30, 2009. (Cited in page 73.)

[145] S. Kato, M. Kitamura, T. Suzuki, and Y. Amano, "Nlos satellite detection using a fish-eye camera for improving gnss positioning accuracy in urban area," *Journal of robotics and mechatronics*, vol. 28, no. 1, pp. 31–39, 2016. (Cited in page 73.)

[146] D. Attia, C. Meurie, Y. Ruichek, and J. Marais, "Counting of satellites with direct gnss signals using fisheye camera: A comparison of clustering algorithms," in *Intelligent Transportation Systems (ITSC), 2011 14th International IEEE Conference on*, pp. 7–12, IEEE, 2011. (Cited in pages 73, 76 and 105.)

[147] R. Toledo-Moreo, D. Bétaille, F. Peyret, and J. Laneurit, "Fusing gnss, dead-reckoning, and enhanced maps for road vehicle lane-level navigation," *IEEE Journal of Selected Topics in Signal Processing*, vol. 3, no. 5, pp. 798–809, 2009. (Cited in page 73.)

[148] A. Bourdeau, M. Sahmoudi, and J.-Y. Tourneret, "Constructive use of gnss nlos-multipath: Augmenting the navigation kalman filter with a 3d model of the environment," in *Information Fusion (FUSION), 2012 15th International Conference on*, pp. 2271–2276, IEEE, 2012. (Cited in page 73.)

[149] M. Sahmoudi and M. G. Amin, "Robust tracking of weak gps signals in multipath and jamming environments," *Signal Processing*, vol. 89, no. 7, pp. 1320–1333, 2009. (Cited in page 73.)

[150] M. Sahmoudi and M. G. Amin, "Fast iterative maximum-likelihood algorithm (FIMLA) for multipath mitigation in the next generation of GNSS receivers," *IEEE Transactions on Wireless Communications*, vol. 7, no. 11, 2008. (Cited in page 73.)

[151] N. Viandier, D. Nahimana, J. Marais, and E. Duflos, "GNSS performance enhancement in urban environment based on pseudo-range error model," in *Position, Location and Navigation Symposium, 2008 IEEE/ION*, pp. 377–382, IEEE, 2008. (Cited in page 73.)

[152] N. Blanco-Delgado and F. D. Nunes, "Multipath estimation in multicorrelator gnss receivers using the maximum likelihood principle," *IEEE Transactions on Aerospace and Electronic Systems*, vol. 48, no. 4, pp. 3222–3233, 2012. (Cited in page 73.)

[153] C. Cheng, Q. Pan, V. Calmettes, and J.-Y. Tourneret, "A maximum likelihood-based unscented kalman filter for multipath mitigation in a multi-correlator based gnss receiver," in *Acoustics, Speech and Signal Processing (ICASSP), 2016 IEEE International Conference on*, pp. 6560–6564, IEEE, 2016. (Cited in page 73.)

[154] N. Zheng, L. Cai, H. Bian, and L. Cong, "Hybrid particle filtering algorithm for gps multipath mitigation," *Transactions of Nonferrous Metals Society of China*, vol. 24, no. 5, pp. 1554–1561, 2014. (Cited in page 73.)

[155] M. Ortiz, F. Peyret, V. Renaudin, and D. Bétaille, "From lab to road test: Using a reference vehicle for solving gnss localization challenges," *Inside GNSS*, vol. 8, no. 5, p. 19p, 2013. (Cited in pages xii, 74 and 92.)

[156] F. Brunner, H. Hartinger, and L. Troyer, "Gps signal diffraction modelling: the stochastic sigma-δ model," *Journal of Geodesy*, vol. 73, no. 5, pp. 259–267, 1999. (Cited in page 77.)

[157] T. Herring, R. King, and S. McClusky, "Documentation of the gamit gps analysis software release 10.4," *Department of Earth and Planetary Sciences, Massachusetts Institute of Technology, Cambridge, Massachusetts*, pp. 1–171, 2010. (Cited in page 78.)

[158] B. Li, L. Lou, and Y. Shen, "Gnss elevation-dependent stochastic modeling and its impacts on the statistic testing," *Journal of Surveying Engineering*, vol. 142, no. 2, p. 04015012, 2015. (Cited in pages 78 and 100.)

[159] R. M. Neal, "Markov chain sampling methods for dirichlet process mixture models," *Journal of computational and graphical statistics*, vol. 9, no. 2, pp. 249–265, 2000. (Cited in page 79.)

[160] N. Viandier, *Modélisation et utilisation des erreurs de pseudodistances GNSS en environnement transport pour l'amélioration des performances de localisation.* PhD thesis, Ecole Centrale de Lille, 2011. (Cited in pages 79, 81, 82, 83 and 102.)

[161] A. Rabaoui, N. Viandier, E. Duflos, J. Marais, and P. Vanheeghe, "Dirichlet process mixtures for density estimation in dynamic nonlinear modeling: Application to gps positioning in urban canyons," *IEEE Transactions on Signal Processing*, vol. 60, no. 4, pp. 1638–1655, 2012. (Cited in pages 79 and 81.)

[162] Y. W. Teh, M. I. Jordan, M. J. Beal, and D. M. Blei, "Sharing clusters among related groups: Hierarchical dirichlet processes," in *Advances in neural information processing systems*, pp. 1385–1392, 2005. (Cited in page 79.)

[163] J. Sethuraman, "A constructive definition of dirichlet priors," *Statistica sinica*, pp. 639–650, 1994. (Cited in page 80.)

[164] D. Blackwell and J. B. MacQueen, "Ferguson distributions via pólya urn schemes," *The annals of statistics*, pp. 353–355, 1973. (Cited in page 80.)

[165] B. Ristic, S. Arulampalam, and N. Gordon, *Beyond the Kalman filter: Particle filters for tracking applications.* Artech house, 2003. (Cited in page 83.)

[166] H. Kuusniemi, *User-level reliability and quality monitoring in satellite-based personal navigation.* Tampere University of Technology, 2005. (Cited in page 98.)

[167] N. Zhu, D. Bétaille, J. Marais, and M. Berbineau, "GNSS Integrity Enhancement for Urban Transport Applications by Error Characterization and Fault Detection and Exclusion (FDE)," in *Géolocalisation et Navigation dans l'Espace et le Temps, Journées Scientifiques 2018 de l'URSI*, p. 11p, 2018. (Cited in pages 121 and 181.)

[168] C. Legrand, *Contribution à l'évaluation de la sécurité de systèmes de localisation ferroviaires basés sur les GNSS par la formalisation des concepts d'intégrité étendue*. PhD thesis, Université de Lille 1, 2016. (Cited in pages xiii and 125.)

[169] N. Zhu, D. Bétaille, J. Marais, and M. Berbineau, "Extended kalman filter (EKF) innovation-based integrity monitoring scheme with C/N_0 weighting," in *2018 IEEE 4th International Forum on Research and Technology for Society and Industry (RTSI) (RTSI 2018)*, (Palermo, Italy), Sept. 2018. (Cited in pages 148, 181 and 182.)

[170] U. I. Bhatti and W. Y. Ochieng, "Detecting multiple failures in gps/ins integrated system: a novel architecture for integrity monitoring," *Journal of Global Positioning Systems*, vol. 8, no. 1, pp. 26–42, 2009. (Cited in page 149.)

[171] C. Call, M. Ibis, J. McDonald, and K. Vanderwerf, "Performance of honeywell's inertial/gps hybrid (high) for rnp operations," in *Position, Location, And Navigation Symposium, 2006 IEEE/ION*, p. 244, IEEE, 2006. (Cited in page 149.)

[172] Ç. Tanıl, S. Khanafseh, M. Joerger, and B. Pervan, "Kalman filter-based INS monitor to detect GNSS spoofers capable of tracking aircraft position," in *Position, Location and Navigation Symposium (PLANS), 2016 IEEE/ION*, pp. 1027–1034, IEEE, 2016. (Cited in pages 149, 155, 158 and 162.)

[173] M. Joerger and B. Pervan, "Kalman filter-based integrity monitoring against sensor faults," *Journal of Guidance, Control, and Dynamics*, vol. 36, no. 2, pp. 349–361, 2013. (Cited in pages 149, 158 and 159.)

[174] R. G. Brown and P. Y. Hwang, "Introduction to random signals and applied kalman filtering: with matlab exercises and solutions," *Introduction to random signals and applied Kalman filtering: with MATLAB exercises and solutions, by Brown, Robert Grover.; Hwang, Patrick YC New York: Wiley, c1997.*, 1997. (Cited in pages 150 and 151.)

[175] O. Le Marchand, "Autonomous approach for localization and integrity monitoring of a ground vehicle in complex environment," *Theses, Université de Technologie de Compiègne, June*, 2010. (Cited in page 156.)

[176] O. Garcia Crespillo, A. Grosch, J. Skaloud, and M. Meurer, "Innovation vs residual kf based gnss/ins autonomous integrity monitoring in single fault scenario," in *Proceedings of the 30th International Technical Meeting of The Satellite Division of the Institute of Navigation*, no. EPFL-CONF-234322, pp. 2126–2136, 2017. (Cited in pages 158, 160 and 162.)

[177] N. Zhu, D. Bétaille, J. Marais, and M. Berbineau, "GNSS Integrity Monitoring Schemes for Terrestrial Applications in Harsh Environments," *IEEE Intelligent Transportation Systems Magazine (Special Issue on GNSS for ITS) (submitted the 1st September 2018)*. (Cited in pages 181 and 182.)

[178] G. Agamennoni, J. I. Nieto, and E. M. Nebot, "An outlier-robust kalman filter," in *Robotics and Automation (ICRA), 2011 IEEE International Conference on*, pp. 1551–

1558, IEEE, 2011. (Cited in page 183.)

[179] J.-A. Ting, E. Theodorou, and S. Schaal, "A kalman filter for robust outlier detection.," in *IROS*, pp. 1514–1519, 2007. (Cited in page 183.)